Dust Formation and Evolution in the Ejecta of Core-collapse Supernovae

Inauguraldissertation
zur
Erlangung der Würde eines Doktors der Philosophie
vorgelegt der
Philosophisch-Naturwissenschaftlichen Fakultät
der Universität Basel

von

Arkaprabha Sarangi
aus Indien

Basel, 2015

Genehmigt von der Philosophisch-Naturwissenschaftlichen Fakultät auf Antrag von:

Prof. Dr. Friedrich-Karl Thielemann
PD Dr. Isabelle Cherchneff
Dr. Rubina Kotak

Basel, October 14, 2014

Prof. Dr. Jörg Schibler

The Dean of Faculty

Namensnennung-Keine kommerzielle Nutzung-Keine Bearbeitung 3.0 Schweiz
(CC BY-NC-ND 3.0 CH)

Sie dürfen: **Teilen** — den Inhalt kopieren, verbreiten und zugänglich machen

Unter den folgenden Bedingungen:

Namensnennung — Sie müssen den Namen des Autors/Rechteinhabers in der von ihm festgelegten Weise nennen.

Keine kommerzielle Nutzung — Sie dürfen diesen Inhalt nicht für kommerzielle Zwecke nutzen.

Keine Bearbeitung erlaubt — Sie dürfen diesen Inhalt nicht bearbeiten, abwandeln oder in anderer Weise verändern.

Wobei gilt:

- **Verzichtserklärung —** Jede der vorgenannten Bedingungen kann **aufgehoben** werden, sofern Sie die ausdrückliche Einwilligung des Rechteinhabers dazu erhalten.
- **Public Domain (gemeinfreie oder nicht-schützbare Inhalte) —** Soweit das Werk, der Inhalt oder irgendein Teil davon zur Public Domain der jeweiligen Rechtsordnung gehört, wird dieser Status von der Lizenz in keiner Weise berührt.
- **Sonstige Rechte —** Die Lizenz hat keinerlei Einfluss auf die folgenden Rechte:
    - Die Rechte, die jedermann wegen der Schranken des Urheberrechts oder aufgrund gesetzlicher Erlaubnisse zustehen (in einigen Ländern als grundsätzliche Doktrin des **fair use** bekannt);
    - Die **Persönlichkeitsrechte** des Urhebers;
    - Rechte anderer Personen, entweder am Lizenzgegenstand selber oder bezüglich seiner Verwendung, zum Beispiel für **Werbung** oder Privatsphärenschutz.
- **Hinweis —** Bei jeder Nutzung oder Verbreitung müssen Sie anderen alle Lizenzbedingungen mitteilen, die für diesen Inhalt gelten. Am einfachsten ist es, an entsprechender Stelle einen Link auf diese Seite einzubinden.

Quelle: http://creativecommons.org/licenses/by-nc-nd/3.0/ch/ Datum: 12.11.2013

Dedicated to my parents. . .

Looking for cosmic dust !!

Abstract

Observations of local supernovae over the past couple of decades have reported the presence of dust in the ejecta. The dust masses inferred from observations in mid-infrared and submillimeter wavelengths differ by a factor of 10^2 to 10^4. The composition of dust in the ejecta is yet to be determined with precision. The reddening of the high redshift quasars also indicate the presence of large masses of dust in the early galaxies, the source of which is not yet clear. The sizes of the dust grains in the ejecta control their probability of survival against the reverse-shock(s) in the remnant phase and their contribution to the total dust budget of the galaxy. Core-collapse supernovae and AGB stars are the most important sources of dust in a given galaxy, however their relative contributions are still uncertain.

This project aims to quantify the role of core-collapse supernovae as dust producers in the galaxy. I study the production of dust in Type II-P supernova ejecta by coupling the gas-phase chemistry to the dust nucleation and condensation phases using a chemical kinetic approach. Several supernova progenitor masses with homogeneous and clumpy ejecta is assessed to estimate the chemical type and quantity of dust formed. Grain size distributions are derived for all dust components as a function of post-explosion time. The obtained dust properties are used to calculate the spectral energy distributions which are then compared to the estimated fluxes from SN1987A. The chemistry of the gas-phase and the simultaneous formation of dust clusters are described by a chemical network that includes all possible processes efficient at high gas temperatures and densities. The formation of key bimolecular species (e.g., CO, SiO) and dust clusters of silicates, alumina, metal carbides and sulphides, pure metals, and amorphous carbon is considered.

The findings suggest the formation of dust in the ejecta with final masses between 0.3-0.14 $M_\odot$ depending on the physical conditions. Silicates, alumina and amorphous carbon stand out as the leading dust components. The grain size distributions are slewed towards large grains, and differ from the usual Mathis, Rumpl, & Nordsieck power-law distribution characterising interstellar dust. An increase in the degree of clumpiness and a decrease in the amount of radioactive ^{56}Ni induce an early formation of dust leading to larger dust mass and bigger grains ($\sim$ 0.1-1 μm). These grains are most likely to survive the shock phases and enrich the dust budget of the galaxy. The mass of the progenitor dictates the relative abundances C-rich and O-rich dust components. Our results highlight the fact that dust synthesis in Type II-P supernovae is not a single and simple process, as it is often assumed. They confirm the total dust mass gradually builds up over a time span of $\sim$ 5 years post-outburst, and provide a genuine explanation for the discrepancy between the small amounts of dust formed at early post-explosion times and the large dust masses derived from recent observations of supernova remnants.

Acknowledgements

All the research works I have done in 4 years of my PhD would not have been possible without the guidance, support and encouragement of many people with whom I share a wonderful professional or personal relation. First of all, I would like to express my sincere gratitude towards my supervisor PD Dr. Isabelle Cherchneff (University of Basel) for introducing me to the field. I am grateful to her, for her guidance, suggestions and critical remarks regarding my scientific works. She has always encouraged me to express my ideas freely, which has helped my understanding to mature. Moreover she has allowed me to participate in several international conferences, which has given me a lot of exposure and opportunity to acquaint with the dignified scientific community. It was a valuable experience to learn all the basics of research under her supervision and throughout my scientific career I shall remain grateful for this.

I am thankful to Prof. Dr. F.-K. Thielemann (University of Basel) for accepting me as a part of his Astrophysics group. He has always been very encouraging and I have a high regard for the friendly and supportive work environment in the group. Next I would like to acknowledge the guidance of Prof. Dr. John Plane (University of Leeds), who has provided me the inputs to formulate the grain condensation model. A special thank goes to Dr. Rubina Kotak (Queen's University Belfast) for interesting discussions and for kindly agreeing to referee my PhD thesis as an examiner. I am also grateful to Prof. Dr. Thomas Rauscher (University of Hertfordshire, University of Basel), Prof. Stefan T. Bromley (University of Barcelona) and Dr. Roger Wesson (European Southern Observatory) for important feedbacks, collaborations and discussions, which have enlightened our research.

I appreciate the support of all the EuroGENESIS CoDustMas group members for their precious inputs and discussions at various meeting and conferences over the last 4 years. Further and most importantly, I acknowledge the Swiss National Science Foundation for granting financial support to my research. Nothing would have been possible without the benevolent support of SNSF throughout the years of my PhD.

I am grateful to all my colleagues and seniors at the University of Basel, specially Ms. Chiara Biscaro and Mr. David Gobrecht, for a wonderful 4 years of working together. I would like to convey my regards to Dr. Matthias Hempel for useful discussions in office. I express my heartfelt gratitude to all my professors from my Bachelors and Masters days to whom I owe all my knowledge of physics.

I am also thankful to many of my friend, mainly Mr. Sutirtha Sengupta (MPI Bonn) for convincing me that stars can also be important ! Dr. Sandip De (IBM India,

University of Basel) has helped me to master many computational techniques for which I am grateful. Finally, I do not have enough word to thank my parents and my girlfriend for bearing with me through all the tough times and always being there to morally boost my confidence.

Contents

List of Figures

List of Tables

1 Introduction

The solid grains in space which may vary in size from the dimension of a few molecules to the order of microns, are broadly classified as cosmic dust. Cosmic dust has a diverse chemical composition, which includes carbon (amorphous and graphite), silicates (olivines, pyroxenes, both amorphous and crystalline), metal oxides (alumina, fayalite, magnesia, spinel), silica, pure metals (iron, magnesium, silicon), metal sulphides, carbides and some other species yet to be determined with certainty (Molster et al., 2010; Cherchneff, 2013a). Dust accounts for about 1-2% of the total mass in the universe. On the other hand, it is responsible for up to 60% of the total radiation from some galaxies which rightfully justifies its importance. Dust grains are efficient in absorbing and scattering UV, optical and near-infrared (IR) radiations, and re-emitting the absorbed energy in the mid-IR and submillimeter (submm) wavelengths (Martin, 1978). Owing to their continuum opacities, the dust grains absorb and emit over a large swathe of the electromagnetic spectrum. Cosmic dust profoundly influence the spectra and colours of stars and galaxies. Most importantly, dust in space act as the building blocks for the planets in a stellar system and eventually we are all made up of stardust. The branches of science related to the study cosmic dust has flourished over last three decades (Grün et al., 2001). Importantly, it has brought together researchers from various disciplines and expertise to concentrate on this unique field with diverse challenges. Table 1.1 briefly summarises the significant contributions of astronomers, meteoriticists, astrophysicists, chemists and mineralogists to enrich the study of dust in space. But did the field attain this enticing state of art, all of a sudden? Well, certainly not. Therefore, it is more than necessary at this point to quickly skim through the history of the field before introducing the issues that need further investigation.

TABLE 1.1: The roles played by various disciplines of science in the field

Field	Contributions to the study of cosmic dust
Astronomy	Quantification of cosmic dust: Identification of potential galactic and extra-galactic sources and study of the spectral energy distributions (SED)
Meteoritics	Morphology and compositions of dust grains in presolar meteorites, and samples collected from moon, comets or deep sea-sediments
Astrophysics	Genesis of cosmic dust and their life cycle through analytical modelling and simulations
Astrochemistry	The leading chemical processes in gas phase as well as on the grain surfaces in space through laboratory analysis
Mineralogy	The chemical types, the opacities and optical properties of dust grains

1.1 The history and background

The presence of dark regions in the milky way was first pointed out by Sir William Herschel in 1785 in his article 'On the Construction of the Heavens', where he termed these dark regions as 'holes in the heavens' (Herschel, 1785). The perception that these dark regions in space, of shapes like that of holes, lanes or filaments are regions void of stars, continued for another hundred years. At the beginning of the twentieth century astronomers started to realise, that the dark patches are not void, but are instead dense opaque regions that are obstructing the light from background stars (Barnard, 1919). The existence of solid particles in the interstellar clouds was then confirmed by the discovery of the colour excesses and interstellar reddening (Trumpler, 1930). The scattering of light by solid particles are wavelength dependant, with shorter the wavelength greater the effect. Therefore, blue light is affected more than the red, causing a reddening of the radiation from the background sources. These solids present in space were vaguely termed as cosmic dust. Images of dust cloud Bernard 68 (by European Southern Observatory) situated at a distance of about 500 light-years towards the southern constellation Ophiuchus (Figure 1.1), taken at different wavelengths ranging between the blue band at 440 nm to the Ks-band at 2.16 μm in near-IR, shows the diminishing effects of extinction with the increase of wavelength. However, from the early to middle years of the twentieth century, clouds of gas and solid particles in space was regarded only as an annoyance to the astronomers which prevented the accurate measurements of distant stars and galaxies. After the advent of IR astronomy in the 1960s, study of cosmic dust in space found a

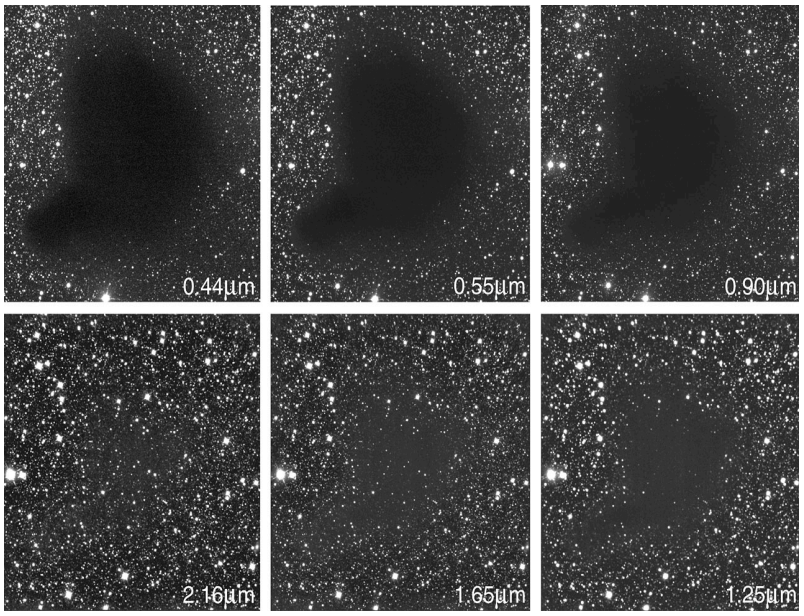

FIGURE 1.1: Dark Cloud Bernard 68 (distance $\sim$ 500 light-years) at different wavelengths **top-panel:** The dark patch indicates a concentration of interstellar dust, which obscures the light from the background stars at visible wavelengths. **bottom-panel:** The near-IR image of Bernard 68 revealing the presence of background stars as the obstruction by the cloud decreases with the increase of the probing wave-length (Courtesy: European Southern Observatory).

whole new meaning, and ever since, the field has only expanded leading to several astounding discoveries.

1.1.1 Infrared astronomy

Infrared astronomy holds the key to the understanding of cosmic dust. The infrared region of the electromagnetic spectrum ranges from 700 nm (the red edge of the visible spectrum) to approximately 1 mm. It is further subdivided into near-IR, mid-IR and far-IR regions in the order of increasing wavelength. IR astronomy deals with the detection and study of infrared radiation from various objects in the universe. Photometry and infrared spectroscopy form the backbone of IR astronomy. Photometry deals with the measurement of intensities and fluxes from celestial radiations. On the other hand, spectroscopy deals with the resolution and analysis of the spectral energy distributions of these radiations.

Large amount of informations can be derived from IR astronomy. Most of the energy in the IR is thermal, as any object which has a temperature radiates in

the mid-IR, far-IR or longer wavelengths. The following are the highlights of the otherwise unknown informations that IR astronomy can reveal to us.

- The hidden universe: The molecular and dust clouds block the radiation from stars and galaxies in the background in the visible region of the electromagnetic spectrum. However, at longer wavelengths in the near-IR it can pass through the clouds as scattering decreases considerably at these wavelengths. This enables us to study the centre of our galaxy, or regions of stellar nurseries (new star forming regions).

- Molecules: The radiation from molecules occur at the UV-optical regions for electronic transitions and in the IR for vibrational bands. Due to strong scattering, and presence of bright stars, the detection of molecules is difficult in the visible wavelengths. However, the vibrational transitions of molecules in the IR leads to the detection and identification of several molecules in space.

- Dust: The dust grains in space re-emit the absorbed radiation in the mid- and far-IR. Study of the dust continuum in the IR leads to the understanding of dust types and quantifies the dust masses. Dust is the prime focus our study, and therefore shall be addressed in the text time and again.

- Planets: Owing to the presence of bright stars, planets at distant galaxies cannot be detected. In the IR however, the radiation from the planets are the strong, and therefore they can be identified in the stellar system. In a similar analogy, also other cool objects such as cool stars, IR galaxies, nebulae can be detected in space.

- The early universe: The recession of distant galaxies away from us leads to the redshift of the radiation from these sources. At large redshifts, all of the ultraviolet and much of the visible light from distant sources is shifted into the infrared part of the spectrum by the time it reaches our telescopes. Therefore, IR astronomy helps us in understanding the early universe.

The biggest challenge for the IR astronomy is that, only a small part of the IR spectrum can actually be observed ('observed' shall hereafter mean recorded by telescopes) from ground, owing to the absorption by earth's atmosphere, mainly by water vapour. Although Sir William Herschel discovered IR radiation in 1800, not

much progress in the field of IR astronomy could be achieved in the next 150 years, apart from some pioneering works by Piazzi Smyth, Samual Pierpont Langley and Thomas Alva Edison. After the discovery of the colour excesses, and the presence of dust and gas clouds in space, the IR astronomy became a more relevant science. By the 1960s astronomers realised that, to explore the IR spectrum from space, the telescopes should record data at high altitude, in order to negate the effects of atmospheric shielding. Three possible ways to achieve that, are a) to set up telescopes on the top of high altitude mountain peaks, b) to raise the telescope above the atmosphere by helium balloons, and c) to attach the telescopes in jet transport aeroplanes. Between 1959 and 1980, several balloon experiments were launched (John Hofkins University, Goddard Institute of Space Science, University College London), IR telescopes were set up on Mauna Kea Observatory in Hawaii at 4200 m and Kuiper Airborne Observatory was mounted on jet transport plane C-141A by NASA (Walker, 2000). In 1983, the research gained further impetus with the launch of the first IR satellite telescope, IRAS which made up an all sky survey from 10 μm to 100 μm. It was followed up by several other space telescopes with increasing resolution like COBE (1989), ISO (1995), IRTS (1995), MSX (1996) in the next decade. The ground-based telescopes with IR capabilities are also developed including the Gemini and Keck, DENIS telescopes. Some of the most important telescopes operating in the near-IR, mid-IR, far-IR and submm launched in the 21^{st} century are Spitzer space telescope (3-180 μm), AKARI (2-200 μm), Herschel space observatory (55-700 μm) and WISE (3-25 μm). Recently developed Atacama Large Millimeter/submillimeter Array (ALMA), situated high on the Chajnantor plateau in Chile is a high resolution millimeter-submillimeter telescope which can study radiations from the coldest objects in the universe.

1.1.2 First analyses

The IR astronomy has provided all the necessary tools required to study dust in space. Our understanding has developed over the last half of the 20^{th} century through the observation and analysis of dust in galactic and extragalactic sources. Some of the pioneering works are mentioned here, which has thereafter led to the foundation of many new fields of studies.

In solar system: Comet Ikeya-Seki, named after its discoverers, was observed in the mid-IR in the year 1965. The comet seemed much brighter than it should

be, if it would only reflect sunlight. Therefore, it was evident that the comet is radiating on its own in the mid-IR, which confirms the presence of solid grains in it. Additionally, using its distance from the sun, the temperature of the comet was estimated to be around 750 K. However, when the same is derived using the IR colour temperatures, it was roughly 1150 K, which is about 400 K hotter (Becklin and Westphal, 1966). Physically the solid grains inside the comet are absorbing the visible light from the sun, and emitting it in the mid-IR which is $\sim$ 10 μm. When a grain is smaller in dimension compared to the wavelength it emits, the efficiency of emission is low. Therefore, in reality, the grains are absorbing sunlight efficiently, but are not radiating it in the same rate, which leads to a rise in their temperature. The estimated size of these particles are around $\sim$ 1 μm or smaller, which is of the same order of dust grains that we experience on earth. Hence the name is justified.

Star dust: The 76 cm telescope with a mid-IR detector built at the University of Minnesota was used in the 1960s to probe stars in the galaxy. An excess in the mid-IR luminosities were reported from the red giant stars. A more precise analysis showed a prominent feature at 10 μm from these stars (Ney and Gould, 1964). Further studies by Bob Gehrz and Nick Woolf found similar features in many evolving red giant stars (Gehrz and Woolf, 1970). The 10-11 μm band is a known characteristic of silicate rocks on earth and therefore the stardust in space was identified to belong to the silicate family. Notable astronomer Sir Fred Hoyle in his book 'Frontiers of Astronomy' intuitively foretold the presence of carbon dust in stellar atmospheres, where he mentioned the condensation of atomic carbon into small solid dust particles in the stellar winds pushed outwards by radiation (Hoyle, 1955). Silicates and carbon remain the most abundant dust types in space till date, and evidences of dust is reported from several other stellar sources in recent years in the Milky Way or nearby galaxies.

Dust in early universe: The reddening of the background quasars and Lyα systems at high redshift (z>6) indicates the presence of dust (Pei et al., 1991; Pettini et al., 1994). Large masses of dust of the order 1-5$\times10^8$ $M_\odot$ is estimated to be present in Sloan Digital Sky Survey (SDSS) J1148+5251, a hyperluminous quasar at z=6.4 (Bertoldi et al., 2003; Dwek et al., 2007). Figure 1.2 shows the location of high redshift galaxies on the cosmic time scale where presence of large dust masses are reported. The Population III stars present in these galaxies are predominantly massive and a large section is assumed to be in binary form. The

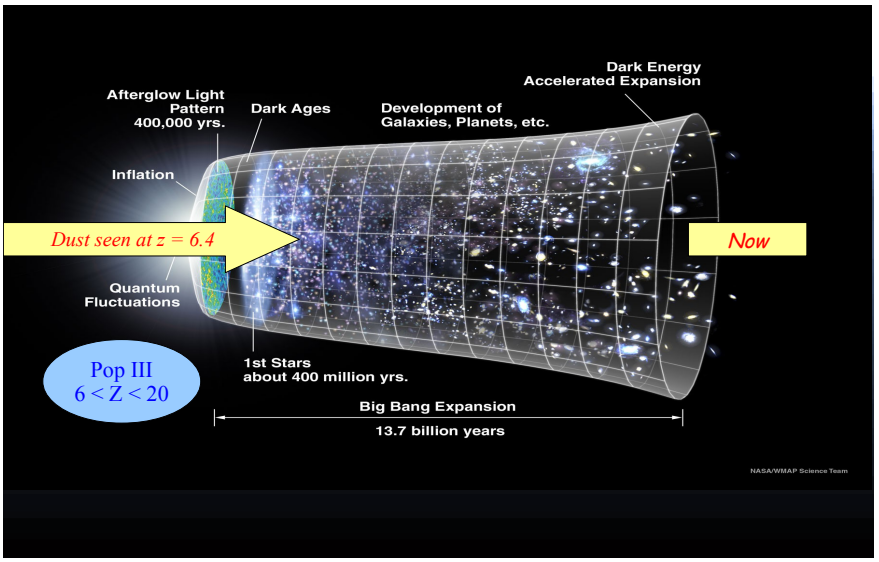

FIGURE 1.2: Evidence of large masses of dust reported from the far-IR spectrum of hyperluminous galaxy SDSS J1148+5251 at high redshift z = 6.4 (Bertoldi et al., 2003; Dwek et al., 2007) (Photo courtesy: NASA WMAP)

sources of such large masses of dust, and the formation mechanisms are yet to be understood with confidence. The following section now discusses the potential dust sources in local as well as the high redshift universe.

1.2 Origin of Dust

The presence of dust in space has been established with the help of IR astronomy as discussed in the previous section. The following is a bigger challenge which involves the investigation of the origin and the types of cosmic dust. Generically cosmic dust is formed of large clusters of chemical compounds. Synthesis of cosmic dust requires chemical processes which are sensitive to the local gas densities and temperatures. The chemical processes that prevail are those relevant at moderately high temperatures ∼1000-2000 K and high gas densities. Such physical conditions are encountered in winds, outflows and ejecta of evolved stars (Cherchneff, 2010, 2013b). However, the required temperature and densities in these evolving circumstellar environments persist only for a short timescale making the entire mechanism more complicated. Apart from circumstellar environments, growth of dust is also attributed to the dense molecular clouds in the interstellar medium.

Circumstellar environments: The evolved stellar environments responsible for dust formation in the galaxies are presented in Figure 1.3 with their respective position

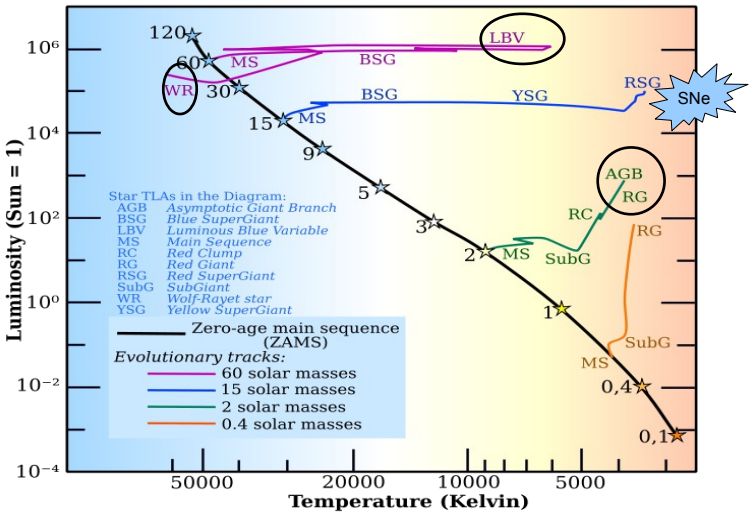

FIGURE 1.3: Hertzsprung-Russell diagram showing luminosity-temperature relation of stars at their evolutionary phases as function of main sequence mass. The potential stellar sources of cosmic dust are marked with circles. The core-collapse supernovae (SNe), the final fate of the RSG (red super giant) phase as shown in the diagram, is a major source of dust formation.

on the Hertzsprung-Russell diagram. The winds of the low mass (< 8 $M_\odot$) Asymptotic Giant Branch (AGB) stars are major dust producers in galaxies (Cherchneff, 2012; Gobrecht and Cherchneff, 2013). In oxygen-rich AGB stars, silicates, alumina and spinel are the expected dust types, whereas in C-rich stars amorphous carbon, graphite and silicon carbide are dominant. The massive (8-30 $M_\odot$ MS mass) stars which evolve to red supergiants (RSG) and ultimately lead to type II supernovae, marked in the figure (not in the scale of the H-R diagram), is a prime site for dust formation. Type II supernovae and AGB stars are the main stellar sources of dust. This study aims at quantifying the role of supernovae as dust producer in the galaxies (Sarangi and Cherchneff, 2013, 2014). The periodic eruptions in the massive Luminous Blue Variable stars (LBV) in the form of binaries also contribute to the total dust in the universe (Hillier et al., 2001; Ferland et al., 2005). The Wolf-Rayet stars undergo massive mass loss in its evolutionary stages where presence of dust has been inferred (Harries et al., 2004). Near the stellar envelopes the temperatures are too high for stable grains to exist as they are likely to be evaporated. In the case of stellar winds the effective temperature is mainly maintained by radiation and not by the ambient gas. This is typical to environments with low densities (lower than the earth atmosphere), which is the case for stellar winds or the supernovae ejecta after a few days from explosion. Therefore, in case of stellar outflows, the dust temperatures are functions of the

distance from the star. For the case of supernova ejecta, where the stellar core has already collapsed, the physical conditions evolve very fast and the entire processes of dust synthesis occurs in less than a decade.

Interstellar medium: Dust in the ISM is characterised by solid cores surrounded by ice mantles. The grains grow in mass in the time spans of the order of the molecular clouds. For significant growth of dust grains in the ISM the necessary conditions are a) the presence of preexisting grains cores on which accretion takes place b) The accretion timescales must be shorter than the lifetime of the clouds (Dwek and Cherchneff, 2011). Interstellar silicates are predominantly amorphous, whereas stardust silicate samples from meteorites are about 20% crystalline (Kemper et al., 2005). This indicates that all the dust in the ISM have not originated in the CSE. The presence of ice mantles in the dense interstellar clouds compared to the small dust present in the diffuse ISM confirms the growth of grains in the clouds. However synthesis of new seeds from the gas phase is highly unlikely in the ISM due to low densities and temperatures.

In order to explain the large masses of dust at high redshift galaxies, Dwek and Cherchneff, 2011 assumed the contribution from all possible dust producers in the galaxy and its balance with the galactic star formation rate. Massive stars evolve much faster compared to the low mass stars. Therefore, in the timescales of the lifetime of the early galaxies, supernovae are estimated to be the main source of dust. If a mass of 1 $M_{\odot}$ of dust is produced by core-collapse supernovae and reprocessed in the remnant phase, and a top-heavy Initial Mass Function is assumed for primeval stars, then the dust observed at high redshift can be explained. However, Cherchneff and Dwek, 2009, 2010 inferred a mass of 0.1-0.15 $M_{\odot}$ of silicate dust formed in the massive pair-instability supernovae as an upper limit. Moreover, the destruction of dust by the reverse shock in the ejecta or by UV photolysis in the ISM are yet to be quantified. AGB stars can only contribute as a major dust producer if the galactic age is assumed to be much larger (400 Myrs). Even though the observed dust mass are yet to be explained by the theoretical studies, in general supernovae are conclusively the prevalent dust source in the high redshift galaxies.

Out of all the potential sources, we focus on the role of local type II supernovae as a dust producer in the galaxy. Synthesis of dust in a suitable environment proceeds in two steps: the nucleation and the condensation, in local as well as the high z galaxies. The evolving media provide sufficient time for the gas to react

chemically forming molecules & clusters and concurrently to condense the clusters to form solid grains. In our study we trace the evolving ejecta through its molecule and dust synthesis phases. Therefore, understanding of molecule formation is the bottle-neck to the dust chemistry. Observational studies also support the argument by the establishment of correlation between molecules and dust dominated SED's (discussed later in this chapter and also chapter 5). In the analysis, we shall focus on the study of molecules with equal emphasis.

1.3 Types of supernovae

The previous section has introduced supernovae as major dust producers in the galaxies. Supernovae as a whole is a collection of several subclasses with diverse characteristics. Specifically, the study shall deal with the dust formation scenario in type II-P core-collapse supernovae. But before that, a general overview of supernovae and its types shall be handy to drive the analysis to the current state of art. Energetic stellar explosion which marks the end of a star's life is termed as a supernova. Supernovae are classified broadly on the basis of their optical spectra and some subclasses are defined by the nature of their light curves. The taxonomy is progressively developing since 1941 (Minkowski, 1941) and is extensively reviewed by Filippenko, 1997 & Wheeler and Benetti, 2000. A schematic presentation of the supernovae types are shown in Figure 1.4. The main classes of supernovae are type I and type II based on the presence of H lines in their spectra. Further, they are divided into subclasses as type Ia, Ib, Ic and type IIb, IIP, IIL, IIn respectively. The taxonomy does not take into account the explosion mechanism, which mainly depends on their main sequence mass and their late phase evolution pattern.

Type Ia: Supernovae type Ia is characterised by the absence of hydrogen lines in the spectra. The mechanism of explosion is thermonuclear and they commonly occur in low mass stars (Branch et al., 1995). Generally type Ia supernovae are associated to white dwarfs in binary systems. They are differentiated spectroscopically from other type I supernovae by the presence of silicon absorption lines. Type Ia supernovae are used as standard candles to determine the distances in space. Observations suggest, type Ia supernovae are not significant dust producers in the galaxy (Gomez et al., 2012a).

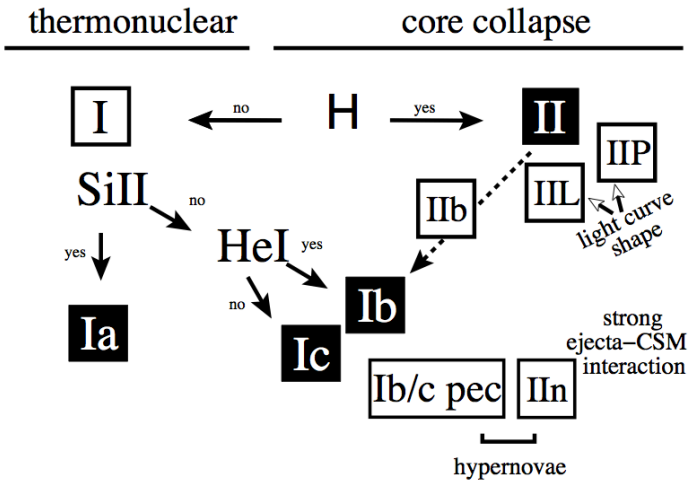

FIGURE 1.4: The current classification of supernovae done on the basis of the spectral types and light curves. On the basis of explosion mechanism, supernova explosion categorised as thermonuclear or core-collapse (Turatto, 2003).

Type Ib: The spectra of type Ib supernovae are characterised by the absence of H and Si II lines and the presence of He I (Barbon et al., 1999). They are associated with core collapse of massive stars (generally higher than 25 $M_{\odot}$ at main sequence) which have been stripped of their hydrogen envelope. They show evidences of shock interactions with dense circumstellar environments (Chevalier, 1982).

Type Ic: Supernovae type Ic is defined by the absence of He I lines which differentiates it from type Ib. Additionally, the oxygen lines are relatively stronger in type Ib and the nebular emission lines are broader (Matheson et al., 2000a). They are assumed to have lost both the H and He envelope in the late evolution stages due to strong stellar winds or interaction with close companion stars.

Type IIb: Type IIb are core collapse supernovae which has an early time signature similar to type II (presence of prominent H lines) and a late time spectra similar to type Ib (Matheson et al., 2000b). The decline of the light curve in type IIb are much faster compared to other type II which implies a smaller mass of the ejecta. Due to the absence of the other H envelope after explosion, the ejecta expands faster, and the typical gas densities are lower (Nozawa et al., 2010) when compared to a type IIP. Hence, a type IIb supernovae do not form dust as efficiently as type IIP's (Biscaro and Cherchneff, 2014).

Type IIP: The supernovae type II-P (Plateau) is the most abundant type of core-collapse supernovae in the local universe (Barbon et al., 1979). It differs from type

I's by the presence of prominent H lines in the spectra. The light curve is controlled by the radioactive decay of ^{56}Ni and ^{56}Co. The light curve is characterised by a flat plateau type nature during the first few months after explosion. Massive stars in the 8-25 $M_{\odot}$ range can result to a type II-P supernovae at the end of their lives. The presence of a large H envelope as the outer shell of the ejecta, makes the ejecta massive and the hence the densities of the expanding He core remains $\sim 10^2/10^3$ higher than type IIb's. The ejecta of type IIP supernova is a prime site of dust formation (Szalai and Vinkó, 2013; Sarangi and Cherchneff, 2013) which is also the main focus of the study.

Type IIL: The type II-L (Linear) supernovae have similar spectral characters as type IIP, however the light curve follows a gradual uninterrupted linear decline. There are not any significant differences between type IIL and IIP's and many observed objects fall in the intermediate category (Clocchiatti et al., 1996). The H shell after explosion in type IIL is estimated to be around 1-2 $M_{\odot}$ which is 5-10 times smaller than the type IIP's. Based on the degree of stripping of the envelope, supernovae can be arranged in sequence as type IIP-IIL-IIb-Ib-Ic (Nomoto et al., 1995) in the ascending order. Moreover, this is also the order of importance in terms of dust synthesis.

Type IILn: This category of core-collapse supernova is characterised by the presence narrow emission lines (Schlegel, 1990). The spectra of these objects undergo slow evolution dominated by strong Balmer emission lines and broad absorption bands are missing. Observations indicate early interaction between the ejecta and the circumstellar medium (Smith et al., 2012), which leads to a velocity shear followed by shocks. Many recent studies have reported the presence of warm dust at the region of interaction (Fassia et al., 2001; Mauerhan et al., 2013).

Apart from the observed supernovae which can be assigned to a particular class, there are a set of supernovae which exhibits rather uncommon features. They are commonly termed as Type II-pec or peculiar supernovae. Massive stars larger than 40-60 $M_{\odot}$ range explode through pair-instability mechanism and commonly termed as hypernovae when the explosion energies are much higher compared to the type II's. These kind of explosions are assumed to be a dominant supernova mechanism at high red-redshifts.

1.4 Observations of dust in local supernovae

Apart from the difficulties in IR observations as explained in the text above, also core-collapse supernovae are not common in our galaxy. Therefore, scientists have successfully traced only a few hundred of occurrences in last couple of decades. Nevertheless, with the advent of high resolution telescopes, more informations can be derived from a single observation and a general trend of dust formation in supernovae can be studied. The formation of warm dust in the ejecta is characterised by, a) an excess in the mid-IR region of the spectral energy distribution due to thermal emission (Roche et al., 1991; Bouchet and Danziger, 1993) b) a sharp decline in the optical light curve (Danziger et al., 1991) c) a progressive and systematic blue-shift of emission line profiles when the receding part of the ejecta is increasingly blocked by newly formed dust (Lucy et al., 1989) d) diminishing line emission of elements and molecules compared to the adjacent continuum, owing to depletion into dust (Bouchet and Danziger, 1993; Kotak et al., 2009). The first two cases might also arise either due to the an IR echo due to pre-existing dust in the circumstellar material (Smith et al., 2012) or escape of radioactive luminosity due to decrease in optical depth in the ejecta. But occurrence of any three or all the four phenomena concurrently clearly indicates the formation of new dust in the ejecta.

Type II supernova SN1987A which appeared in the Large Magellanic Cloud in February 1987 has been closely monitored by the observers from different parts of the world. The best monitored supernova till date shows the evidence of new dust formation in the ejecta around 500 days post explosion Lucy et al., 1989. Following that, warm dust has been detected in several type II supernovae over the last decade. Table 1.2 presents a list of some well studied supernovae and their dust masses as derived from mid-IR observations. The findings suggest a moderate mass of dust in the 10^{-5} to 10^{-2} $M_{\odot}$ range is produced in the ejecta between 100-1000 days of explosion. The dust masses are derived by fitting the mid-IR excess and the final estimate depends on the choice of dust composition, optical constants, grain sizes, and importantly on the degree of clumping. All these parameters can affect the derived mass by a factor or more than 10 (Ercolano et al., 2007). Some supernovae which showed early signs of dust formation, like SN2007it (Andrews et al., 2011), SN2004A (Szalai and Vinkó, 2013) , etc., when traced over a few hundred days, the mass of dust present in the ejecta seems to decrease at late times (Table 1.2). This can explained by the efficient cooling of

TABLE 1.2: The observed and derived masses of dust in several local type II-P supernovae and remnants in the IR and submm wavelengths (Gall et al., 2011; Szalai and Vinkó, 2013)

Infrared			
Name	Epoch (days)	Mass ($M_\odot$)	Reference
SN2007od	300	1.7(-4)	Inserra et al., 2011; Andrews et al., 2010
	455	1.9(-4)	Andrews et al., 2010
	667	1.8(-4)	Andrews et al., 2010
SN2007oc	415	3.7(-3)	Szalai and Vinkó, 2013
SN2007it	351	1.6-7.3(-4)	Andrews et al., 2011
	718	8.0(-5)	Andrews et al., 2011
	944	4.6(-5)	Andrews et al., 2011
SN2005af	214	4.0(-4)	Kotak, 2008; Smartt et al., 2009
SN2004A	445	2.0(-3)	Szalai and Vinkó, 2013
	563	1.8(-3)	Szalai and Vinkó, 2013
SN2004et	300	3.9(-5)	Kotak et al., 2009; Smartt et al., 2009
	464	6.6(-5)	Kotak et al., 2009
	795	1.5(-4)	Kotak et al., 2009
SN2004dj	270	0.3-2.0(-5)	Kotak et al., 2005; Szalai et al., 2011
	652	3.2(-5)	Meikle et al., 2011
	996	5.0(-5)	Meikle et al., 2011
SN2003gd	499	2.0-17(-4)	Sugerman et al., 2006
	678	2.7-20(-3)	Sugerman et al., 2006
SN2003J	471	7.1(-3)	Szalai and Vinkó, 2013
SN1999m	510	1.0(-4)	Smartt et al., 2009; Elmhamdi et al., 2003a
SN1987A	615	3.7-31(-5)	Wooden et al., 1993
	615	2-13(-4)	Ercolano et al., 2007
	775	5.9-50(-5)	Wooden et al., 1993
	775	2-7.5(-4)	Ercolano et al., 2007
	1153	5.0(-4)	Dwek et al., 1992
Submillimeter			
SN1987A	24 yrs	0.4-0.7	Matsuura et al., 2011
SN1987A	27 yrs	0.2	Indebetouw et al., 2014
The Crab	∼1000 yrs	0.02-0.24	Gomez et al., 2012b
Cas A (IIb)	∼330 yrs	0.06-0.085	Barlow et al., 2010

dust leading to non-detection in mid-IR. The other possibility that newly formed dust has been destroyed in the freely evolving ejecta at early time is highly unlikely. Considering molecule as tracers of dust formation, a brief summary of molecules from observations are listed in Chapter 5 Table 5.2. The first overtone transition ($\Delta\nu = 2$) of CO molecule at 2.3 μm has been reported as early as 100 days after explosion (Danziger et al., 1988). The fundamental band $\Delta\nu = 1$ at 4.65 μm has also been observed between 130-260 days (Catchpole et al., 1988). Emission from vibrationally excited silicon monoxide molecule was reported by Aitken et al., 1988 in SN1987A at 160 days post-explosion. The mid-IR observations of SN2004et by Spitzer Space Telescope, suggests the presence of SiO molecules in the ejecta in the

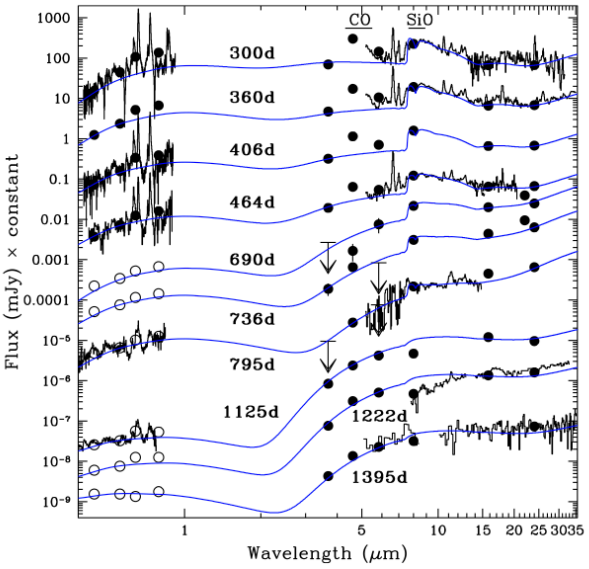

FIGURE 1.5: Mid-IR spectra of SN2004et between day 300 to day 1395 obtained from Spitzer Space Telescope is presented and analysed by Kotak et al., 2009. The coexistence of SiO lines and silicate emission features are reported. The gradual decline of SiO mass is correlated to the silicate formation sequence.

300-460 day period after the explosion (Kotak et al., 2009). Further investigation of the same supernova at times later than 690 days indicates the fading of SiO lines and the increase in strength of the continuum from dust. The spectra could be well fitted using a combination of SiO molecules and silicate dust (Figure 1.5). It was proposed that the depletion of SiO molecules in silicate dust attributes to the decline of the SiO emission lines in the ejecta.

Recent observations in the supernovae remnants by Spitzer, Akari, Herschel, ALMA telescopes point at much larger masses of dust (Gomez, 2013). A summary of the findings is presented in Table 1.2. SN1987A observed in the 100-700 μm wavelengths reveal the presence of cool dust at $\sim$20 K of mass between 04-0.7 $M_\odot$ (Matsuura et al., 2011). Observations with ALMA in 2013 reported an upper limit of 0.2 $M_\odot$ of dust in the same supernovae. An estimate of 0.02-0.24 $M_\odot$ of dust is derived from the study of the Crab Nebula through Spitzer and Herschel data (Gomez et al., 2012b). Overall the dust masses reported in the remnants are a factor of 10^2 to 10^4 larger than the masses estimated in the ejecta. This can be justified if either a) the dust formation processes continues over a timescale of decades and thus the mass grows from 10^{-5} $M_\odot$ to the order of $\sim$0.1 $M_\odot$ from the ejecta to the remnant phase b) the dust formed in the ejecta cools rapidly and thereby escapes observation in the mid-IR. Recent studies confirmed that after the encounter with the reverse shock in the remnant, new grains of dust cannot

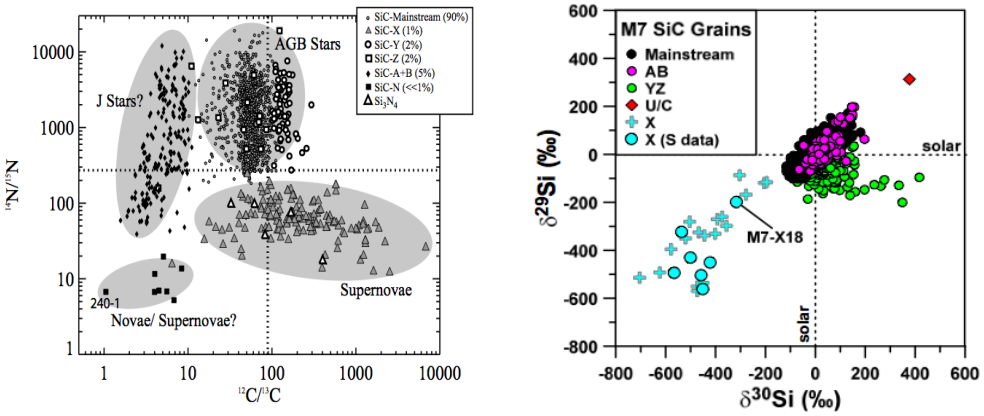

FIGURE 1.6: **Left panel:** The C and N isotopic ratio in the presolar SiC samples identifying their respective sources (Nittler, 2008). **Left panel:** Si-isotopic composition in presolar SiC grains. The X grains given by a '+' or filled circles trace supernovae origin (Hoppe et al., 2012)

reform from their gas phase precursors (Biscaro and Cherchneff, 2014). This disparity between the IR and submm observations remain unresolved till now and shall be addressed while discussing the open questions in the field.

1.4.1 Presolar stardust from meteorites

Indirect evidence for the formation and growth of dust grains in supernovae is provided by the study of pre-solar grains from meteorites. The samples of the presolar grains are collected and grouped according to the isotopic ratios of known elements such as C, N or Si. Depending on the known isotopic signatures from low mass J stars, AGB stars or supernovae, the origin of the grains are estimated. Some of those, called Type X grains of SiC, bear the isotopic anomaly signatures characteristic of supernovae. These include the presence of radiogenic ^{44} Ca, which stems from the decay of short-lived ^{44}Ti, an isotope only produced in supernovae (Zinner, 2007). Pre-solar grains of silicates, carbon, silicon carbide, and silicon nitride formed in SN ejecta have been identified (Hoppe, 2010). Typical lower limits for grain sizes are in the $0.1 - 1$ μm range, with some evidence of very large grains, e.g., one SiC grain produced in supernovae and with a radius of 35 μm has been found (Zinner et al., 2010). The isotopic anomaly signatures of Type X grains imply mixing in the ejecta whereby the innermost and outermost zones might have been in contact during or after the explosion. These results indicate the dust formed in the ejecta can survive the remnant phase, be incorporated to the Interstellar Medium, and travel to the Solar System.

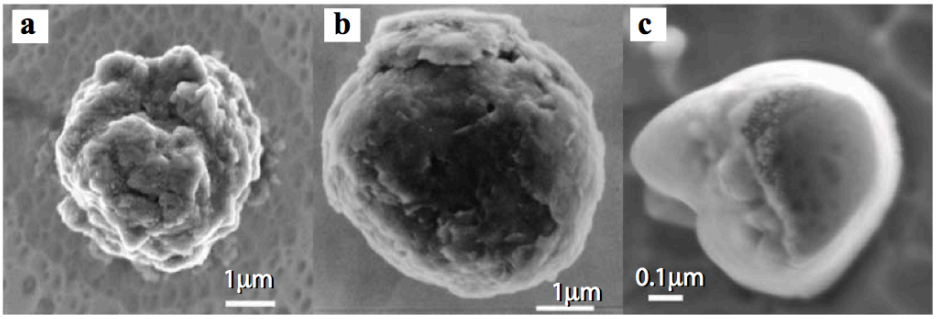

FIGURE 1.7: Scanning electron micrograph of presolar grains a) SiC b) Graphite c) Alumina (Clayton and Nittler, 2004; Nittler, 2008)

Hence, the fact that core-collapse supernovae are dust producers in galaxies has already been established. However the formation processes, the epochs of synthesis, final dust budget, its composition and importantly, the grain sizes, are yet to be determined with confidence.

1.4.2 Dust chemical composition

Compared to dust in earth's atmosphere, dust grains in space have simpler chemical forms as they exist in more hostile and pristine surroundings. The chemical types of cosmic dust and their precursor molecules are not well defined through observations due to lack of high-resolution mid-IR data (Cherchneff, 2013a). Composition of dust in space can be analysed by, a) the laboratory study of presolar grains from meteorites b) fitting of mid-IR spectral energy distribution using known opacities of probable dust species c) modelling of dust condensation from its gas phase precursors. A scanning electron micrograph image of presolar dust grains from meteorites are shown is Figure 1.7. Cosmic dust can be classified chemically as a) oxides (silicates of quartz or metal oxides) b) carbides c) sulphides d) homogeneous elemental clusters. Further they can be either crystalline or amorphous in nature depending on the physical conditions of the environment at the time of synthesis. Stretching and bending modes of vibration within the grains of a given type give rise to their unique emission or absorption features. The dust species can be identified by their mid-IR spectroscopic signatures through laboratory measurements. Table 1.3 gives a summary of known dust species and their mid-IR bands with the references.

TABLE 1.3: Circumstellar dust types derived from mid-IR (5-40 μm) spectra through laboratory experiments (Adopted from Cherchneff, 2013a)

Family	Name	Formula	Bands (μm)	Reference
		Oxides		
Silicates	Pyroxene	$Mg_xFe_{1-x}SiO_3$	10; 20	Dorschner et al., 1995
	Enstatite	$MgSiO_3$	9 – 12; 15.4; 19.5; 36.2	Chihara et al., 2002
	Ferrosilite	$FeSiO_3$	11.3; 20.4; 31.7	Chihara et al., 2002
	Olivine	$Mg_2xFe_{2-2x}SiO_4$	10; 20	Dorschner et al., 1995
	Fosterite	Mg_2SiO_4	10 – 12; 16.3; 19.5 – 24	Koike et al., 2003
	Fayalite	Fe_2SiO_4	10; 18 – 22; 27; 32	Suto et al., 2002
Quartz	Silica	SiO_2	9.1; 12.6; 20.4 – 21.2; 26.1	Fabian et al., 2000
Metal oxides	Alumina	Al_2O_3	13	Koike et al., 1995
	Spinel	$MgAl_2O_4$	13; 16.8; 32	Fabian et al., 2001
	Magnesia	MgO	19	Henning et al., 1995
	Wüstite	FeO	23.4	Henning et al., 1995
	Hematite	Fe_2O_3	9.2; 18; 21; 20	Koike et al., 1981
	Magnetite	Fe_3O_4	17; 25	Koike et al., 1981
	Calcium oxide	CaO	31.4	Hofmeister et al., 2003
		Carbon		
	Amorphous carbon	C	6.2; 8	Colangeli et al., 1995
	Graphite	C	6.3; 11.52	Draine, 1984
		Carbides		
	Silicon carbide	SiC	11.3	Mutschke et al., 1999
		Sulphides		
	Magnesium sulphide	MgS	25 – 39	Hofmeister et al., 2003
	Iron sulphide	FeS	23; 34; 39	Hofmeister et al., 2003

Precise determination of dust types present in a supernova ejecta is difficult. The mid-IR SED's obtained from a certain supernovae are addressed through modified black body fits (Kotak et al., 2009; Temim and Dwek, 2013) or through radiative transfer modelling (Ercolano et al., 2007; Szalai and Vinkó, 2013). The fitting parameters and the choice of opacity tables can affect the estimate of dust compositions (Sugerman et al., 2006; Ercolano et al., 2007). The study of mid-IR data from supernovae points to the presence of silicates and carbon as the main dust components in supernovae (Szalai and Vinkó, 2013; Gallagher et al., 2012; Kotak et al., 2009). In the remnant of SN1987A Matsuura et al., 2011 reported the presence of pure iron grains. Our study considers a bottom-up approach, where synthesis and evolution of various dust types are traced in a ejecta through concurrent phases of nucleation and condensation (Sarangi and Cherchneff, 2013, 2014). As many as nine different dust components are considered in the study which includes silicates, alumina, amorphous carbon, silicon carbide, iron sulphide, silica and pure iron, silicon & magnesium. The stratification of the ejecta dictates the possible types of dust components formed in a certain region. The details of the analysis is described in course of the text and summarised in the final chapter.

1.5 Motivation and open questions

We study the synthesis and evolution of dust in the ejecta of type II-P supernovae with a chemical kinetic approach. The analysis aims to couple the gas phase chemistry to the condensation phase of solid dust grains. The study traces the ejecta from a time few days after explosion to the arrival of the reverse shock in the remnant. The analysis assumes a non-steady state non-equilibrium environment replicating the real ejecta.

Over the past few decades several new discoveries have significantly enriched our understanding of the field. Nevertheless, there still remains some fundamental questions which requires more attention. Our study shall directly and indirectly address some of the unresolved issues in the field. On a broader perspective, we aim to justify the following.

- The disparity between the dust masses inferred from the mid-IR and the submm observations in local supernovae is an open question also termed as the dust dilemma in supernovae. Through the study of dust evolution and modelling of SED's with the new dust compositions, we target to find a plausible solution to the problem.
- The relative contributions of the core-collapse supernovae and evolved red giant AGB stars to the total dust budget of the galaxies, are not well understood. Our analysis shall focus on quantifying the contribution from a typical core-collapse event, and thereby the overall contribution of supernovae can be estimated using the supernova and star-formation rates of a given galaxy.
- The large mass of dust present in the high redshift universe is yet to be justified in theory. Considering supernovae as the prime dust producer, our study shall lead to the foundation of a more consistent model of dust formation in the early universe.

In search of the solution to the above issues, we try to answer all the wh-questions related to dust formation in the ejecta like a) when is the dust formed b) what are its the compositions c) how do the grains evolve in size d) which ejecta layers are efficient dust producers e) what are the contributions to the fluxes etc. In order to establish the consistency of the study we survey the sensitive parameters

and their impact on the scenario. The analysis therefore estimates the role of the following on the dust formation routes: *a*) Degree of clumpiness and density variation *b*) Variation of ^{56}Ni mass produced by the explosion *c*) Different main sequence masses of the progenitor stars.

Finally, the study provides the necessary inputs for other analyses such as,

- All the required inputs for dust radiative transfer modelling of the homogeneous and clumpy ejecta are estimated. The physical conditions of the ejecta are also derived to formulate the RT model.
- The grain size distributions of each dust types that shall encounter the reverse shock in remnants is calculated. The grain sizes will dictate the possibility of the grains to survive the shocks and contribute to the total dust in the galaxy.

This is the first chemical kinetic model to address the dust formation in local supernovae in a non-steady state and non-equilibrium environment.

1.5.1 Existing models

Several other studies have tackled the modelling of dust formation in Type II-P SNe. Dust production in supernovae was initially addressed by Clayton, 1979. The first attempt to model the synthesis of grains in SN1987A was carried out by Kozasa et al., 1989. Later studies dealt with the formation of dust in Type II-P SNe locally (Bianchi and Schneider, 2007) and at high redshift (Todini and Ferrara, 2001; Nozawa et al., 2003). All these studies consider the formation of dust grains from the gas phase using classical nucleation theory (CNT). Some of the models consider the impact of the steady-state formation of CO and SiO from the gas phase, including the destruction of CO by Compton electrons, on the final carbon and silicate dust mass (Todini and Ferrara, 2001; Bianchi and Schneider, 2007). A few of the existing models assume a fully-mixed ejecta (Todini and Ferrara, 2001; Bianchi and Schneider, 2007) whereas others consider stratified ejecta (Kozasa et al., 1989; Nozawa et al., 2003; Kozasa et al., 2009). The applicability of CNT to model dust formation in circumstellar environments was questioned by Donn and Nuth, 1985 and also the deviation from steady state assumptions were pointed out by Cherchneff and Dwek, 2009. The non-steady state dust formation scenario for

carbon and silicates has also been addressed by Nozawa and Kozasa, 2013 without tackling the gas phase chemistry. An initial concentration of carbon and silicate monomers are assumed in order to study the condensation phase. The fitting of SED's is necessary to infer the dust masses. Commonly modified blackbody fitting models with different temperatures (Gomez et al., 2012b; Temim and Dwek, 2013) are used to estimate the fluxes, and in some cases detail radiative transfer modelling is performed (Ercolano et al., 2007; Andrews et al., 2010; Gallagher et al., 2012). In the existing models the parameters used to fit the SED's are chosen intuitively which does not consider the build-up phase of dust. In the final chapter of the text, comparison with the existing models is presented and advantages of the new study are discussed.

1.6 An overview

The following chapters shall discuss the new model and its results in details. The entire study is based of core-collapse supernovae of type II-P considering it as the most prominent dust producer among all the supernovae types. Chapters 2, 3 and 4 are dedicated to the development of the physical & chemical model and the computer codes respectively. In order to justify the initial conditions used in the analysis, we have described the presupernova phases and the explosion mechanism in the first part of chapter 2. In chapter 3, the coupling between the gas phase and the solid phase of dust is discussed which holds the key to the entire chemical kinetic approach. Chapter 4 deals with the technical aspects of the study, where the physical and chemical models are implemented in the form of computer codes. Thereafter all the results are discussed in Chapters 5-8. The outcomes of the standard 15 $M_{\odot}$ progenitor star model is illustrated in a descriptive manner supported by necessary arguments. A 19 $M_{\odot}$ solar mass model is discussed as a surrogate to SN1987A in chapter 7, considering a homogeneous and also a clumpy ejecta case. The impact of ^{56}Ni mass is addressed in chapter 6 and chapter 8 as functions of progenitor mass. Chapter 9 deals with the dust radiative transfer modelling using the obtained results from chapter 4-7. Finally the entire analysis is summarised in chapter 10 and the conclusive remarks are derived.

2 Physical Model of the Ejecta

This chapter is dedicated to the discussion of the relevant physics, which controls the evolution of a typical type II-P supernova ejecta. In parallel the development of the physical model is described in order to justify the approach adopted in the study. The aim of the study is to trace the chemistry of a core-collapse supernova ejecta and determine it role and importance as a dust producer in the galaxy. The dynamic ejecta attains the physical conditions suitable for dust synthesis after 100 days from explosion and onwards. The study investigates the chemistry of the ejecta from day 100 to 5 years post-explosion. In this chapter, before introducing the details of the physical model, a short description of the pre-collapse phases and the core-collapse mechanism of a massive star is stated.

Massive stars with main sequence mass between 8-40 $M_{\odot}$ are expected to end their lives as core-collapse supernovae of type II. The observed local supernovae are mostly estimated to have a progenitor mass between 10-20 $M_{\odot}$. A 15 $M_{\odot}$ progenitor has been chosen as a standard case in the study, and all the general discussions are based on the same.

2.1 Evolutionary phases of massive stars

Protostars are formed in interstellar clouds under hydrostatic equilibrium. Following the virial theorem, the objects contract and their temperature increases. When the core temperature becomes high enough, the fusion of hydrogen to helium starts to occur in the core, termed as the main-sequence hydrogen burning phase. Thereafter the contraction stops due to nuclear energy production which

TABLE 2.1: Core temperatures, time scales, and luminosities of a 15 & a 20 $M_\odot$ progenitor corresponding to it's buring stages, from the main sequence to the onset of collapse (Woosley et al., 2002; Weaver and Woosley, 1993)

	15 $M_\odot$			20 $M_\odot$		
Fuel	T_c (K)	t (years)	L_{phot} $L_\odot$	T_c (K)	t (years)	L_{phot} $L_\odot$
Hydrogen	3.5(7)	1.1(7)	2.8(4)	3.7(7)	8.1(6)	6.3(4)
Helium	1.8(8)	2.0(6)	4.1(4)	1.9(8)	1.2(6)	1.0(5)
Carbon	8.4(8)	2.0(3)	8.3(4)	8.7(8)	9.8(2)	1.4(5)
Neon	1.6(9)	0.73	8.7(4)	1.6(9)	0.6	1.5(5)
Oxygen	1.9(9)	2.6	8.7(4)	2.0(9)	1.2	1.5(5)
Silicon	3.3(9)	4.9(-2)	8.7(4)	3.3(9)	3.0(-2)	1.5(5)

maintains the hydrostatic equilibrium. This is the longest of all the burning stages which spans over more than a million years in case of massive stars. When the hydrogen in the core gets exhausted, the core starts to contract, and the core temperature increases further. This is followed by the helium burning phase, where the helium at the core transforms to C and O. Again, when He in the core gets exhausted, a similar phenomena repeats. Thus, the evolution continues through successive carbon, neon, oxygen and silicon burning phases. The core temperature required to initiate a burning phase increases gradually from one stage to the next. Following the He burning phase, the timescales of the following phases successively get smaller, and the silicon burning is completed within a span of a few days. After the Si burning is over, the star is left with an inert Fe-core (Salaris and Cassisi, 2006). The average binding energy per nucleon for Fe being the highest, fusion of Fe requires energy, instead of releasing it. Therefore, the hydrostatic equilibrium cannot be achieved, and the core continue to continue to collapse at a great pace. The physical parameters corresponding to the evolutionary stages of a massive stars are listed in Table 2.1 for a 15 & a 20 $M_\odot$ progenitor. Massive stars have a life time of a few million years and the lifespan is roughly inversely related to the stellar mass at the main sequence.

The evolution phases succeeding the He-burning phase are qualitatively different when compared to the previous stages in terms of energy balance. Once the temperature of the core exceeds 5×10^8 K, energy losses by neutrinos due to pair annihilation start to dominate the energy carried away by the photons. Radiative energy transport and convection are relevant to determine the structure of the star, however the energy balance is controlled by the neutrino losses and the energy generation by gravitational contraction and nuclear burning. The advanced

burning stages can therefore be described as neutrino-driven contraction phase punctuated by occasional delays, when for a short period the nuclear fusion processes can balance the neutrino energy (Woosley et al., 2002). Due to the steep temperature dependance of the nuclear reactions, each burning phase has their unique physical parameters (Table 2.1). Of the four burning stages (C, Ne, O, Si), carbon and oxygen burning proceed via fusion, whereas the other two by partial photo-disintegration by thermal photons. Neutrino dominated energy loss leads to increasingly shorted burning timescales, but the photon radiation luminosity of the star remains roughly unaltered as the surface evolution fails to keep pace with the core. Owing to this large difference of evolution timescales, the dominant mass loss by stellar winds of these massive stars occur mainly during the hydrogen and helium burning stages only. Hence, the final outcome of the evolution phases is mainly dictated by the size of the C-O core after He burning, and less dependant on the initial progenitor mass on the main sequence (Thielemann et al., 2011).

2.1.1 The core-collapse event

The contraction of the core continues after the Si burning phase is over, as fusion of iron group nuclei are endothermic and cannot provide the necessary energy to attain stability. As a result, the Fe-core gains in mass until it reaches the critical value, the Chandrasekhar mass (maximum mass of a stable white dwarf) and eventually collapse marking the death of the star. The rate of contraction of the core accelerates essentially due to two instabilities arising for the following reasons, a) In the late stage of Si burning, electrons are strongly degenerate and characterised by increasing Fermi energy. This allows the electron capture thereby making the core neutron-rich. The removal of free electrons leads to a fall in electron degeneracy pressure which controls the rate of collapse. b) Photo-disintegration becomes more efficient, producing large number of α-particles (Salaris and Cassisi, 2006). As a result, the binding energy of the core is lower than before, thereby initiating the collapse. Initially, the neutrinos act only as a sink of energy and follow free streaming through the core. In the later part of the collapse, owing to the increasing density, the mean free path of the neutrinos become comparable to the core radius. This means, the neutrinos cannot escape the core without interacting. When densities increase further, the neutrino diffusion velocities becomes smaller than the velocity of the collapsing core, and therefore they get trapped. The evolution of the core is determined by the competition between gravity (causing the

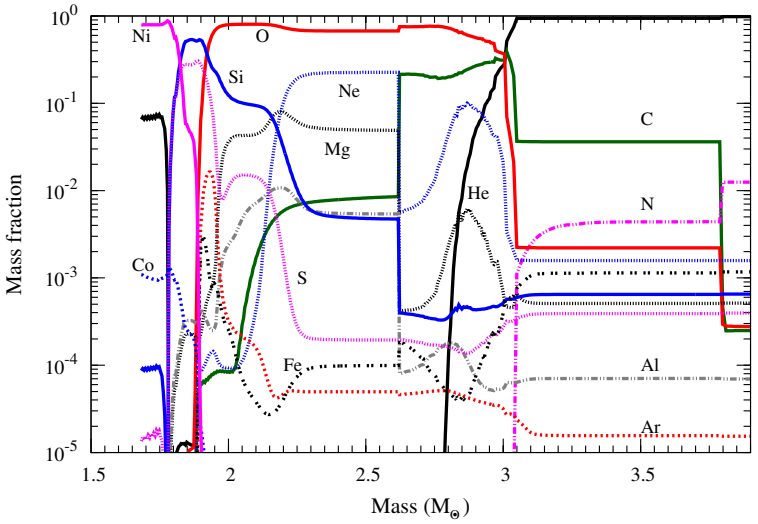

FIGURE 2.1: The post-explosion elemental abundances inside the He-core as a function of mass zones for a 15 $M_{\odot}$ progenitor star which has exploded as a type II-P supernova (Rauscher et al., 2002).

collapse) and the weak interactions (includes the rate of electron capture and the rate or neutrino trapping) (Thielemann et al., 2011). The energy deposition by the neutrinos in the core provide the extra energy to the explosive engine. When the core density reaches the order of $\sim 2\times10^{14}$ g cm^{-3}, which is the nuclear saturation density, the materials become incompressible and the collapse in the centre of the core ceases abruptly. As the compression stops all of a sudden, the core rebounds and interacts with the external layers which are continuing to contract. This creates a shockwave, and the outer portion of the core gets reflected back to its position prior to the collapse. This energy of collision added to the energy deposited by the neutrinos in the core, exceeds the binding energy of the outer shells. Therefore collapse and bounce of the core finally results in the expulsion of the whole stellar envelope. This explosive event is termed as a core-collapse supernova. In case of progenitors smaller than 25 $M_{\odot}$ at main sequence, a neutron star is produced after the explosion, whose mass is comparable to the mass of the iron core before the initiation of the collapse. Stars larger than the 25 $M_{\odot}$ produces a black hole at its core. The entire process of core-collapse occurs within a timescale of few milliseconds.

2.1.2 Post-explosion yields

In order to study the physics and chemistry of the supernova ejecta, the knowledge of the chemical yields from the star after its explosion, is necessary. The massive stars are one of the main sites for nucleosynthesis which takes place through a) the hydrostatic burning stages on timescales dictated by the nuclear energy sources b) explosive burning due to hydrodynamics of the catastrophic collapse phase (Thielemann et al., 2011). The physics of the evolution phases depends on the combination of magneto-hydrodynamics, nuclear reactions, radiation transport and thermodynamic properties. Thermonuclear energy generation shapes the interior of the star and leads to the generation of new chemical elements and nuclei. The nucleosynthesis in the massive stars was addressed in the 90's by Woosley and Weaver, 1995; Thielemann et al., 1996 and Limongi et al., 2000. Further study has been carried out by Rauscher et al., 2002 using revised reaction network, mass-loss rates, neutrino losses and newly derived opacity tables. In this model (Rauscher et al., 2002), the explosion was simulated as a piston moving inwards for 0.45 s to a radius of 500 km and then rebounded back to a radius of 10,000 km. The explosion energy was estimated $\sim 1.2\times10^{51}$ ergs which provides the kinetic energy to the ejecta. The final mass cut was determined by the mass that has settled on the piston at 2.5×10^{4} s after the collapse. The final mass of radioactive ^{56}Ni and ^{44}Ti, which are very important for the post-explosion evolution phases of the ejecta, are sensitive to the precise estimation of the mass cut. The simulations lead to the determination of nucleosynthesis yields from 15, 19, 20, 21, 25 $M_{\odot}$ stars of solar metallicity, which has exploded through core-collapse. The abundances of chemical elements obtained from the simulations by Rauscher et al., 2002 are presented as functions of mass zones in Figure 2.1 & 2.2. The final yields correspond to a timescale of 6-7 hours from the explosion. The post-explosion chemical compositions of the ejecta, which are the initial inputs to our study, are therefore derived using the dataset provided by Rauscher et al., 2002 and the corresponding electronic database.

2.2 The ejecta model

We study the ejecta of a typical type II-P supernova through the development of a homogeneous stratified 1D model. A 15 $M_{\odot}$ star ending its life as a type

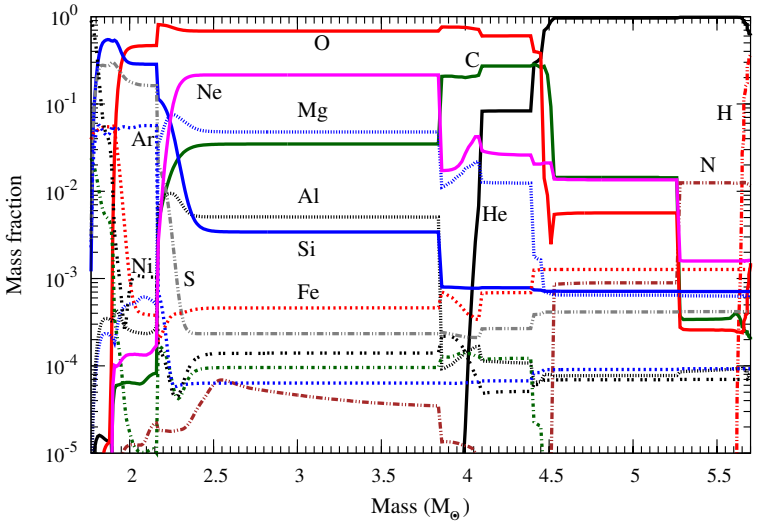

FIGURE 2.2: The post-explosion elemental abundnaces inside the He-core as a function of mass zones for a 19 $M_\odot$ progenitor star which has exploded as a type II-P supernova (Rauscher et al., 2002).

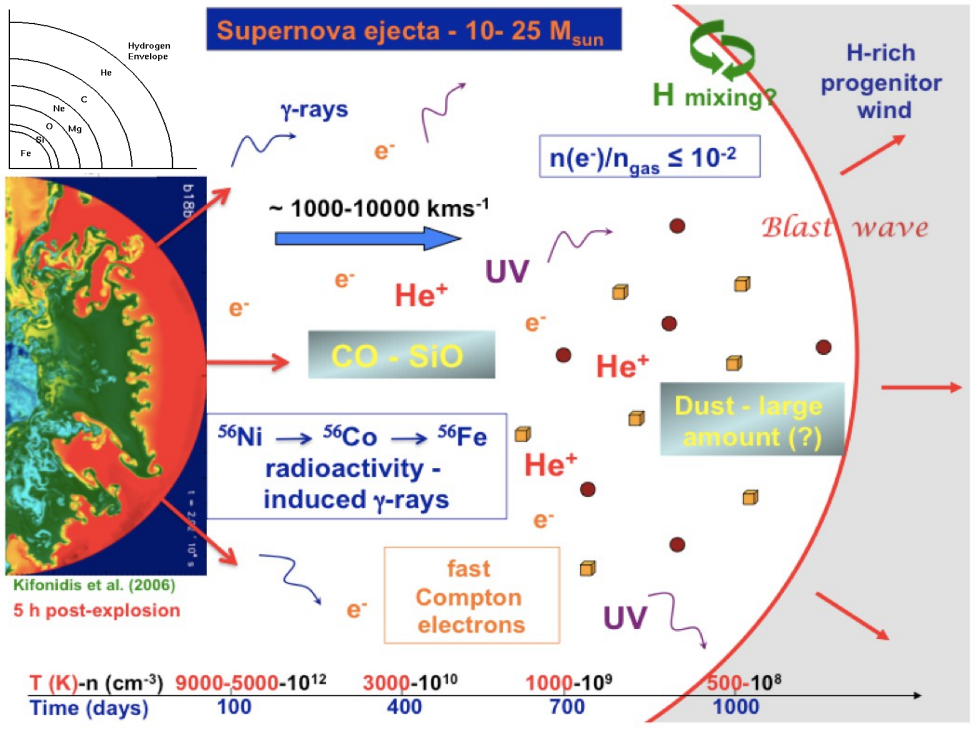

FIGURE 2.3: The schematic diagram represents the evolution of the type II supernova ejecta as a function of time. On the top left corner the stratification of the stellar core and envelope is shown which maintains the signature from the burning phases. Also within a few hours of the explosion the mixing and the Rayleigh-Taylor instabilities arising inside the ejecta are explained (Cherchneff and Sarangi, 2011; Kifonidis et al., 2006).

II-P supernova has been chosen as a standard case, with reference to the observed supernovae which are mostly estimated to be in the range of 12-19 $M_{\odot}$ in their main sequence. Further, the specific case of SN1987A has been tackled using a 19 $M_{\odot}$ model, to compare the results directly to the observational findings. The extreme cases of core-collapse supernovae are discussed through the modelling of a 12 $M_{\odot}$ and a 25 $M_{\odot}$ case in order to define the extreme upper and lower limits of the derived results. In this section, the parameters and the initial input conditions for the physical model is described, which forms the backbone of the entire analysis.

Following the expulsion of the helium core, the ejected materials are crossed by the blast wave which deposits energy in the gas. The neutrino-driven convection during the collapse leads to the Rayleigh-Taylor instabilities and mixing in the helium core. The mixing scenario continue over a few hours after the explosion and leads to partial fragmentation of the core (Joggerst et al., 2010). Thereafter, the chemical species produced by nucleosynthesis flows ballistically as carried by the blast wave. Hence the abundances of the elements presented as functions of mass zones in the ejecta can be safely assumed to remain constant over the next few days until the chemical reactions becomes relevant. A schematic view of the ejecta conditions is presented in Figure 2.3. For the sake of simplicity, a constant ejecta velocity is assumed which is determined by the explosion energy which is converted to the total kinetic energy of the ejecta (given by Equation 2.1) (Cherchneff and Dwek, 2009). The explosion energy is estimated with reference of SN1987A (Woosley, 1988), and a value of $1{\times}10^{51}$ ergs (E_{exp}) is considered for all progenitor cases. The progenitor of SN1987A is estimated to be a 19 $M_{\odot}$ star. Therefore the ejecta velocity can be derived using Equation 2.1 to be $\sim$ 2300 km/s.

$$v_{ej} = \sqrt{\frac{2 \times E_{exp}}{M_{ej}}} \tag{2.1}$$

The role played by the radioactive nuclei in the ejecta is crucial, and it is discussed in detail in the following Section 2.2.2. The evolution of the ejecta is traced by the physical model from a time 100 days post-explosion until day 2000 (Sarangi and Cherchneff, 2013). From the observations of SN1987A and other local supernovae, it can be generally confirmed that molecule or dust formation in the ejecta occurs at times later than 110 days (Catchpole et al., 1988; Danziger et al., 1991; Wooden et al., 1993). The ejecta temperatures are high and the destruction processes

dominate prior to that time. Also late times with $t > 2000$ days, the temperature and densities become too low to support further chemical processes to continue. Therefore the choice of the time range is justified.

2.2.1 Stratification of the ejecta

The post-explosion elemental abundances from Rauscher et al., 2002 as function of mass coordinates remain consistent till day 100, under the consideration that a) no further microscopic mixing takes place after a few hours from explosion b) chemical processes are not effective before day $\sim$ day 100. Figures 2.1 & 2.2 presents the element abundances in a 15 $M_\odot$ and a 19 $M_\odot$ progenitor respectively. The figures clearly indicate that abundance of any given element remains mostly uniform over a certain region of the mass coordinate and thereafter abruptly falls or rises to attain a new value. Moreover, the element abundances are found retain the signatures from the successive core burning stages. Hence on the basis of the abundances, the ejecta was stratified into several zones. The gas within each zone is considered to be fully microscopically mixed. However, no leakage between different zones is assumed. The chemical networks were developed specific to the ejecta zones, controlled by the dominant species. Importantly, the presence of nobel gases such as Ar, Ne or He in good abundances in certain zones compared to others, impacts the productivity of the given zones. The ejecta of the 15 $M_\odot$ progenitor model is divided into 8 zones according to the presence of important elements: 1A (Si/S), 1B(Si/O), 2(O/Si/Mg), 3(O/Ne/Mg), 4A(C/O), 4B(C/O/He), 5(He/C) & 6(He/N). The central oxygen core is made up of zones 1B, 2 and 3, which are the most important regions for synthesis of molecules and dust. The outermost helium shell (zones 5 and 6) is the only site in the ejecta characterised by C/O>1. In case of the 19 $M_\odot$ model, the size of all the zones are comparable to the corresponding zones of the 15 $M_\odot$ case, with the exception of the central oxygen core which is considerably larger. The sizes, the compositions and the C/O ratios of the respective zones are described in Table 2.2 & 2.3 for the 12, 15, 19 & 25 $M_\odot$ progenitor models. The initial mass yields are taken from Rauscher et al., 2002 for 15, 19, 25 $M_\odot$ cases, while that of the 12 $M_\odot$ progenitor data is from Woosley and Heger, 2007.

TABLE 2.2: Initial (post-explosion) chemical composition ($M_\odot$) as functions of progenitor mass and ejecta zones [a]

Zone	μ(gas)	C/O	He	C	O	Ne	Mg	Al	Si	S	Ar	Fe	Co	Ni
$M_\odot$	12 $M_\odot$, He-core : 3.27 $M_\odot$, $\tau_0 = 13$													
1A(1.7-1.76)	32.0	0.21	0	9.8(-8)	6.7(-7)	3.0(-7)	7.3(-6)	1.2(-5)	2.5(-2)	2.4(-2)	3.3(-3)	4.8(-3)	1.5(-3)	3.5(-5)
1B(1.76-1.89)	17.4	3.7(-4)	0	2.9(-5)	0.1	1.3(-5)	5.7(-3)	4.2(-4)	1.6(-2)	2.6(-3)	7.4(-5)	5.7(-5)	1.6(-5)	1.2(-4)
2(1.89-2.03)	17.3	7.9(-3)	0	5.5(-4)	9.2(-2)	3.5(-2)	8.7(-3)	5.6(-4)	6.0(-4)	4.2(-5)	1.2(-5)	1.3(-4)	0	0
3(2.03-2.19)	15.3	0.3	0	3.0(-2)	0.12	7.4(-3)	2.7(-3)	2.1(-4)	1.5(-4)	3.5(-5)	1.4(-5)	8.2(-5)	0	0
4(2.19-2.35)	4.9	15.4	0.12	3.7(-2)	3.2(-3)	2.1(-3)	8.0(-4)	9.3(-6)	1.5(-4)	5.0(-5)	1.3(-5)	1.8(-4)	0	0
5(2.35-3.27)	4.1	1.3	0.91	1.9(-4)	2.0(-4)	1.0(-2)	6.6(-4)	6.8(-5)	7.5(-4)	3.9(-4)	1.0(-4)	1.3(-3)	0	0
$M_\odot$	15 $M_\odot$, He-core : 4.14 $M_\odot$, $\tau_0 = 16$													
1A(1.79-1.88)	35.5	5.9(-2)	0	1.5(-7)	3.3(-6)	0	1.4(-5)	2.0(-5)	3.2(-2)	2.0(-2)	4.0(-3)	1.7(-2)	1.2(-2)	2.8(-4)
1B(1.88-1.98)	20.9	2.1(-3)	0	6.9(-6)	4.4(-2)	1.0(-5)	3.9(-4)	5.0(-5)	3.1(-2)	1.3(-2)	7.4(-4)	1.3(-4)	5.1(-5)	1.2(-7)
2(1.98-2.27)	17.2	5.5(-3)	0	9.3(-4)	0.23	1.5(-2)	1.6(-2)	2.1(-3)	2.1(-2)	2.5(-3)	4.1(-5)	2.3(-5)	0	0
3(2.27-2.62)	17.1	1.6(-2)	0	2.8(-3)	0.23	7.8(-2)	1.8(-2)	1.9(-3)	1.8(-3)	6.8(-5)	1.7(-5)	2.3(-5)	0	0
4A(2.62-2.81)	15.0	0.37	6.1(-6)	4.0(-2)	0.15	3.0(-3)	1.6(-4)	2.3(-4)	7.1(-5)	3.5(-5)	9.6(-6)	2.2(-5)	0	0
4B(2.81-3.04)	10.7	0.74	3.1(-2)	6.2(-2)	0.11	1.4(-2)	7.1(-4)	1.9(-5)	1.1(-4)	4.4(-5)	8.6(-6)	4.0(-5)	0	0
5(3.04-3.79)	4.1	21.3	0.71	2.7(-2)	1.7(-3)	1.2(-3)	3.9(-4)	5.3(-5)	4.8(-4)	2.9(-4)	1.2(-5)	8.4(-4)	0	0
6(3.79-4.14)	4.1	1.2	0.34	9.1(-5)	9.6(-5)	5.5(-4)	1.8(-4)	2.4(-5)	2.3(-4)	1.4(-4)	5.3(-6)	4.1(-4)	0	0

[a]The mean molecular weights are in g, the data for 12 $M_\odot$ progenitor is from Woosley and Heger, 2007 and data for 15 $M_\odot$ progenitor is from Rauscher et al., 2002.

TABLE 2.3: Initial (post-explosion) chemical composition ($M_\odot$) as functions of progenitor mass and ejecta zones [a]

Zone	μ(gas)	C/O	He	C	O	Ne	Mg	Al	Si	S	Ar	Fe	Co	Ni
$M_\odot$	19 $M_\odot$, He-core : 5.62 $M_\odot$, $\tau_0 = 22.3$													
1A(1.77-1.88)	35.4	0.16	1.4(-6)	8.1(-8)	6.9(-7)	0	1.7(-5)	2.5(-5)	3.8(-2)	2.3(-2)	4.5(-3)	2.5(-2)	1.3(-2)	3.3(-4)
1B(1.88-2.18)	22.5	1.3(-3)	0	1.2(-4)	0.12	1.1(-4)	8.8(-4)	2.2(-4)	9.9(-2)	5.6(-2)	1.5(-2)	3.1(-3)	3.3(-4)	6.2(-6)
2(2.18-3.86)	16.9	6.5(-2)	0	5.9(-2)	1.2	0.34	8.4(-2)	9.1(-3)	1.5(-2)	1.3(-3)	1.2(-4)	7.5(-4)	0	0
3(3.86-4.00)	15.1	0.36	0	2.9(-2)	0.11	2.8(-3)	2.0(-3)	1.6(-5)	1.1(-4)	3.2(-5)	8.9(-6)	7.8(-5)	0	0
4(4.00-4.49)	10.3	0.64	7.7(-2)	0.13	0.26	1.3(-2)	5.4(-3)	5.3(-5)	3.8(-4)	1.4(-4)	3.5(-5)	3.8(-4)	0	0
5(4.49-5.26)	4.1	3.93	0.74	1.3(-2)	4.3(-3)	1.1(-2)	5.0(-4)	6.0(-5)	5.5(-4)	3.2(-4)	7.0(-5)	9.8(-4)	0	0
6(5.26-5.62)	4.1	1.8	0.35	1.3(-4)	9.2(-5)	5.7(-4)	2.3(-4)	3.2(-5)	2.6(-4)	1.5(-4)	3.3(-5)	4.6(-4)	0	0
$M_\odot$	25 $M_\odot$, He-core : 8.3 $M_\odot$, $\tau_0 = 33$													
1A(2.1-2.33)	34.3	–	2.9(-6)	0	0	0	4.9(-5)	4.8(-5)	8.9(-2)	5.2(-2)	9.9(-3)	3.2(-2)	2.3(-2)	5.4(-4)
1B(2.33-2.51)	26.2	4.0(-4)	0	8.2(-6)	2.8(-2)	1.7(-5)	5.9(-5)	6.5(-5)	8.9(-2)	4.3(-2)	8.5(-3)	3.8(-4)	5.1(-5)	1.4(-6)
2(2.51-2.98)	19.3	4.2(-4)	0	8.7(-5)	0.28	6.1(-5)	7.2(-3)	7.0(-4)	0.12	3.7(-2)	9.2(-3)	1.3(-4)	0	0
3(2.98-5.69)	17.0	2.3(-2)	0	4.3(-2)	1.95	0.4	0.13	2.1(-2)	5.8(-2)	8.3(-3)	1.1(-3)	1.2(-4)	0	0
4A(5.69-6.22)	15.0	0.33	0	0.10	0.41	5.0(-3)	3.0(-4)	7.2(-5)	1.8(-4)	8.9(-5)	3.2(-5)	4.0(-5)	0	0
4B(6.22-7.11)	12.4	0.49	6.2(-2)	0.23	0.53	4.6(-2)	2.6(-3)	1.4(-4)	3.2(-4)	1.4(-4)	5.0(-5)	7.6(-5)	0	0
5(7.11-8.07)	4.1	35.9	0.92	1.3(-2)	4.8(-4)	1.5(-3)	4.8(-4)	7.2(-5)	6.1(-4)	3.6(-4)	8.6(-5)	1.0(-3)	0	0
6(8.07-8.30)	4.1	1.57	0.23	6.9(-5)	5.8(-5)	3.7(-4)	1.2(-4)	1.8(-5)	1.5(-4)	9.4(-5)	2.1(-5)	2.8(-4)	0	0

[a]The mean molecular weights are in g, the data for 19 and 25 $M_\odot$ progenitors are from Rauscher et al., 2002.

2.2.2 Radioactivity

The supernova light curve is powered by radioactive decays. The initial shock-deposited energy from the explosion is radiated away in a couple of weeks. After that, the bolometric luminosity, which includes the optical, IR and UV emissions is controlled by interactions between high energy radiations with the supernova ejecta. There are several radioactive nuclei produced in the explosion. On the basis of the abundances and the half-lives the most important radioactive nuclei in the ejecta are ^{56}Ni, ^{57}Ni, ^{55}Co, ^{44}Ti and ^{22}Na. ^{56}Ni has a very short life time of 6 days, and quickly decays to ^{56}Co through electron capture. ^{56}Co in turn decays to ^{56}Fe with a half-life is 77.12 days. The light curve of the first few years of SN1987A is dominated by ^{56}Co and a mass of 0.075 $M_\odot$ reproduces the bolometric luminosity. Hence an equal amount of ^{56}Ni is estimated to be produced in the explosion. The ^{56}Co decay through electron capture ($^{56}Co \longrightarrow {}^{56}Fe + \gamma + \nu_e$) and produces energetic γ-rays and electron neutrinos. The total energy emitted by the γ-ray-photon per ^{56}Co nuclei is 3.57 Mev (E_γ) (Woosley et al., 1989; Cherchneff and Dwek, 2009). The energetic γ-rays interact with the ejecta and gets degraded to hard X-rays through Compton scattering. The fast Compton electrons thermalize the ejecta through heating, excitation and ionisation. The hard X-ray gets further degraded to soft X-rays and UV photons through cascades of inverse Compton, and ionization-recombination processes. The entire energy of the γ-rays is not deposited in the ejecta. Study of the SN1987A light curve indicates the presence of macroscopic mixing of ^{56}Ni in the ejecta, which is also confirmed by the early emergence of γ-rays and X-rays, within a few hundred years from explosion. The ejecta is presumably clumpy, and hence a small fraction of the high energy photons can possibly pass through the less dense interclumps unabsorbed (McCray, 1993). However, the opacity of the ejecta is found to increase rapidly at the early times. Hence to an approximation of first order, the fraction of escaping energy becomes negligible. In the study we assume, the entire radioactive energy is uniformly deposited in the ejecta.

The total number of radioactive ^{56}Co present in the ejecta at time t in controlled by Equation 2.2, where, N_0 is the total number at $t = 0$ and τ_{Co} is the life time of

the radioactive nuclei.

$$N(t) = N_0 \ \exp\left(-\frac{t}{\tau_{Co}}\right)$$
$$\tau_{Co} = \frac{t_{1/2}(Co)}{ln\ 2} = \frac{77.12}{ln\ 2} = 111.26\ d \tag{2.2}$$

N_0 is calculated using the initial mass 0.075 $M_\odot$ of ^{56}Co produced in the explosion (Equation 2.3).

$$N_0 = \frac{M_{Co} \times N_A}{m_a(Co)} = \frac{(0.075 \times 1.989 \times 10^{33}) \times (6.022 \times 10^{23})}{56} = 1.6 \times 10^{54} \tag{2.3}$$

The rate of energy deposition in the ejecta by radioactivity of ^{56}Co, is therefore calculated with the help of E_γ (Woosley et al., 1989),

$$L_\gamma = \left|\frac{dN(t)}{dt}\right| \times E_\gamma \times f(\tau(t)) = \frac{1}{\tau_{Co}} N_0 \ \exp\left(-\frac{t}{\tau_{Co}}\right) \times E_\gamma \times f(\tau(t))$$
$$= \frac{1}{111.26 \times 86400} \times (1.6 \times 10^{54}) \times (3.57 \times 1.602 \times 10^{-6}) \times \exp\left(-\frac{t}{\tau_{Co}}\right) \times f(\tau(t))$$
$$= 9.54 \times 10^{41} \times \exp\left(-\frac{t}{\tau_{Co}}\right) \times f(\tau(t))\ (ergs/s) \tag{2.4}$$

where the deposition function $f(\tau(t))$ is the correction factor which accounts for the γ-ray optical depth $\tau(t)$ of the ejecta at time t. The life time of ^{56}Ni being very short, we assume the radioactivity of the ejecta in its first few years is entirely controlled by ^{56}Co and is governed by Equation 2.4. The deposition function $f(\tau(t))$ is expressed as (Cherchneff and Dwek, 2009),

$$f(\tau(t)) = 1 \ - \ \exp[-\tau(t)] = 1 \ - \ \exp[-(\kappa_\gamma \times \phi(t))]$$
$$= 1 - \exp[-\kappa_\gamma \times (\rho(t)R(t))] = 1 - \exp\left[-\kappa_\gamma \times \frac{3M_{He}}{4\pi\ (R(t))^2}\right] \tag{2.5}$$

where κ_γ is the average γ-ray mass absorption coefficient of the ejecta, $\phi(t)$, $R(t)$ and $\rho(t)$ are the mass-column density, the radius and the mass density of the ejecta at time t. M_{He} is the mass of the helium core. When the γ-ray optical depth is large, Equation 2.5 suggests the correction function $f(\tau(t)) \rightarrow 1$. The mass absorption coefficient κ_γ is calculated from a mixed distribution of ^{56}Co in the ejecta by Woosley et al., 1989 through Monte Carlo simulation. We use this

effective value ($\kappa_\gamma = 0.033\ cm^2 g^{-1}$) for all our models. Considering a constant expansion velocity of the ejecta, v, determined by the explosion energy, the column density at some fiducial time t_0 can be expressed as,

$$\phi(t) = \frac{3M_{He}}{4\pi\ (vt)^2}, \quad \phi(t_0) = \frac{3M_{He}}{4\pi\ (vt_0)^2}, \quad \phi(t) = \phi(t_0)\Big(\frac{t}{t_0}\Big)^{-2} \tag{2.6}$$

Hence the simplified form of L_γ is expressed in terms of optical depth τ_0 at time $t_0 (= \kappa_\gamma\ \phi(t_0))$ by Equation 2.7.

$$\begin{aligned} L_\gamma &= 9.54 \times 10^{41} \times \exp\Big(-\frac{t}{\tau_{Co}}\Big)\Big(1 - \exp\Big[-\tau_0\Big(\frac{t}{t_0}\Big)^{-2}\Big]\Big)(ergs\ s^{-1}) \\ &= 5.95 \times 10^{53} \times \exp\Big(-\frac{t}{\tau_{Co}}\Big)\Big(1 - \exp\Big[-\tau_0\Big(\frac{t}{t_0}\Big)^{-2}\Big]\Big)(eV\ s^{-1}) \end{aligned} \tag{2.7}$$

The estimated expression for L_γ has been calculated with reference to SN1987A. The rate of energy deposition is linearly proportional to the total mass of ^{56}Co as shown in Equation 2.3 & 2.4. Hence for any supernovae of this kind, the rate expression for L_γ is given by,

$$L_\gamma = 5.95 \times 10^{53} \times \frac{M_{Co}}{M_{Co}(SN1987A)} \times \exp\Big(-\frac{t}{\tau_{Co}}\Big)\Big(1 - \exp\Big[-\tau_0\Big(\frac{t}{t_0}\Big)^{-2}\Big]\Big) \tag{2.8}$$

For all the progenitor models, the fiducial time t_0 is chosen as 100 days from the time of explosion. The ejecta velocity for a 19 $M_\odot$ progenitor has been derived in Section 2.1 as 2300 Km/s, using the explosion energy of SN1987A. The explosion energy varies marginally depending on the initial mass of the progenitor. Large progenitors are expected to have more energetic explosions (Hamuy, 2003). Due to the proportionality of M_{ej} and E_{exp}, Equation 2.1 suggests the v_{ej} shall remain roughly unaltered. We choose $v_{ej} = 2300$ Km/s for all the progenitors. The γ-ray optical depths ($\tau_0 = \kappa_\gamma\ \phi(t_0)$) are estimated using Equation 2.6 for 12, 15, 19 and 25 $M_\odot$ progenitors as 13, 16.4, 22.3 and 33 respectively (Table 2.2, 2.3).

2.2.3 Temperature and density evolution

Evolution of gas temperature in the ejecta is controlled by the degradation of γ-rays and X-rays and deposition of their energy. Therefore it also depends on the elemental abundances at a given time. Through observations (Fransson and

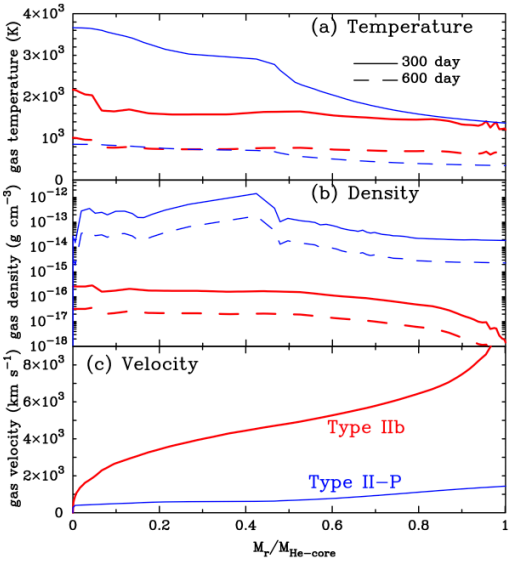

FIGURE 2.4: The temperature and density profile for a 17 $M_\odot$ progenitor core-collapse supernova model at day 300 and 600 after explosion. The comparison is shown between type II-P and type IIb supernovae ejecta conditions (Umeda and Nomoto, 2002; Nozawa et al., 2010).

Chevalier, 1989) and modelling (Kozasa et al., 1989) of SN1987A, the ejecta temperatures were estimated. The ejecta is assumed to undergo a quasi-adiabatic expansion (Cherchneff and Dwek, 2009) with time. The variation of temperature is then given in terms of an 'adiabatic' index γ as,

$$T_{gas}(M_r, t) = T_{gas}(M_r, t_0) \times \left(\frac{t}{t_0}\right)^{3(1-\gamma)} \quad , \tag{2.9}$$

where M_r is the position in the mass-coordinate. t_0 is a fiducial time, which is chosen to be equal to 100 days post-explosion, as the analysis of the chemistry starts from day 100. The temperature and density evolution of a typical type II-P supernovae has been modelled by Umeda and Nomoto, 2002 and Nozawa et al., 2010 presents the profiles corresponding to day 300 and 600 (Figure 2.4). Comparing the two epochs, the index γ is calculated to have a value of 1.42. Thereafter, the initial temperatures at day 100 are also calculated using Equation 2.9 for each zone, using the correct mass-coordinates from Figure 2.4. Table 2.4 summarises the temperature evolution in various ejecta zones for a 15 and a 19 $M_\odot$ model. In Figure 2.5 (left-panel) the profiles are shown as function of post-explosion time. The three lines correspond to zone 1A (red), 2 (blue) and 5 (magenta) respectively of the standard 15 $M_\odot$ case.

After the explosion, the shock wave propagates through the envelope. The changes

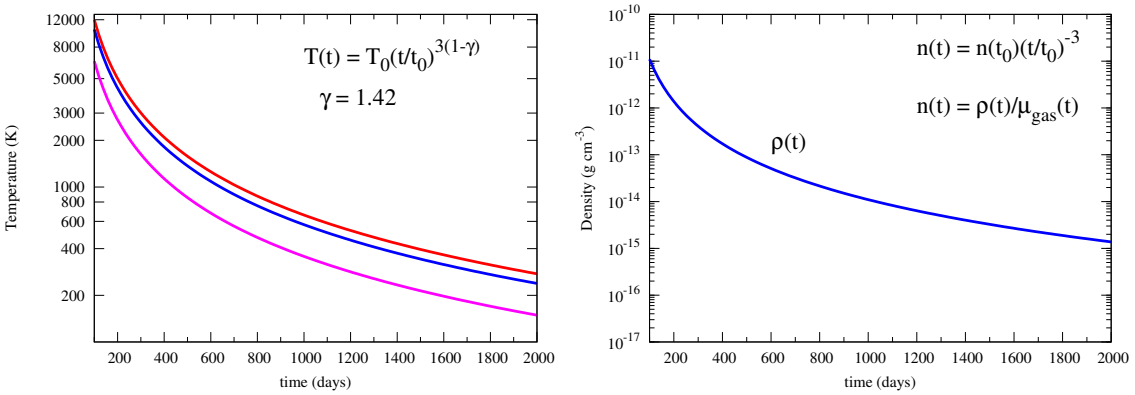

FIGURE 2.5: **Left Panel:** The temperature profiles for inner most (red), the central O-core (blue) and the outermost zone (magenta) are presented as a function of post-explosion time. **Right Panel:** The density profile for the standard case, considering the initial density to be 1.1×10^{-11} g cm^{-3} at day 100 after explosion, as derived from Nozawa et al., 2010 (Sarangi and Cherchneff, 2013).

in the temperature and density profiles are associated with the shock propagation through the ejecta (Shigeyama and Nomoto, 1990). This causes a velocity shear, and within one day of explosion, the ejecta shell expands homologously (Nozawa et al., 2003). The variation of density $\rho(t)$ is hence is given by,

$$\rho_{gas}(M_r, t) = \rho_{gas}(M_r, t_0) \times \left(\frac{t}{t_0}\right)^{-3}. \tag{2.10}$$

According to the gas density profile in Figure 2.4, for days 300 and 600, we derive the initial density at 100 days as $\rho_{gas}(100) = 1.1 \times 10^{-11}$ g cm^{-3}. A constant initial mass density is assumed for the entire ejecta, independent of mass coordinate M_r. Figure 2.5 (right-panel) shows the evolution of gas mass density with time. The mean molar weight μ_{gas} at day 100 for each zone is calculated from the initial abundances. Table 2.2 & 2.3 present the mean molecular weights corresponding to each ejecta zone (Sarangi and Cherchneff, 2013). The number density at day 100 and its evolution with time is derived from the mean molar weight as,

$$\begin{aligned} n_{gas}(M_r, 100) &= \rho_{gas}(M_r, 100) \times \frac{A_v}{\mu_{gas}(100)} \\ n_{gas}(M_r, t) &= n_{gas}(M_r, 100) \times \left(\frac{t}{100}\right)^{-3} \end{aligned} \tag{2.11}$$

The number densities are different from one zone to the other due to the different elemental composition and different mean molecular weights (A_v is the Avogadro number). In case of the SN1987A model in Chapter 7, the initial gas density at

TABLE 2.4: Ejecta temperature T_{gas} and number density n_{gas} for the homogeneous, stratified SN ejecta with 15 and 19 $M_\odot$ stellar progenitors as a function of post-explosion time and ejecta zones (SC13). The mass coordinates of each zone in the He-core are listed. (Sarangi and Cherchneff, 2014)

15 $M_\odot$ progenitor														
Zones	1A (1.79-1.88)		1B (1.88-1.98)		2 (1.98-2.27)		3 (2.27-2.62)		4A (2.62-2.81)		4B (2.81-3.04)		5 (3.04-3.79)	
Day	T	n_{gas}	T	n_{gas}	T	n_{gas}	T	n_{gas}	T	n_{gas}	T	n_{gas}	T	n_{gas}
100	12000	1.8(11)	11600	3.1(11)	10400	3.7(11)	8779	3.8(11)	7980	4.3(11)	7580	6.1(11)	6490	1.6(12)
300	3006	6.7(9)	2906	1.1(10)	2605	1.4(10)	2199	1.4(10)	1998	1.6(10)	1899	2.3(10)	1626	5.9(10)
600	1255	8.3(8)	1213	1.4(9)	1088	1.7(9)	918	1.8(9)	835	2.0(9)	793	2.8(9)	679	7.4(9)
900	753	2.5(8)	728	4.3(8)	653	5.1(8)	551	5.2(8)	501	5.9(8)	476	8.4(8)	407	2.2(9)
1200	524	1.0(8)	507	1.8(8)	454	2.1(8)	383	2.2(8)	349	2.5(8)	331	3.5(8)	283	9.3(8)
1500	396	5.3(7)	382	9.2(7)	343	1.1(8)	289	1.1(8)	263	1.3(8)	250	1.8(8)	214	4.7(8)
2000	275	2.3(7)	266	3.9(7)	239	4.6(7)	201	4.8(7)	183	5.4(7)	174	7.6(7)	149	2.0(8)
19 $M_\odot$ progenitor														
Zones	1A (1.77-1.88)		1B (1.88-2.18)		2 (2.18-3.86)		3 (3.86-4.00)		4 (4.00-4.49)		5 (4.49-5.26)		6 (5.26-5.62)	
Day	T	n_{gas}	T	n_{gas}	T	n_{gas}	T	n_{gas}	T	n_{gas}	T	n_{gas}	T	n_{gas}
100	12400	7.2(10)	12000	1.2(11)	9980	1.5(11)	7190	1.7(11)	6390	2.5(11)	6000	6.3(11)	5900	6.4(11)
300	3106	2.7(9)	3006	4.3(9)	2500	5.7(9)	1801	6.4(9)	1601	9.3(9)	1503	2.3(10)	1478	2.4(10)
600	1297	3.3(8)	1255	5.4(8)	1044	7.1(8)	752	8.0(8)	668	1.2(9)	628	2.9(9)	617	3.0(9)
900	778	9.8(7)	753	1.6(8)	626	2.1(8)	451	2.4(8)	401	3.5(8)	377	8.7(8)	370	8.8(8)
1200	542	4.1(7)	524	6.7(7)	436	8.9(7)	314	1.0(8)	279	1.5(8)	262	3.7(8)	258	3.7(8)
1500	409	2.1(7)	396	3.4(7)	329	4.6(7)	237	5.1(7)	211	7.5(7)	198	1.9(8)	195	1.9(8)
2000	285	9.0(6)	275	1.5(7)	229	1.9(7)	165	2.2(7)	147	3.2(7)	138	7.9(7)	135	8.0(7)

day 100 is corrected to a lower value of 4.4×10^{-12} g cm^{-3} in order to be consistent with the clumpy model. The evolution and gas density for a 15 $M_\odot$ and a 19 $M_\odot$ model is listed in Table 2.4.

2.3 A clumpy model

The stratified homogeneous 1D model of the ejecta is capable to indicate trends which are congruent with physics of the real supernovae. Nevertheless, a real supernova ejecta is neither homogeneous nor spherically symmetric. Observations indicate to the possibility of macroscopic mixing of ^{56}Ni in the outer layers of the H-He core (McCray, 1993; Kifonidis et al., 2003). Moreover the multi-D explosion models report the presence of Rayleigh-Taylor unstable filaments in the non-homogeneous ejecta (Joggerst et al., 2010; Hammer et al., 2010) of type II supernovae. The explosion energy is imparted in the ejecta in form of kinetic energy which triggers the outward motion at a velocity of 2000-2500 Km/s as calculated in Section 2.1. If all the materials in the He-core to travel at a constant velocity v, the density (ρ) should fall according to t^{-2} (Woosley, 1988). However, the radioactive decay $^{56}Ni \rightarrow ^{56}Co \rightarrow ^{56}Fe$, deposits the extra energy in the innermost Ni-Co core. Further, the neutrino-driven convection in the ejecta creates inhomogeneity between the layers (Joggerst et al., 2010). This creates a velocity shear across the zones of the ejecta, and the inner zone with extra energy tends to expand

TABLE 2.5: Parameters for the clumpy ejecta model with a 19 $M_\odot$ stellar progenitor taken from Jerkstrand et al., 2011; Sarangi and Cherchneff, 2014

Ejecta zones	Zone 1A	Zone 1B	Zone 2	Zone 3	Zone 4	Zone 5	Zone 6	Total
Zone mass in $M_\odot$	0.11	0.302	1.68	0.141	0.486	0.774	0.358	3.85
Clump number	44	118	654	55	189	301	139	1500
f_c	2.9(-2)	4.1(-3)	7.3(-2)	2.0(-2)	2.0(-2)	1.5(-2)	1.5(-2)	–
n_c(day 100) in cm^{-3}	2.47(12)	2.83(13)	2.11(12)	8.60(12)	1.26(13)	4.24(13)	4.29(13)	–

faster (Woosley, 1988). The velocity shear induces homologous expansion where the density decreases as t^{-3}. Therefore, the fast moving, low density Ni-layers penetrate in the high density overlying zones of the ejecta. This density inversion occurs within a day of the explosion, thereby creating the Rayleigh-Taylor instabilities. The mixed Ni-bubbles further deposit energy in the O-core, which is in turn accelerated through the outer He/N/C zones. These instabilities lead to the fragmentation of the He-core, but the chemical stratification persists over time. Hence there is no microscopic mixing between zones, and the so general assumption of intrazonal chemistry remains valid. Importantly though, this velocity sheer results in clumping of the ejecta very early after the explosion.

We study a non-homogeneous, clumpy ejecta for the 19 $M_\odot$ stellar progenitor, which we choose as a surrogate to SN1987A and other massive supernovae. We build up a simple empirical model for a clumpy ejecta as follows: for each zone, we use the volume filling factor f_c derived by Jerkstrand et al., 2011 in their modelling of the ultraviolet, optical, and near-IR emission lines observed in SN1987A. We assume a fiducial number of 1500 for the total number of clumps in the ejecta, in agreement with radiative transfer models of the IR spectral energy distribution of various supernova ejecta (Gallagher et al., 2012). Using the He-core mass for the 19 $M_\odot$ stellar progenitor listed in Table 2.5, we derive a typical clump mass of $\sim 2.6 \times 10^{-3}$ $M_\odot$ for all clumps, a value which agrees well with typical clump masses derived from 3-D explosion models (e.g., Hammer et al., 2010). The enhancements over the homogeneous gas densities at day 100 are then calculated using the volume filling factors, and the gas number density n_c in the clumps are estimated. All parameters are listed in Table 2.5 as a function of ejecta zones. The gas temperature and initial atomic yields are those of the 19 $M_\odot$ homogeneous model given in Tables 2.4 and 2.3, and the gas number density given in Table 2.5 for all the zones, also follows a time variation as that used in the homogeneous case.

To be honest, neither the homogeneous stratified 1D model, nor the clumpy ejecta

model can account for the entire physics of a complicated supernova ejecta. Yet the study clearly indicates, that the trends obtained from the analysis can successfully address a lot of questions related to the field. Hence the use of these empirical models as surrogate to real supernovae ejecta is justified.

3 The Chemical Model

The chemistry of the ejecta of a typical type II-P supernova has been explored through a chemical kinetic approach. The study adopts a bottom-up approach which concentrates on the synthesis of molecules, small clusters and dust grains in the ejecta. This Chapter shall focus on the aspects of the chemical model used in following analysis.

3.1 Chemical Kinetics

Chemical kinetics deals with the dynamics of chemical reactions and the conditions affecting reaction rates. It is controlled by the concentration of the reactants, temperature of the medium and the enthalpy of the individual reactions. The supernova ejecta has a very dynamic physical environment as explained in Section 2.2.3. The passage of the supernovae blast wave through the helium core and the deposition of radioactive energy in the ejecta creates a complex physical environment whose chemistry is neither at steady state nor can be considered to be at thermodynamic equilibrium (TE). Following the explosion, the ejecta moves at a velocity ∼2000Km/s and the density and temperature fall rapidly. The rich chemical composition of the ejecta is controlled by a large set of chemical reactions with diverse reaction rates. All these chemical reactions occur simultaneously and are coupled to each other. Each individual species is linked to the chemical network through a series of formation and destruction pathways, which comprises of both thermal and non-thermal processes. Therefore, with the alteration of temperature and density conditions in the ejecta, the relative importance of specific reactions in the network also change. These factors not only ensures the complexity of the

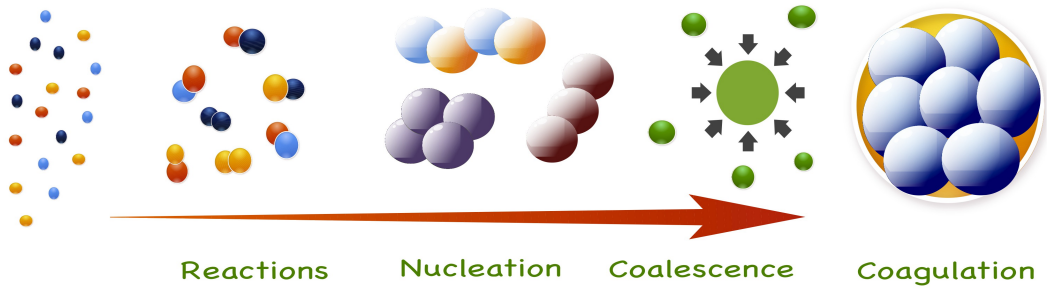

FIGURE 3.1: The synthesis of molecules, clusters and dust grains in the ejecta through nucleation and condensation phase

expected chemical yields, but also creates a case which is far from the steady state condition (Cherchneff and Dwek, 2009).

The chemical pathway proceeds through simultaneous phases of nucleation and condensation (Figure 3.1). The nucleation phase comprises of chemical reactions which lead to the synthesis of molecules from atoms and small clusters from molecules. The condensation phase couples the gas phase chemistry to the solid phase of dust. The small clusters formed in the gas phase, condense through coagulation and coalescence to form large grains of dust. A small fraction of the ejected materials condenses to form dust grains and leaves the chemical network. The types of reactions involved in the process and the equations guiding the formalism are explained in the following sections.

3.1.1 Types of reaction

We include all possible chemical pathways relevant to the hot and dense environments in our study. The network consists of more than 500 reactions of different kinds in the gas phase. The reactions can be categorised into thermal and non-thermal processes (Cherchneff and Dwek, 2009).

Thermal Processes: The balanced chemical reactions which depend on the temperature of the media and the respective enthalpies of the reactants and the products can be classified as thermal processes. Further, there are several types of thermal reactions that are important for the network.

- **Termolecular reactions:** These are three-body processes where the formation of new molecules occur through collision with the ambient gas. The

extra energy of the reaction is carried away by the gas at the end of the reaction. They are only efficient at high density media and hence at early times. They are generally exothermic in nature.
The three body processes where all the three reactants take part in formation of new species, are very less relevant for the context of the study, due to the minimal probability of occurrence and small reaction rates. Therefore they are not included in the network.

$$X + Y + M \rightarrow XY + M^* \tag{3.1}$$

- **Thermal fragmentation:** It is the inverse process of the termolecular reaction. The molecules in this case absorb the energy through collision with the ambient gas and gets fragmented. The reactions are highly endothermic, and hence associated with large energy barriers.

$$XY + M^* \rightarrow X + Y + M \tag{3.2}$$

- **Bimolecular reactions:** Bimolecular processes builds the most significant part of the chemistry, as most of the important formation and destruction processes falls under this category. They are also termed as neutral-neutral processes. The reactions with energy barriers are efficient mostly at high temperatures, whereas the processes with no activation energy can proceed efficiently even at low temperatures at later times in the ejecta.

$$X + AB \rightarrow AX + B \tag{3.3}$$

- **Ion-molecule reactions:** These are charge induced reactions, predominantly free of energy barrier and hence can contribute at low temperatures also. They can be either formation-destruction reactions or charge exchange reactions as explained in Equation 3.4.

$$\begin{aligned} X^+ + AB &\rightarrow XB^+ + A \\ X^+ + Y &\rightarrow X + Y^+ \end{aligned} \tag{3.4}$$

- **Radiative association:** This is a temperature independent process. Formation of new products occurs through collision of two species and subsequent emission of photon which carries away the excess energy of formation.

$$X + Y \rightarrow XY + h\nu \tag{3.5}$$

Nonthermal Processes: The photon induced reactions related to excitation and de-excitation of energy levels or fragmentation of the reactants, are categorised as non-thermal processes. The supernovae ejecta is powered by the decay of radioactive elements. Hence the downscattering of γ-rays produced by radioactivity in the ejecta, leads to nonthermal processes including the destruction of molecules by energetic Compton electrons and UV photons (Section 2.2.2). The detail of its impact on the chemistry has been explained in the following section.

3.1.2 Master equations

The reaction network for the gas phase is built with a set of ∼600 reactions of the above types. The reactions are characterised by the respective reactions rates. Hence the temporal variation of number density of a certain species i, located at mass zone M_r in the ejecta, at a certain time t, is give by (Cherchneff and Dwek, 2009),

$$\frac{\partial n_i(M_r, t)}{\partial t} = P_i - L_i = \sum_j k_{ji} n_j n_i - \sum_k k_{ik} n_i n_k, \tag{3.6}$$

where, P_i represents the sum over the all the production (formation) processes whereas L_i, the sum over all the destruction processes. The term k_{ij} represents the temperature dependant reaction rates between the i^{th} species and the j^{th} species. The rate of formation or destruction of a certain species through a chemical reaction is given by the product of reaction rate and the densities of the species involved in the reaction. The time derivative of the net number density of the i^{th} species is hence determined by the difference between the sum of all the formation and the sum over all the destruction processes relevant to that species (Equation 3.6). The reaction rate k_{ij} is expressed in terms of the modified Arrhenius equation as,

$$k_{ij}(T) = A_{ij} \times \left(\frac{T}{T_0}\right)^{\nu} \times \exp(-E_{ij}/T), \tag{3.7}$$

where T_0 is a reference temperature chosen as 300K for the study. A_{ij} is the Arrhenius rate coefficient expressed in s^{-1}, cm^3s^{-1} or cm^6s^{-1} depending on the order of reaction and E_{ij} is the activation energy in the unit of K^{-1}. The factor ν represents the time dependance of the pre-exponential factor of the general Arrhenius equation. Typical values of the ν-factor range between -1 to 1. Thus the gas phase chemistry is overall controlled by N number of stiff coupled nonlinear ordinary differential equations similar to Equation 3.6, where N is the number of species that has been included in the study. This entire set of differential equations are solved simultaneously and the time evolution of the abundances for each species are estimated. The reaction rates are either theoretically calculated using translation theory or estimated in the laboratory. Standard chemical data bases such as NIST, KIDA, UMIST, etc., have been used as a reference for the reaction rates used in the network. Due to the lack of documentation, in case of some reactions, the rates are estimated through educated guess, using the knowledge of similar reactions with known reaction rates. The entire set of chemical reactions used in the survey are listed in Cherchneff and Dwek, 2009, 2010 & Sarangi and Cherchneff, 2013.

The rate coefficients for the nonthermal processes are estimated using the theory explained in Section 2.2.2. The rate of deposition of radioactive energy by the thermalized γ-rays in the ejecta is given as (Equation 2.8),

$$L_\gamma = 5.95 \times 10^{53} \times \frac{M_{Co}}{M_{Co}(SN1987A)} \times \exp\left(-\frac{t}{\tau_{Co}}\right)\left(1 - \exp\left[-\tau_0\left(\frac{t}{t_0}\right)^{-2}\right]\right) \tag{3.8}$$

The fast Compton electrons produced by the degradation of the γ-rays play important role in the chemistry. Interaction of the ejecta materials with these Compton electrons leads to excitation, ionisation and dissociation. This is a significant destruction pathway for the stable atoms, molecules and clusters present in the ejecta (Liu and Dalgarno, 1994, 1995; Clayton et al., 1999). The Compton electrons further degrade in energy through collision with the ejecta. The branching ratio between the energy deposited by electron through excitation, ionisation ($A \rightarrow A^+ + e^-$) and fragmentation ($AB \rightarrow A + B^+ + e^-$) depends on the mean

energy per ion pair. The mean energy per ion pair, W_d is defined as,

$$W_d(p,i) = E_p \times \frac{X_i}{N_d(p,i)}, \tag{3.9}$$

where, N_d & X_i are the number of ion pairs produced by the species in this process and the abundance of that species in the ejecta, respectively. E_p is given by the energy of the primary electron that has been degraded through this process. The mean energy per ion pair is a function of the species i, as well as the type of destruction process p. Assuming the entire radioactive energy to get uniformly distributed in the ejecta, the rate of destruction of species i by Compton electrons through process p is given by,

$$k_c(p,i) = \frac{5.95 \times 10^{53}}{W_d(p,i) \times N_{total}} \times \frac{M_{Co}}{M_{Co}(SN1987A)} \times \exp\left(-\frac{t}{\tau_{Co}}\right) \times \left(1 - \exp\left[-\tau_0 \left(\frac{t}{t_0}\right)^{-2}\right]\right), \tag{3.10}$$

where N_{total} is the sum over total number of particles present in the ejecta. Liu and Dalgarno, 1995 explains the formalism of dissociation and ionisation to CO^+ to ions of C or O and to CO^+ ion in the O-rich core of the ejecta. We choose the same W_d values as calculated in the analysis. The rates of destruction by Compton electrons are expressed as a function of time whereas the Arrhenius rate coefficients are functions of temperature. Based on the time dependence of temperature as explained in Section 2.2.3, the rate k_c can be expressed as a function of ejecta temperature. The rate $k_c(T)$ is thereafter fitted with Equation 3.7 by a two parameter fit (A_{ij}, T) within the relevant range of temperature. The estimated values of A_{ij} for the destruction by Compton electron is given in Table A.3 along with the values for W_d and their references. The downgradation of γ-rays also produces UV fields in the ejecta. The effect of UV radiation fields on the chemistry of supernovae ejecta has been estimated by Cherchneff and Dwek, 2009. The finding suggests, the destruction of molecules and clusters by UV fields is not important compared to the impact of Compton electrons. Hence the destruction by Compton electrons are the only nonthermal process considered in the study.

TABLE 3.1: The set of atoms, ions, molecules, and molecular clusters considered in the study (Sarangi and Cherchneff, 2013, 2014)

Elements						
He	C	N	O	Ne	Mg	Al
Si	S	Ar	Ti	Fe	Co	Ni
Molecules						
CO	CO_2	NO	O_2	MgO	AlO	SiO
SO	FeO	S_2	CN	SiC	CS	SiS
FeS	MgS	N_2				
Ions						
He^+	C^+	N^+	O^+	Ne^+	Mg^+	Al^+
Si^+	S^+	Ar^+	Fe^+	CO^+	SiO^+	SO^+
$O_2{}^+$	$N_2{}^+$	$C_2{}^+$				
Molecular clusters						
C_2	C_3	C_4	C_5	C_6	C_7	C_8
C_9	C_{10}	C_{11}	C_{12}	C_{13}	C_{14}	C_{15}
C_{16}	C_{17}	C_{18}	C_{19}	C_{20}	C_{21}	C_{22}
C_{23}	C_{24}	C_{25}	C_{26}	C_{27}	$\mathbf{C}_{28}$	
$(SiO)_2$	Si_2O_3	$(SiO)_3$	Si_3O_4	$(SiO)_4$	Si_4O_5	$(SiO)_5$
$MgSi_2O_3$	$MgSi_2O_4$	$Mg_2Si_2O_4$	$Mg_2Si_2O_5$	$(MgSiO_3)_2$		
$Mg_3Si_2O_6$	$Mg_3Si_2O_7$	$Mg_4Si_2O_7$	$\mathbf{(Mg_2SiO_4)_2}$			
Al_2	$(AlO)_2$	$(AlO)_3$	AlO_2	Al_2O	Al_2O_3	
$(Al_2O_3)_2$	$(Al_2O_3)_3$	$\mathbf{(Al_2O_3)_4}$				
Si_2	Si_3	$\mathbf{Si}_4$	Mg_2	Mg_3	$\mathbf{Mg}_4$	
Fe_2	Fe_3	$\mathbf{Fe}_4$	$(FeS)_2$	$(FeS)_3$	$\mathbf{(FeS)}_4$	
$(MgS)_2$	$(MgS)_3$	$(MgS)_4$	$(SiC)_2$	$(SiC)_3$	$\mathbf{(SiC)}_4$	
$(MgO)_2$	$(MgO)_3$	$(MgO)_4$	$(FeO)_2$	$(FeO)_3$	$(FeO)_4$	

3.2 Species of interest

The study of the gas phase chemistry focus on about 120 species, which comprises of atoms, ions, molecules, intermediate clusters and dust precursors. Table 3.1 presents the entire set of all the species that has been considered in the network. The important species in a certain ejecta zone, depends mainly on the initial compositions and correspondingly the chemical network also vary to some extent from one zone to other. The network does not separate isotopes of a single element in the chemistry. The elements such as O, C, Si, S, Al, Mg, Fe, N actively take part in the formation of new species in the chemistry. The nobel gases such as He, Ne and Ar also has a significant contribution to the chemistry, which is explained in more detail in Section 5.4.2.

The molecular clusters make up for a large percent of the important species in the gas phase. The molecular clusters forms in the ejecta mainly through nucleation. They can be classified further into two categories: the intermediate molecular clusters and the dust precursors. The dust precursors preside as the final product in the chain of molecular network (in bold font in Table 3.1). They simultaneously condense to form dust grains. The intermediate molecular clusters form in the gas phase as an intermediate step in the path of formation of the dust precursors. A fraction of these species remains in the gas at later times as uncondensed clusters, only to be destroyed by the reverse shock. The following sections focus on the nucleation chemistry of the molecular clusters and the condensation scheme for the dust grains.

3.3 Nucleation Scheme

Molecular clusters act as the building block of the dust in supernova ejecta. Hence the nucleation scheme is the bottleneck of the entire dust synthesis formalism. A stochastic, kinetically driven approach has been adopted to study the nucleation of gas molecules to small clusters. The vaporisation experiments in the laboratory and the study of ceramic synthesis in the flames provide the insight to similar nucleation processes under non-steady state environment. The important species that demand detail analysis are oxygen rich clusters of magnesium silicates, alumina and Si_mO_n molecules, carbon chains, rings and fullerenes, silicon carbide, metallic sulphides and oxides, and pure metallic clusters. The upper limit of the cluster size in the nucleation network is not defined very specifically. The geometry of the molecules is the backbone to determine the final product of nucleation and the dust precursor in the network (Table 3.1 in bold font). The clusters that attain a three dimensional structure like a cage or twisted rings, has a larger collision cross section for coagulation (Cherchneff and Dwek, 2010). Moreover they are energetically more stable, and hence likely to be resilient under the destruction processes in the gas phase. In some cases, the favoured chemical routes for nucleation network are derived from quantum chemical calculations. The formation chemistry of various molecular clusters in the ejecta are discussed separately in this Section. All the reaction rates for the nucleation routes of silicate and silica clusters are tabulated in Appendix A. The structures of some of the stable clusters formed through the nucleation scheme is shown Figure 3.3.

FIGURE 3.2: The nucleation scheme for silicates leading to the formation of the enstatite and forsterite dimers, which act as the seed in the condensation formalism. The reactant species are given on the side of the directional arrows in the schematic diagram (Goumans and Bromley, 2012)

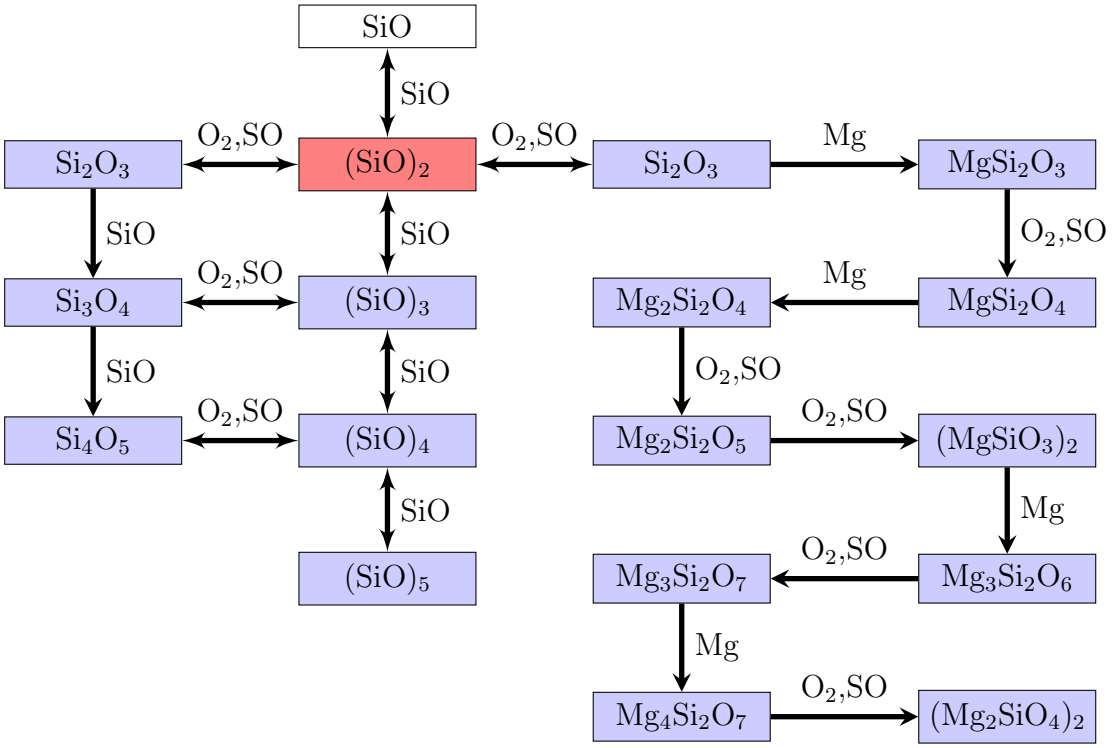

Magnesium-silicates & Silica: Amorphous and crystalline silicates are the most abundant of all dust types present in space. However the synthesis of silicates from gas molecules does not follow a straight forwards pathway. In the laboratory, flame aerosol technology experiments provides the insight to the possible seed clusters for the formation of silicate compounds (McMillin et al., 1996; Pratsinis, 1998; Cherchneff and Dwek, 2010). Table 3.1 lists all possible clusters of magnesium silicates that can be synthesised in such environment. The Gibb's energies for the most probable structures of these molecular clusters are calculated using density function theory by Goumans and Bromley, 2012 (GB12). The favoured chemical pathway for silicate nucleation is based on the study by GB12. The nucleation network for silica and silicates are presented as a schematic diagram in Figure 3.2. The right side of the diagram represents the silicate network, whereas the left columns depict the pathway for the nucleation of silica.

The synthesis of $(SiO)_2$ and Si_2O_3 from silicon monoxide is the bottleneck of this network. The branch of silicate nucleation thereafter proceeds by consecutive phases of Mg-addition and oxidation. We consider the oxidation (single O addition) of intermediate magnesium silicates by O_2 and SO molecules and

also by atomic O. The addition of atomic O takes place by termolecular reactions ($cluster + O + M \rightarrow [cluster + O] + M$) or by radiative association ($cluster + O \rightarrow [cluster + O] + h\nu$). On the other hand, the reactions between clusters and O_2 or SO occurs through bimolecular oxidation processes. The typical orders of reaction rates are $\sim 10^{-17} cm^3/s$ for bimolecular oxidation and $\sim 10^{-20} - 10^{-30}\ cm^6/s$ in case of RA or termolecular processes. Hence the nucleation pathway preferably follows the O_2, SO oxidation routes. In principle any oxygen bearing diatomic molecule can act as an oxidising agents to the clusters. However, the bond energy of CO is much higher compared to O_2 and SO, and SiO prefers the formation of $(SiO)_2$ dimers are over oxidation processes. Similarly AlO also choses the route of formation of Al_2O_3 over the oxidation of silicate clusters. Hence the chemistry of magnesium silicates proceed via O_2 and SO oxidation channels. The destruction of the clusters takes place by thermal fragmentation and degradation by Ne^+ and Ar^+ ions. The nucleation pathway leads to the synthesis of enstetite $(MgSiO_3)_2$ and forsterite $(Mg_2SiO_4)_2$ dimers. The closed structure of the forsterite dimers are energetically stable, and survive the possible destruction routes in the gas. They later act as the seed of silicate dust in condensation phase. All the processes in the silicate network starting from Si_2O_3 are downhill in energy (GB12), hence the reaction rates does not have any activation energy associated with it (Sarangi and Cherchneff, 2013).

The left-half of the Table 3.2 corresponds to the nucleation of Si_mO_n molecules, where $n = m, m+1$. The structures of $(SiO)_n$ (n=1,5) has been illustrated by Cherchneff and Dwek, 2010 as adapted from Lu et al., 2003. The $(SiO)_5$ is considered to have a twisted ring-like structure expected to be stable. The possible structure of Si_4O_5 has been derived by Reber et al., 2008 combining theoretical and laboratory studies. We consider these two species as the largest polymer in the nucleation chemistry of Si_mO_n molecules. The reaction rates for the polymerisation of SiO ($(SiO)_m + (SiO)_n \rightarrow (SiO)_{m+n}$) and the fragmentation ($(SiO)_{m+n} \rightarrow (SiO)_m + (SiO)_n$) of such molecules are estimated from Zachariah and Tsang, 1993. Also the termolecular reactions are included among the destruction processes.

The tendencies of chemical bonding of Si and O are very different. Si commonly prefers tetrahedral coordinations on the other hand O favours bonds with one, two or sometimes up to three atoms. The Si-O bonds are however stronger compared to Si-Si or O-O bonding. Hence these clusters quite stable in energy and segregation is not easily feasible. Due to combined effect of these two factors, the structure of

the polymers of Si_mO_n type forms separate domains of O-rich and Si-rich regions (Reber et al., 2008). In case of large polymers a possible disproportionation shall lead the formation of silica (SiO_2) and pure-Si clusters. Study of IR spectra from Cassiopeia A suggests the presence of Silica as a potential dust type is supernova (Rho et al., 2008). However, a detail analysis of the chemical processes leading to the synthesis of silica has been ignored in the present study.

Alumina: Alumina is the second most important O-rich dust type in supernovae after silicates. In the O-core of the ejecta, the presence of Al and O in abundance, leads to the synthesis of several Al_xO_y type molecules. Ground state energy calculation of the several such molecules indicate Al_2O_3 to the most stable form. We have derived a nucleation scheme for Al_2O_3 using the reference to Si_2O_3 because of their structural similarities. The network includes dimerisation of AlO molecules to $(AlO)_2$ followed by oxidation also by AlO as explained in Equation 3.11 (Biscaro and Cherchneff, 2014; Sarangi and Cherchneff, 2014).

$$\begin{aligned} AlO + AlO &\rightarrow (AlO)_2 \\ (AlO)_2 + AlO &\rightarrow Al_2O_3 + Al \end{aligned} \tag{3.11}$$

The tetramer of Al_2O_3 is considered to the end step of alumina nucleation channel. The polymerisation process takes place by addition of monomer and dimer units.

$$Al_2O_3 + (Al_2O_3)_n \rightarrow (Al_2O_3)_{n+1}, \quad n = 1, 3 \tag{3.12}$$

The destruction channels for Alumina are also similar to the silica and silicate network. The main routes for destruction of Al_2O_3 are fragmentation and through attack of Ne^+.

$$\begin{aligned} Al_2O_3 + M &\rightarrow (AlO)_2 + O + M \\ Al_2O_3 + Ne^+ &\rightarrow (AlO)_2 + O^+ + Ne \end{aligned} \tag{3.13}$$

Similar destruction channels also apply to other Al_xO_y molecules. $(Al_2O_3)_4$ thus synthesised then enters the condensation phase to form alumina dust.

Amorphous carbon: The chemistry of carbon is the most versatile of all elements due to its unique bonding properties. A large variety of molecular species of pure carbon forms spontaneously in carbon vapour. In hydrogen free environment where C/O ratio is greater than 1, pure carbon chains are formed of sp-hybridization to C_9. Monocyclic ring structure is dominant in case of C_{10} over the

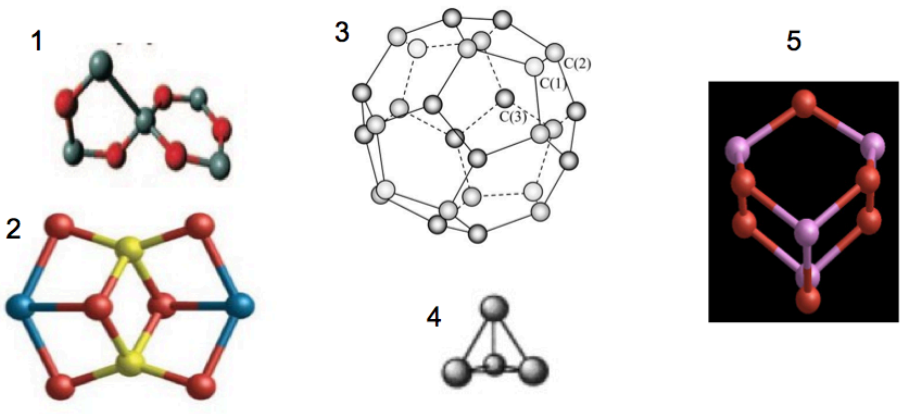

FIGURE 3.3: 1) $(SiO)_5$ (Reber et al., 2008) 2) $(MgSiO_3)_2$ (Goumans and Bromley, 2012), 3) C_{28} (Makurin et al., 2001) 4) Mg_4 (Cherchneff and Dwek, 2010), 5) $(Al_2O_3)_2$ (David Gobrecht: Private communications)

linear chains (Cherchneff and Dwek, 2010). These rings act as the building blocks for caged fullerenes through further coalescence and C-addition processes. Pulsed laser vaporisation experiments show evidence of formation of fullerene-like soots as the condensates (Lu et al., 1993; Jäger et al., 2009) in the vapour. Fullerenes are closed cage carbon molecules pentagons and hexagons of carbon. In theory pure carbon molecules can assume such a structure from C_{20} onwards. However cluster beam experiments suggest, the smallest stable structure of fullerene present in carbon vapour is C_{28} (Dunk et al., 2012). The types of reactions in the network is also guided by the geometry of the polymers. The network assumes the radiative association of carbon chain (Clayton et al., 1999) as in Equation 3.14.

$$C + C_n \rightarrow C_{n+1} + h\nu, \quad n = 1, 9 \tag{3.14}$$

The reaction rates are relatively lower for $n = 1$ ($\sim 10^{-17}$), than for larger chains. Owing to numerous degree of freedoms, the larger chains stabilise faster from the formation complex, hence the reactions proceed with rates $\sim 10^{-10}$. Furthermore, the open-ended chains can also grow by end to end addition through mutual collision. The network hence also includes addition reactions of the form (Clayton et al., 2001),

$$C_m + C_n \rightarrow C_{m+n} \quad n = 2, 8 \tag{3.15}$$

with estimated rates $\sim 10^{-10}$. The polymers of type C_n where n>9 are cyclic rings and hence they can only grow via atomic carbon and C_2 addition ($C_2 + C_n \rightarrow C_{n+2}$, $n < 27$). Carbon rings grow this way to form the first stable fullerene

cage is formed at C_{28}. Depending of the abundances of C_2 in gas, the fullerene cages shall continue to grow as molecules without cage fragmentation up to stable C_{60}. We consider the stable C_{28} synthesis as the terminal step of the nucleation network, as due to scarcity of growing agent C_2 in the supernovae ejecta, the gas phase chemistry does not continue up to C_{60} cages.
The dominant destruction channels are thermal fragmentation of chains through collision with the ambient gas (Equation 3.16).

$$\begin{aligned} C_{2n+1} + M &\rightarrow C + C_{2n} + M \\ C_{2n} + M &\rightarrow C_2 + C_{2n-2} + M \end{aligned} \tag{3.16}$$

The species with even polymer index n is relatively more stable compared to the odd counterparts. Therefore the degradation through thermal fragmentation leads to formation of polymers or even order. Also the chains are susceptible to oxidation by O as,

$$C_n + O \rightarrow C_{n-1} + CO, \tag{3.17}$$

where the end-cap carbon is taken away by O-atom to form CO. The other destruction paths relevant to the carbon chains, occur through collision with Compton electrons and by the attack of He^+ (Sarangi and Cherchneff, 2013),

$$\begin{aligned} C_n + He^+ &\rightarrow C^+ + C_{n-m} + He \\ C_n + e^-_{Compton} &\rightarrow C_m + C_{n-m} + e^-_{Compton} \end{aligned} \tag{3.18}$$

The stable fullerene cage of C_{28} acts as the seed to the corresponding condensation phase of carbon dust.

Silicon carbide: Presence of Silicon carbide dust in evolved circumstellar environments has been reported by Molster, 2003. The α-SiC grains in presolar meteorites bear isotopic signatures specific of supernovae ejecta (Bernatowicz et al., 1987). Considering no interzonal mixing as mentioned in Section 2.2.1, SiC synthesis is fisible in the region where C/O>1, which is the outermost layer of the He-core. The relevant reaction chemistry in such environment is explained by

$$\begin{aligned} Si + CO &\rightarrow SiC + O \\ Si + C_2 &\rightarrow SiC + C \\ Si + C &\rightarrow SiC + h\nu \end{aligned} \tag{3.19}$$

The SiC molecules subsequently nucleate through addition with other $(SiC)_n$ units as shown in Equation 3.22 to grow to $(SiC)_4$. The $(SiC)_4$ is assumed to possess a cage-like structure which eventually takes part in coagulation.

$$SiC + (SiC)_n \rightarrow (SiC)_{n+1}, \quad n = 1, 3 \tag{3.20}$$

The destruction processes are similar to Amorphous carbon, which is mainly dominated by the attack of He^+ ions and thermal fragmentation through collision.

Other metal oxides: Apart from Alumina, there has also been evidences of the presence of metallic oxides of Magnesium and Iron in evolved circumstellar environments. The network includes the formation of such molecules through oxidation by O_2, SO or CO_2.

$$\begin{aligned} Mg + O_2 &\rightarrow MgO + O \\ Fe + O_2 &\rightarrow FeO + O \\ Mg + SO &\rightarrow MgO + S \\ Fe + SO &\rightarrow FeO + S \\ Mg + CO_2 &\rightarrow MgO + CO \\ Fe + CO_2 &\rightarrow FeO + CO \end{aligned} \tag{3.21}$$

These oxides are estimated to contribute 20 μm and 23 μm bands in young stars or SNe remnants. The tetramers of such molecules assume a cubic structure (Koehler et al., 1997) which are energetically stable, hence should survive the phases of destruction channels in the ejecta.

$$\begin{aligned} MgO + (MgO)_n &\rightarrow (MgO)_{n+1}, \quad n = 1, 3 \\ FeO + (FeO)_n &\rightarrow (FeO)_{n+1}, \quad n = 1, 3 \end{aligned} \tag{3.22}$$

The destructions pathways are controlled by thermal fragmentation through collision with the surrounding gas molecules. MgO clusters are likely to be synthesised in the O-rich core. Hence due the presence of free O, the destruction channels for MgO is also heavily influenced by the reverse Mg-reactions of Equation 3.21.

Metal sulphides: The existence of metal sulphides has been verified through the history of IR observations of various circumstellar environments. Specifically the sulphides such as MgS and FeS attribute to the broad 30 μm and 23 μm

emissions lines in proto-planetary and planetary nebulae (Cherchneff and Dwek, 2010). However there is no documentation available for reactions of metals with sulphur. Hence we derive the reaction rates with the knowledge of O-reactions, because of the isovalence between S and O. The following reactions are responsible for the formation of FeS or MgS molecules,

$$\begin{aligned} Mg + S_2 &\rightarrow MgS + S \\ Fe + S_2 &\rightarrow FeS + S \\ Mg + SO &\rightarrow MgS + O \\ Fe + SO &\rightarrow FeS + O \end{aligned} \tag{3.23}$$

Further the polymerisation occurs through addition processes as explained in the previous sections. The nucleation network leads to the formation of the tetramers as stable clusters in the gas phase. The destruction routes are mainly dominated by thermal fragmentation processes.
The current network does not include the polymerisation scheme for SiS. Again due to the isovalance between S and O, the large clusters of SiS exhibit similar properties as explained in the case of $(SiO)_n$ molecules. Hence it should be tackled differently than other sulphides present in the ejecta.

Pure metals: The free atoms of metals in the ejecta leads to formation of metallic clusters. The nucleation scheme considers the formation of Magnesium, Iron and Silicon clusters. There is no direct evidence of such species in space from observations. However the study of the IR excess from Cas A by Rho et al., 2008 and submillimeter data from SN1987A by Matsuura et al., 2011 considers the metallic dust-clusters as a potential dust agent in the ejecta. The fourth polymer unit for these clusters are estimated to have a tetrahedral nature and should be able to withstand the impact of the destruction processes. (Cherchneff and Dwek, 2010). The following chemical routes of formation and destruction processes define the chemistry of such molecules.

$$\begin{aligned} X + X_n + M &\rightarrow X_{n+1} + M, \quad n = 1, 3 \\ X_2 + X_2 &\rightarrow X_4 \\ X_2 + X_2 &\rightarrow X_3 + X \\ X_{n+1} + M &\rightarrow X_n + X + M \\ X_n + e^-_{Compton} &\rightarrow X_{n-1} + X + e^-_{Compton} \end{aligned} \tag{3.24}$$

In Equation 3.24, X stands for Si, Mg or Fe. These residual clusters in the tetramer form thereafter remains in the gas as end product from nucleation, and their fate is decided by the following condensation scheme.

3.4 The condensation model

We terminate the nucleation network of each component at a modest size of molecular cluster which in general possess a compact cage-like structure and is energetically stable. All these species, specific to each dust type are listed in bold font in Table 3.1. Once formed, they are unlikely to break into smaller fragments owing to their stability to withstand the destruction routes in the network. Hence these dust precursors act as seeds in the condensation scheme, where they grow by coagulation to form large grains. We use the formalism developed by Jacobson, 2005, where the variation of the number density of a grain of specific volume v with time is described by the integro-differential coagulation equation given by,

$$\frac{dn_v(t)}{dt} = \frac{1}{2}\int_0^v \beta_{v-v',v} n_{v-v'} n_{v'} dv' - n_v \int_0^\infty \beta_{v,v'} n_{v'} dv'. \tag{3.25}$$

Here, t is the time, v' and $(v-v')$ are the volumes of the two coagulating particles, n_v is the number density of grains with volume v, and $\beta'_{v,v'}$ is the rate coefficient of coagulation between particles with volume v and v'. Typical gas number densities in SN ejecta at 300 days post-explosion range between $10^9 - 10^{11}$ cm^{-3}. Therefore, the ejecta gas is characterised by a free-molecular regime, which is defined by $\lambda_p \gg a_i$, where λ_p is the mean free-path of a particle in the gas and a_i is the radius of the i^{th}particle. The rate of coagulation β_{v_i,v_j} for particles i and j is controlled by physical processes such as Brownian diffusion, convective Brownian motion enhancement, gravitational collection, turbulent inertial motion, and Van der Waal's forces. In a free-molecular regime, Brownian diffusion prevails, whereas the other processes are relevant in case of larger particles and denser media. Brownian diffusion accounts for the scattering, collision, and coalescence of the grains through Brownian motion. For the sake of simplicity, we rename the rate coefficient of coagulation β_{v_i,v_j} as $\beta_{i,j}$ between two grains i and j of radii a_i and a_j, respectively.

The rate is given by

$$\beta_{i,j} = \frac{4\pi(a_i + a_j)(D_{c,i} + D_{c,j})W_{i,j}}{\frac{(a_i+a_j)}{(a_i+a_j)+\sqrt{\delta_i^2+\delta_j^2}} + \frac{4(D_{c,i}+D_{c,j})}{(a_i+a_j)\sqrt{v_{p,i}^2+v_{p,j}^2}}} \tag{3.26}$$

where $D_{c,i}$ & $D_{c,j}$ are the diffusion coefficients for particle i and j, respectively, $v_{p,m}$ is the mean thermal velocity for particle m, δ_i is the mean distance of particle i from the centre of a sphere traveling a distance λ_p, and $W_{i,j}$ is the enhancement factor due to the effect of Van der Waal's dispersion forces (Saunders and Plane, 2006; Jacobson, 2005). In the free-molecular regime, we have $\sqrt{\delta_i^2 + \delta_j^2} \gg (a_i+a_j)$, and Equation 3.26 reduces to

$$\beta_{i,j} = \pi(a_i + a_j)^2\sqrt{v_{p,i}^2 + v_{p,j}^2}W_{i,j}. \tag{3.27}$$

The Van der Waal's forces develop weak, local charge fluctuations that enhance the rate of coagulation for particles with size in the molecular range. The interaction potential between two particles separated by a distance r is defined by the Hamaker's theory using London dispersion forces (Sceats, 1989; Alam, 1987),

$$V(r) = -kT \times \frac{A'}{12}\left(\frac{1}{(\frac{r}{a_i+a_j})^2 - 1} + \frac{1}{(\frac{r}{a_i+a_j})^2} + 2\ln\left(1 - (\frac{a_i + a_j}{r})^2\right)\right) \tag{3.28}$$

where A' is given by

$$A' = \frac{A}{kT}\frac{4a_i a_j}{(a_i + a_j)^2}. \tag{3.29}$$

In the above equation, A is the Hamaker constant which varies according to the physical properties of individual dust species. The enhancement factor $W_{i,j}$ due to the Van der Waal's dispersion forces is given by

$$W_{i,j} = \left(\frac{r_T}{a_i + a_j}\right)^2 e^{\frac{-V_{ij}(r_T)}{kT}} \tag{3.30}$$

where r_T is the separation between the two particles at the transition state between attractive and repulsive potentials (Sceats (1989)). This situation is described by $\frac{\partial}{\partial r}(V(r) - 2kT\ln r) = 0$.

TABLE 3.2: Initial grain size a_0 equivalent to the size of the largest dust cluster formed in the gas phase from chemical kinetics and the Hamaker constant A for different dust components.

Dust type	a_0 (Å)	A (10^{-20} J)
Forsterite	3.33	6.5[a, b]
Alumina	3.45	15[a, b, d]
Carbon	3.92	47 [c]
Pure Magnesium	2.29	30 [c, d]
Silicon Carbide	2.15	44 [d]
Pure Silicon	2.46	21 [e]
Pure Iron	2.81	30 [c, d]
Iron Sulphide	3.0	15 [f]

[a] Rosenholm et al., 2008. [b] Rosenholm et al., 2008.
[c] Hosokawa et al., 2012. [d] Israelachvili, 2011.
[e] French et al., 1995. [f] Bergström, 1997.

According to Equation 3.27, the coagulation rate, β_{ij}, is defined as a combination of Brownian diffusion and coalescence (through W_{ij}). It is controlled by the gas temperature, but also depends on the ratio of the collider radii $f_a = a_i/a_j$, with $a_i > a_j$. The Brownian coagulation is proportional to f_a, i.e., the process is more efficient when $a_i \gg a_j$. Conversely, the coalescence factor W_{ij} is inversely proportional to f_a and reaches a maximum when $f_a \to 1$. W_{ij} acts as an enhancement factor to β_{ij}, with a value comprised between 1 and 5. However the rate coefficient is dominated by Brownian coagulation. The coagulation rate β_{ij} is thus minimum when $a_i = a_j$, i.e., when the two colliders are of the same size, and increases when f_a is large. Hence, relatively large grains present in the ejecta efficiently coagulate with the newly formed small grains, which warrants the efficient growth of large dust grains. Typical values for β_{ij} are in the range $10^{-9} - 10^{-4}$ cm^{-3} s^{-1}.

A semi-implicit volume conserved model has been developed to solve Equation 3.25 Jacobson, 2005; Saunders and Plane, 2006). Dust grains are assumed to maintain a spherical morphology and compact structure. The grains of individual dust species are assigned to discrete bins, following a volume ratio distribution given by $v_n = \gamma^{n-1} v_0$, where v_n is the volume of the n^{th} bin, γ is a constant defined as the ratio of the volumes of adjacent bins, and v_0 is the volume of the first bin, determined by the size of the gas-phase precursor. At each time step, the volume of the first bin, v_0 corresponds to the radius a_0 of the stable, largest clusters produced from chemical kinetics in the nucleation phase. Particles with volumes intermediate to any two consecutive bins are allocated following a volume fractionation formalism (Jacobson and Turco, 1994). The various quantities are

then calculated according to Equations 3.27 − 3.30, Equation 3.25 is integrated, and the grain sizes of individual dust components are derived for each time step. Values for a_0 and the Hamaker coefficient A are summarised in Table 3.2 for the dust types considered in this study.

To explore how dust grains are distributed over size, we define the grain size distribution function $f(a)$ as

$$N_{tot}(a) = \sum_a f(a) \times \Delta a, \tag{3.31}$$

where $N_{tot}(a)$ is the total number of grains with radius a summed over all zones. The quantity $N_{tot}(a)$ is calculated from the number density $n(a)$ of grains with radius a and by assuming spherical symmetry for the various ejecta zones. The size distribution $f(a)$ has thus the units of $N_{tot}(a)$ Å^{-1}.

The mass fractions of grains with radius a, $m_f(a)$ is given by

$$m_f(a) = \frac{n(a) \times v_n(a)}{\sum_a n(a) \times v_n(a)} \tag{3.32}$$

as all the grains are assumed to have the same densities. $v_n(a)$ is the volume of the n^{th} bin which corresponds to size a. The total mass of dust with size a, is then defined by,

$$m(a) = m_f(a) \times M_{tot} \tag{3.33}$$

where M_{tot} is the total mass of grains (condensed or in gas phase) present at that epoch, which is calculated with the help of the masses of the ejecta zones. Hence N_{tot} is calculated as,

$$N_{tot}(a) = \frac{m(a)}{v_n(a) \times \rho(a)} \tag{3.34}$$

We couple this condensation scheme to the nucleation network discussed before. Thus, the investigation of the gas phase chemistry and the solid phase of dust grains proceed simulnatenously. The sophisticated chemical model discussed in this Chapter is an ideal tool to tackle the chemistry of any ejecta or stellar outflow with a non-steady state environment.

4 The Computer Codes

The physical and the chemical model described in the previous chapters of the text are mounted on computer codes in order to successfully carry out the calculations. The problem in question is analytical in nature, which means given the initial conditions, there exist a unique solution to each specific case. This chapter is dedicated to the brief description of the computational techniques and the development of the codes. The first section deals with the chemical kinetic code NECSA and its subroutines. The second section introduces the radiative transfer code MOCASSIN used to estimate the SED's of the obtained dust distribution. MOCASSIN is not an analytical code but instead based on simulation methods.

4.1 Principal code NECSA

Non-steady state Ejecta Chemistry Solver Algorithm
Author: Isabelle Cherchneff, Revision: Arkaprabha Sarangi

The FORTRAN 77 code was initially introduced to study the gas phase chemistry and cluster formation with a non-steady state approach in the population III supernova ejecta of the early universe (Cherchneff and Dwek, 2009, 2010). The first version of the code was developed by Isabelle Cherchneff and Simon Lilly at ETH Zurich. Later it is revised by Arkaprabha Sarangi in order to couple the gas phase chemistry and the dust formation scenario in local supernovae. NECSA is a chemical kinetic code which can trace the evolution of all chemical species (atoms, molecules, molecular clusters, dust grains) in a dynamic ejecta or outflow model. The prime target of the code is to solve the gas phase master equation (Equation

3.6) and the coagulation equation (Equation 3.25) simultaneously. The inputs necessary as starting parameters are a) the chemical network which includes all reactions with reaction rates, energy barriers and temperature dependance b) the initial abundances of the elements c) the temperature and density functions along with their initial values d) the molecular weights of the species in interest and the size of the given zone. The body of the main code takes care of the conservation of the total mass. Following the chemical processes, the initial element concentrations get distributed among a large set of chemical species both in gas as well as solid phase. The elements that have already condensed as dust at a given step is taken away from the gas phase network and the rest continue to participate in the gas phase chemistry in the following step. The task of carrying out the calculations are divided strategically into the following 4 different subroutines.

(a) **Diffun:** Takes care of the temperature and density evolution of the gas at each time step. The initial temperatures and the densities are used as arguments.
(b) **Cse-order:** Estimates the major formation and destruction processes for each species. The reaction rates and the gas phase outputs at each epoch are the arguments to the subroutine.
(c) **LSODE:** The gas phase chemistry solver. The initial abundances, the reaction rates and the tolerance parameters are the required arguments.
(d) **CADSO:** The condensation subroutine for dust phase calculations. The gas density, temperature and the abundances of all the dust precursors synthesised in the gas phase are used as arguments.

The time-steps are decided mainly on the basis of accuracy. In the current analysis the time steps used in NECSA are $\sim$ 3 days. As outputs to the analysis at each step, the abundances of all the chemical species in gas and solid phase are determined. In the following subsections deal with discussion of the two principal subroutines in the code which establishes the connection between the gas and the solid phase.

4.1.1 Subroutine LSODE

Livermore Solver for Ordinary Differential Equations

Author: Alan C Hindmarsh

The code LSODE is a first-order ordinary differential equation (ODE) solver developed by A. C. Hindmarsh (Hindmarsh, 1982) in FORTRAN. It is useful to tackle problems of the following form,

$$\frac{dy_i(\xi)}{d\xi} = f_i(y_1(\xi), y_2(\xi).....y_N(\xi), \xi) \quad (i = 1, N) \tag{4.1}$$

As starting conditions, the initial values, $y_i(\xi_0) = y_{i,0}$ are considered to be known. Once the initial conditions are defined, the code is equipped to solve the equations iteratively within a given interval (ξ_0, ξ_{end}). We use LSODE to solve the set of coupled non-linear stiff first-order differential equations which are derived from the reaction rates of the chemical network. The solution method developed in LSODE replaces the ODE's with difference equations to solve them in steps. A stiff ODE system like that of the current problem consists of both rapidly as well as very slowly evolving terms. The N×N Jacobian matrix whose elements are defined as $J_{ij} = \partial f_i/\partial y_j$ has a widely variant set of Eigen values λ_i. The real part of the Eigen values are predominantly negative, which is also a confirmation of the stiffness. Under such conditions, standard ODE solution techniques like Runge-Kutta and Adam's method face difficulties to maintain numerical stability. LSODE package use the Backward Differentiation Formula (BDF) method (Gear, 1971) to tackle the set of ODE's. The BDF method possesses the property of stiff stability. Therefore, the step size constraints does not affect the stability. The step sizes are determined depending upon the accuracy requirement of the case study. To maintain the accuracy the step sizes are generally considered to be of the order of $1/max(Re(\lambda_i))$. The entire code is made up of as many as 21 subprograms and a block data module. However, the advantage of the code is a) the user interface is highly flexible b) it is segregated into small modules c) it uses dynamic storage allocation and different linear algebra modules (Byrne and Hindmarsh, 1987). The error control parameters RTOL (Relative tolerance parameter) and ATOL (Absolute tolerance parameter) are assigned in the principal code. Significantly, LSODE does not require (almost) any modification in order to adjust with specific cases of interest. The dynamic storage allocation allows to minimise the storage requirements as the array declarations are automatically estimated from array

dimensions in the main code. Therefore it can be used as subroutine to our mother code NECSA just by calling the necessary input parameters.

4.1.2 Subroutine CADSO

Condensation Algorithm for Dust in Stellar Outflows

Author: Arkaprabha Sarangi

The code CADSO, written in FORTRAN, is used in the formalism to couple the gas phase chemistry to the condensation phase of dust grains. The CODE is equipped to address the coagulation and coalescence among particles ranging between molecular to millimeter orders in dimension. The main goal is to solve the coagulation equation given in chapter 3 (Equation 3.25) and to check for conservation. The grains are discrete particles and hence they are assigned to bins identical to their volume. A volume fractionation technique is adopted to tackle the grains of intermediate in sizes to two adjacent bins (Jacobson, 2005). Considering a volume V of a new grain which is intermediate in volume between bins k and $k+1$, the fractionation is done as,

$$\begin{aligned} f_k &= \left(\frac{v_{k+1}-V}{v_{k+1}-v_k}\right)\frac{v_k}{V} \qquad && (v_k \leq V < v_{k+1}) \\ f_k &= 1 - f_{k-1} && (v_{k-1} < V < v_k) \end{aligned} \tag{4.2}$$

The technique used in the method of solving is called semi-implicit coagulation solution introduced by Jacobson and Turco, 1994. Between two consecutive time steps (∼3 days) in the gas phase chemistry, the coagulation equation is solved in smaller steps (∼45 min) in order to study the fate of the gas phase precursors already synthesised in the previous steps. Thereafter, in the next step, new monomers from gas phase appear and again enter the condensation sequence. The semi-implicit method substitutes the number density $n_{j,t}$ in the coagulation equation by $n_{j,t-h}$, where j is the size bin of the population and h is the time step of used in CADSO. This way, the conservation of volume and volume concentration is achieved, where volume $v_{j,t} = v_j n_{j,t}$. The final solution for volume concentration of particles in each bin is given by (Jacobson, 2005),

$$v_{k,t} = \frac{v_{k,t-h} + h\sum_{j=1}^{k}\left(\sum_{i=1}^{k-1} f_{ijk}\beta_{ij}v_{i,t}n_{j,t-h}\right)}{1 + h\sum_{j=1}^{N_B}((1-f_{kjk})\beta_{kj}n_{j,t-h})} \quad , \tag{4.3}$$

where N_B is the total number of bins. The code involves a large number of integration steps as the condensation of grains are traced up to 5 years post explosion in the steps of 45 minutes. The computation time depends on the concentration of the grains and the number of total number of bins assumed. CADSO is equipped to tackle any number of dust species present in the ejecta concurrently. In the current study 8 types of dust components are considered, however they are specific to ejecta zones. As outputs, CADSO provides the information on a) grain density as function of size b) total number of grains as function of size c) mass abundances of each size grain d) mass of condensed dust. The derived outputs are printed in files specific to each time step of the mother code and each grain component.

Therefore the total package developed for the current study is a powerful tool which can in parallel address the chemistry of gas phase and solid phase in a dynamic non-steady state environment.

4.2 Radiative transfer code MOCASSIN

MOnte CArlo SimulationS of Ionized Nebulae

Author: Barbara Ercolano, Revision: Roger Wesson

The fluxes from the dust formed in the ejecta are calculated in the current study using MOCASSIN code. It uses a Monte Carlo (MC) technique to study radiative transfer (RT) through various media. MC is a method of using random numbers in scientific computing. In MC RT the radiation field is treated a flow of large but finite number of photon packages. Each individual photon is followed along its journey through the dusty medium. The focus remains on the following: a) the injection of the photon to the computational domain b) to randomly determine its interaction point with the dust medium c) absorption and scattering of the incident photons (Steinacker et al., 2013). The dust emission is in turn considered the second source of photons and the RT from the primary photon source and the secondary photon source are computed simultaneously. The characteristics determining the path of the each photon are estimated in a probabilistic way by generating random numbers from an appropriate probability density function. At the end the radiation field is recovered from the statistical analysis of photon paths. Thus MC uses a simulation method instead of explicitly solving the RT equations.

Radiative transfer code MOCASSIN is developed at University College London (UCL) by Barbara Ercolano (Ercolano et al., 2005). Later it is modified by Roger Wesson through addition of modules and debugging. It is written in FORTRAN90. MOCASSIN is a fully 3D or 2D photoionisation and dust radiative transfer code which employs a MC approach to the transfer of radiation through media of arbitrary geometry and density distribution. It was originally developed for the modelling of photoionised regions like HII regions and planetary nebulae and has since expanded and been applied to a variety of astrophysical problems, including modelling clumpy dusty supernova envelopes, star forming galaxies, protoplanetary disks and inner shell fluorescence emission in the photospheres of stars and disk atmospheres. The code can deal with arbitrary Cartesian grids of variable resolution, it has successfully been used to model complex density fields from SPH calculations and can deal with ionising radiation extending from Lyman edge to the X-ray. The dust and gas microphysics is fully coupled both in the radiation transfer and in the thermal balance (Courtesy: MOCASSIN manual). The dust RT code allows a multigrid resolution approach suitable for studying a clumpy ejecta. The radiation field is assumed as discrete monochromatic packets of energy over the whole spectrum (Ercolano et al., 2007).

The fully parallel and modular code focus on the radiative transfer through dusty supernova ejecta with a spherical symmetry assumption. The dust grains are considered to be distributed inside a spherical shell either uniformly or as clumpy dense cells. The parameters such as the dust compositions, grain size distributions and dust opacities are used as input conditions. These dust properties derived at each epoch from NECSA therefore directly acts as inputs to MOCASSIN. A further description of the specific cases are given in chapter 9. The outputs are obtained in terms of energy densities which is then revised by the distance of the given supernova from earth to determine the fluxes. The effective optical depth of the medium is also calculated at the given epoch.

5 The Standard 15 $M_\odot$ Model

A supernova ejecta is a unique natural laboratory which is associated with a variety of nuclear, chemical, radioactive and hydrodynamic processes. Some of these physical phenomena are coupled to each other, whereas the other processes are relevant at different time scales. The preceding Chapters have described in details, the physical (Chapter 2), chemical (Chapter 3) and the computational (Chapter 4) aspects of the study. Using the formalism as explained before, we analyse the ejecta of several type II-P supernovae. In this Chapter we focus on the study of a 15 $M_\odot$ progenitor case, which have chosen as a standard case for a typical type II-P supernova. We investigate the evolution of atoms, molecules and clusters in the gas phase and the budget of dust in the ejecta. The Section 5.1 reports on the concentration of important molecules and small clusters as a function of the ejecta zones and explains the chemistry with the help of relevant reactions. The following Section 5.3 deals with the dust components, the dust masses and the size distributions of different dust species specific to this progenitor type. Lastly in this chapter we shall concentrate on the depletion of elements into different molecules and dust in the ejecta. It is important to throw light on the crucial rule played by the nobel gases on the chemistry. The last Section 5.4.2 shall illustrate the impact of nobel gases with regard to the entire study. The initial abundances of elements in different zones are tabulated in Table 2.2. The mass range of each zone, and the important elements to look for in the respective layers are hereby tabulated in the following Table 5.1.

TABLE 5.1: The range of each mass zone ($M_\odot$) in the ejecta, and the important species which control the chemistry in the respective zones

Zone 1A	Zone 1B	Zone 2	Zone 3	Zone 4A	Zone 4B	Zone 5	Zone 6
1.79-1.88	1.88-1.98	1.98-2.27	2.27-2.62	2.62-2.81	2.81-3.04	3.04-3.79	3.79-4.14
Si/S/Fe	Si/O	O/Mg/Si	O/Ne/Mg	O/C	He/O/C	He/C	He/N

5.1 The molecules

The zones of the He-core are efficient in forming different kinds of molecules. However, as we assume the no possibility of H-mixing in the inner He-core, the chemistry remains hydrogen free. Because of this, the network is relatively limited to a few important species. This can as well be supported by the fact, that ever since only two molecules CO and SiO has been confirmed through observations (Roche et al., 1991; Kotak et al., 2005; Rho et al., 2009), to be present in the ejecta. Table 5.2 enlists all the observational cases of these molecules reported in different supernovae. The synthesis of diatomic molecules namely SiO, CO, O_2, SO and SiS are important in the ejecta in terms of their abundances and epochs of formation. There are a traces of few other molecules like CO_2, N_2, CS, etc., also synthesised in relatively smaller proportion. We begin our analysis of the ejecta chemistry from day 100 after the explosion. The conditions of the ejecta prior to that, are not suitable for any active chemical process take place. The composition of the zones dictate the synthesis of molecules. Hence we have presented the results for molecules as functions of ejecta zones. The results corresponding to all the gas phase species (molecules, residual molecular clusters) are summarised in Table 5.3.

5.1.1 CO

In the harsh environment of the supernova ejecta characterised by fast moving shock waves, radioactive decays and passage of X-rays and γ-rays, the early detection of molecules is itself a special event. However the first overtone transition ($\Delta\nu = 2$) of CO molecule at 2.3 μm has been reported as early as 100 days after explosion in SN1987A (Danziger et al., 1988). Along with that, the fundamental band $\Delta\nu = 1$ at 4.65 μm has also been observed between 130-260 days for the same (Catchpole et al., 1988). Similar detections have also been reported for CO in SN2004dj (Kotak et al., 2005) and many other supernovae in last 20 years as listed in Table 5.2. Both in case of SN1987A and SN2005af the flux of the first overtone

TABLE 5.2: The summary of CO and SiO observational evidences reported in various type II supernovae in recent years (Cherchneff and Sarangi, 2011)

Name	CO 1^{st} overtone (2.3 μm)	CO fundamental (4.65 μm)	SiO fundamental (8.1 μm)	Reference
SN1987A	✓			Spyromilio et al., 1988
		✓		Catchpole et al., 1988
			✓	Aitken et al., 1988
	✓	✓		Danziger et al., 1988
			✓	Roche et al., 1991
SN1995ad	✓			Spyromilio and Leibundgut, 1996
SN1998S	✓			Gerardy et al., 2000
	✓			Fassia et al., 2001
SN1998dl	✓			Spyromilio et al., 2001
SN1999em	✓			Spyromilio et al., 2001
SN2002hh	✓			Pozzo et al., 2006
SN2004dj		✓		Kotak et al., 2005
		✓		Szalai et al., 2011
SN2005af		✓	✓	Kotak et al., 2006
SN2004et		✓	✓	Kotak et al., 2009

band peaks around ∼200 days and then gradually declines in magnitude up to 600 days, after which it becomes unobservable. This is either due to the change in CO mass or due to the different excitation conditions owing to the change in gas temperature. The fundamental of CO lines, which in optically thick in case of SN1987A, is observed to change in absolute strength at a much slower rate compared to the fundamental. This aspect may refer to the origin of the CO in different zones in the ejecta. The estimation of mass from the observational data requires the modelling of temporal variation of temperature and density and the optical depths. Such study by Liu et al., 1992 using local and non local thermodynamic equilibrium (LTE & non-LTE) gives the masses of CO in the order or 10^{-3} to 10^{-2} $M_{\odot}$ between the time span of 200 to 600 days. Recent observations by ALMA detected the presence of CO molecules in the cold debris of SN1987A after 28 years from explosion. The lower limit of CO mass as reported by Kamenetzky et al., 2013 is 0.01 $M_{\odot}$. Further calculations using the filling factors from Jerkstrand et al., 2011, the estimated mass comes out to be ∼0.2 $M_{\odot}$. This indicates the CO molecules, which were formed in the ejecta at early times must have there remained since that time and have increased in abundance to some extent over this period.

The evolution of CO mass with post-explosion time for the He-core is presented in Figure 5.1 as a function of the ejecta zones. CO molecules are essentially synthesised in the C/O rich zone 4A and 4B, followed by the central region on the O-core, zones 2 and 3 (Table 5.3). CO formation follows very efficient chemical

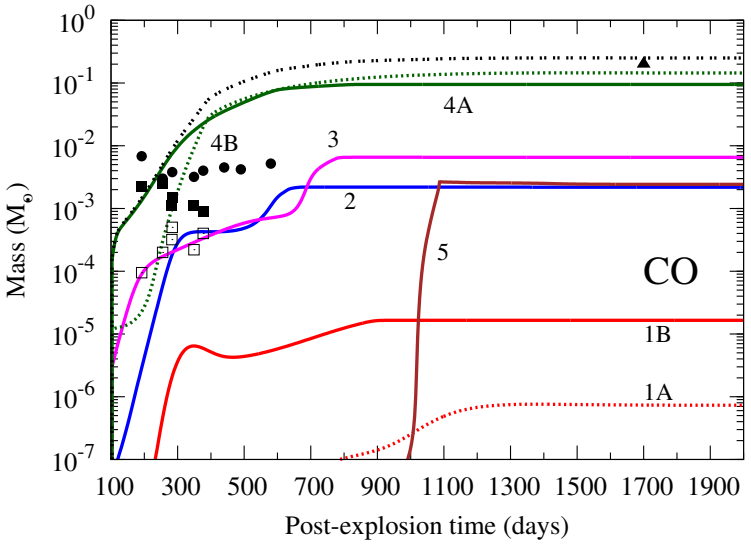

FIGURE 5.1: Mass of CO in a 15 $M_\odot$ model presented in $M_\odot$ as a function of various ejecta zones as labelled by the side of the line. The black dotted line corresponds to the total over all the zones. CO masses derived from the observations of SN1987A are shown as, LTE open squares, non-LTE: squares (Liu et al., 1992), thermal assumption: circles (Liu and Dalgarno, 1995), ALMA data: triangle (Kamenetzky et al., 2013). The ALMA data is not true to the time axis, but rather indicates the final mass at late times as compared to our results.

routes. Hence the abundance increases as early as 150 days and becomes constant in mass by 700 days post-explosion. Due to the strong chemical bonds, once formed in the ejecta, the CO molecules are found to withstand the harsh environment conditions and possible destruction mechanisms. The masses are limited by the abundances of C in the ejecta. Since both in zone 4A and 4B, C/O ratio is less than 1, all the carbon in these zones, gets locked up in CO. The final mass of CO reaches 0.25 $M_\odot$ at around 700 days and it remains constant after that (Table 5.3). The final masses are in accord with the estimations by Kamenetzky et al., 2013 and also it matches well at $\sim$ 300 days (4×10^{-3} $M_\odot$) with the IR observations. However at times 400-600 days, the estimated mass of CO from the study is more than one order of magnitude larger compared to the analysis by Liu and Dalgarno, 1995. In zone 5, the formation of CO is delayed due to the presence of He^+ in the gas. The mass of CO pumps up as soon as the He^+ recombination occurs at around 1000 days as explained in Section 5.4.2. The chemical pathways important for CO formation are mainly,

$$
\begin{aligned}
O + C_2 &\rightarrow CO + C \\
C + O &\rightarrow CO + h\nu \\
C + O_2 &\rightarrow CO + O
\end{aligned}
\tag{5.1}
$$

The formation of C_2 occurs via radiative association very early on, but due to the presence of atomic O, they quickly gets converted to CO (Equation 5.1) by oxidation. Around 300 days, the radiative association of C and O becomes an important contributor to the formation path of CO. Even later to that, also the reaction with dioxygen is a notable process of CO formation. The destruction routes are mainly controlled by neutral-neutral processes with Si, S, Al, etc., and to some extent by formation of CO_2. However the forward rates clearly win over the destruction channels. Since the abundances of nobel gases in zone 4A and 4B are not significant, the early formation of CO molecules in the ejecta is assured (Sarangi and Cherchneff, 2013). There is no evidence of depletion of CO molecules with time as analysed in the study. Hence it can be safely claimed, that CO does not act as a precursor to the Carbon dust. It has been explained in detail later in Section 5.3.

5.1.2 SiO

Emission from vibrationally excited silicon monoxide molecule was reported by Aitken et al., 1988 in SN1987A at 160 days post-explosion. The fundamental band of SiO in the mid-IR (8.1 μm) is detected from observation in the period of 160-520 days in case of SN1987A (Roche et al., 1991; Lucy et al., 1989). Nevertheless no further emission was recored at later times after 530 days from explosion. The mid-IR observations of SN2004et by Spitzer Space Telescope, suggests the presence of SiO molecules in the ejecta in the 300-460 day period after the explosion. Further investigation of the same supernova at times later than 690 days indicates the fading of SiO lines and the increase in strength of the continuum from dust. The spectra could be well fitted using a combination of SiO molecules and silicate dust (Kotak et al., 2009). Hence it was proposed that the depletion of SiO molecules in silicate dust attributes to the decline of the SiO emission lines in the ejecta. The masses of SiO derived from several observations in mid-IR for SiO molecules in different supernovae are in the range between 10^{-4} to 10^{-3} $M_{\odot}$.

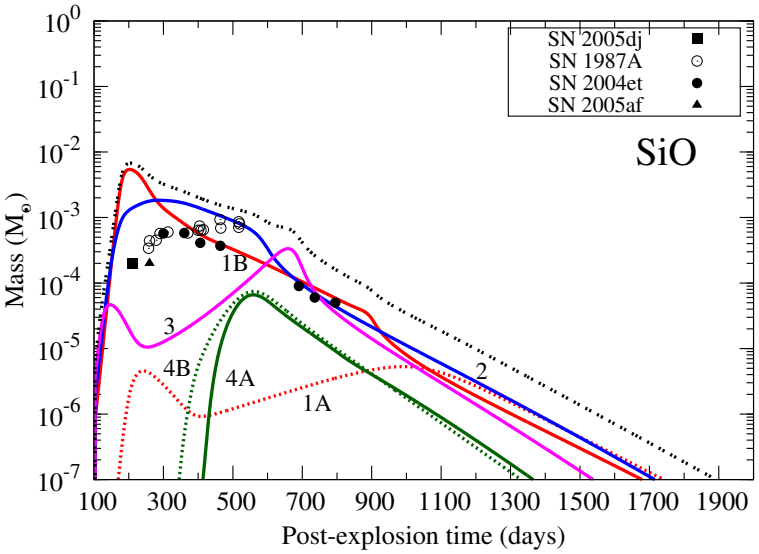

FIGURE 5.2: Evolution of SiO mass ($M_\odot$) with post-explosion time in days as a function of different zones in the ejecta. The black dotted black line corresponds to the sum over the SiO mass from all the zones. The solid square, circle, and triangle indicates the mass of SiO reported from observations in IR from several supernovae as specified in the legend box (Sarangi and Cherchneff, 2013)

.

The evolution of SiO mass with time in different zones of the ejecta is presented in Figure 5.2. The final masses of SiO molecules are also tabulated in Table 5.3 as function of each zones. SiO is formed mainly in the central zones of the O-core, named as zones 1B, 2 & 3. The SiO increases rapidly to 8×10^{-3} $M_\odot$ at day 200 from explosion in these zones. In case of zone 4A and 4B, SiO formation is delayed to $\sim$ 400 days due to smaller initial abundances of Si. The important formation processes worthy to mention in this context are listed in Equation 5.2.

$$\begin{aligned} Si + CO &\rightarrow SiO + C \\ Si + O &\rightarrow SiO + h\nu \\ Si + O_2 &\rightarrow SiO + O \end{aligned} \tag{5.2}$$

The synthesis of SiO in zones 1B and 3 are controlled by the interactions with ions like the Ar^+ & Ne^+. The presence of such ions in abundance provides an important pathway of destruction as explained by Equation 5.3. However the overall abundances of Si and O being quite high in zones 1B and 2, the effect of the nobel gas ions are not visible from the Figure. In case of zone 3, the relative abundance of Ne is much more than Si. The evidence in clear in Figure 5.2 where the SiO formation remains suppressed till almost day 700, and the rapid increase

like in case of zones 1B and 2 does not take place. Due to the presence of a lot of atomic O in these zones, also the destruction through collision with atomic O becomes important at times later to 400 days.

$$\begin{aligned} SiO + Ar^+ &\rightarrow Si^+ + O + Ar \\ SiO + Ne^+ &\rightarrow Si^+ + O + Ne \\ SiO + Ar^+ &\rightarrow Si + O^+ + Ar \\ SiO + Ne^+ &\rightarrow Si + O^+ + Ne \\ SiO + O &\rightarrow Si + O_2 \end{aligned} \tag{5.3}$$

The mass of SiO formed in the ejecta however does not remain constant like in case of CO. The rapid formation SiO molecules in the ejecta is subsequently also followed by rapid conversion into small clusters. The schematic diagram of Figure 3.2 in Chapter 3 best explains the fate of SiO molecules after its formation. Following the nucleation channels, the SiO molecules gets depleted to silica and silicate clusters in all the ejecta zones. The mass of SiO hence goes down from $\sim 10^{-2}$ at 200 days to 10^{-8} $M_\odot$ after 2000 days post-explosion. This way the SiO molecules act as a direct tracer of silicates and silica dust. This shall be again addressed in Section 5.3. The trend of decrease of SiO mass can be correlated to the IR observations of SN2004et and SN1987A (Kotak et al., 2009). The masses of SiO estimated from the study are also in good agreement with the masses reported from observations in several type II supernovae in time range between day 200-700 (Sarangi and Cherchneff, 2013).

5.1.3 O_2

Apart from SiO and CO, the most important molecule in the ejecta is most certainly the dioxygen molecule. Due to symmetry and zero dipole moment of O_2, the vibrational transitions in the IR are absent. However the atomic being the most abundant species in zones 1B, 2, and 4 the formation of dioxygen molecules are inevitable. The time evolution of O_2 mass is explained in Figure 5.3 (left panel) and the final contribution from different zones are tabulated in Table 5.3. The dioxygen molecules appear in the ejecta around day 600, and rapidly increase in mass to attain a mass of $\sim$ 0.4 $M_\odot$. The early time formation of such molecules

TABLE 5.3: Masses ($M_\odot$) of molecules, intermediate clusters and uncondensed dust-clusters in the gas phase at 2000 days post-explosion in the ejecta (Sarangi and Cherchneff, 2013, 2014)

Zones	Z1A	Z1B	Z2	Z3	Z4A	Z4B	Z5	Z6	Total
Molecules									
Mass	9.6(-2)	9.5(-2)	0.292	0.347	0.195	0.225	0.75	0.347	2.35
SiO	2.0(-8)	1.3(-8)	1.3(-8)	2.1(-9)	...	...	...	...	4.8(-8)
O_2	...	2.8(-5)	0.15	0.16	6.2(-2)	4.9(-3)	...	...	0.38
CO	7.5(-7)	1.7(-5)	2.2(-3)	6.6(-3)	9.5(-2)	0.14	2.9(-3)	...	0.25
SO	...	1.5(-2)	3.8(-3)	1.0(-4)	1.1(-4)	...	...	...	1.9(-2)
SiS	4.3(-2)	2.1(-7)	...	...	...	...	...	...	4.3(-2)
CO_2	...	...	1.7(-5)	2.7(-5)	...	...	...	...	4.4(-5)
CS	...	...	...	...	...	...	1.5(-4)	...	1.5(-4)
N_2	...	...	...	3.2(-7)	3.5(-7)	...	3.1(-3)	...	3.1(-3)
Total	4.3(-2)	1.5(-2)	0.156	0.167	0.157	0.15	6.2(-3)	0	0.695
Efficiency(%)	44.8	15.8	53.4	48.1	80.5	66.7	0.8	0	29.6
Intermediate molecular clusters									
$^\dagger Si_mO_n$	...	5.5(-2)	3.4(-2)	2.9(-3)	...	...	...	...	9.0(-2)
C_{2n}	...	...	...	...	...	...	5.5(-3)	...	5.5(-3)
Fe_n	8.2(-5)	...	...	...	...	...	...	...	8.2(-5)
Total	8.2(-5)	5.5(-2)	3.4(-2)	2.9(-3)	...	...	5.5(-3)	...	9.6(-2)
Uncondensed dust clusters									
$(Mg_2SiO_4)_2$	...	9.9(-6)	4.1(-5)	1.7(-5)	2.2(-6)	2.0(-6)	1.9(-5)	...	9.1(-5)
$(Al_2O_3)_4$	...	3.4(-6)	4.8(-5)	4.7(-5)	...	...	...	...	9.9(-5)
C_{28}	...	...	...	...	...	...	1.0(-8)	...	1.0(-8)
Mg_4	...	...	1.4(-5)	1.8(-5)	...	...	...	...	3.2(-5)
Si_4	9.7(-6)	...	...	...	...	...	...	...	9.7(-6)
Fe_4	6.5(-6)	...	...	...	...	...	...	...	6.5(-6)
SiC_4	...	...	...	...	...	...	1.1(-5)	...	1.1(-5)
FeS_4	2.2(-7)	...	...	...	...	...	...	...	2.2(-7)
Total	1.6(-4)	1.3(-5)	1.0(-4)	8.2(-5)	2.2(-6)	2.0(-6)	3.0(-5)	...	2.5(-4)

†The masses of Si_mO_n molecules are results from an incomplete analysis (see section 5.2.2).

take place through radiative transfer process (Equation 5.4).

$$O + O \rightarrow O_2 + h\nu \tag{5.4}$$

But it gets quickly depleted to form CO and SiO molecules as mentioned in Equations 5.1 & 5.2. After most of the atomic C and Si gets locked up in molecules, the residual O_2 molecules appears in the ejecta around 600 days after explosion. Apart from destructions by C and Si, also the dioxygen molecule gets destroyed by neutral-neutral reactions with Aluminium and Sulphur such as,

$$\begin{aligned} Al + O_2 &\rightarrow AlO + O \\ S + O_2 &\rightarrow SO + O \end{aligned} \tag{5.5}$$

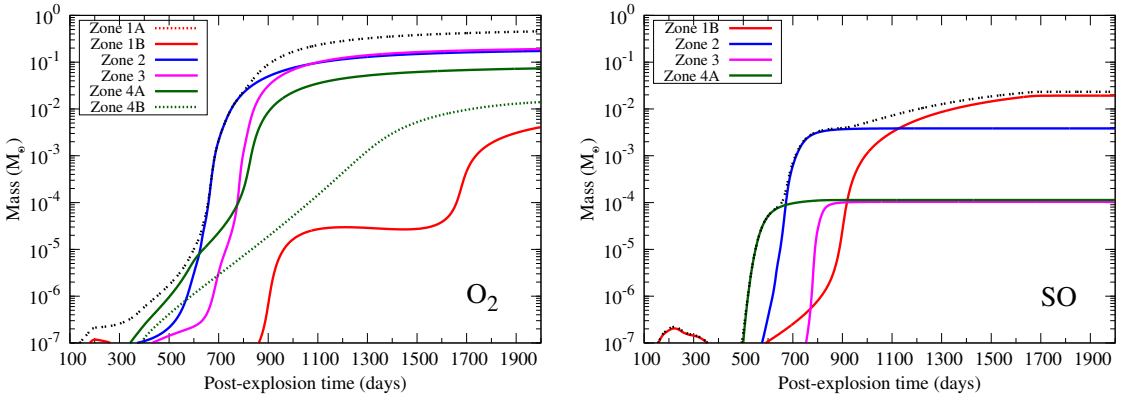

FIGURE 5.3: **Left panel:** The mass of O_2 molecules are presented are presented as a function of post-explosion time for all the ejecta zones. **Right panel:** The evolution of SO molecules in the ejecta as a function of post-explosion time for different ejecta zones. The black dotted line indicates the total over all the zones for both the cases (Sarangi and Cherchneff, 2013)

.

The most of the dioxygen molecules are formed in the zones 2 and 3 as expected and is followed by zones 4B and 4A respectively. The mass of O_2 remains relatively small in zones 4A and 1B directly reflects to the fact, that these zones are the leading producers of CO and SiO molecules where most of the O atom is hence locked up. Once formed, the O_2 molecules continue to act as oxidising agents for O-rich clusters of silica, silicates or alumina through reactions like

$$Cluster(silica/silicate/alumina) + O_2 \rightarrow [Cluster + O] + O \qquad (5.6)$$

Hence formation of dioxygen molecules acts as the bottleneck of the entire nucleation scheme for O-rich clusters.

5.1.4 SO

The other important oxygen rich diatomic molecule in the ejecta is SO. Figure 5.3 (right panel) shows the evolution of SO molecules in different zones in the ejecta. SO molecules are essentially synthesised in zone 1B and 2. The Si/S/O rich zone 1B, is the prime site for the formation of SO, and the final mass reaches 0.02 $M_\odot$ at 2000 days from explosion (Table 5.3). The molecules starts to appear in the ejecta at roughly 400 days, due to formation in zone 4A, and then consecutively formation of SO starts in zone 2 and 1B. The main reactions of formation are either radiative transfer or neutral-neutral processes.

$$\begin{aligned} S + O &\rightarrow SO + h\nu \\ O + S_2 &\rightarrow SO + S \\ S + O2 &\rightarrow SO + O \end{aligned} \tag{5.7}$$

Synthesis of S_2 occurs early in zone 1B and hence catalyses the formation of SO in this zone. The destruction paths for SO are mainly by collision with C or O, leading to the formation of CO or O_2. Furthermore, the SO already synthesised in the ejecta also has an oxidising effect on the small clusters, similar to that of Equation 5.6 in case O_2.

$$Cluster(silica/silicate/alumina) + SO \rightarrow [Cluster + O] + S \tag{5.8}$$

5.1.5 SiS

The innermost layer of the He-core, zone 1A, has a composition rich in Silicon and Sulphur. This zone has a very different texture compared to other zones in the ejecta, owing to its very low O-content. Several O-free molecules and small clusters are synthesised in this zone. Most of these species shall be discussed elaborately in the following sections. One of the important diatomic molecule abundantly synthesised in this specific zone is SiS. The formation pathways are mainly,

$$\begin{aligned} Si + S &\rightarrow SiS + h\nu \\ Si + S_2 &\rightarrow SiS + S \end{aligned} \tag{5.9}$$

The reaction rates for the second reaction in Equation 5.9 is not well characterised. Due to the lack of documentation, we used rates similar to the reactions between atomic C and disulphur. Also as a test case, the reaction was excluded from the network. Then the formation processes is dominated by the first reaction only, and the final masses for SiS does not alter to a notable extent. Hence it can be safely inferred, that zones rich with Si and S and scarce in oxygen will advocate the formation of SiS molecules. The mass of SiS has been presented against post-explosion time in Figure 5.4(left panel). The red-dotted line corresponds to zone 1A, where formation starts as early as 150 days, and final mass reaches 0.043 $M_\odot$

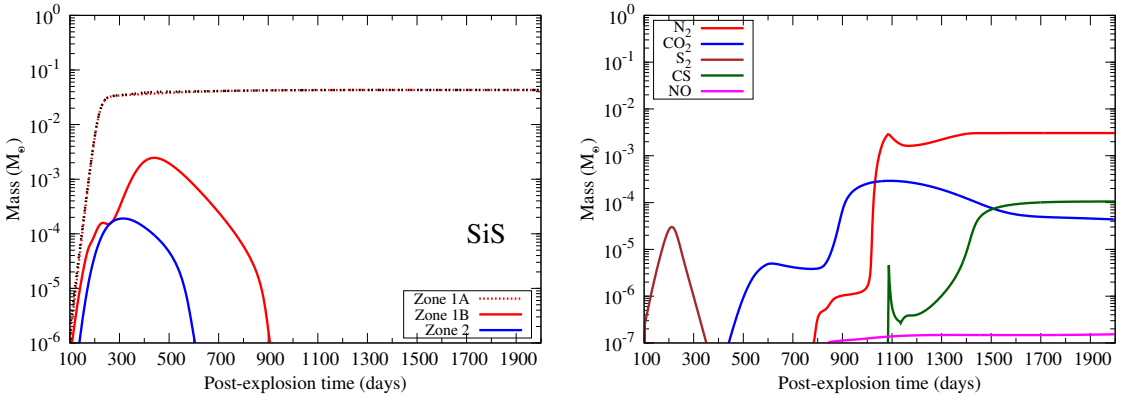

FIGURE 5.4: **Left panel:** The mass of SiS_2 molecules are presented are presented as a function of post-explosion time for different the ejecta zones. The black dotted line indicates the total over all the zones (Sarangi and Cherchneff, 2013). **Right panel:** The masses of N_2, CO_2, S_2, CS and NO summed over all the zones in the ejecta is presented as a function of post-explosion time in days. The contribution of different zones to the total mass of each species can be obtained from Table 5.3.

at the end of 2000 days from the day of explosion (Table 5.3). SiS also forms in zone 1B and 2 through radiative transfer. However later on it gets destroyed through collision with O, or by the attack of Ar^+ or Ne^+ ions present in abundance in these zones (Sarangi and Cherchneff, 2013).

5.1.6 Traces of other molecules

Apart from the molecules mentioned before, also molecules such as N_2, CO_2, S_2, CS and NO are formed in the ejecta in a smaller quantity. In Figure 5.4 (right panel), the trace of all these molecules are presented as a function of post-explosion time. The masses plotted in the figure for each molecule, is the sum over all the zones. The final masses at 2000 days for each of the molecules with the break-up of zones are also summarised in Table 5.3. In case of S_2, the formation is mainly in zone 1A through radiative transfer. Later on it gets depleted also rapidly leading to the formation of SiS according to Equation 5.9. CO_2 molecules are formed mostly in zone 2 and 3 due to the presence of excess O. The formation and destruction routes are both controlled by reactions with SiO as following,

$$\begin{aligned} CO + SiO &\rightarrow CO_2 + Si \\ CO_2 + Si &\rightarrow CO + SiO \end{aligned} \tag{5.10}$$

The final mass of CO_2 remains in the order of $5{\times}10^{-5}$ $M_\odot$ at day 2000 from explosion.

N_2 is formed in zone 5, where according to the initial abundances, N comes third in order, after helium and carbon. Also this zone is responsible for the formation of CS molecules. Other than CO and SiO, also the presence of CS in supernova ejecta also has some observation proofs. The broad emission features at 3.8 μm in SN1987A at late times was proposed to come from CS by Meikle et al., 1993. Due to the detrimental effects of He^+ in the gas in zone 5, the formation of all molecular species are delayed up to ∼1050 days after explosion. The formation chemistry of N_2 and CS are coupled to each other through CN. At around 1100 days, CS formation pumps up rapidly through radiative association. This leads to the formation of CN as shown in Equation 5.11.

$$\begin{aligned} C + S &\rightarrow CS + h\nu \\ CO + S &\rightarrow CN + S \end{aligned} \tag{5.11}$$

Following this, CN in turn again interacts with N atoms to form N_2. Later on, the mass of CS again increases gradually through neutral-neutral reactions between CO and S (Equation 5.12).

$$\begin{aligned} CN + N &\rightarrow C + N_2 \\ S + CO &\rightarrow O + CS \end{aligned} \tag{5.12}$$

The outermost zone of the He-core, zone 6 has also a rich abundance of atomic N. Nevertheless helium constitutes more than 99% of the composition in this zone and the prejudicial effects of He^+ dominates the chemistry even after 2000 days. Therefore, no stable molecules are formed in this zone.

The aluminium monoxide is also formed in the ejecta in significant amount. The AlO thereafter rapidly goes on to form alumina dust. Hence we have merged our discussion regarding AlO molecules, with the section dealing with alumina dust. The total mass of molecules in the ejecta at 2000 days for the 15 $M_\odot$ case is hence given by 0.695 $M_\odot$. The efficiency of molecule formation is hence is 30%, which means this much percentage of the entire ejecta remains in pure molecular form (excluding the molecular clusters) at late times (Table 5.3). Zones 4A and 4B are the most efficient in forming molecules, where almost 80% of the mass goes on to molecules. Again the nobel gases, mainly helium play important role in controlling the efficiency of molecule formation. The outer layers of He-core, zones 5 and 6

contain 46 % of the entire ejecta mass and the composition is mostly made up of helium. Helium being a nobel gas does not take part in molecule formation, on the contrary due to the interaction with He^+ other stable molecules cannot form in these zones with ease.

5.2 Molecular clusters through nucleation

Following the chemical reactions leading to the formation of diatomic molecules, molecular clusters start to form in the ejecta through nucleation. Nucleation proceeds via diverse chemical routes specific to each species, as discussed in details in Section 3.3. The cluster formation mechanisms are skewed towards stable (energetically and structurally) units, which act as dust precursors. The dust formation process through condensation is synchronous to the nucleation phase. So in the end, a large portion of the clusters leave the gas phase and resides as solid dust grains. Nucleation is the bottle-neck to the entire dust formation scenario. To study the outcome from nucleation processes, we discuss the results in two sections. In the first section, the total budget of small clusters synthesised in the gas phase prior to condensation is addressed. Next we shall report on the residue that remain in the gas post-condensation.

5.2.1 Clusters pre-condensation

In this section the formation and formation mechanisms of small molecular clusters are explained, which takes place before these small clusters can actually coagulate and grow in size. In the O-core, the dimers of Mg_2SiO_4 and the tetramers of Al_2O_3 appear. The nucleation of $(Mg_2SiO_4)_2$ follows a complicated route shown in the Figure 3.2. However, as the reaction chains are downhill in energy, the formation of $(Mg_2SiO_4)_2$ in the gas-phase is favoured. These clusters start to form in zone 1B and 2 at times between day 300 to 600. A similar network exists for $(Al_2O_3)_4$ and the zones of formation are mainly 2 and 3 around day 700. The stable $(Mg_2SiO_4)_2$ and $(Al_2O_3)_4$ survive the destruction routes in the gas and eventually gets depleted in dust. Pure carbon clusters are the other most important molecular cluster formed in the gas. The formation mechanism of Carbon significantly differs from the O-clusters. The population of carbon gets distributed among C-chains (C-C_9), C-ring (C_{10}-C_{20}) and hollow spherical fullerenes (C_{2n}, n$\geq$11). The increase

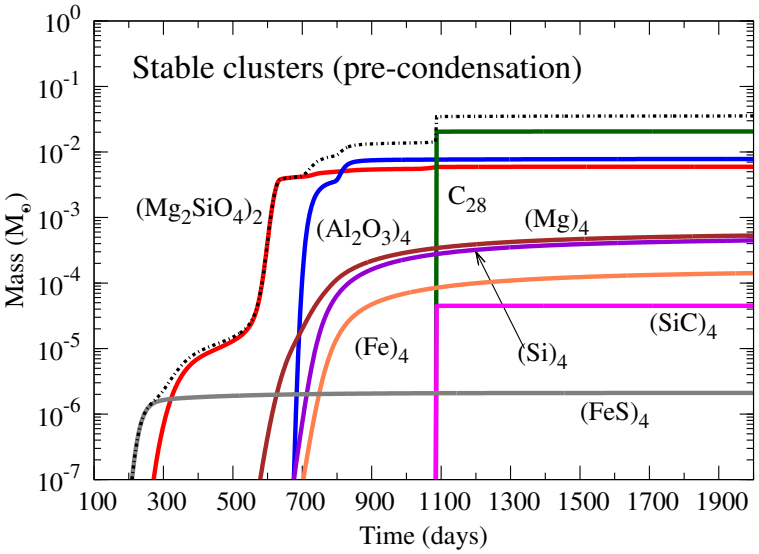

FIGURE 5.5: The masses of all the dust precursors are shown prior to condensation. These monomers gets depleted into dust over time. Therefore, this figure represents the final masses of gas phase monomers which eventually participate in dust formation (Sarangi and Cherchneff, 2013).

in C-content of the cluster molecules are attributed to the availability of free C and C_2 molecules in the gas. Our findings suggest, C_{28} is the first most stable cluster formed through the nucleation scheme. On the basis of mass, the carbon clusters are the most abundant, but on the other hand they also condense very efficiently and leaves the gas phase. The other molecular clusters synthesised in the ejecta at different times and at different zones are $(Si)_4$, $(Fe)_4$, $(FeS)_4$ (Zone 1A), $(Mg)_4$ (Zones 2, 3), $(SiC)_4$ (Zone 5). $(FeS)_4$ is the first stable dust precursor formed in the gas around day 200. However its mass prior to condensation remains limited to only $\sim 10^{-6}$ $M_\odot$. The mechanism of formation follows polymerisation routes described in Section 3.3. The masses of all the stable molecular clusters are shown in Figure 5.5 prior to condensation. Important to note is that, the condensation is an efficient process and therefore these clusters, which act as seeds to condensation, get spontaneously depleted in larger particles. The fate of these small clusters are shown in Figure 5.7 post-condensation. Even though the stable molecular clusters in the gas phase are short-lived in the chemical chain of molecules $\rightarrow$ clusters $\rightarrow$ dust, the nucleation end-products dictate following dust formation phase. Primarily, they dicate the composition of dust and the epoch of synthsis. A gradual build up of cluster masses (from 10^{-6} to 0.037 $M_\odot$) between day 300 to day 1500 presented in Figure 5.5 is akin to the dust mass profiles discussed in the following section, confirming efficient condensation.

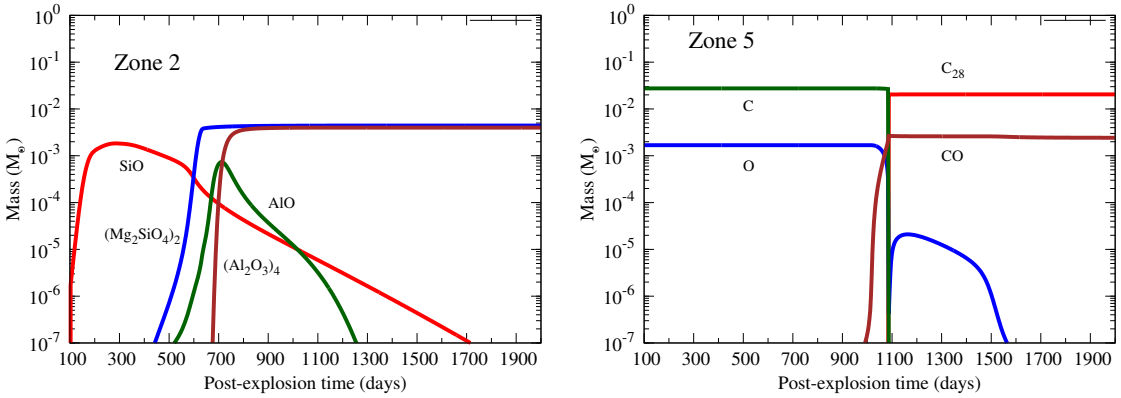

FIGURE 5.6: **Left panel:** The correlation between the oxygen rich dust precursors and the diatomic molecules are established with reference to zone 2. The figure shows the depletion of SiO and AlO to form stable gas phase monomer units of silicate and alumina dust. **Right panel:** The figure indicates the non-correlation between the synthesis mechanisms of CO molecules and the stable fullerene rings of carbon with reference to zone 5, which is the site of formation for carbon clusters. (Sarangi and Cherchneff, 2013)

In order to investigate the role of molecules as tracers to these clusters, we present two different cases. Figure 5.6 illustrates the scenario in zone 2 (left-panel) and zone 5 (right-panel), the main sites for synthesis of O-rich and C-rich clusters. The figure shows, in zone 2, the SiO molecules are formed early through radiative association ($Si + O \rightarrow SiO$) reactions which is favoured by large abundances of atomic Si present in the zone and high reaction rates. However the formation of $(Mg_2SiO_4)_2$ and other intermediate clusters are delayed up to $\sim$ day 550 due to the lack of stable oxidising agents such as O_2 or SO in the ejecta zone. On the other hand, AlO formation is delayed owing to the destructions by ions and atoms ($AlO + Ne^+ \rightarrow Al^+ + O + Ne$, $AlO + O \rightarrow Al + O_2$) in the ambiant gas. The formation of AlO molecules in zone 2 is initiated around day 600, and the tetramers of Al_2O_3 appears around day 700. The findings suggest rapid depletion of AlO follows the formation of $(Al_2O_3)_4$ clusters as shown in the figure. The profiles of [SiO, $(Mg_2SiO_4)_2$] and [AlO, $(Al_2O_3)_4$] together clearly indicates that in both the cases, these diatomic molecules act as tracers to the O-rich stable molecular clusters. The scenario is different in zone 5 though. In the right-panel of Figure 5.6 the balance between CO molecules and C-clusters are illustrated with the budget of C and O atoms. Firstly, formation of CO is concurrent with the formation of stable fullerenes of C_{28} at day 1100, which proves their formation processes are non-correlated. Also the figure shows that the formation of CO is initiated around day 1000, and saturates by day 11000, when all the O gets locked up in CO. Immediately after that, the residual C in zone 5 spontaneously forms

clusters through carbon nucleation scheme (discussed in Section 3.3). The masses of the gas phase clusters of C_{28} is therefore only a function of the C/O ratio.

5.2.2 Post-condensation residue

The previous section has illustrated that molecular clusters do form efficiently in the ejecta. However, most of them are short-lived in the gas phase. It is primarily due to two reasons a) all the nucleation paths drive the molecular clusters towards stable cluster units, therefore the final mass of intermediate clusters are small b) the stable monomers act as precursors to dust, and efficiently condenses into larger particles in solid phase. Here we present the summary of the residual molecular clusters that remain as gas phase molecules after condensation.

Intermediate molecular clusters: Besides the stable dust precursors discussed in the previous section, there are several other intermediate small clusters in the ejecta which remains as gas phase molecules. The fate of such molecules in the ejecta remains uncertain, and the demands further analysis.

The Si_mO_n molecules: These silicon-oxygen clusters grow in the O-core, essentially in zone 1B and 2. Figure 3.2 suggests the synthesis routes for molecules where n=m or m+1. Due to the scarcity of Mg in zone 1B, the silicate formation channels freezes after a certain time. The residual SiO molecules follow the nucleation scheme towards forming such intermediate molecules. Section 3.3 explains the subsequent stages for the synthesis of silica (SiO_2) from Si_mO_{m+1} like molecules (Reber et al., 2008). Therefore we consider such species, as the precursor of silica dust. However the entire mass of these molecules shall not eventually convert to silica. The formation paths are controlled by the amount of available SiO is the ejecta. The fast decrease in SiO mass from day 300 to 500 indicates, the final mass of silica shall be limited to the orders of 10^{-4} to 10^{-3} $M_\odot$. We present study does not deal with the silica nucleation, and hence the mass of such molecules in the ejecta as given in Table 5.3 is certainly an incomplete estimation.

The C_{2n} molecules: In zone 5 of the helium core, the carbon rings tend to grow in size mainly through C_2 addition. The rings grow towards the formation of first stable fullerene, the C_{28}. However, due to the shortage of available growing agent C_2, all the carbon clusters cannot end up in forming fullerenes. A residual amount of 5.5×10^{-3} $M_\odot$ remains in gas which constitutes of C_{20}, C_{22}, C_{24}, C_{26} etc.

The Fe_n molecules: The nucleation of pure iron atoms take place in zone 1A.

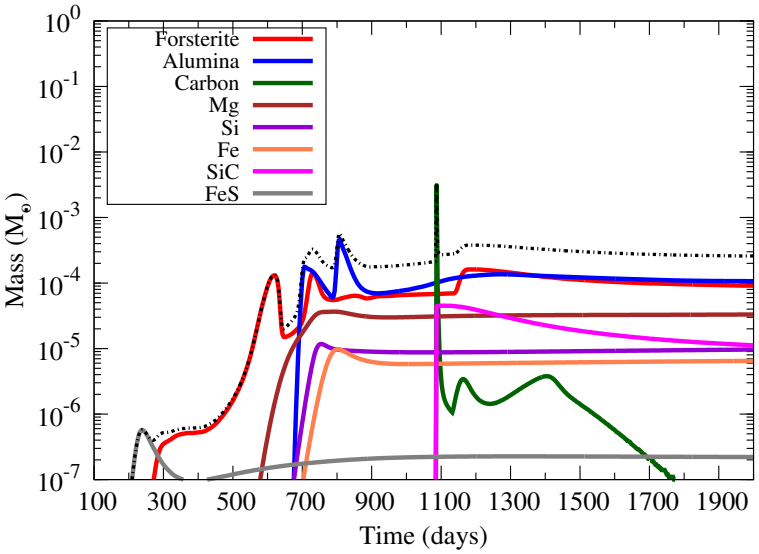

FIGURE 5.7: The masses of uncondensed dust clusters which have remained as gas molecules, is presented in this figure as a function of time. The dotted line in black signifies the total mass of uncondensed dust precursors in the ejecta as evolved over time. See Section 5.2.2 for the explanation of this rather complicated figure.

The nucleation process gains impetus at late times. Therefore, due to low densities and low abundances of Fe, the nucleation channels are not efficient enough to trigger the rapid formation of stable Fe_4. A fraction of Fe_2 and Fe_3 remains in the ejecta and their combined mass is roughly 8×10^{-3} $M_\odot$.

The uncondensed dust precursors: The stable dust precursors are formed through nucleation and subsequently take part in the condensation scheme. However the entire mass of these clusters could cannot grow large enough to be classified as dust. A small fractions of these molecules remaining in gas phase even after 2000 days from explosion. The masses of these species are listed in Table 5.3. Figure 5.7 illustrates the residual masses of each cluster type as function of post-explosion time. This important figure acts as the linkage between the gas phase chemistry and the solid dust components. Each profile can be explained by three phenomena: the increase of mass through nucleation, a sudden decline due to efficient condensation, and then a nearly constant phase at later times, which indicates, the large dust grains no longer coagulates with the residual small molecules. Hence they shall continue to remain in the gas phase. The amplitude of the spikes in each profile symbolises the efficiency of the condensation, and the width of the same stands for the time-scale for the condensation process to take place. The total mass of uncondensed dust precursors at the end of 2000 days is

given by the $\sim 2.5 \times 10^{-3}$ $M_{\odot}$.

5.3 The dust components

The dust precursors synthesised in the gas phase of the ejecta simultaneously condense to form dust grains following the formalism explain in Section 3.4. The dust components comprises of silicates, alumina, carbon, iron sulphide, silicon carbide and pure metallic clusters of magnesium, iron and silicon. The analysis traces the evolution mechanism of all these dust components individually. The formation of dust grains in the ejecta is found to be highly sensitive to the gas densities and the concentration of the specific clusters in consideration. Hence the dust formation scenario varies to a great extent from one zone to the other even for a single dust type. We estimate the mass of each the dust component and the size distributions of the grains over all times through our condensation subroutine CADSO. This section is dedicated to the review of the specific cases related to each individual dust species in the ejecta. Before going in to the detail analysis of each component, we shall focus on the overall picture of dust formation scenario for the 15 $M_{\odot}$ progenitor case.

There is no specific threshold in size to differentiate between the large molecular clusters and the dust particles. From the observational point of view, the dust formation in the ejecta is characterised by an excess in mid-IR spectral energy distribution and blue shift of optical emission lines. From the modelling perspective we choose a fiducial size of 10 Å as the minimum size of grains in the ejecta which can be categorised as dust. The grains smaller in size are considered as molecular clusters which remains in gas phase as mentioned in the previous Section. Figure 5.8 illustrates the evolution of dust masses of all the dust components from day 100 to 2000 after explosion. The masses of dust components in the Figure are presented as the sum over all the ejecta zones. The contributions from individual zones are mentioned in Table 5.4.

Formation of dust dawns after 200 days post-explosion time with the formation of iron sulphide grains. Later on in the period of 300-400 days silicates (forsterite) starts to form mainly in zone 1B. The mass of dust surges up at ∼550 days due to synthesis of silicates in zone 2. The process of gradual increase of dust mass continue with the advent of alumina at day 800 and lately by amorphous carbon at

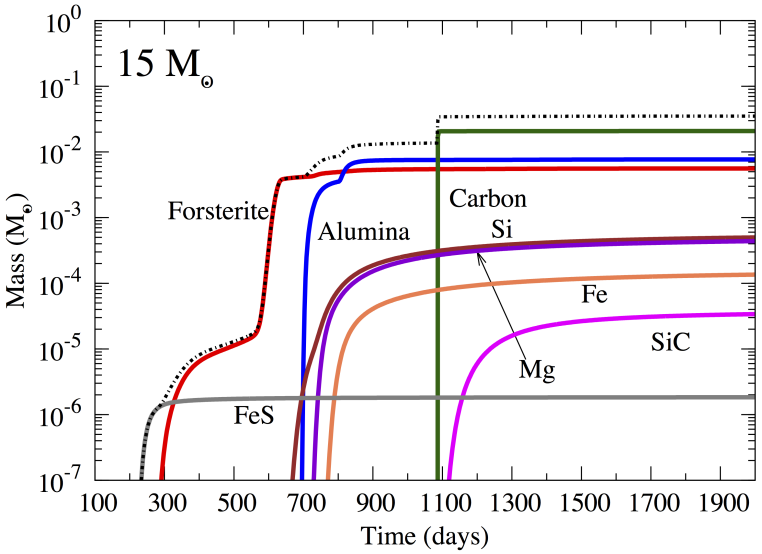

FIGURE 5.8: Dust mass for grains with radius larger than 10 Å summed over all ejecta zones as a function of post-explosion time and dust type. The dotted black line corresponds to the total dust mass formed in the homogeneous ejecta with progenitor mass 15 $M_\odot$ (Sarangi and Cherchneff, 2014). The dotted line in black signifies the total mass of dust in the ejecta as evolved over time.

1100 days. This way the dust mass increases from 10^{-5} $M_\odot$ at 400 days to 0.035 $M_\odot$ at the end of four years (Table 5.5). Amorphous carbon, alumina and forsterite are the most abundant dust types in the ejecta. The range of the dust masses perfectly agrees with the estimated masses of dust derived from observational data. At times between 200-600 days, the mid-IR observations predict the presence of dust in the ejecta with masses typically in the order of 10^{-5} to 10^{-3} $M_\odot$ (Kotak et al., 2009, 2005; Elmhamdi et al., 2003b; Moseley et al., 1989; Wooden et al., 1993; Inserra et al., 2011; Sugerman et al., 2006; Gallagher et al., 2012). These values are consistent with our findings as presented by the total dust mass in Figure 5.4. Submm observations however reports the presence of much larger masses of dust in the remnants. In Cas A, ∼0.08 $M_\odot$ of dust as inferred from Herschel data (Barlow et al., 2010). In case of SN1987A, Matsuura et al., 2011 has derived masses of dust in the range of 0.4-0.7 $M_\odot$ to be present in the ejecta after 28 years from explosion. Recent ALMA observation of the same concluded the final dust mass to be about 0.2 $M_\odot$. Also for the filaments of Crab nebula an estimated mass of 0.1-0.2 $M_\odot$ is required to fit the Herschel data as explained by Gomez et al., 2012b. The final mass of dust estimated in our study ends up in 0.035 $M_\odot$, and we suppose the dust mass will remain consistent till the advent of reverse shock in the remnant. The trends we derive do match well with the results of submm observations. However the final masses reported from these late time observational datas are 2-10 times

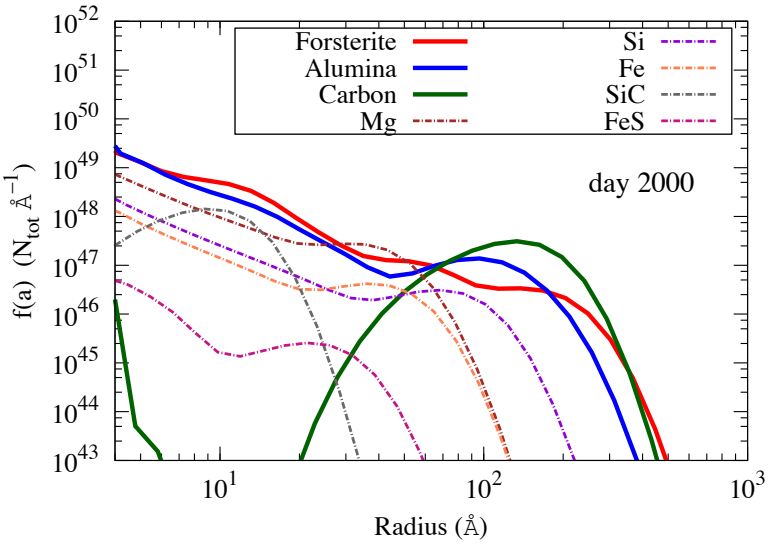

FIGURE 5.9: The final size distribution $f(a)$ of dust grains at 2000 days post-explosion is presented for all the dust components (Sarangi and Cherchneff, 2014). The distribution function is expressed in terms of total number of particles per unit radius (N_{tot}(a). Å^{-1}).

larger than our assessment. Importantly though, all the masses reported from observations are derived by fitting the spectral energy distributions at IR and submm wavelengths where some composition of dust has been assumed. The dust masses from observations hence can be sensitive to the choice of dust components, their compositions and sizes. Finally there are several options for the choice of optical constants related to each dust type, and the results vary significantly from one to the other. In most of the cases the size distribution were assumed to either follow a power law profile as like the standard Mathis-Rumpl-Nordsieck (MRN) distribution (Mathis et al., 1977) or the grains were chosen to be of constant size. All these factors add some uncertainty to the estimation of dust masses from observational data.

The trends obtained from nucleation of small clusters can be correlated to the evolution pattern of dust masses in the ejecta. This signifies that the condensation scheme is extremely efficient both in time and mass. The masses of the small clusters reported by Sarangi and Cherchneff, 2013 hence is indeed the upper limit of the dust masses that can form in the ejecta. About 99% of all the dust precursors synthesised in the ejecta goes on to form dust grains larger than 10 Å. If we consider also the uncondensed intermediate carbon rings in the gas phase, the condensation efficiency comes down to 87%. Nevertheless, only 1.5% of the entire ejecta mass remains in the form of dust after 4 years from explosion. Among the zones, the

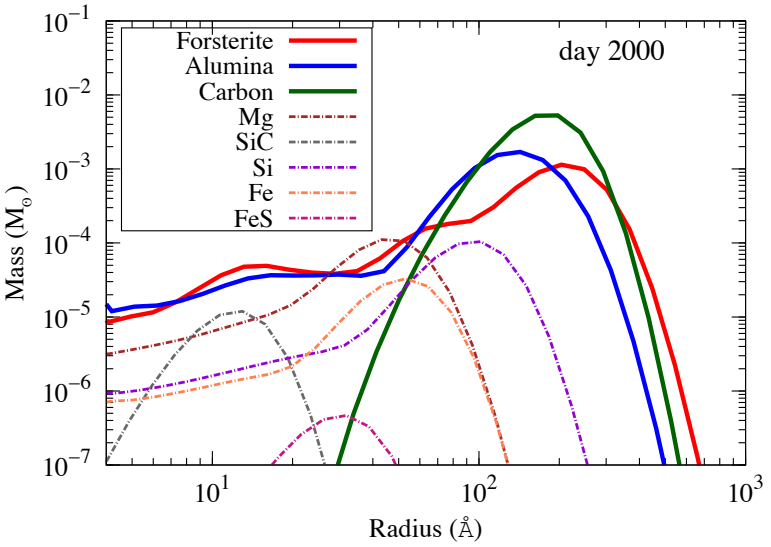

FIGURE 5.10: The mass distribution ($M_\odot$) as a function of grain sizes of individual dust components at 2000 days post-explosion(Sarangi and Cherchneff, 2014).

central zone of the O-core, zone 2 and the outer layer of the He-core, zone 5 are the most significant dust producers (Table 5.4).

5.3.1 Size distributions

The dust grains grow in size through coagulation and coalescence. The grains thus gets distributed into particles of different sizes. The size distribution function defines the number of grains per unit of particle radius under spherical assumption. We have derived the size distribution function $f(a)$ in Section 3.4 with regard to the condensation model. The size distribution function evolves with time, with the alteration of grain composition and masses. Figure 5.9 illustrates the final size distribution functions for each dust components in the ejecta at day 2000 from the day of explosion. Again total number of particles at a particular size range is calculated through sum over all the ejecta zones. The main three dust components carbon, alumina and forsterite are presented in solid colours. These three dust components being abundant, also grows to form larger grains in the order of 200-500 Å. The size distribution function of one dust species differ in behaviour from the other, and hence cannot be defined by a single mathematical expression. The distribution functions have a peak or sometimes found to have multiple peaks (a_{peak}). To be precise, a_{peak} does not stand for the largest sizes of grains of each type, rather it symbolises the size where the maximum grains

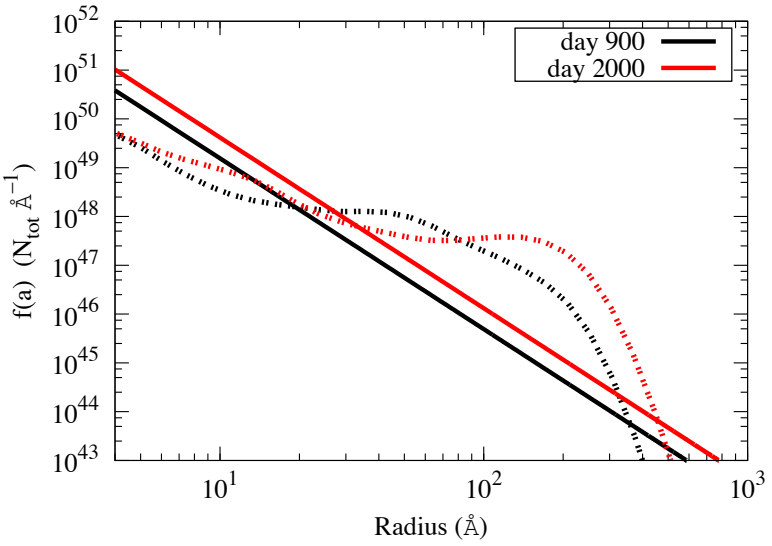

FIGURE 5.11: The total size distribution function combining all the dust species is compared with the standard MRN distribution defined by a power profile with $\alpha = -3.5$. The solid lines correspond to the MRN distributions and the dotted lines corresponds to the our model. The comparison at two epochs, 900 and 2000 days indicates notable difference between the two distribution patterns (Sarangi and Cherchneff, 2014; Mathis et al., 1977).

lie, hence can also be loosely called as the average size of dust grains for each component. The cases of each dust type has been addressed individually in the following Sections to explain the differences in behaviours. Figure 5.10 presents the mass distribution of the grains as a function the grain sizes. We see, the dust masses resides mainly in the larger grains, even though the population of large grains may be less than that of relatively smaller grains in the ejecta. The evolution of grains sizes with time is explained by the four panel Figure 5.13 where the size distribution function for all the components are presented at 500, 700, 900 and 1200 days respectively. It is evident from the pattern in these figures that the condensation is an efficient process in the ejecta, and once the large grains are formed they are unlikely to segregate to smaller size fragments. The mass distributions of grains at early times marking the epochs of dust formation are explained in Figure 5.13. The left panel day 600 pattern compared to the right panel day 900 pattern shows rapid change in dust distribution in the small span of 300 days owing synthesis of dust precursors in the gas phase and simultaneous condensation to larger size grains.

In Figure 5.11, the total size distribution calculated by summing over all dust size distributions, is shown for days 900 and 2000. It is plotted along with a dust size distribution function for a similar initial total dust number density following the

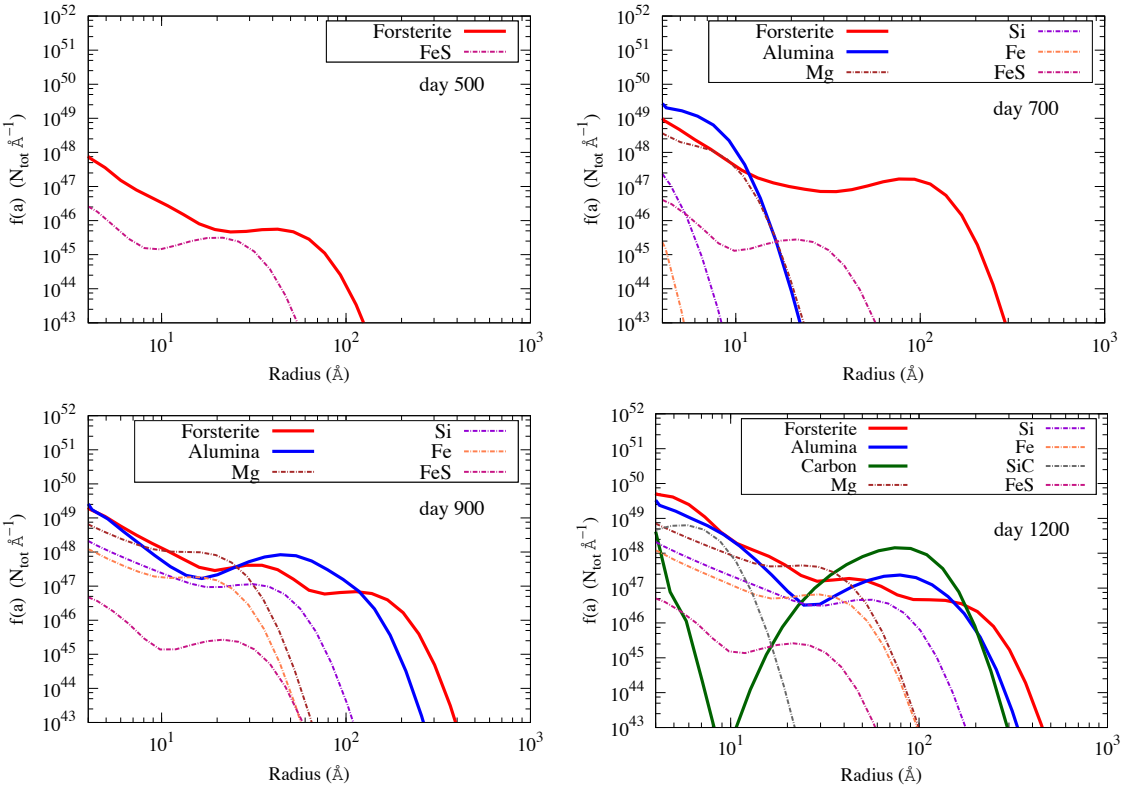

FIGURE 5.12: The size distribution of dust grains $f(a)$ at 500 days (top-left), 700 days (top-right), 900 days (bottom-left) and 1200 days (bottom-right) post-explosion is presented (Sarangi and Cherchneff, 2014). The distribution function is expressed in terms of total number of particles per unit radius (N_{tot}(a). Å^{-1}).

Mathis-Rumpl-Nordsieck power law distribution (thereafter MRN) with exponent $\alpha = -3.5$ characteristic of interstellar dust (Mathis et al., 1977). The size distributions of the dust produced by supernovae do not follow a MRN size variation, both for single dust type and for the total dust distribution. Our size distributions have less small grains with radius $a < 30$ Å, and are skewed towards large grains in the size range $40 - 1000$ Å, compared with the MRN distribution. This result clearly indicates that the use of a MRN dust distribution for either modelling the flux emitted by supernovae grains or dust sputtering in the supernovae remnant phase may lead to erroneous results on the derived dust mass formed in supernovae and the dust mass that survives shock processing in the remnants. Ideally if there at all exists a distribution function for supernovae dust grains, that should be defined by the dust size patterns of a single dust component, and not over a sum of all the species. The analysis clearly indicates none of the dust components follow a power law pattern of dust sizes at any epoch. We have also compared our results with power law profiles by changing exponent values to -3, -2.5 and -2. A similar argument persists for all the cases as well.

TABLE 5.4: Masses ($M_\odot$) of various dust components in the ejecta at 2000 days for different zones (Sarangi and Cherchneff, 2014)

Zones	Z1A	Z1B	Z2	Z3	Z4A	Z4B	Z5	Z6	Total
					Dust				
Mass	9.6(-2)	9.5(-2)	0.292	0.347	0.195	0.225	0.75	0.347	2.35
Forsterite	...	5.2(-4)	4.4(-3)	5.7(-4)	2.4(-5)	2.5(-5)	8.3(-5)	...	5.6(-3)
Alumina	...	9.3(-5)	4.0(-3)	3.6(-3)	8.9(-6)	2.8(-5)	...	...	7.7(-3)
Carbon	...	...	...	...	...	...	2.1(-2)	...	2.1(-2)
Pure-Mg	...	...	2.3(-4)	2.7(-4)	...	...	...	...	5.0(-4)
Pure-Si	4.4(-4)	...	...	...	...	...	...	...	4.4(-4)
Pure-Fe	1.4(-4)	...	...	...	...	...	...	...	1.4(-4)
Silicon Carbide	...	...	...	...	...	...	3.4(-5)	...	3.4(-5)
Iron Sulphide	1.8(-6)	...	...	...	...	...	...	...	1.8(-6)
Total	5.8(-4)	6.1(-4)	8.6(-3)	4.4(-3)	3.3(-5)	5.3(-5)	2.1(-2)	0	0.035
Efficiency(%)	0.6	0.6	2.9	1.26	2.0(-2)	2.0(-2)	2.8	0	1.5

5.3.2 Forsterite

The forsterite dust is synthesised in the ejecta through condensation of dust phase precursor $(Mg_2SiO_4)_2$. The prime loci for formation of these silicates in the ejecta are zones 1B, 2 and 3. In zone 1B, the final mass depends on the amount of magnesium present in the gas phase. In case of zone 2 and 3, the upper limit is decided by the amount of silicon present. Figure 5.13 (left panel) illustrates the evolution of forsterite mass with time in different zones. Small grains of these silicates appear in the ejecta as early as 300 days mainly due to early synthesis in zone 1B. Zone later on after 600 days, the forsterite mass is boosted by contribution from zone 2. At ∼600 days, the average size of grains remains to a modest size of roughly 50 Å, because of the small masses in zone 1B compared to zone 2 (Figure 5.13, right panel). The forsterite dimers efficiently starts forming larger grains at ∼ day 700 from zone 2 where the gas temperature is ∼ 1000 K, and the peak of the distribution curve shifts from 50 Å to 100 Å. The decrease in the number of small grains around 20 Å is attributed to the formation of larger grains. After 1000 days, the gas density is quite low and no new nucleation seeds (small clusters) form. The concentration of large grains ($a > 200$ Å) is also low, and their growth is stopped. However small grains still participate in the coagulation process by replenishing the grain population with size 10 Å $< a <$ 100 Å, albeit with a lower efficiency. When coagulation is completed at day 2000, the silicate grain size distribution has a peak of 170 Å (Table 5.5), and the largest grains grow over ∼ 500 Å. The final mass of forsterite grains larger than 10 Å is 5.6×10^{-3} $M_\odot$ (Table 5.4). Most of the mass as well as the large grains come from zone 2.

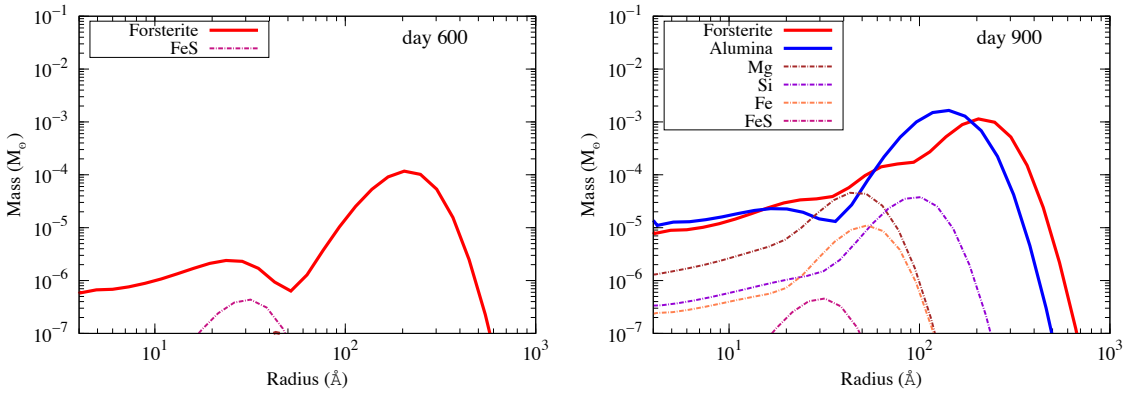

FIGURE 5.13: The mass distribution ($M_\odot$) as a function of grain sizes of individual dust components at 600 days (left panel) and 900 days (right panel) post-explosion(Sarangi and Cherchneff, 2014).

5.3.3 Alumina

Alumina is the second dust component to form in the O-rich core $\sim$ day 700 after explosion. The main layers of formation are zones 2 and 3. The alumina grains undergo very fast and efficient condensation to form large grains peaking at $\sim$ 60 Å at day 900, when the gas temperature is in the range $600 - 800$ K. As explained of Section 5.4 and also in Sarangi and Cherchneff, 2013, most atomic aluminium present in the O-rich core gets locked up in molecules and dust clusters, hence no new Al_2O_3 tetramers are formed after day 900. Due to the scarcity of the seed from gas phase, the condensation route from small to large grains gets limited. The size distribution pattern for alumina therefore rapidly evolves between day 700 to day 900. This can be verified by the Alumina profile in Figure 5.13 for these two epochs. A growth trend similar to that of forsterite applies to alumina. The alumina dust growth results in the production of grains peaking around 100 Å (Table 5.5), with a population of large grains with size over $\sim$ 400 Å at day 2000. The mass of alumina at this epoch remains at 7.7×10^{-3} $M_\odot$ (Table 5.4) most of which had already condensed by day 1000 post-explosion.

5.3.4 Amorphous Carbon

The outer layer of the helium core, zone 5, is responsible for the formation of amorphous carbon dust. The synthesis of carbon dust is reliant on the C/O ratio of the particular zone. The formation pathways leading to CO being very efficient, all the carbon in the each zone primarily gets locked up in CO molecules.

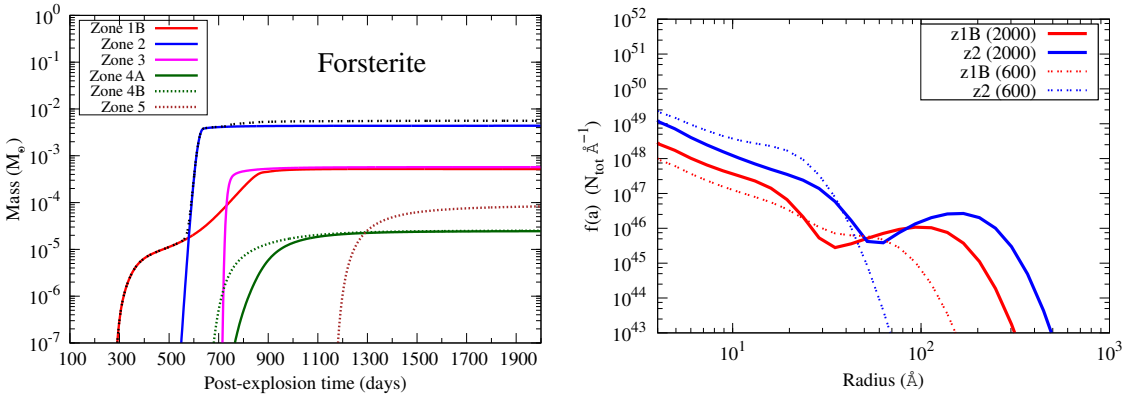

FIGURE 5.14: The mass evolution of forsterite dust ($M_\odot$) is illustrated in the left panel for the individual zones in the ejecta. The back dotted line is the total over all the zones and hence is same as the forsterite profile in Figure 5.8 (Sarangi and Cherchneff, 2013) The size distribution function $f(a)$ of forsterite grains at two epochs day 600 and day 2000 post-explosion is presented in the right panel for two ejecta zones 1B and 2 separately. These two zones are the prime contributors to the total mass as verified from the figure in the left panel.

Hence synthesis of carbon dust is only feasible in the environment characterised by C/O>1. In case of zone 5, the remaining carbon, after forming CO molecules, undergoes nucleation through C_2 addition towards forming cages of C_{28}. This C_{28} thereafter acts as the seed to the carbon dust formation mechanism. Furthermore, The formation of carbon dust in the outermost ejecta zone is strongly affected by the presence of He^+. The synthesis of stable C_{28} cages occurs as late as 1050 days after outburst once the abundance of He^+ ions has decreased to negligible values (Sarangi and Cherchneff, 2013). Then the carbon chains, rings and cages form almost instantaneously with large abundances along with the efficient condensation of the cage C_{28} in carbon grains. This results in a sudden high concentration of large carbon grains with peak radius of $\sim$ 100 Å at day 1200. This creates is a special case different from other dust components, where all the modest size particles (5-20 Å) condense to form relatively large dust grains. Because of the low gas temperature ($\sim$ 300 K) and low gas densities at that time, the condensation process becomes less efficient. However, owing to a large abundance of carbon cages in the gas phase, the condensation of grains proceeds even at these low gas temperatures. The carbon grain size distribution does not vary after day 1500, peaks at a grain radius of $\sim$ 150 Å (Table 5.4), and coexists with a small population of large grains with radius 500 Å or larger. The final mass of amorphous carbon dust in the ejecta is 0.021 $M_\odot$. In the standard case of 15 $M_\odot$ progenitor, amorphous carbon is the most abundant dust species. Nevertheless due to late

TABLE 5.5: Dust masses at different post-explosion epochs for the 15 $M_{\odot}$ progenitor, standard case. The peak size a_{peak} of each size distribution is also indicated (Sarangi and Cherchneff, 2014)

Dust type	Post-explosion time (days)							a_{peak} (Å)
	500	700	900	1100	1200	1500	2000	
Forsterite	1.1(-5)	4.2(-3)	5.3(-3)	5.5(-3)	5.5(-3)	5.6(-3)	5.6(-3)	64; 168
Alumina	-	6.1(-6)	7.4(-3)	7.6(-3)	7.6(-3)	7.7(-3)	7.7(-3)	96
Carbon	-	-	-	2.0(-2)	2.0(-2)	2.0(-2)	2.1(-2)	134
Pure Magnesium	-	2.5(-6)	1.9(-4)	3.2(-4)	3.6(-4)	4.4(-4)	5.0(-4)	29
Pure Silicon	-	-	1.5(-4)	2.7(-4)	3.1(-4)	3.8(-4)	4.4(-4)	69
Pure Iron	-	-	4.1(-5)	9.1(-5)	9.4(-5)	1.2(-4)	1.4(-4)	36
Silicon Carbide	-	-	-	-	6.1(-6)	2.6(-5)	3.4(-5)	9
Iron Sulphide	1.7(-6)	1.8(-6)	1.8(-6)	1.8(-6)	1.8(-6)	1.8(-6)	1.8(-6)	21
Total	1.3(-5)	4.3(-3)	0.013	0.034	0.034	0.035	0.035	

condensation, the grains of carbon dust does not outgrow the size of the largest forsterite grains.

5.3.5 Other dust components

Apart from the previous three prevalent dust components, iron sulphide, pure metal, and silicon carbide grains also condense in the ejecta. The size distribution of these species are marked in dotted lines in Figures 5.10 & 5.13. Either due to very small abundances or late synthesis of these dust species, the average size of grains remain much smaller than reach 100 Å. The final masses for these components are presented in Table 5.5 along with the a_{peak} values of the respective size distributions profiles.

- **Iron Sulphide:** Iron sulphide, FeS, is the first dust component to appear in the ejecta. FeS forms at early time in the innermost zone, zone 1A, and reaches its final mass and size distribution at day 500. The abundance of FeS is however low, and the peak of the distribution curve lies at 25 Å. The formation as early as 300 days implies condensation at high densities, which in a way compensates for the low abundances.

- **Pure Si and Fe:** Pure silicon and iron grains start forming at day 700 in zone 1A, where most of the silicon is locked in the molecule SiS or in atomic form (Sarangi and Cherchneff, 2013). Iron is mainly in atomic form in this zone but some pure iron clusters form after day 700. The size distribution of Si grains is the most extended of all pure metal dust grains, and peaks at

$\sim$ 70 Å with the production of grains sizes over 200 Å though the overall grain population remains small because of the modest amounts of pure Si clusters formed in the gas phase. A similar scenario applies to pure iron grains, for which the distribution peaks at 40 Å and the largest grains have size of $\sim$120 Å at day 2000.

- **Pure Mg:** The pure magnesium grains are synthesised from the Mg_4 clusters formed in the O-rich zones at day 600. In zone 1B all the magnesium gets locked in magnesium silicates. However in zone 2 and 3, there are some Mg still left in the ejecta succeeding the formation of silicates. The fraction of this residual magnesium form pure-Mg dust. The size distribution reaches its final shape at day 1200, with a peak at $\sim$ 30 Å, and a small population of grains with sizes over 120 Å.

- **Silicon Carbide:** Silicon carbide forms in the He/C-rich zone 5 after day 1100, and captures the available silicon and the carbon left over from the condensation of carbon dust. The low abundance of SiC clusters combined to the low gas temperature and densities at the epoch of its formation result in small masses of SiC grains characterised by small sizes in the range $5-11$ Å. The survival probability of these small grains during the passage of reverse shock in the remnants remains doubtful.

The grain size distributions normalized by the total number of grains at day 2000 post-explosion are listed in Appendix B Table B.1 & Table B.2. The overall dust formation scenario in the ejecta, as described above, results in a gradual build-up of various dust grain populations in the different ejecta zones. The study clearly indicates, the dust masses and grain sizes are strongly time-dependant. Therefore, the dust observed at IR wavelengths at post-explosion day 500 differs in type, mass, and size distribution, from the dust observed at submm wavelength. This late dust is the outcome of a complete series of nucleation and coagulation event over a time span of $\sim$ 5 years after outburst.

5.4 The elements

The previous sections in this chapter has thrown lights on the importance of molecules, small clusters and dust grains in the ejecta. Nevertheless only 30-40

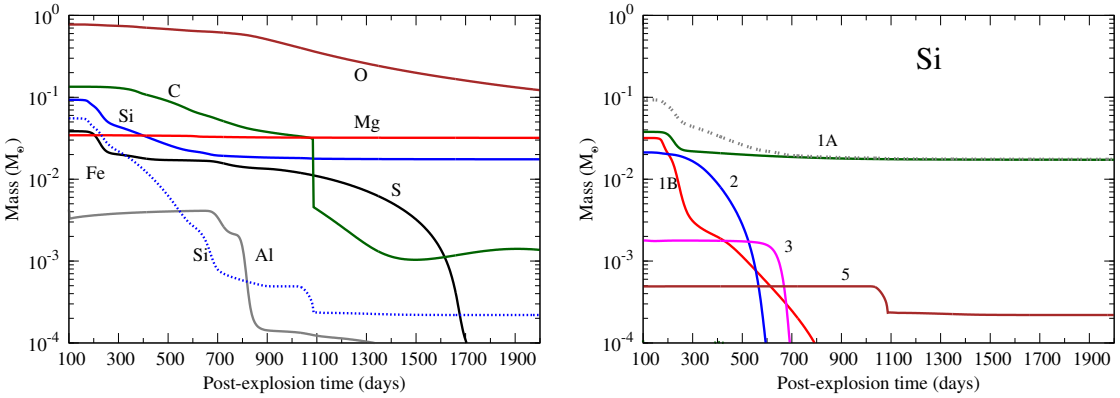

FIGURE 5.15: The evolution elements in the ejecta as sum over all the zones is illustrated in the left panel. The case solid line for Si corresponds to the sum of all the zones, while the dotted blue line represents the mass evolution of Si in all other zones excluding zone 1A. The specific case of Si is further explain in the figure in the right panel where the evolution pattern of Si has been presented as functions of different zones (Sarangi and Cherchneff, 2013).

% of the ejecta comprises of molecules and dust. The rest of the ejecta materials continue in atomic form, either neutral or in the form of cations. The masses of the elements that actively take part in the chemistry, have been presented in Figure 5.15 (left panel) as function post-explosion time. The case of the nobel gases is addressed in Section 5.4.2. The masses of O and Al remains consistent till $\sim$ 800 days, and then O undergoes gradual decline. Mass of Al falls rapidly, marking the onset of alumina synthesis. The profile of atomic sulphur has two decline phases, one at 200 days indicating the formation of SiS and later at 1000 days due to synthesis of SO. The smooth decline of atomic carbon between 300 to 1000 days attributes to the formation of CO molecules in different zones. The sharp fall thereafter at day 1100 marks the formation of carbon dust in zone 5. Magnesium gets slowly depleted in to silicates and pure Mg dust. In case of Silicon, the behaviour in zone 1A differs from all the zones. In Figure 5.15 (right panel) the evolution of Si mass is shown for all the zones separately. The oxygen free zone 1A leads to formation of SiS, limited by the mass of available sulphur. The rest of Si remains in atomic form thereafter. On the other hand, all other zones advocate the formation of silicates and silica clusters depleting the entire mass of atomic Si.

Early time observations of SN1987A by Lucy et al., 1989 reports the blue shift of atomic emission lines around 530 days indicating the synthesis of dust in the ejecta. The enhancement in the rate of decline for [O I] 6300 Å line also supports the presence of dust mixed in the O-core of the ejecta. A similar trend is observed

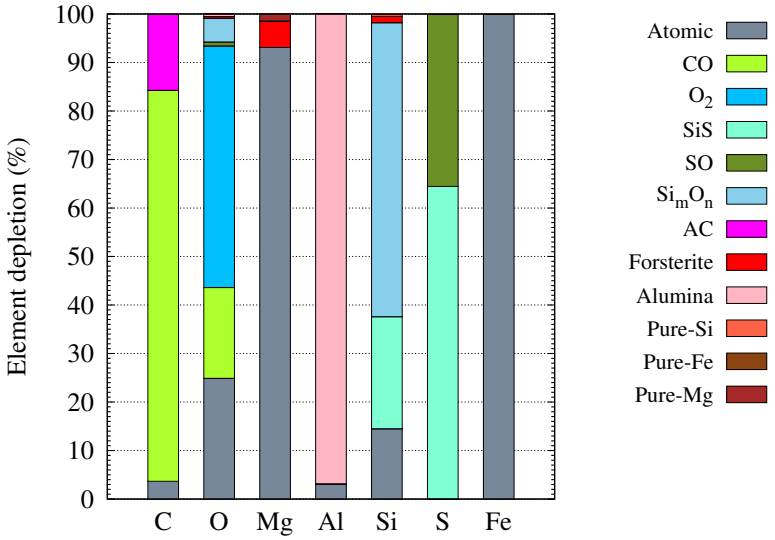

FIGURE 5.16: The depletion percentages of each element into molecules, clusters and dust grains in the ejecta after 2000 days post-explosion shown has been shown in the histogram

in Mg I] 4571 Å lines in the period between day 500-800. The fall of [Si I] emission line of 1.644 μm between 500 and 600 days appears faster than the 1.6 μm and 2.1 μm continuum decay rates. This indicates either to the depletion of Si in silicate grains or to temperature effects induced by strong cooling in Si-zones. This interpretations are supported by outcomes of the present analysis. The fading of atomic O abundances can are verified by the trends shown in Figure 5.15. For magnesium the decay of masses ver time takes place rather at a slow pace almost non-deductive from the figure. However the appearance of magnesium-silicates in the ejecta between 500-800 days can be correlated to the observational phenomena. On the other hand, the fast decline of Si lines also can be linked to the combined effect of extinction and the formation of silica and silicates in the oxygen core. The fall of atomic Si mass in all the O-rich layers from and after 550 days also support in favour of the argument.

5.4.1 Depletion of elements

Figure 5.16 shows the final depletion percentages of elements like C, O, Mg, Al, Si, S and Fe into molecules, clusters or dust grains after 2000 days from explosion. About 80% of carbon ends up in CO molecules, and about 15% in amorphous carbon. The coexistence of CO and carbon dust clearly indicates they formation of amorphous carbon is not powered by CO molecules. Oxygen resides in several

oxygen bearing diatomic molecules, dioxygen, and also in oxygen rich dust grains. 20% of it however remains in atomic form and about 50% as O_2. In case of Magnesium, 93% remains atomic, and the rest mostly as forsterite. The upper limit of available Si dictates the final mass of these silicates, and hence the depletion percentages of magnesium. A lot of Si gets trapped as silica clusters, the fate of which we have already addressed in Section 5.2.2. Iron present in zone 1A essentially comes from the radioactive decay of ^{56}Ni. Small fractions of it proceed towards forming iron sulphides and pure iron dust grains. But more than 99% of iron is found to remains in atomic form in the ejecta of the supernova even after 2000 days.

5.4.2 The case of nobel gases

The γ-rays in the ejecta produced by radioactivity, undergo Compton scattering and degrade to X-rays. The energetic Compton electrons further lose energy by excitation and ionisation the gas. This way by day 100, most of the atoms in the ejecta gets ionised to their corresponding cation through collision with the fast Compton electrons. The ions of the nobel gases, namely helium, neon and argon also produced this way, plays important role in the chemistry (Lepp et al., 1990). The ground state energy level of their inert parents being very low, the cations of He, Ne and Ar actively participate in charge exchange processes with newly synthesised molecules, leading to their destruction. The impact is clearly evident in zone 5, where the detrimental effects of He^+ delays the appearance of stable molecules and clusters in the ejecta till $\sim$ day 1000 (Equation 5.13).

$$\begin{aligned} CO + He^+ &\rightarrow C^+ + O + He \\ C_n + He^+ &\rightarrow C_{n-1} + C^+ + He \end{aligned} \tag{5.13}$$

Also in the O-core, Ne^+ (in zones 2 & 3) and Ar^+ (in zone 1B) exercise similar dominance as explained by Equation 5.14 (Also true of CO, AlO, SiS, Si_2O_3, etc.). Nevertheless, the electron recombination process also goes on simultaneously, controlling the mass of these ions (Equation 5.15).

$$\begin{aligned} SiO + Ne^+/Ar^+ &\rightarrow Si^+ + O + Ne/Ar \\ O_2 + Ne^+/Ar^+ &\rightarrow O^+ + O + Ne/Ar \end{aligned} \tag{5.14}$$

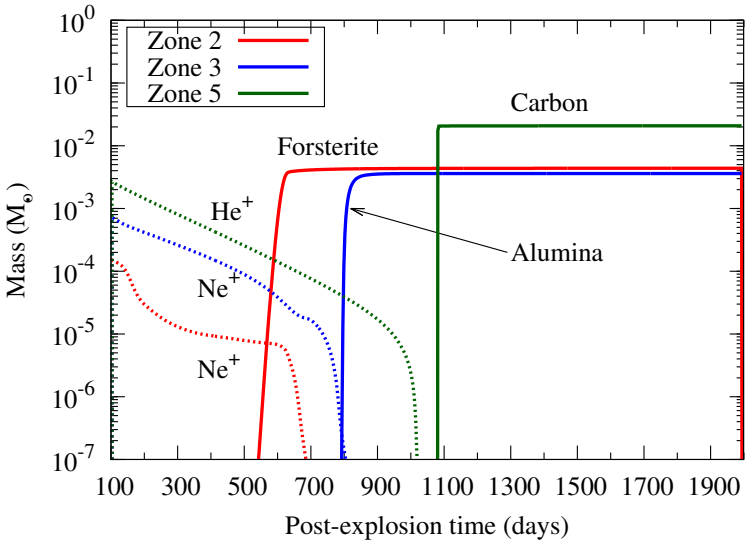

FIGURE 5.17: The impact of nobel the cations of He and Ne is shown on the epochs of dust synthesis in zones 2, 3 and 5. The ions and the dust mass from a particular zone are labelled in same colour, with solid and dotted lines respectively.

With the passage of time, effect of radioactivity decreases, as most of the ^{56}Co already gets converted to stable ^{56}Fe. The energy from the γ-rays and X-rays gets deposited in the ejecta and a small fraction escapes outside the core. Thereafter, the abundance of Compton electrons also falls rapidly, and all the cations eventually recombines back to their stable inert parents. The molecule and dust synthesis gains in efficiency when the cations of cations of He, Ne and Ar are no longer present in the ejecta.

$$He^{+}/Ne^{+}/Ar^{+} + e^{-} \rightarrow He/Ne/Ar \tag{5.15}$$

This way, the nobel gases indirectly controls the chemistry and the epochs of molecule and dust formation. The impact on the dust formation scenario is illustrated by Figure 5.17 for zones 2, 3 and 5. The sharp decline in mass of Ne^{+} in zones 2 and 3 marks the prelude of forsterite and alumina synthesis respectively. Similarly, the correlation between carbon and He^{+} is evident from the zone 5 profiles in the figure. Other molecules or clusters in these zones also follow similar trends.

6 The Impact of ^{56}Ni

The ^{56}Ni mass produced by supernovae can be derived from the variation of the optical light curves and H_α luminosities in the nebula phase (Elmhamdi et al., 2003a). From direct identification or by comparison with explosion models, a mass for the supergiant progenitors can be inferred. Table 6.1 lists some Type II-P supernovae, the estimated ^{56}Ni mass and the progenitor mass range. Most of the supernovae have progenitor masses between 12 and 20 $M_\odot$ and typical ^{56}Ni mass of 0.01-0.09 $M_\odot$, with large progenitors producing more ^{56}Ni mass. This phenomena reflect the trends derived by Hamuy, 2003, that more massive supernovae produce more energetic explosions, and supernovae with greater energies produce larger ^{56}Ni masses. We study the impact of the ^{56}Ni mass on the ejecta chemistry of our standard 15 $M_\odot$ progenitor by considering a low ^{56}Ni (0.01 $M_\odot$) mass produced in the explosion while all other factors remains unaltered (Sarangi and Cherchneff, 2013). Also the case of a low mass progenitor (12 $M_\odot$) has been addressed in Chapter 8 where again the impact of ^{56}Ni shall come in limelight.

The energy deposited by the radioactive ^{56}Ni is linearly proportional to the its mass as stated in Equation 2.8. Therefore, the Arrhenius rate coefficients for the destructions by energetic Compton electrons are directly connected to the mass of ^{56}Ni produced in the explosion. Physically, a smaller ^{56}Ni mass in the ejecta reduces the number of Compton electrons resulting from the degrading of a lower amount of γ-rays. Therefore less ions such as Ar^+, Ne^+, and He^+ are produced, enhancing the rate of recombination. The destruction of molecules from which clusters form (e.g., SiO, C_2, AlO) is not as severe for the low ^{56}Ni mass case as it is for the standard case, because of the lower Ne^+ and He^+ ejecta content. So the chances of survival for the molecules and clusters increases, thereby also

TABLE 6.1: ^{56}Ni masses ($M_\odot$) from observed supernovae are presented along with the lower and upper limits of pre-explosion progenitor masses ($M_\odot$) for each supernova (Sarangi and Cherchneff, 2013)

Name	^{56}Ni mass	Mass (min)	Mass (max)	Reference
SN1999em	0.02	12	14	Elmhamdi et al., 2003a
SN2003gd	0.016	8	12	Smartt et al., 2004; Hendry et al., 2005
SN2004dj	0.095	12	20	Wang et al., 2005; Vinkó et al., 2009
SN2004et	0.068	23	25	Kotak et al., 2009
SN2005ef	0.027	13	15	Kotak et al., 2006
SN2005cs	0.003	10	15	Pastorello et al., 2009
SN2007od	0.02	10	11	Andrews et al., 2010; Inserra et al., 2011
SN2009bw	0.022	11	15	Inserra et al., 2012
SN2009js	0.007	6	16	Gandhi et al., 2013
SN2011ht†	0.01	8	10	Mauerhan et al., 2013
		SN remnants		
SN1987A	0.075	18	20	Woosley, 1988
Cas A	–	18	20	Krause et al., 2008
The Crab	–	8	12	Davidson and Fesen, 1985; MacAlpine and Satterfield, 2008

†The supernovae is classified as type IIn-P, which can also have large progenitor $\geq 25 M_\odot$ with substantial ejecta fall-back

leading to early condensation of dust grains. In the following sections we discuss the results from the study of an ejecta model which is identical to the standard 15 $M_\odot$ progenitor case with a revised mass of ^{56}Ni = 0.01 $M_\odot$ produced in the explosion.

6.1 The molecules

The budget of all the important molecules (CO, SiO, O_2, SO, N_2, SiS, etc.) in the ejecta is presented in Table 6.2 as functions of the ejecta zones. Also the evolution patterns of CO and SiO mass in different zones are described in Figure 6.1. Due to the diminished impact of He^+, CO molecules form spontaneously in zone 4B as early as 150 days. Zones 4A and 4B are the prime contributors to CO mass as expected. Even though the synthesis is abrupt, the final mass of CO does not change when compared to the standard case, because it is controlled by the amount of C-atoms present in the all the ejecta zones characterised by C/O<1. The evolution pattern of SiO molecules reflects to the trend of early nucleation and efficient depletion. The decline of SiO mass in the 200-700 day period traces the observed behaviour of SiO in various supernovae given in the figure. Rapid depletion of SiO molecules in zones 1B, 2 and 3 is directly correlated to the silicate dust evolution, which is addressed in the next section of the text. The total mass of molecules in the ejecta at day 2000 post-explosion is 0.789 $M_\odot$which is about 14% higher than the standard case. O_2 and CO accounts for more than 90% of

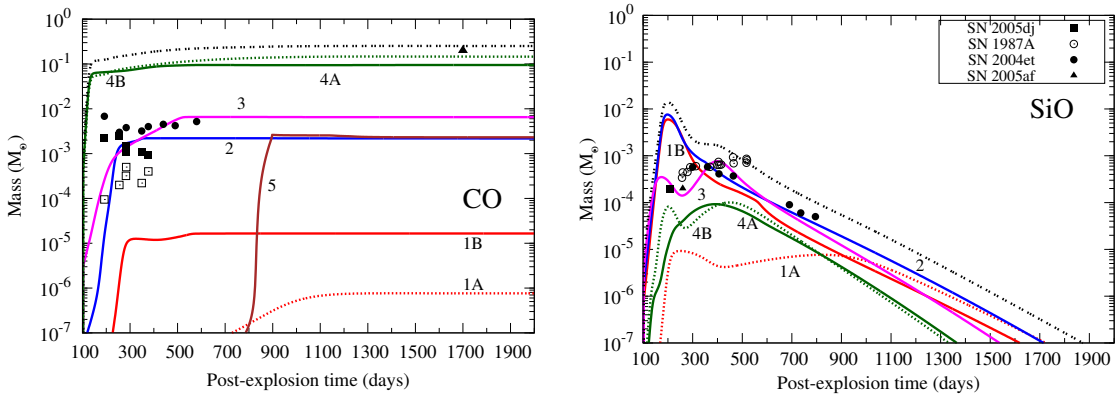

FIGURE 6.1: **Left Panel:** The mass evolution of CO in different zones of the ejecta is presented for the ^{56}Ni = 0.01 M$_\odot$ model. CO masses derived from the observations of SN1987A are shown as, LTE open squares, non-LTE: squares (Liu et al., 1992), thermal assumption: circles (Liu and Dalgarno, 1995), ALMA data: triangle (Kamenetzky et al., 2013). The ALMA data corresponds to a time 27 years after explosion. The label in the figure just indicates the mass 1700 days only indicates the derived mass. **Right Panel:** The figure shows the evolution of SiO mass as a function of different ejecta zones. For both the molecules, the dotted black line indicates the total mass from all the zones.

TABLE 6.2: Masses (M$_\odot$) of molecules at 2000 days post-explosion, in various zones of the ejecta (Sarangi and Cherchneff, 2013)

Zones	Z1A	Z1B	Z2	Z3	Z4A	Z4B	Z5	Z6	Total
					Molecules				
Mass	9.6(-2)	9.5(-2)	0.292	0.347	0.195	0.225	0.75	0.347	2.35
SiO	1.8(-8)	...	1.3(-8)	...	...	...	...	...	4.2(-8)
O_2	...	5.4(-3)	0.17	0.20	7.7(-2)	1.5(-3)	...	...	0.47
CO	7.6(-7)	1.7(-5)	2.2(-3)	6.5(-3)	9.5(-2)	0.15	2.3(-3)	...	0.25
SO	...	1.9(-2)	3.9(-3)	1.0(-4)	8.0(-5)	...	...	...	2.3(-2)
SiS	4.3(-2)	2.1(-7)	...	...	...	...	...	...	4.3(-2)
CO_2	...	...	3.1(-5)	6.7(-5)	...	...	...	...	9.8(-5)
CS	...	...	...	...	...	...	1.1(-4)	...	1.1(-4)
N_2	...	...	...	3.3(-7)	3.5(-7)	...	3.1(-3)	...	3.1(-3)
Total	4.3(-2)	2.4(-2)	0.176	0.207	0.172	0.152	5.5(-3)	0	0.789
Efficiency(%)	44.8	25.3	60.3	59.7	88.2	67.6	0.7	0	33.6

the molecular budget. Compared to the ^{56}Ni = 0.075 M$_\odot$ model, the efficiency of molecule formation gets boosted in all the zones other than zone 5. In case of zone 5, the final molecular mass is smaller than the standard case, as C and O-atoms preferably get locked up in dust. Zone 4 (A & B) remains the most active zone for molecule synthesis with efficiency ∼70-90%. The mass of all other molecules, namely SO, CS, CO_2, N_2, etc., are akin to the previous values listed Table 5.3. At the end of 2000 days from the time of explosion, one-third of the entire ejecta is in the form of stable molecules.

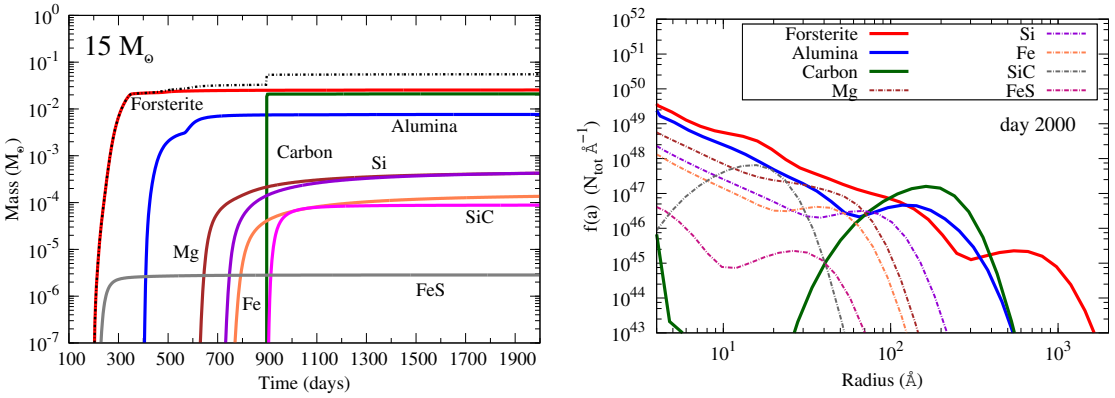

FIGURE 6.2: **Left Panel:** The evolution of the dust masses for different dust components in the ejecta are presented summing over the contribution over all the zones. The dotted balck line stands for the total dust mass. **Right Panel:** The grains size distribution functions $f(a)$ for all the dust components at day 2000 post-explosion are illustrated in the figure (Sarangi and Cherchneff, 2014).

6.2 The dust components

The study of dust components in the ejecta are based on the same formalism as described for the standard case. Figure 6.2 (left panel) illustrates the evolution of dust masses as a function of post-explosion time. The break-up of the final (day 2000) dust masses from each zones and for each dust component is presented in Table 6.3. The dust formation is pumped up by rapid condensation of silicates in zones 1B and 2 at around 250 days from explosion. The final mass of forsterite becomes constant at 0.025 $M_{\odot}$ most of it coming from zone 2. As for the standard case, alumina and amorphous carbon are the next two most important dust types. Formation of carbon dust after 900 days boosts the final dust mass to 0.055 $M_{\odot}$. The final masses of the metallic clusters are in $\sim 10^{-4}$ $M_{\odot}$ whereas silicon carbide and iron sulphide are in the range of 10^{-5} $M_{\odot}$. Zone 2 and Zone 5 remains the most efficient dust formation cites in the ejecta. The overall efficiency of dust formation in the ejecta in such case is 2.3%.

The grain size distribution functions for each dust types are derived from the condensation scheme. We present the final size distribution of dust grains at day 2000 in Figure 6.2 (right panel). Early nucleation of silicate precursors in gas triggers to early condensation for grains. Owing to the high dust densities at early times (day 250 onwards), the grains of forsterite grow quickly to reach a peak size $\sim$550 Å while the largest grains even reach the size 0.2 μm. The same scenario also remains valid for alumina and carbon and the epochs of synthesis

TABLE 6.3: Masses ($M_\odot$) of various dust components in the ejecta at 2000 days for different zones and the peak (a_{peak}) of the size distribution function in Å (Sarangi and Cherchneff, 2014).

Zones	Z1A	Z1B	Z2	Z3	Z4A	Z4B	Z5	Z6	Total	a_{peak} (Å)
					Dust					
Mass	9.6(-2)	9.5(-2)	0.292	0.347	0.195	0.225	0.75	0.347	2.35	
Forsterite	...	6.5(-4)	2.3(-2)	1.8(-3)	1.2(-4)	6.3(-5)	1.7(-4)	...	2.5(-2)	131; 543
Alumina	...	9.4(-5)	3.9(-3)	3.6(-3)	1.9(-6)	1.7(-5)	...	...	7.6(-3)	117
Carbon	...	...	...	...	...	...	2.1(-2)	...	2.1(-2)	162
Pure-Mg	...	...	7.0(-5)	3.5(-4)	...	...	...	...	4.2(-4)	53
Pure-Si	4.4(-4)	...	...	...	...	...	...	...	4.4(-4)	69
Pure-Fe	1.4(-4)	...	...	...	...	...	...	...	1.4(-4)	36
Silicon Carbide	...	...	...	...	...	...	8.8(-5)	...	8.8(-5)	16
Iron Sulphide	2.8(-6)	...	...	...	...	...	...	...	2.8(-6)	26
Total	5.8(-4)	7.4(-4)	2.7(-2)	5.8(-3)	1.2(-4)	8.0(-5)	2.1(-2)	0	0.055	
Efficiency(%)	0.6	0.8	9.2	1.67	6.0(-2)	4.0(-2)	2.8	0	2.34	

are approximately day 400 and day 900 respectively. The peak of the distribution functions (a_{peak}) lie in the 100-200 Å range. The final masses of forsterite and carbon are comparable, however due to high density condensation, average grains of forsterite are about 10 times larger. The mass as well as the grain sizes for silicon carbide increases more than 2 times in case of a low ^{56}Ni mass progenitor. The story for all other dust species remains almost unaltered when compared to the standard 15 $M_\odot$ model. The size distribution functions do not follow a power law profile.

6.3 Comparison with the standard case

The two models are solely distinguished by the different ^{56}Ni content, all other physical factors remaining unaltered. The impact of ^{56}Ni mass on the dust formation chemistry is illustrated in Figure 6.3. The left-panel compares the dust mass evolution of forsterite, alumina and amorphous carbon, for the two models. As evident from the figure, in the low ^{56}Ni mass case, formation of stable dust grains starts about 200-300 days earlier than the standard case. However, the final mass of alumina and carbon does not change. This is mainly because, the final mass is limited by the presence of available Al-atoms in the O-core or C-atoms in outer zone 5. On the contrary, in case of silicates early condensation also results to a final mass 5 times higher than the standard case. The explanation lies in the complicated silicate nucleation network in zone 2, where Si, O and Mg atoms all are abundant. The masses of pure-metal dusts of Si and Fe in zone 1A does not change due to the variation in ^{56}Ni mass, as the impact of Ar^+ is not very

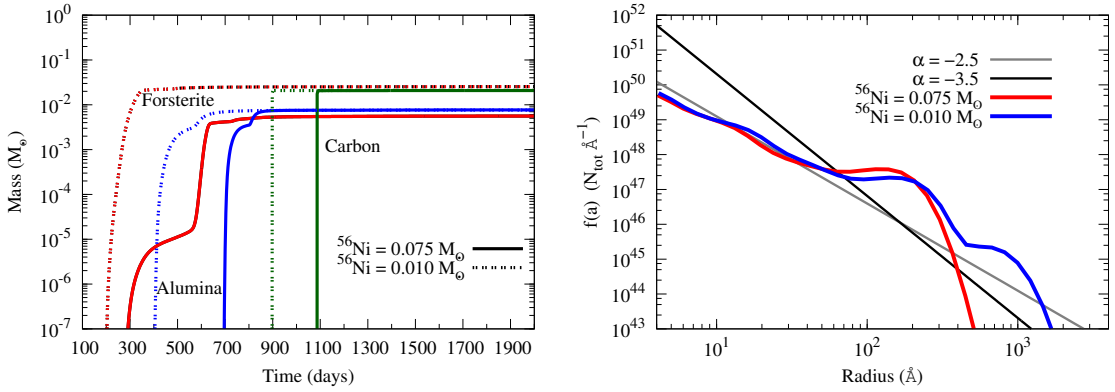

FIGURE 6.3: **Left Panel:** The time evolution of dust mass for forsterite, alumina and carbon for standard (solid lines) and the low ^{56}Ni mass model (dotted lines) are compared (Sarangi and Cherchneff, 2013) **Right Panel:** The grains size distribution functions $f(a)$ as sum over all dust components at day 2000 are illustrated for the two progenitor models with different ^{56}Ni content. They are compared to power law distributions with exponent -2.5 (grey line) and -3.5 (black line) respectively (Sarangi and Cherchneff, 2014).

significant in this zone. Overall in the ^{56}Ni = 0.01 M$_\odot$ model, the final dust mass is $\sim$ 57% (0.055/0.035 M$_\odot$) larger than the standard case. Also the contribution of each dust type to the total mass changes from 60% carbon, 22% alumina, 16% forsterite in the standard case to 45% Forsterite, 38% carbon, 14% alumina in the low ^{56}Ni mass model.

The overall grain size distribution functions for the two models are presented in Figure 6.3 (right panel) as sum over all dust components. The obtained distribution functions are further compared to the power-law profiles with exponents $\alpha = -2.5, -3.5$. The grain distributions obtained from both the models indicate notable contrast with the MRN distribution (α = -3.5 profile). The smaller grains <50 Å follow a pattern similar to the α = -2.5 power-law distribution. However, the size distribution function $f(a)$ for grains larger than $\sim$50 Å has a visible peak for the standard case, and two visible peaks in the ^{56}Ni = 0.01 M$_\odot$ model. The peak in $f(a)$ at a $\sim$ 200-250 Å range in case of both the models is attributed to amorphous carbon in zone 5. Owing to the large grains of forsterite formed from the early condensates, there is a further peak at around 800 Å in the low ^{56}Ni mass case. Comparing the largest sizes, in standard case a maximum of 400-500 Å grains are expected. On the other hand, the grains can grow up to $\sim$0.2μm in this model.

Each supernovae listed in Table 6.1 can be modelled individually, and depending on the estimated progenitor masses and the ^{56}Ni content, the picture of dust

formation will have its own characteristics. However in this chapter, we have compared the two extreme cases of a single progenitor to define the boundaries of the impact, that any alteration of ^{56}Ni mass can cause to the chemistry.

7 SN1987A: A Case Study

Though assigned to one single class, type II-P supernovae in itself provide a large amount of diversity controlled by the pre- and post-explosion conditions of the star and its surroundings. From the experience of modelling it can be concluded with conviction, that it is impossible to generalise a single model which can efficiently address the observations from various type II-P supernovae in recent years. SN1987A has been by far the most studied supernova leading to ∼480 publications solely dedicated to its analysis (Reference: ADS) and several others considering it as an example case. Nevertheless there still remains a lot of questions which demand proper justification. In this regard, this chapter tries to throw lights on the molecule and dust formation scenario of SN1987A using the ejecta model explained before.

SN1987A is a type II supernova first observed in February 1987. It is located in the Large Magellanic Cloud, a dwarf galaxy ∼ 51 Kpc away from the earth with metallicity one-third solar. The early time observations of the light curve are consistent with the explosion of a star, which on main sequence had a total mass 19±3 $M_\odot$ with a 6 $M_\odot$ helium core (Woosley, 1988). The explosion produced approximately 10^{51} ergs of energy and the study of the bolometric light curve suggests the production of 0.075 $M_\odot$ of radioactive ^{56}Ni.
In order to be consistent with the real supernovae, we use the same parameters and model a 19 $M_\odot$ progenitor exploding as a Type II-P supernova case. The initial abundances after explosion are derived from Rauscher et al., 2002 as presented in Figure 2.2. Similar to the 15 $M_\odot$ case, the specifications of the stratified ejecta is given in Section 2.2.1. As a difference from the 15 $M_\odot$ case, a 19 $M_\odot$ progenitor has a much larger O-core (O/Ne/Mg zone), however the other zones are comparable

TABLE 7.1: The range of each mass zone ($M_\odot$) in the ejecta, and the important species which control the chemistry in the respective zones

Zone 1A	Zone 1B	Zone 2	Zone 3	Zone 4	Zone 5	Zone 6
1.77-1.88	1.88-2.18	2.18-3.86	3.86-4.00	4.00-4.49	4.49-5.26	5.26-5.62
Si/S/Fe	Si/O	O/Ne/Mg/Si	O/C	He/O/C	He/C	He/N

in mass. Nevertheless, the initial composition of the ejecta zones also comes into play to dictate the chemistry, hence study of various progenitors can yield different results. This chapter shall deal with the results obtained from the study of the homogeneous and clumpy model of a 19 $M_\odot$ progenitor supernova. Table 7.1 briefly summarises the stratification of the zones which were described elaborately in Chapter 2.

7.1 Homogeneous model

All the physical parameters related to the homogeneous model has been discussed in Chapter 2. The physical model of the 19 $M_\odot$ homogeneous ejecta model of is similar to the 15 $M_\odot$ progenitor case, other than the fact that the densities are slightly on a lower side. Nevertheless, the difference in zone masses and the their composition (from that of 15 $M_\odot$ model) already makes it an interesting case to study. This section reports on the results obtained from our analysis.

7.1.1 The molecules

Molecules such CO, SiO, O_2, SO, N_2, SiS, etc., are synthesised in the ejecta in the first few years from the day of explosion. The molecular budget for the homogeneous ejecta model is given in the upper compartment of Table 7.2. The time evolution of CO mass is presented in Figure 7.1 (left panel). Zone 4 being a C-O rich zone, leads to formation of maximum CO followed by zone 2. The CO formation gets hindered up to 400 days in zone 4 essentially due to the activities of He^+. In zone 2 also presence of Ne^+ plays important role in arresting the fast increase of CO mass at early times. Zone 3 however contributes as early as 150 days, but the final mass is limited 0.07 $M_\odot$ as it is a small zone. The final mass of CO after 5 years from explosion remains in the range of $\sim$0.5 $M_\odot$. The derived masses of CO from IR data are about one order of magnitude smaller than our

TABLE 7.2: Masses of molecules ($M_\odot$) in the gas phase at 2000 days post-explosion in the ejecta, for the homogeneous and the clumpy model (Sarangi and Cherchneff, 2013, 2014)

Zones	Z1A	Z1B	Z2	Z3	Z4	Z5	Z6	Total
				Homogeneous case				
Mass	0.11	0.302	1.68	0.141	0.486	0.774	0.358	3.85
SiO	8.1(-8)	1.5(-8)	1.2(-7)	...	...	...	...	2.2(-7)
O_2	...	5.9(-7)	0.64	4.0(-2)	3.6(-2)	...	...	0.72
CO	1.6(-7)	2.7(-4)	0.135	6.7(-2)	0.28	7.2(-3)	...	0.49
SO	...	2.6(-2)	1.9(-3)	1.6(-4)	...	...	...	2.8(-2)
SiS	4.6(-2)	...	...	...	...	...	...	4.6(-2)
CO_2	...	...	2.6(-4)	...	...	...	...	2.6(-4)
CS	...	...	...	...	...	3.4(-4)	...	3.4(-4)
N_2	...	3.6(-6)	7.1(-5)	1.5(-6)	...	6.7(-4)	...	7.5(-4)
Total	4.6(-2)	2.6(-2)	0.78	0.108	0.316	8.2(-3)	0	1.25
Efficiency(%)	41.8	8.6	46.4	76.6	65.0	1.1	0	32.5
				Clumpy case				
SiO	3.5(-9)	...	9.4(-9)	...	...	...	...	1.3(-8)
O_2	...	1.7(-2)	1.0	6.7(-2)	9.2(-2)	...	...	1.2
CO	...	4.2(-6)	0.13	6.6(-2)	0.30	6.5(-3)	...	0.50
SO	...	8.3(-2)	1.9(-3)	2.1(-6)	3.6(-5)	...	...	8.5(-2)
SiS	4.5(-2)	...	...	...	...	...	...	4.5(-2)
CO_2	...	4.2(-4)	5.1(-3)	3.1(-3)	1.8(-3)	...	...	1.0(-2)
CS	...	...	...	...	...	7.5(-6)	...	7.5(-6)
N_2	...	...	7.1(-5)	1.7(-6)	9.2(-7)	6.8(-4)	...	7.6(-4)
NO	...	7.9(-6)	2.3(-6)	...	5.7(-7)	...	...	1.1(-5)
Total	4.5(-2)	0.10	1.14	0.136	0.394	7.2(-3)	0	1.82
Efficiency(%)	40.9	33.1	67.9	96.4	81.1	0.93	0	47.3

estimated masses in the 150-700 days range. The CO masses from the study of ALMA data ranges in between 0.01-0.2 $M_\odot$ (Kamenetzky et al., 2013; Jerkstrand et al., 2011), so the upper limit is round about close to our results. The study as well as the observations, neither indicate any evidence of decrease in CO mass. Hence like the 15 $M_\odot$ case, CO does not facilitate the formation of carbon dust. Figure 7.1 (right panel) shows the evolution of SiO as functions of different zones in the ejecta. Zones 1B and 2 are the major loci for SiO synthesis. The large zone 2 (1.68 $M_\odot$) is also rich in Ne^+ which is the reason why SiO mass reaches its maximum in this zone almost after 800 days from explosion. As explained in the 15 $M_\odot$ case, the formation of SiO is immediately followed by nucleation to silica and silicate clusters. The total mass of SiO thus derived are within one orders of the masses reported from IR observations (Liu and Dalgarno, 1994).

O_2 is the most abundant molecule in the gas, making up ∼19% of the ejecta after 3-4 years from the explosion. The final mass is of O_2 is 0.72 $M_\odot$ mostly formed in

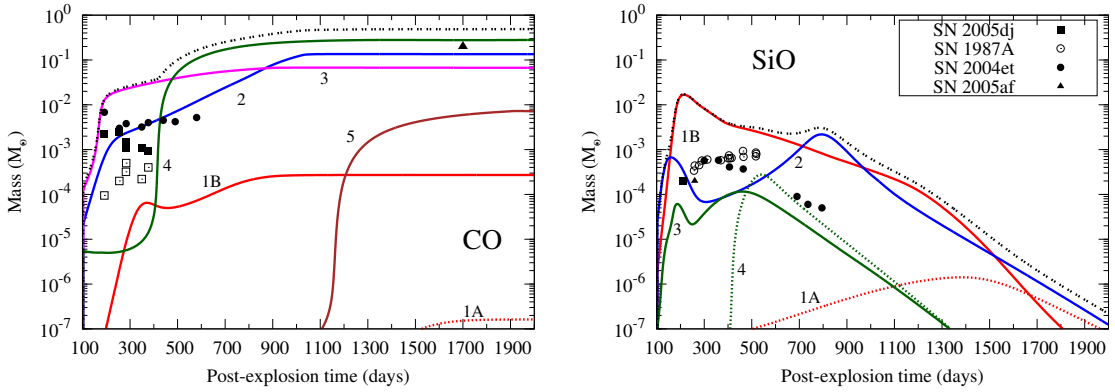

FIGURE 7.1: Results for the homogeneous model **Left Panel:** The mass evolution of CO in different zones of the ejecta is presented. CO masses derived from the observations of SN1987A are shown as, LTE open squares, non-LTE: squares (Liu et al., 1992), thermal assumption: circles (Liu and Dalgarno, 1995), ALMA data: triangle (Kamenetzky et al., 2013). The ALMA data corresponds to a time 27 years after explosion. The label in the figure just indicates the mass 1700 days only indicates the derived mass. **Right Panel:** The figure shows the evolution of SiO mass as a function of different ejecta zones. The empty circles indicates the derived masses from IR observations of SN1987A. For both the molecules, the dotted black line indicates the total mass from all the zones.

the large O-core. SO synthesis occurs in S-O rich zone 1B, whereas all the oxygen free molecular species are found in the innermost (1A) or the second outermost (5) zones of the He-core. The mass of O_2, SiS, SO, CS, N_2, etc., are tabulated in Table 7.2. The total mass of molecules in the gas, at day 2000 post-explosion is 1.25 $M_\odot$ with an efficiency of 32.6%. Zones 3 and 4 are the most efficient zones for molecule formation. The outer layer of He-core, zone 6, fails to produce any stable molecules due to the catastrophic impacts of abundant He^+.

7.1.2 The dust components

The dust formation occurs in the ejecta in tandem with the gas phase nucleation processes. Similar to the 15 $M_\odot$ case, the main dust components in the ejecta are namely olivines (forsterite), alumina, carbon, silicon carbide, iron sulphide and pure metals. The final contribution of each ejecta zone, to the total mass of dust is presented in Table 7.3. Figure 7.2 (left panel) on the other hand, explains the evolution of dust masses as sum over all the zones. The minimum threshold for grain sizes is set at 10 Å to be considered as dust. Dust formation sets in ∼300 days with the synthesis of iron sulphide in zone 1A and forsterite in zone 1B. The presence of Ne^+in zone 2 delays the formation of SiO and O_2 molecules which has

in turn hinders the synthesis of forsterite in this zone. Mass of forsterite increases with a smaller gradient between 400 and 900 days leading to a final mass 8.0×10^{-3} $M_\odot$. Alumina is the most abundant dust type, with total mass of 0.017 $M_\odot$ which forms steadily in zone 2 $\sim$ day 1000. The final mass of carbon dust depends solely on the C/O ratio of zone 5. The C/O ratio is only about 4 in zone 5 for this progenitor, compared to 21 for 15 $M_\odot$ case. Therefore the final mass of carbon dust remains limited to 7.5×10^{-3} $M_\odot$. The total dust mass undergoes restrained increase between 300 to 2000 days after explosion, starting from 10^{-6} $M_\odot$ at 300 days to 0.025 $M_\odot$ at day 1200 and finally ending up in 0.032 at day 2000. The range of dust masses in the time frame of one to three years of explosion can be compared to the IR data of SN1987A (Moseley et al., 1989; Wooden et al., 1993) with good agreement. Only 0.8% of the entire ejecta mass remains in the form of dust.

Grain size distributions: Figure 7.2 (right panel) depicts the grain size distribution functions $f(a)$ (defined in Section 3.4) for each dust component at day 2000. The distribution functions are calculated considering the contributions from all the zones. Table 7.4 presents the peak(s) (a_{peak}) of distribution functions for all dust types. Owing to the low gas densities in the homogeneous model, the ejecta forms medium size grains. Forsterite grains grow largest, with a small population above 200 Å. Even though alumina is much more abundant than forsterite, forsterite condensed in zone 1B as early as 400 days gets the advantage of high density to grow larger. The double waves nature in the forsterite distribution curve indicates to the different peaks from zone 1B and 2. Carbon dust condenses very late, approximately 1900 days after explosion. The ejecta is too thin and cool at this epoch to trigger effective condensation. As a result carbon dust in this case, forms small grains with peak distribution around 20 Å and largest grains of size 70 Å. The metallic clusters of Si, Mg and Fe are low in abundance (10^{-5} to $10^{-4}M_\odot$) and the size distribution functions for these grains have peaks smaller than 20 Å. The final composition comprises of 53% of alumina and 23% each for forsterite and carbon. The efficiency of condensation is about 99% considering all the dust precursors, and taking into account gas phase uncondensed carbon rings ($\sim1.7\times10^{-3}M_\odot$) also, the condensation efficiency becomes 95%.

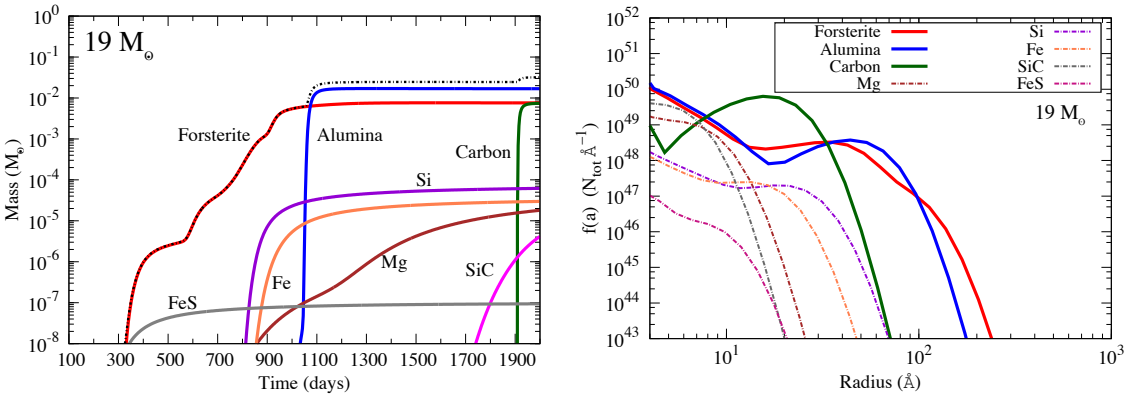

FIGURE 7.2: Results for the homogeneous model **Left Panel:** The evolution of the dust masses for different dust components in the ejecta are presented summing over the contribution over all the zones. The dotted balck line stands for the total dust mass. **Right Panel:** The grains size distribution functions $f(a)$ for all the dust components at day 2000 post-explosion are illustrated in the figure (Sarangi and Cherchneff, 2014).

TABLE 7.3: Masses ($M_\odot$) of different dust components at 2000 days post-explosion in the ejecta, for the homogeneous and the clumpy model (Sarangi and Cherchneff, 2014)

Zones	Z1A	Z1B	Z2	Z3	Z4	Z5	Z6	Total
				HOMOGENEOUS				
Mass	0.11	0.302	1.68	0.141	0.486	0.774	0.358	3.85
Forsterite	-	2.3(-3)	5.1(-3)	9.1(-5)	1.0(-4)	-	-	7.6(-3)
Alumina	-	-	1.7(-2)	3.9(-6)	6.5(-5)	-	-	1.7(-2)
Carbon	-	-	-	-	-	7.5(-3)	-	7.5(-3)
Pure-Mg	-	-	1.7(-5)	2.1(-7)	5.4(-7)	-	-	1.8(-5)
Pure-Si	6.2(-5)	-	-	-	-	-	-	6.2(-5)
Pure-Fe	3.0(-5)	-	-	-	-	-	-	3.0(-5)
Silicon Carbide	-	-	-	-	-	3.7(-6)	-	4.1(-6)
Iron Sulphide	9.4(-8)	-	-	-	-	-	-	9.4(-8)
Total	9.2(-5)	2.3(-3)	2.2(-2)	9.5(-5)	1.7(-4)	7.5(-3)	0	0.032
Efficiency(%)	8.4(-2)	0.76	1.31	6.7(-2)	3.5(-2)	0.97	0	0.83
				CLUMPY				
Forsterite	-	2.4(-3)	4.8(-2)	5.4(-4)	1.6(-3)	3.0(-4)	-	5.3(-2)
Alumina	-	4.0(-4)	1.7(-2)	1.3(-5)	6.3(-5)	-	-	1.8(-2)
Carbon	-	-	-	-	-	7.3(-3)	-	7.3(-3)
Pure-Mg	-	-	2.1(-2)	1.2(-3)	4.0(-3)	-	-	2.6(-2)
Pure-Si	1.7(-2)	-	-	-	-	-	-	1.7(-2)
Pure-Fe	1.7(-2)	-	-	-	-	-	-	1.7(-2)
Silicon Carbide	-	-	-	-	-	1.7(-5)	-	1.7(-5)
Iron Sulphide	1.1(-4)	-	-	-	-	-	-	1.1(-4)
Total	3.4(-2)	2.8(-3)	8.6(-2)	1.8(-3)	5.6(-3)	7.6(-3)	0	0.138
Efficiency(%)	30.9	0.93	5.1	1.28	1.15	0.98	0	3.6

7.2 Clumpy model

The empirical clumpy model of 19 $M_\odot$ progenitor based on SN1987A, provides the basis to study the dust formation scenario in the dense clumps of the ejecta. The physical description of the model parameters are explained in Section 2.3. The variation of filling factors from one zone to other results to different initial density of clumps in each zones. The impact of clumpiness on the ejecta chemistry is the centre of discussion in this section.

7.2.1 The molecules

Similar to all the models discussed before, molecules occupy a handsome portion of the entire ejecta mass after a few years from explosion. The time evolution of CO and SiO mass in different ejecta zones are illustrated in Figure 7.3 left and right panel respectively. Owing to high densities, CO synthesis takes place at great pace from 120 days in zone 4. The final mass of CO is 0.5 $M_\odot$ with contributions from zones 4, 2 and 3 in order of abundance. The mass of CO falls in zone 1B leading to the formation of CO_2 molecules. The obtained masses are two order of magnitude larger than the estimated CO masses from IR data. Synthesis of SiO essentially takes place in zones 2 and 1B. However, due to high gas densities in the clumps of zone 1B, the nucleation processes get aggravated and all the SiO molecules in this zone rapidly gets depleted to silicates and silica clusters within 400 days. The mass of SiO in zone 2 gradually declines from 0.01 to 10^{-7} $M_\odot$ between day 200 and 1700 post-explosion. The total mass of SiO molecules make a perfect agreement with IR observations in the 200-900 day range.

Other than CO and SiO, several molecules are synthesised in good abundances again essentially because chemical processes becomes efficient at high densities. Table 7.2 gives the details for the masses of CO_2, SiS, N_2, CS and NO formed in different zones. SiS forms in zone 1A whereas CS at late times in zone 5. The CO_2 molecule forms at day 500 in zone 3, and grows in mass from a second formation event in zone 2 starting at day 800. At day 2000, the total CO_2 mass reaches $\sim 1 \times 10^{-2}$ $M_\odot$. The molecules N_2 and NO also form with a mass of 7.5×10^{-4} $M_\odot$ and 1.1×10^{-5} $M_\odot$, respectively, at day 2000. In the homogeneous case, CO_2 forms with a low mass of 3×10^{-4} $M_\odot$. The large reservoir of CO produced in the clumpy case provides an effective formation channel for CO_2 via

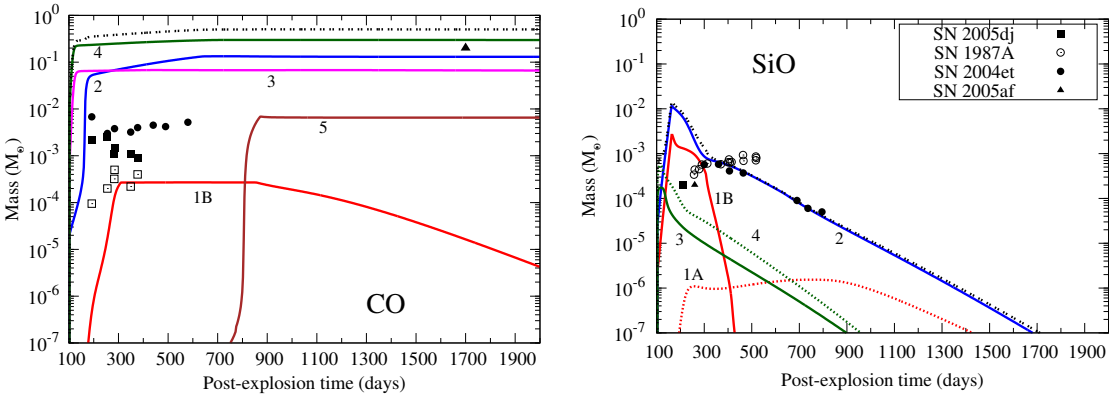

FIGURE 7.3: Results for the clumpy model **Left Panel:** The mass evolution of CO in different zones of the ejecta is presented. CO masses derived from the observations of SN1987A are shown as, LTE open squares, non-LTE: squares (Liu et al., 1992), thermal assumption: circles (Liu and Dalgarno, 1995), ALMA data: triangle (Kamenetzky et al., 2013). The ALMA data corresponds to a time 27 years after explosion. The label in the figure just indicates the mass 1700 days just indicates the derived mass. **Right Panel:** The figure shows the evolution of SiO mass as a function of different ejecta zones. The empty circles indicates the derived masses from IR observations of SN1987A. For both the molecules, the dotted balck line indicates the total mass from all the zones.

CO recombination. Carbon dioxide is thus a tracer of clumpiness in the O-rich core of the 19 $M_\odot$ ejecta. A total mass of 1.82 $M_\odot$ is present in the ejecta in the form of molecules, which is ∼48% of the entire ejecta mass.

7.2.2 Nucleation end-products

The molecule synthesis is simultaneously accompanied by the nucleation phase. The nucleation scheme deals with the formation of the small clusters. The clusters either attain a critical size and act as a dust precursor, or remain as intermediate molecular clusters in gas. The nucleation (molecules → clusters) and the condensation (clusters → dust) are concurrent processes, therefore the nucleation end products deplete quickly from the gas phase to solids. Nevertheless, the nucleation phase is the key to understand the following dust formation scenario. In the clumpy model, the O-rich clusters dominate the entire cluster budget. The central O-core, 2 $M_\odot$ in mass, is responsible for the synthesis of $(Mg_2SiO_4)_2$ and $(Al_2O_3)_2$ clusters through their respective nucleation networks described in Section 3.3. Figure 7.4 shows the correlation between the diatomic molecules and the O-rich clusters with respect to zones 1B and 2. Zone 1B has the highest clumpy densities among all the zones which induces efficient formation of SiO at ∼ day

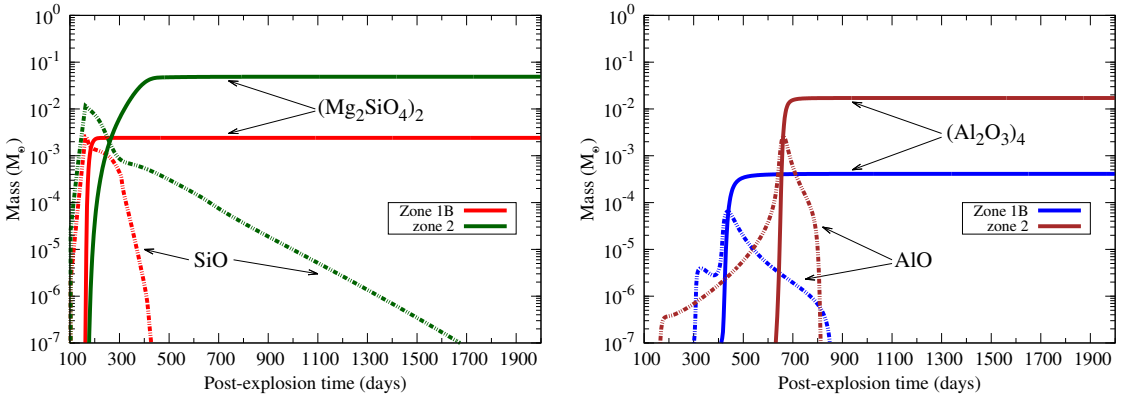

FIGURE 7.4: Results for the clumpy model (pre-condensation) **Left Panel:** The correlation between the SiO molecules and the $(Mg_2SiO_4)_2$ clusters are shown with respect to zones 1B and 2, the central regions of the O-core. **Right Panel:** The correlation between AlO molecules and $(Al_2O_3)_4$ is shown with respect to the main formation zones 1B and 2.

120. However, due to nucleation under high gas densities around day 200, all the SiO gets quickly depleted into $(Mg_2SiO_4)_2$ molecules. However the mass of the clusters is limited by the size of the zone, and amount of Mg present. Similar scenario is also experienced in zone 2, where the mass is higher, but the formation of clusters are less abrupt (left-panel of the figure). A similar argument is also prevalent for $(Al_2O_3)_2$ clusters shown in the right-panel of Figure 7.4, only the time scales of formation are delayed to day 400 in zone 1B and day 700 in zone 2. Apart from the $(Mg_2SiO_4)_2$ and $(Al_2O_3)_2$ clusters, the C_{28} fullerenes are synthesized in zone 5 and the metallic clusters of $(Si)_4$ and $(Fe)_4$ in the innermost zone 1A of the ejecta. All these stable clusters act as monomer seeds to the respective dust types, and therefore leave the gas phase to efficiently form larger grains. There are some intermediate molecular clusters which do not reach the critical monomer unit in the timescales of the evolution of the ejecta. Therefore, they remain as intermediate uncondensed molecular clusters. They are mainly in the form Si_mO_n or $C_{2n}, n < 14$, with masses $8{\times}10^{-4}$ and $3{\times}10^{-3}$ respectively.

7.2.3 The dust components

Following the molecular synthesis and nucleation of small clusters, the dust grains start appearing in the ejecta through condensation. The evolution of dust masses can be summarised from Figure 7.5 (left panel) for all the dust types. The contribution from different zones to the total mass of individual dust components are listed in Table 7.3. Similar to chemical reactions, also the condensation of dust

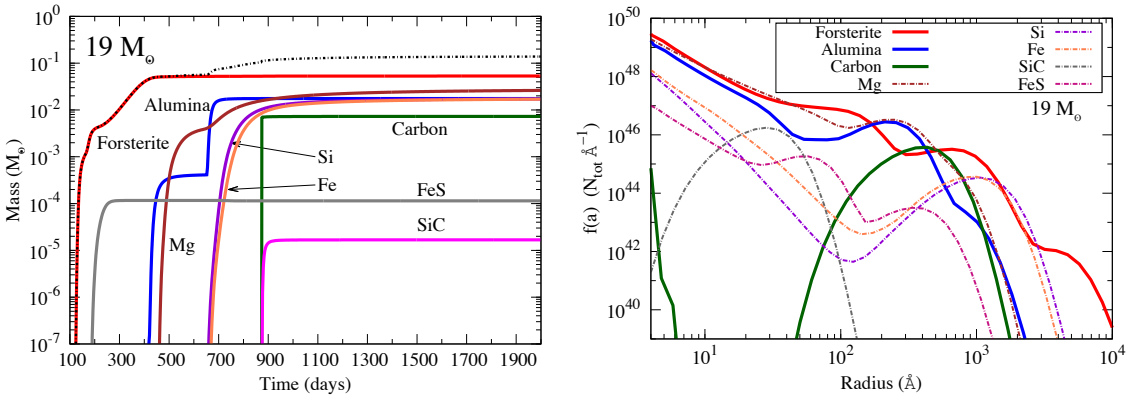

FIGURE 7.5: Results for the clumpy model **Left Panel:** The evolution of the dust masses for different dust components in the ejecta are presented summing over the contribution over all the zones. The dotted balck line stands for the total dust mass. **Right Panel:** The grains size distribution functions $f(a)$ for all the dust components at day 2000 post-explosion are illustrated in the figure (Sarangi and Cherchneff, 2014).

grains gets boosted by high densities. Forsterite grains start forming rapidly in zone 1B from 120 days which is also consistent with the depletion of SiO as shown in Figure 7.2. The overall dust mass is always dominated by forsterite, earlier by zone 1B and later by zone 2. The final mass of forsterite is 0.053 $M_{\odot}$after five years post explosion. Alumina also forms in zone 1B and 2, finally ending up in 0.017 $M_{\odot}$. Importantly, the pure metal dusts of Si, Fe and Mg get a perfect boost under these circumstances, and the masses (0.01-0.03 $M_{\odot}$) are drastically higher compared to the homogeneous case. Carbon dust as expected is synthesised in zone 5, where He^{+} dominates the chemistry. In this case though, due to the high densities the recombination of He^{+} happens faster. Carbon dust forms with a sudden kick around 900 days. The mass of carbon dust remains consistent at 7.6×10^{-3} $M_{\odot}$ thereafter. The total dust mass in the ejecta settles at 0.138 $M_{\odot}$.

Grain size distribution: The grain size distribution profiles in the clumpy model bring out the most intriguing aspects of the ejecta chemistry. In this case, large grains of dust are estimated to form in the ejecta. Again the density factor comes into play in two ways: firstly early synthesis means high gas densities and hence more dust precursors, and secondly more dust precursors means high grain densities and hence efficient coagulation. Thus, the condensation scheme gets stimulated to form largest grains of μm order. The size distribution functions are presented in Figure 7.5 (right panel) for all the dust species.

TABLE 7.4: Final dust mass ($M_\odot$) at 2000 days, the percentage contribution from each dust species, and the peak (a_{peak} in Å) of the grain size distribution function are presented (Sarangi and Cherchneff, 2014)

	HOMOGENEOUS			CLUMPY		
Dust	Mass	%	a_{peak}(Å)	Total	%	a_{peak}(Å)
Forsterite	7.6(-3)	23.8	35, 63	5.3(-2)	38.4	77, 661, 3170
Alumina	1.7(-2)	53.0	44	1.8(-2)	13.0	211, 562
Carbon	7.5(-3)	23.4	16	7.3(-3)	5.3	435
Pure-Mg	1.8(-5)	0.06	8	2.6(-2)	18.8	252
Pure-Si	6.2(-5)	0.19	18	1.7(-2)	12.3	1066
Pure-Fe	3.0(-5)	0.09	14	1.7(-2)	12.3	1003
Silicon Carbide	4.1(-6)	0.013	7	1.7(-5)	0.012	29
Iron Sulphide	9.4(-8)	3(-4)	8	1.1(-4)	0.08	57, 334
Total	0.032	100	-	0.138	100	-

Owing to the small filling factor in zone 1B, $f_c = 0.004$, the clumps are comparatively more dense than other zones. That is why, the silicates grows very early leading to the size distributions with peak at 3100 Å, and largest size of 2-3 μm grains. Nevertheless, the 1B is a small zone compared to zone 2, so the mass of silicates in zone 2 is larger, and the sizes reach a peak distribution of 660 Å. Figure 7.6 (right panel) shows the $f(a)$ for forsterite at day 600 and 2000 respectively in zones 1B and 2. The pattern indicates, that the largest grains are formed also very early on, and by 600 days the $f(a), a > 1000$ Å remains mostly unchanged. The intermediate size grains in the 10-1000 Å range however continue to grow towards larger sizes. The mass distribution of the grains are presented in Figure 7.6 (left panel). The values of a_{peak} for all the components are listed in Table 7.4. A similar scenario applies to alumina which forms essentially in zone 1B at $\sim$ day 450 and zone 2 at $\sim$ day 700. The alumina size distribution thus shows a peak around $\sim$ 240 Å, which corresponds to the grains formed in zone 2, and a tail of large grains produced in zone 1B and with a size over 0.1 μm. The formation of three populations of grains of pure silicon, pure iron, and iron sulphide pertains to zone 1A. Despite their late formation at day 650, pure silicon and Fe grain condensation is boosted compared to the homogeneous case because of the higher gas density in zone 1A. This leads to grain populations that peak around 0.12 μm for both pure silicon and iron dust. This peak size is almost two orders of magnitude greater than in the homogeneous case. Grains of FeS condense at day 200, and thus grow over time to relatively large sizes ($\sim$ 400 Å). However the final FeS dust mass remains low owing to a modest mass of FeS clusters that form in zone 1A. Finally, the outermost zone 5 forms carbon and SiC grains. The carbon

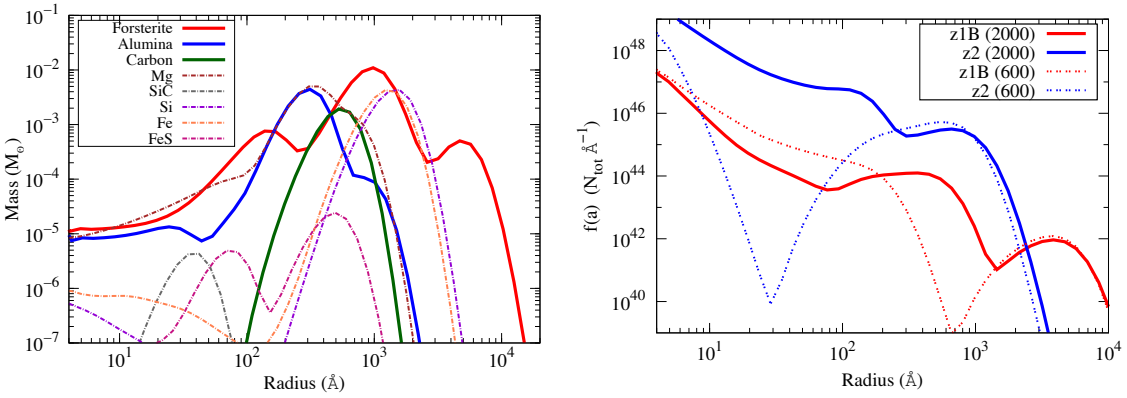

FIGURE 7.6: Results for the clumpy model **Left Panel:** The mass distribution ($M_\odot$) of dust grains in the ejecta are presented for all the dust components **Right Panel:** Grain size distributions for forsterite in zones 1B and 2 at two epochs, day 600 day 2000 from explosion (Sarangi and Cherchneff, 2014).

grains form at day 870, a much earlier epoch than for the homogeneous case, where carbon forms at day 1900. This results in a size distribution dominated by larger grain sizes peaking at 520 Å, while the carbon size distribution peaks at 70 Å for the homogeneous ejecta. The grain size distributions normalized by the total number of grains at day 2000 post-explosion are listed in Appendix B Table B.3 & Table B.4.

The grain size distribution profile for neither the homogeneous nor the clumpy ejecta follow the standard MRN type power law distribution. The variation of the power law exponent α also does lead to any considerable fit to the obtained distribution function. Therefore we safely infer, that in case of newly formed dust in supernova ejecta over a few years from explosion, the grain growth through coagulation and coalescence does not result to a power law distribution.

7.3 Comparison between the two models

The consecutive discussion of the homogeneous and clumpy model emphasises on the prime issues that differentiate the two model. The following points summarise these important features with reference to Table 7.2, 7.3 & 7.4.

- The efficiency of molecule formation gets boosted from 30 to 48% as the final mass of increase from 1.25 to 1.82 $M_\odot$ in the clumpy case.

- High densities facilitate early recombination of He^+, Ne^+ & Ar^+ thereby diminishing their impact. Thus all the chemical processes becomes more efficient.
- The efficiency of dust formation increases from 1 to 3.6%, and the final mass in the clumpy case is a factor 4 times larger than that of the homogeneous model.
- About 45% of the dust composition in the clumpy model is made up by metallic clusters, unlike the homogeneous case where the dust is all in the form of silicates, carbon and alumina.
- Lastly and most importantly, the average grains sizes increases almost a 100 times larger in case of the clumpy model.

As clearly explained, the dust condensation scenario is highly sensitive to the ejecta densities, and hence the dust formation epochs. A clumpy ejecta leads to early synthesis of all types of dust components, compared to the standard homogeneous case. The dust components can be further categorised into two classes. The gas phase clusters of alumina, amorphous carbon and silicon carbide undergo a fast and efficient formation, but the upper limit is controlled by the availability of atomic Al, C or Si in the ejecta respectively. Hence the mass of these dust species does not significantly vary due to any change in ejecta conditions which favours dust formation. On the contrary, the final masses of silicates and metallic clusters is controlled by the variations in the conditions. Silicates are formed through a more complex Si-chemistry and atomic Mg is abundant in the ejecta. Due to this, the upper limit of silicate mass can vary within a factor of 10-20. Owing to low abundances of atomic Si and Fe in zone 1A, the respective clusters does not form efficiently in the homogeneous case. But inside the high density clumps the masses of these metallic clusters increase by roughly two orders of magnitude. This has a significant impact on the overall condensation picture. The average grain sizes for the first category of dust components vary at most by a factor of 10 from standard to special case. The grain sizes for forsterite however is found to increase from 60 Åto 3200 Å, and for metallic clusters by three orders of magnitude in the clumps. Moreover the study of the clumpy model indicates the presence of a small of mass of very large grains ($\sim\mu$m) and a large mass of moderate ($\sim$ 500 Å) size grains in the ejecta, which is unlike the standard case. This might be an interesting case study to access the further processing of dust in the shocks.

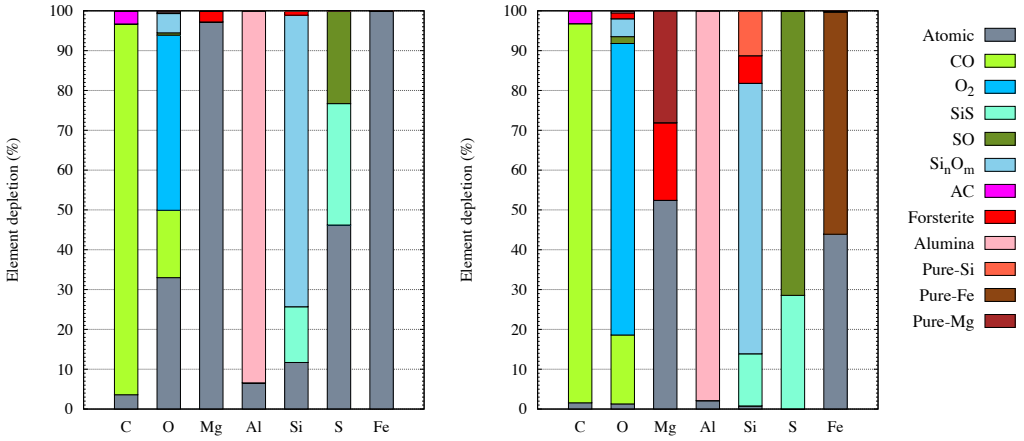

FIGURE 7.7: Element depletion for the homogeneous and the clumpy case at day 2000 post-explosion (Sarangi and Cherchneff, 2014).

Depletion of elements: We calculate the depletion of elements in molecules, dust clusters and grains to assess the impact of ejecta clumps on the depletion fraction. Results for both homogeneous and clumpy SN ejecta with the 19 $M_{\odot}$ stellar progenitor are shown in Figure 7.7 for the various elements of interest.

In the homogeneous case, the fraction of elements staying in atomic form is large for oxygen and sulphur, and almost 100 % for both magnesium and iron. Carbon is essentially depleted in CO for both homogeneous and clumpy ejecta, with a few % going to amorphous carbon. The oxygen depletion changes drastically in the clumpy ejecta with $\sim$ 70 % of oxygen in the form of O_2, and a larger depletion in SO and forsterite. While more than 96 % of magnesium is atomic for the homogeneous ejecta, almost 50 % of magnesium is trapped in forsterite and pure Mg when the ejecta is clumpy. For both cases, aluminium is heavily depleted in alumina, with a fraction exceeding 93 %, and the rest left in atomic form. Sulphur is not depleted in metal sulphides for both cases as the amount of FeS formed in both ejecta is small. Sulphur is depleted in the molecules SO and SiS, and the depletion becomes total for the clumpy case. Finally, clumpiness has a strong impact on iron. In the homogeneous ejecta, almost all iron is in atomic form since the mass of formed FeS is very small. However, in the clumpy case, 56 % of iron is in large grains of pure iron, as seen in Figure 7.5.

For both cases, we see that a large fraction of Si atoms is trapped in clusters which enter the formation process of silica, SiO_2. These clusters labelled, Si_mO_n, will not all be included in the final silica mass, as their growth process is controlled by the amount of available SiO. As mentioned in Section 5.2.2, we have not studied the

nucleation and condensation of silica in this study, but an assessment of the silica mass based on the SiO mass at day 300 or the assumption that all Si_mO_n clusters turn into silica leads to values ranging between 10^{-5} $M_\odot$ and 10^{-2} $M_\odot$, respectively, at day 2000. More generally, we see that a clumpy ejecta depletes almost all elements in molecules, dust clusters and grains, except for magnesium and iron, which retain some large mass fraction in atomic form. However, clumpiness induces a large mass fraction in pure magnesium and iron grains.

8 The Extreme Cases

In the previous chapters, the dust formation scenario has been tested with the variation of a) degree of clumpiness b) mass of ^{56}Ni. In this chapter, the we shall consider two extreme progenitors masses of type II supernovae and try to determine how the initial mass of the progenitors can affect the formation of dust. Stars between 10-25 $M_{\odot}$ are estimated to end their lives in the form of core-collapse supernovae, out of which type II-P is the most common. Several observed local supernovae such as SN1999em (Elmhamdi et al., 2003a), SN2003gd (Hendry et al., 2005), SN2004dj (Vinkó et al., 2009), SN2005af (Kotak et al., 2006), SN2009bw (Inserra et al., 2012) falls in the 10-15 $M_{\odot}$range. The massive progenitors ($>$ 20 $M_{\odot}$) are rare in the local universe and are mainly important in terms of some large luminous stars with high mass loss rates which explode as type IIn supernovae (Kiewe et al., 2012). In this chapter, we choose a 12 $M_{\odot}$ progenitor and a 25 $M_{\odot}$progenitor star as test cases to carry out the analysis. Variation of main sequence progenitor mass leads to alterations in nucleosynthesis burning phases and post-explosion yields (Woosley et al., 2002). This implies, the initial relative abundances of the elements engaged in dust formation are differ from one progenitor to other. Secondly, more massive the progenitor is, the explosion becomes more energetic (Hamuy, 2003) and a larger mass of ^{56}Ni is produced. As a combination of the two, the scenario of dust formation in the two extreme models have some contrasting features which are discussed in the following text. The formalism used in the study remains identical to the previous standard case, and for both the progenitors a homogeneous stratified ejecta is considered. The rates for Compton electron induced destruction processes are estimated for all the models separately (Table A.3), as they are functions of the ^{56}Ni mass and the γ-ray optical depths specific to each progenitor.

TABLE 8.1: 12 $M_\odot$ model: The range of each mass zone ($M_\odot$) in the ejecta, and the important species which control the chemistry in the respective zones

Zone 1A	Zone 1B	Zone 2	Zone 3	Zone 4	Zone 5
1.7-1.76	1.76-1.89	1.89-2.03	2.03-2.19	2.19-2.35	2.35-3.27
Si/S/Fe	Si/O	O/Ne/Mg/Si	O/C	He/C	He/N

8.1 12 $M_\odot$ progenitor with low ^{56}Ni

The ejecta of a typical 12 $M_\odot$ progenitor supernova is stratified on the basis of abundances of the important elements. Table 8.1 shows the mass ranges of each zone and their important species. The ejected mass of the He-core is only 1.57 $M_\odot$ out of which a large outermost layer exists which is essentially consists only helium and a small trace of nitrogen. The initial abundances of each zone is given in Table 2.2 as derived from Woosley and Heger, 2007. Several supernovae in the local universe listed in Table 6.1 which belongs to the 10-15 $M_\odot$ range have a low ^{56}Ni mass in the order of 0.01-0.03 $M_\odot$. To replicate a similar case, we consider a mass of 0.01 $M_\odot$ of ^{56}Ni produced by the explosion. The dust formation and evolution is studied in the ejecta of the small progenitor case and the results are discussed below. The chemistry proceeds via simultaneous steps of nucleation and condensation. We present the final results related to the dust budget in the ejecta at day 2000 post explosion.

8.1.1 Dust masses

Similar to the standard case, the dominant dust components in the ejecta are silicates, alumina and carbon. Other types of dust such as metallic clusters, silicon carbide and iron sulphide are also synthesised in a small proportion. Figure 8.1 (left-panel) presents the evolution of dust masses as function of post-explosion time as sum over all the zones. The contribution from each zone at day 2000 are given in Table 8.2. Owing to the low mass of ^{56}Ni the destruction routes induced by He^+, Ne^+ and Ar^+ are not efficient. Dust formation triggers inside the O-core zones 1B and 2 as early as day 200 and rapidly build up to 10^{-2} $M_\odot$ by day 300. Zone 1B forms dust at an efficiency of 10% which one of the highest considering any progenitor mass we have addressed. The outer zones, 4 and 5 have a C/O ratio greater than 1 supporting formation of carbon dust. As a result of high C/O ratio ($\sim$ 15) and reduced effects of He^+, carbon dust formation is pumped up at

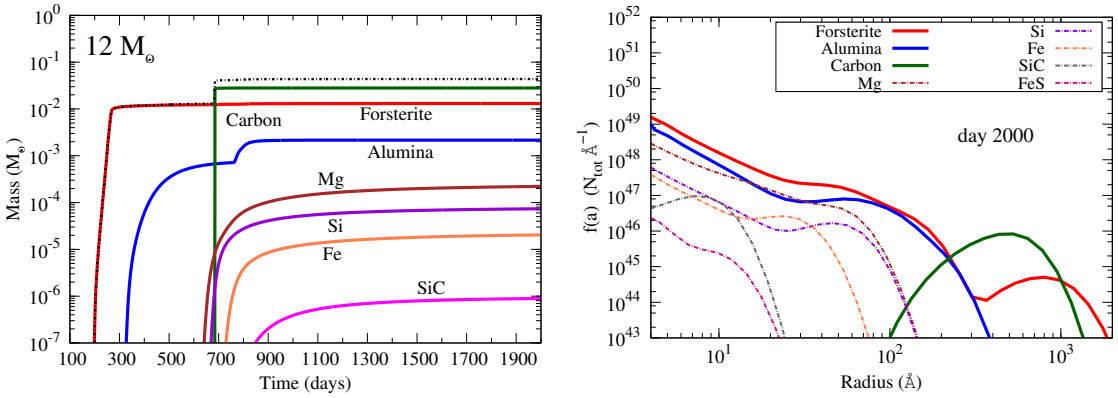

FIGURE 8.1: Results for the 12 $M_{\odot}$model **Left Panel:** The evolution of the dust masses for different dust components in the ejecta are presented summing over the contribution over all the zones. The dotted black line stands for the total dust mass. **Right Panel:** The grains size distribution functions $f(a)$ for all the dust components at day 2000 post-explosion are illustrated in the figure.

TABLE 8.2: 12 $M_{\odot}$ model: Masses ($M_{\odot}$) of different dust components at 2000 days post-explosion in the ejecta

Zones	Z1A	Z1B	Z2	Z3	Z4	Z5	Total
			12 $M_{\odot}$case				
Mass	0.06	0.13	0.14	0.16	0.16	0.92	1.57
Forsterite	-	1.2(-2)	2.9(-4)	2.2(-4)	2.3(-4)	-	1.3(-2)
Alumina	-	7.7(-4)	1.0(-3)	3.4(-4)	-	-	2.2(-3)
Carbon	-	-	-	-	2.8(-2)	-	2.8(-2)
Pure-Mg	-	4.4(-6)	2.0(-4)	2.1(-5)	-	-	2.2(-4)
Pure-Si	7.4(-5)	-	-	-	-	-	7.4(-5)
Pure-Fe	2.0(-5)	-	-	-	-	-	2.0(-5)
Silicon Carbide	-	-	-	-	9.0(-7)	-	9.0(-7)
Iron Sulphide	5.6(-8)	-	-	-	-	-	5.6(-8)
Total	9.4(-5)	1.3(-2)	1.5(-3)	5.8(-4)	2.8(-2)	0	0.044
Efficiency(%)	0.16	10.0	1.1	0.36	17.5	0	2.8

$\sim$ day 680 in zone 4. It grows to a mass of 0.028 $M_{\odot}$ instantaneously and the formation efficiency in this zone is about 17 %. Zones 1-4 of total mass 0.65 $M_{\odot}$ actively participates in dust formation resulting to a dust mass of 0.044 $M_{\odot}$. The outermost shell in the helium core, termed as zone 5 (0.92 $M_{\odot}$), is an inert core only made up of 99% helium. The overall efficiency of dust formation is about 2.8 %. In spite of a small ejected mass of 1.57 $M_{\odot}$, the dust masses are larger compared to the standard case due to the a low value of ^{56}Ni initiating early condensation. About 64% of the total dust is in made up by amorphous carbon followed by 30 % of silicates. Table 8.3 summarises the percentage contributions of each dust type. In the order of importance dust species in a 12 $M_{\odot}$ progenitor case can be arranged as carbon > forsterite > alumina.

TABLE 8.3: Final dust mass ($M_\odot$) at 2000 days, the percentage contribution from each dust species, and the peak (a_{peak} in Å) of the grain size distribution function are presented for the 12 $M_\odot$ and the 25 $M_\odot$ progenitor models.

Progenitor	12 $M_\odot$			25 $M_\odot$		
Dust	Mass	%	a_{peak}(Å)	Total	%	a_{peak}(Å)
Forsterite	1.3(-2)	29.5	42.6, 804	2.6(-2)	32.5	76.6, 248
Alumina	2.2(-3)	5.0	79.2	4.1(-2)	51.2	96.4
Carbon	2.8(-2)	63.6	526	1.0(-2)	12.5	75.3
Pure-Mg	2.2(-4)	0.5	43.1	1.6(-3)	2.0	29.1
Pure-Si	7.4(-5)	0.17	46.4	1.5(-3)	1.9	68.7
Pure-Fe	2.0(-5)	0.05	24.2	1.9(-4)	0.23	29.5
Silicon Carbide	9.0(-7)	2.0(-3)	7.2	7.5(-5)	0.09	8.8
Iron Sulphide	5.6(-8)	1.3(-4)	8.1	1.3(-6)	1.6(-3)	11.9
Total	0.044	100	-	0.080	100	-

8.1.2 Grain sizes

The grain size distribution function $f(a)$ for all the dust components at day 2000 are presented in Figure 8.1 (right-panel). In Table 8.3 all the peaks (a_{peak}) of the size distribution functions are given. The early condensation of silicates in zone 1B results in a size distribution of medium to large grain population. The peak of the distribution for silicates is around 800 Å and few of the grains grow up to about 0.2 μm in size. Carbon is the most abundant dust species that has average grains in the order of 530 Å and largest ones above 0.1 μm. The other dust components populate the ejecta with modest size grains. Alumina is the third most important species that has a peak value a_{peak} around 80 Å. The pure metallic clusters start forming in the day 700-800 window. They have moderate masses between 10^{-5} to 10^{-3} $M_\odot$and condense in low concentrations forming biggest grains in order of 100 Å. The MRN power law profile with α = -3.5 does not justify the grain size distributions estimated from the analysis.

8.2 25 $M_\odot$ progenitor with high ^{56}Ni

We study the role of large progenitor of main sequence mass 25 $M_\odot$ as a dust producer after its explosion. A homogeneous stratified ejecta is assumed for the analysis. The respective zones are given in Table 8.4. The initial abundances of all the elements are given listed in Table 2.3 with reference to Rauscher et al., 2002. The helium core is dissected into 8 zones, where zone 1-5 are conductive to

TABLE 8.4: 25 $M_\odot$ model: The range of each mass zone ($M_\odot$) in the ejecta, and the important species which control the chemistry in the respective zones

Zone 1A	Zone 1B	Zone 2	Zone 3	Zone 4A	Zone 4B	Zone 5	Zone 6
2.1-2.33	2.33-2.51	2.51-2.98	2.98-5.69	5.69-6.22	6.22-7.11	7.11-8.07	8.07-8.30
Si/S/Fe	Si/O	O/Si/Mg	O/Ne/Mg	O/C	He/O/C	He/C	He/N

dust formation but zone 6 remains inert. The 6.2 $M_\odot$ helium core consists of a large O-core spanning over zones 1B, 2 and 3 of total mass 3.4 $M_\odot$. As mentioned earlier, larger the progenitors have more powerful explosions. In case of the 25 $M_\odot$ model, Rauscher et al., 2002 estimated a mass of about 0.2 $M_\odot$ of ^{56}Ni produced by the explosion. We consider an identical value for ^{56}Ni mass and study the impact of high ^{56}Ni masses on the overall dust formation scheme. Umeda and Nomoto, 2008 derived the typical amounts of ^{56}Ni that can be produced in large progenitors. Several recent observations of type IIn supernovae (Smith et al., 2012; Kiewe et al., 2012) indicate that the progenitors more massive than 20-30 $M_\odot$ at main sequence can produce energetic explosions leading to a larger mass of ^{56}Ni. Therefore the current study shall address a case to some extent similar to the type IIn supernovae and try to investigate its contrasts with the standard case.

8.2.1 Dust masses

The summary of dust mass evolution with time is presented in Figure 8.2 (left-panel). The relative contributions from each zone are illustrated in Table 8.5. The relatively high mass of ^{56}Ni present in the ejecta plays decisive role in controlling the epochs of dust synthesis. Similar to the previous cases, forsterite, alumina and carbon are the leading dust species. Forsterite grains, synthesised in zone 2 and 3, dominates the dust budget up to day 800. The massive zone 3, rich in Ne^+ at early time, delays the formation of forsterite up to $\sim$ day 700, whereas in zone 2 the mass builds up gradually from day 300. Alumina forms in O-rich zone 3 and rapidly builds up to a mass of 0.04 $M_\odot$. Alumina remains the most abundant dust component overall making up about 51 % of the total dust. In spite of efficient destructions by He^+, amorphous carbon appear in the ejecta as stable dust species at around day 1200 owing to a high C/O ($\sim$ 36). But the final mass of dust is dominated by O-rich dust components at all times which is unlike the 12 $M_\odot$ case. The large O-core is responsible for producing 85 % of all the dust as shown in

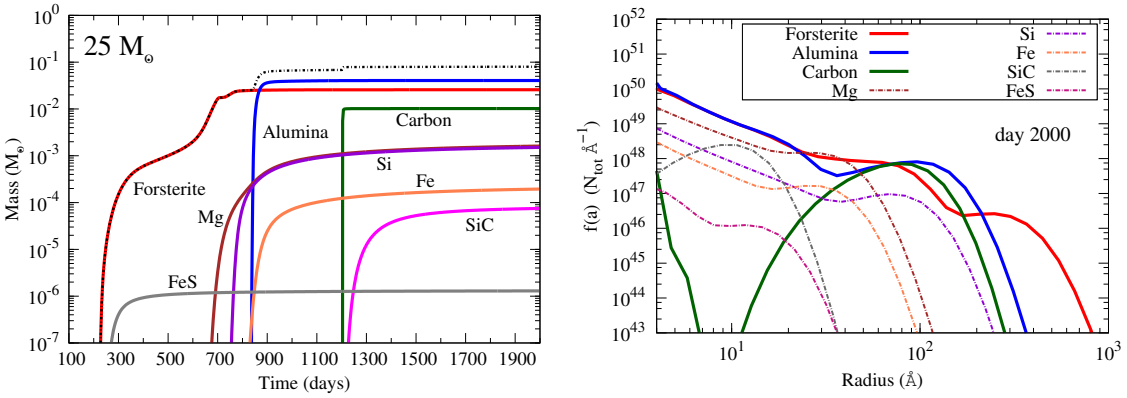

FIGURE 8.2: Results for the 25 $M_{\odot}$model **Left Panel:** The evolution of the dust masses for different dust components in the ejecta are presented summing over the contribution over all the zones. The dotted black line stands for the total dust mass. **Right Panel:** The grains size distribution functions $f(a)$ for all the dust components at day 2000 post-explosion are illustrated in the figure.

TABLE 8.5: 25 $M_{\odot}$ model: Masses ($M_{\odot}$) of different dust components at 2000 days post-explosion in the ejecta

Zones	Z1A	Z1B	Z2	Z3	Z4A	Z4B	Z5	Z6	Total
				25 $M_{\odot}$case					
Mass	0.23	0.18	0.47	2.72	0.53	0.89	0.96	0.23	6.2
Forsterite	-	4.6(-5)	1.8(-2)	7.6(-3)	2.4(-5)	7.7(-5)	2.1(-6)	-	2.6(-2)
Alumina	-	-	1.3(-3)	3.9(-2)	5.3(-5)	2.3(-4)	-	-	4.1(-2)
Carbon	-	-	-	-	-	-	1.0(-2)	-	1.0(-2)
Pure-Mg	-	-	-	1.6(-3)	-	-	-	-	1.6(-3)
Pure-Si	1.5(-3)	-	-	-	-	-	-	-	1.5(-3)
Pure-Fe	1.9(-4)	-	-	-	-	-	-	-	1.9(-4)
Silicon Carbide	-	-	-	-	-	-	7.5(-5)	-	7.5(-5)
Iron Sulphide	1.3(-6)	-	-	-	-	-	-	-	1.3(-6)
Total	1.7(-3)	4.6(-5)	1.9(-2)	4.8(-2)	7.7(-5)	3.1(-4)	1.0(-2)	0	0.080
Efficiency(%)	0.74	2.6(-2)	4.04	1.76	1.5(-2)	3.5(-2)	1.0	0	1.3

Table 8.3. The total mass of dust in the ejecta is 0.08 $M_{\odot}$ at day 2000 which is 1.3 % of the total ejected mass.

8.2.2 Grain sizes

Figure 8.2 (right-panel) shows the grains size distributions for each dust component at day 2000. The peak of the distribution functions are listed in Table 8.3. In case of grain sizes, the epoch of formation holds the key, as condensation is more efficient at high concentrations. In lights of that, forsterite, like any other model, forms the biggest grains in this case as well. The largest of the grains grow to sizes of the order of 0.1 μm whereas the distribution peaks at 250 Å. Alumina is the

next important component, which is made up of grains averaging between 100-300 Å. Amorphous carbon and pure silicon dust remains limited to modest sizes less than 200 Åin radius. All other components are formed in small proportion in mass and therefore form small grains. Also in the same analogy as other models, a MRN type power law distribution does not fit any of the derived size distribution functions.

9 Dust radiative transfer

Dust grains are efficient in absorbing and scattering UV, optical and near-infrared (IR) radiations, and re-emitting the absorbed energy in the mid-IR and submillimeter (submm) wavelengths. Only 1-4% of the ejected mass from the stellar explosion gets locked up in dust, as shown in the previous chapters. However, owing to its continuum opacities, dust is capable to dominate the radiation from a significant section of the electromagnetic spectrum. When the ejecta is probed in the IR or submm, thermal emission from dust dominates the spectral energy distribution (SED). Astronomers derive the SED's by studying the telescope data from several local supernovae. Thereafter, the masses and the epochs of formation can be estimated by fitting the SED continuum using the known properties of the possible dust components. Importantly, these estimates provide the boundary condition for our studies.

We derive the spectral energy distributions controlled by dust in a typical type II-P supernova ejecta. The dust properties (dust masses, grain sizes, relative abundances with time, etc.) derived from the model are used here to set up the necessary input conditions. Radiative transfer in dust requires multidimensional approach, and hence we have used the radiative transfer code MOCASSIN (described in Section 4.2) to derive the fluxes as function of wavelength. Pioneering works has been done with MOCASSIN to address the dust radiative transfer in local supernovae like SN1987A (Sugerman et al., 2006; Ercolano et al., 2007), SN2006bc (Gallagher et al., 2012), SN2007od (Andrews et al., 2010), SN2005af (Szalai and Vinkó, 2013) and few others. However this is the first time, the chemical kinetic model has been associated with radiative transfer. The study adopts a bottom-up strategy which aims to couple the chemically controlled dust synthesis

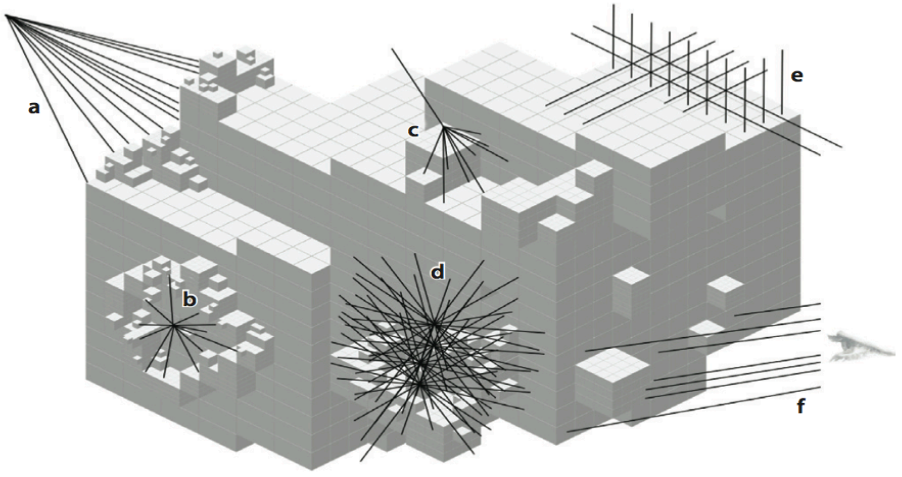

FIGURE 9.1: A schematic diagram for dust radiative transfer in a certain section of the ejecta (Steinacker et al., 2013). *a* represents the central heating source, *b* stands for radiation from the diffuse source, *c* is a scattering event by a certain dust grain, *d* presents the region inside the clump with optical depth near 1, *e* shows the course grid and *f* represents the re-emitted radiation towards the observer at infinity.

in the ejecta to the thermal emission by dust grains in the mid-IR and submm regimes. The radiative transfer phenomena is highly sensitive to the particular ejecta conditions. The simplistic 1D homogeneous model may not replicate a real supernova ejecta. Therefore, the results presented in this chapter using radiation transport, are still in the preliminary stage of the analysis. Figure 9.1 explains the radiative transfer phenomena in a certain section of the ejecta, which is numerically divided into cells. The following section will illustrate the physical parameters used as inputs for the model.

9.1 Modelling with MOCASSIN

MOCASSIN is a 3D Monte Carlo radiative transfer (RT) code capable to study the radiative transfer phenomena through a dusty medium. The specifications of the code is described in details in Section 4.2. The model is equipped to study radiations from both the a) smoothly varying dust density distribution b) clumpy distribution, where dust is concentrated in small regions in space and surrounded by almost empty interclump regions. As the central approach of the chemical kinetic model assumes homogeneous ejecta, we have only considered a uniform density variation profile to perform RT simulations. For the purpose of the study

we have used the dust-only RT mode which allows a multigrid resolution approach in order to enhance the spatial resolution. The radiation field is described by discrete monochromatic packets of energy (Abbott and Lucy, 1985) whose trajectories through the dusty medium is determined by the absorption, scattering and emission controlled by local opacities and emissivities. As considered for the kinetic model, the ejecta is considered symmetric, and therefore all the dust is present within a spherical shell. The energy conservation is ensured at each location, and all the energy packets are traced until they escape the shell (Ercolano et al., 2007). For the entire RT calculation, data from SN1987A is used as a reference to define the boundary conditions.

9.1.1 Important parameters

There are various input parameters which form the backbone of the model. Considering the study, as a continuation to the chemical kinetic model, most of the parameters at a given time are specified by the ejecta conditions. There are few others which are free to be varied within certain limits in order to attain a good fit with the observational data. The following is a short description of the input parameters defined in the study.

Diffuse source: After few days from explosion, the bolometric luminosity of the type II supernovae is maintained by radioactivity of ^{56}Ni. The γ-rays produced by the radioactive decay of ^{56}Ni is responsible for the heating of the ejecta through deposition of energy. A diffuse illuminating source of energy is assumed to be distributed in the ejecta, which surrogates the energy deposition by radioactivity. The diffuse source is considered to radiate as a blackbody, whose temperature is a free parameter, however bound by the near-IR SED obtained from observations. The luminosity of the diffuse source can varied within a limit, where the observed luminosities from SN1987A provides the reference (Bouchet and Danziger, 1993).

Dust composition: The dust composition is estimated directly from the obtained results of the chemical kinetic model. Dust composition includes 3 main parameters a) total dust mass b) relative contribution of each dust type c) the grain size distribution function, as functions of time. As mentioned earlier, forsterite, alumina and carbon are the only abundant species of dust in case of the homogeneous model (Sarangi and Cherchneff, 2014).

Dust opacities: In small grains where $\lambda > 2\pi a$ (a is the radius of a grain considered spherical), the opacities are maintained by the interaction between the dielectric properties of the dust material and the electromagnetic field of the incident or emergent radiation. In order to calculate the opacities as functions of wavelength, the laboratory measured values for the real and the imaginary parts of the complex refractive index are necessary. The standard n-k data sets are used to determine the optical constants for silicates (Ossenkopf et al., 1992), carbon (Zubko et al., 1996) and alumina (Begemann et al., 1997).

Inner shell-boundary R_{in}: The inner boundary of the shell is determined by the approximate distance the ejecta might have travelled at a given epoch. Considering a uniform velocity v, the inner shell radius at day d is given by $R_{in} = v \times (d \times 86400)$. Considering $v = 2300$ km/s as calculated for the ejecta model, the value of R_{in} at a given time, say, day 615 would be, $R_{in}(day\ 615) = 2300 \times 10^5 \times (615 \times 86400) = 1.2 \times 10^{16}$ cm. With a similar notion, the outer radius of the shell is calculated for all relevant epochs.

Outer shell-boundary R_{out}: To derive the outer shell boundary, the thickness of the shell ΔR needs to be estimated. The thickness ΔR is derived from the thickness of the ejecta and as it evolves. In general, the blue supergiant stars are smaller than the red supergiants and their typical radius does not exceed an order of 10^{13} cm. As the progenitor of SN1987A is estimated to be a blue supergiant, we consider at the time of explosion, the size of the envelope is of the same order. Post explosion, the ejecta undergoes mixing due to a velocity shear and finally starts to expand homologously after a few hours (explained in Section 2.2.3). As the density falls with an exponent of -3 of time, keeping the total mass intact, the volume correspondingly increases with an exponent of 3. Hence the radius scales linearly with time. Considering $\Delta R(d = 1) = 10^{13}$, then at day d, ΔR is equal to $d \times 10^{13}$. Therefore, $R_{out} = R_{in} + \Delta R = 1.2 \times 10^{16} + 615 \times 10^{13} = 1.82 \times 10^{16}$ cm (at day 615). Similarly the inner radius can be calculated for other epochs.

Density distribution: All the dust grains are considered to exist inside the spherical shell. In order to be consistent with the homogeneous ejecta model, we have chosen a smooth distribution of dust density, where density of dust varies with distance as $\rho \propto r^{-2}$. This might be an over simplification, as in reality the ejecta is stratified and different dust components dominate in different layers. In case of MOCASSIN however, the general assumption is that all the dust components is mixed inside the shell according to its relative proportion.

Grid structure: The ejecta has been considered to be spherically symmetric. Using the symmetry arguments only 1/8 of the total volume was computed (Ercolano et al., 2007). This positive domain of the geometric space was divided into 17^3 cells. We have tested by increasing the number of cells, and it does not seem to affect the sensitivity. The choice of total cells are therefore limited to control the computational time.

9.2 SN1987A data

The estimated fluxes are compared to the IR and the mid-IR observations of SN1987A. The epochs of observation used in the study correspond to day 615, day 775 (Wooden et al., 1993; Ercolano et al., 2007) and day 1157 (Dwek et al., 1992) observational data. There are recent observations of cool dust in 87A at submm by Herschel and ALMA telescopes (Matsuura et al., 2011; Indebetouw et al., 2014). Due to the lack of enough optical constants for all the dust components at λ >100 μm range, for the time we did not address the submm data with radiative transfer. One important aspect which is beyond the scope of the current analysis is the rate of cooling for the dust components. The solid grains, as it grows in size, also cool at a faster rate. As the synthesis of dust is a gradual phenomena, in reality all the dust may not be warm enough at a given epoch to emit in the mid-IR wavelengths. We have addressed this issue again while discussing the day 1157 case. In our study, the 15 and 19 $M_\odot$ progenitor models adopt the explosion energy and ^{56}Ni mass from the estimated values of 87A. In Chapter 7, while discussing a homogeneous and a clumpy model, we chose a lower initial homogeneous density in order to be consistent with Jerkstrand et al., 2011, whereas for the standard case initial gas densities are derived from Nozawa et al., 2010. In this analysis we have used an identical initial gas density of 1.1×10^{-11}g cm^{-3} (at day 100), which is same as the standard case for both the 15 and 19 $M_\odot$ model. The results for the 19 $M_\odot$ case are same as the one presented in Sarangi and Cherchneff, 2013. As because the ejecta conditions for the standard 15 $M_\odot$ and homogeneous 19 $M_\odot$ model are alike, and they only differ in initial element abundances, we have used both the models to fit the observed data from SN1987A. The homogeneous 19 $M_\odot$ model is termed as case I and the standard 15 $M_\odot$ model as case II in the following discussion. The ejecta of SN1987A has been taken to be at a distance of 50 kpc away from earth in order to estimate the fluxes.

TABLE 9.1: The input parameters used in the model with MOCASSIN are presented in this table. L_{diff} stands for the luminosity of the diffuse source with temperature T(BB). M_d is the total dust mass whose composition is given in the next three columns. For all the epochs, the corresponding grain size distribution functions derived from the chemical model have been used.

Epoch	L_{diff}	T(BB)	R_{in}	R_{out}	M_d	Silicates	Alumina	A-Carbon
(days)	($L_\odot$)	(K)	(AU)	(AU)	($M_\odot$)	(%)	(%)	(%)
Case I								
615	5.5(5)	8000	802	1211	7.7(-4)	99	1	–
775	1.6(5)	4000	1029	1564	5.4(-3)	95	5	–
1157	2.1(4)	2500	1590	2432	2.6(-2)	35	65	–
1157†	1.3(4)	2700	1590	2432	1.0(-3)	92	8	–
Case II								
615	7.3(5)	7000	802	1211	1.6(-3)	99	1	–
775	1.8(5)	5000	1029	1564	8.0(-3)	59	41	–
1157	4.7(4)	2200	1590	2432	3.5(-2)	18	21	61
1157†	4.7(4)	2500	1590	2432	2.1(-2)	2	3	95

†In the second case of day 1157, only the dust formed over last 150 days is considered to be warm enough to be detected (see text)

9.2.1 Day 615

The fitting of the observational data with the derived spectral energy distributions is shown in Figure 9.2 and the input parameters listed in Table 9.1. The values of R_{in} and R_{out} are calculated as explained before. The temperature of the diffuse source are generally determined by the near-IR data points, as it emits in the form a black body. The unattenuated energy contributes to the near-IR points whereas the data energy density for $\lambda > 5$ μ corresponds to the emission from dust. The SED's obtained from Case I and II are both matching well with the observational data points. At times prior to day 600, only silicates are formed in the ejecta as stable dust component. The grain sizes are also within small to modest limits. The luminosity of the diffuse source ranges between 5.5-7$\times10^5$ $L_\odot$ which is comparable to the observed value of 6.6$\times10^5$ $L_\odot$ from SN1987A by Bouchet and Danziger, 1993. The opacities of forsterite, alumina and carbon largely vary in the 2-20 μm window. As because carbon has a smooth extinction coefficient in the mid-IR regimes, many of the existing models (Ercolano et al., 2007; Gallagher et al., 2012) using MOCASSIN have assumed amorphous carbon or graphite as the only potential dust type. But from chemical kinetic calculations, it is shown that synthesis of amorphous carbon is controlled by the recombination of He^+, and therefore it gets delayed to a much a later time. Another important factor is the

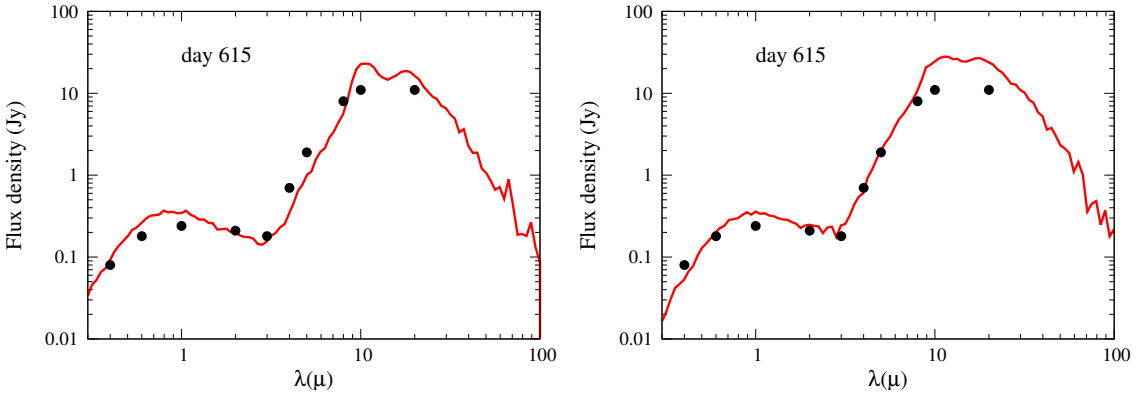

FIGURE 9.2: **Day 615** The derived SED's for Case I (left panel) and case II (right panel) using the ejecta conditions given in Table 9.1 is compared to the observations (filled circles) of SN1987A (Wooden et al., 1993). There are no error-bars on the observational points because the actual data was not accessible, and the points are derived from the figures given by Ercolano et al., 2007.

choice of R_{in} and R_{out}, which controls the dust densities, and therefore directly impacts the obtained SED's. Compared to other studies, the derived values for inner shell radius is larger whereas the shell thickness ΔR is much smaller.

9.2.2 Day 775

The observational data corresponding to day 775 of SN1987A (Wooden et al., 1993) is compared to the SED's derived from the model. Table 9.1 gives all the input conditions for case I and II at day 775 and the comparison is shown in Figure 9.3. The R_{in} and the ΔR, calculated with a similar notion as explained in the text above, are 1.54×10^{16} cm and 8.0×10^{15} cm respectively. In case I, all the dust is still in the form of silicates only, whereas in case II newly synthesised warm alumina dust makes up about 40% of the total, beside the rest being in silicates. In Figure 9.3, we see that both the 15 $M_\odot$ and 19 $M_\odot$ models well reproduce the observations, despite the models having different dust composition and grains sizes. The diffuse source luminosity and temperatures have decreased from day 615 to day 775, as expected.

9.2.3 Day 1157

The observational data points in the day 1150-1160 range of SN1987A are obtained from Dwek et al., 1992 and the point at 50 μm is obtained from Patrick Owen at

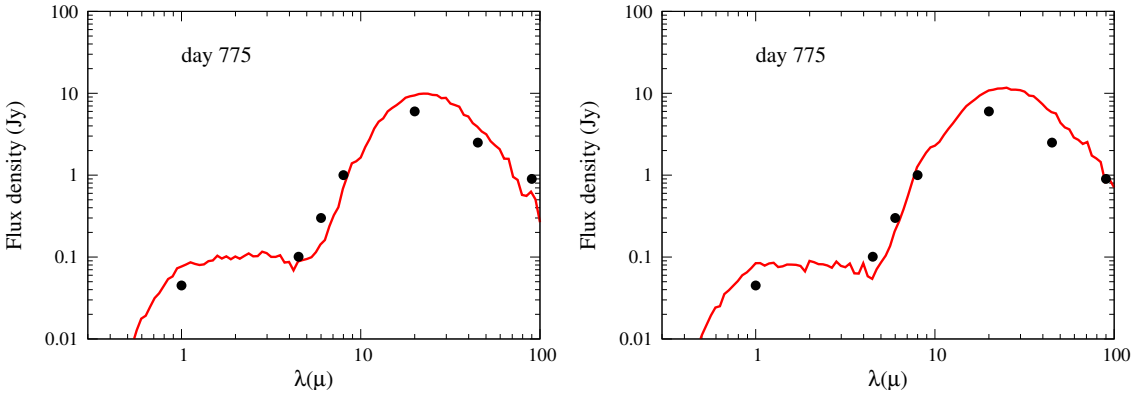

FIGURE 9.3: **Day 775** The derived SED's for Case I (left panel) and case II (right panel) using the ejecta conditions given in Table 9.1 is compared to the observations (filled circles) of SN1987A (Wooden et al., 1993). There are no error-bars on the observational points because the actual data was not accessible, and the points are derived from the figures given by Ercolano et al., 2007.

UCL through private communication. The Figure 9.4 presents the derived SED's and the observational points. The R_{in}, ΔR and the R_{out} are calculated with the same formulae and listed in Table 9.1 along with other parameters. From the figure it is evident that case I, corresponding to a 19 $M_{\odot}$ model, cannot provide a good fit to the observations, whereas the standard 15 $M_{\odot}$ model as case II can produce a moderately good agreement. The dust compositions differ between the two cases: the masses are 1.5 times larger in case II, which is dominated by newly formed carbon dust. The composition of case I is made up by 35% of silicates and 65 % of alumina, carbon grains is yet to form in the ejecta.

In reality, after the formation of dust grains, they efficiently radiate in the mid-IR and cool down in the process. The study does not take into account the necessary instruments to study the cooling rates. At days later to 1150, the gas temperature goes below 400K. Most of the silicates and alumina are formed in the range between day 500 to 900. Therefore, they possibly get sufficient time to get cool enough and escape mid-IR observations. As a test case, we consider that all the dust which formed earlier to day 1000 does not radiate in the mid-IR anymore. Under such an assumption, the dust mass of case I is only 10^{-3} $M_{\odot}$ with 92% of silicates and only 8% of alumina. On the other hand, in case II, which is the 15 $M_{\odot}$ standard model, warm carbon dust of mass 2.1×10^{-2} $M_{\odot}$ is formed around 1050 days, which controls the emission in mid-IR. Figure 9.5 shows the results for the test case. But it again clearly shows that case II fits the observations with a good match, whereas the SED from case I model does not reproduce the observations. Hence it can be generally concluded that carbon dust must formed

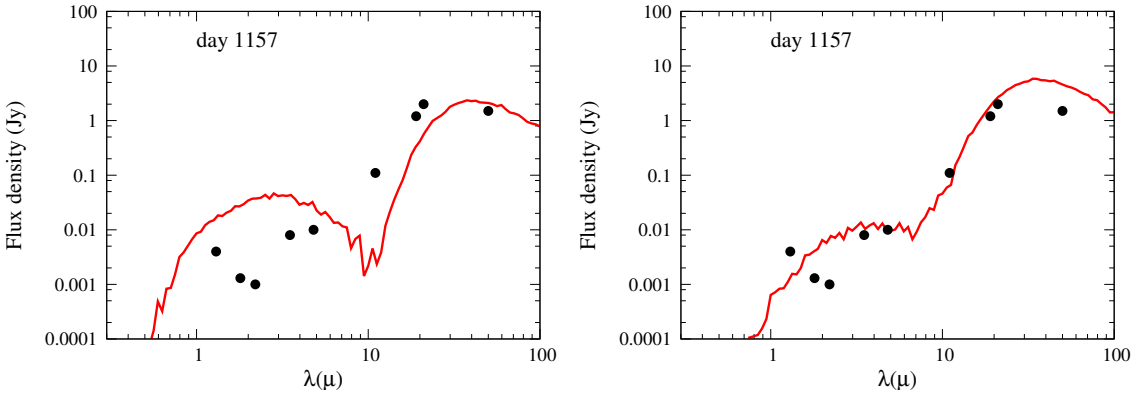

FIGURE 9.4: **Day 1157** The derived SED's for Case I (left panel) and case II (right panel) using the ejecta conditions given in Table 9.1 is compared to the observations (filled circles) of SN1987A (Dwek et al., 1992). There are no error-bars on the observational points because the actual data was not accessible. The points are derived from the figures given by Dwek et al., 1992 and with the help of Patrick Owen through private communication.

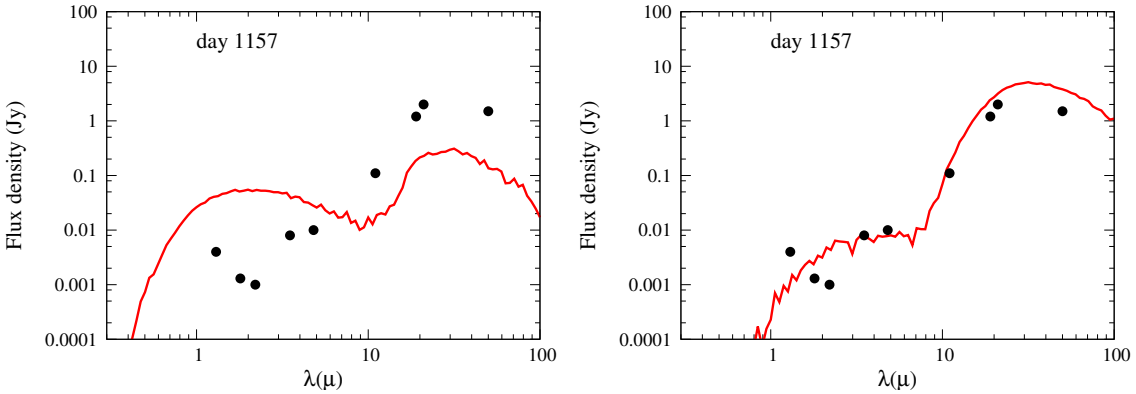

FIGURE 9.5: **Day 1157 (dust formed later than day 1000)** Considering all the grains formed before 1000 days have already cooled, and do not contribute to the mid-IR, the derived SED's for Case I (left panel) and case II (right panel) is compared to the observations (filled circles) of SN1987A (Dwek et al., 1992). The ejecta conditions are given in Table 9.1. There are no error-bars on the observational points because the actual data was not accessible. The points are derived from the figures given by Dwek et al., 1992 and with the help of Patrick Owen through private communication.

in the ejecta by day 1150. The main difference between the two results resides in the post-nucleosynthesis abundances derived from Rauscher et al., 2002, where the C/O in the outer zone of He-core is 21 for case II and only 4 in case I. On the other hand, in the clumpy case, the synthesis of carbon dust triggers around 900 days. Therefore, it should be a better candidate to fit the observations. The estimation of cooling rates require more attention in order to achieve a better fit.

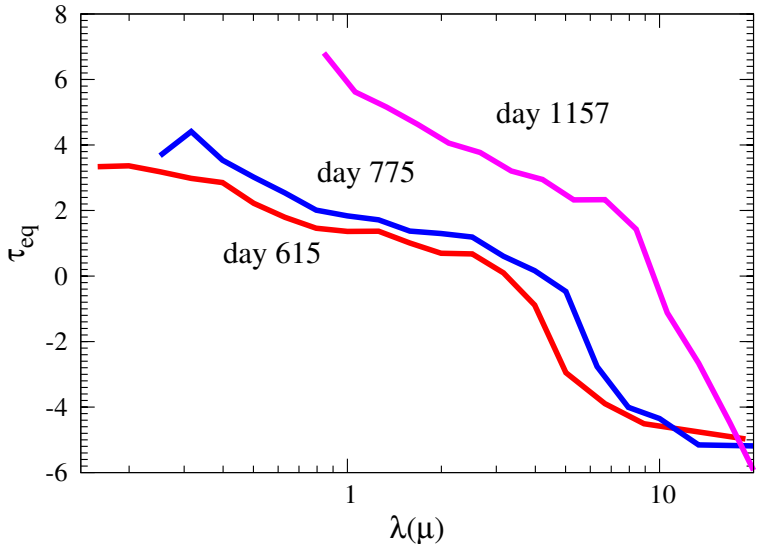

FIGURE 9.6: Effective optical depths at day 615, day 775 and day 1157 are calculated using Equation 9.1.

9.2.4 Effective optical depths

In case of the ejecta, the heating is controlled by sources distributed all over the ejecta, which is replicated as a diffuse source in the model. Under such assumption, the optical depth along the line of sight is not physically relevant. This is due to the fact that, photons emitted from different locations of the ejecta will encounter different opacities. An expression for effective optical τ_{eff} depth is derived by Ercolano et al., 2007 as Equation 9.1,

$$\tau_{eff} = ln\Big(\frac{F_\lambda^0}{F_\lambda}\Big), \tag{9.1}$$

where, F_λ^0 is the unattenuated flux at λ for the case where dust is not present, and F_λ is the emergent flux after interaction with the dust. The method is independent of the geometry. It also takes into account the effects of photon scattering by the dust grains, which increases their path lengths and thereby enhances the probability to get absorbed by dust. Figure 9.6 illustrates the effective optical depths of the ejecta as functions of wavelength at day 615, 775 and 1157. The effective optical depths become negative when the emergent flux is greater than the incident energy. This is the case at mid-IR wavelengths where dust emits efficiently, whereas the incident radiation is heavy in the visible and near-IR regimes. In the RT model, the radiation field is considered as monochromatic packets of energy. The trajectories of the photons are traced through the field. Therefore,

the estimated optical depths confirm that the obtained fluxes in the mid-IR, that are used to fit the observed SED's are indeed the contributions from dust emission. With the increase in time, the switch between positive to negative values of τ_{eff} shifts towards larger wavelengths, which is attributed to the diffuse source getting cooler with time.

10 Discussions & Inferences

We have presented exhaustive models of dust synthesis in various homogeneous and clumpy ejecta of Type II-P supernovae, where the gas-phase chemistry, including the formation of dust clusters (i.e., nucleation phase), is coupled to the coagulation and coalescence of these clusters into dust grains (i.e., condensation phase). In this chapter we intend to summarise our findings and drive the discussion towards concluding remarks. Besides that, we shall compare our studies with other existing models which focus on the study of dust in supernovae.

10.1 Summary of the results

In the introductory chapter, while discussing the motivation of the study, we emphasised the impact of *a*) Different main sequence masses of the progenitor stars *b*) Variation of ^{56}Ni mass produced by the explosion *c*) Degree of clumpiness and density variation. On the basis of that, we have focused on 6 different models of type II-P supernovae listed in Table 10.1. Our results suggest all three factors significantly influence the dust formation scenario in the ejecta. The final yields from each model are summarised in Table 10.2.

TABLE 10.1: The 6 different models we studied are numbered for the sake of easy reference, which have been mentioned as 'M' in the following discussion.

Model 1: 15 $M_\odot$ ^{56}Ni = 0.075 $M_\odot$, homogeneous	Model 2: 15 $M_\odot$ ^{56}Ni = 0.01 $M_\odot$, homogeneous
Model 3: 19 $M_\odot$ ^{56}Ni = 0.075 $M_\odot$, homogeneous	Model 4: 19 $M_\odot$ ^{56}Ni = 0.075 $M_\odot$, clumpy
Model 5: 12 $M_\odot$ ^{56}Ni = 0.01 $M_\odot$, homogeneous	Model 6: 25 $M_\odot$ ^{56}Ni = 0.20 $M_\odot$, homogeneous

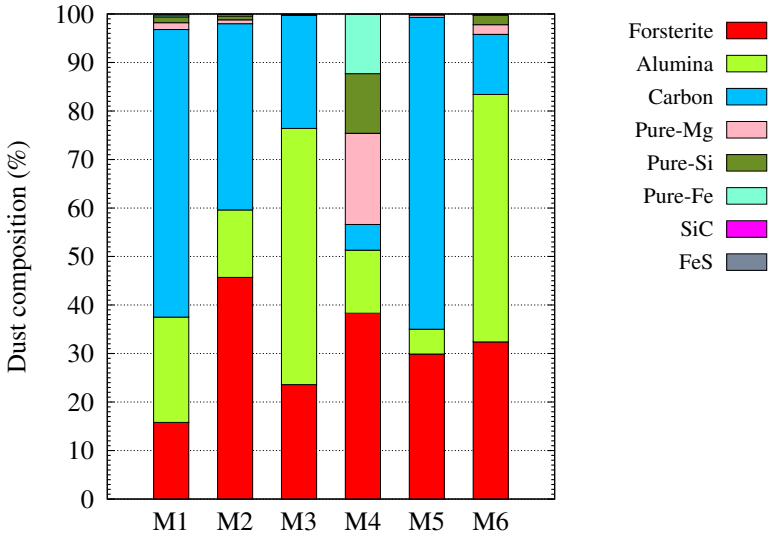

FIGURE 10.1: The relative proportion (in %) of various dust components in the ejecta as functions of different models are presented.

Progenitor mass: A difference in progenitor masses result in variations of post-explosion yields. This directly impacts the composition of dust. Two factors which can be generalised in this place is a) final mass of carbon dust depends solely on the C/O ratio of the outer zone b) more massive the progenitor is, the relative abundances of O-rich dusts go up. This can be confirmed from Figure 10.1, where the percentage contribution of each dust type is shown. Importantly, a larger progenitor essentially implies a larger O-core, whereas the mass of the other zones remain comparable (Rauscher et al., 2002). For example, in the 12 $M_{\odot}$ model, the O-core is about 0.4 $M_{\odot}$ and on the other hand in the 25 $M_{\odot}$ case it is as large as 3.4 $M_{\odot}$. The impact of C/O ratio can be inferred from the contrast shown by the 19 $M_{\odot}$ model. In this case, the C/O ratio in the outer zone is ~ 3.9, a value much smaller then its other counterparts. This is directly reflected in the final yield of amorphous carbon, which remains limited to a modest mass of $7{\times}10^{-3}$ $M_{\odot}$ only.

Amount of ^{56}Ni: A small ^{56}Ni mass favours the synthesis of dust at early post-explosion time in the various ejecta zones predominantly forming silicates, metal oxide, and carbon. Therefore, the early synthesis of dust is expected in low-mass progenitors, as for example, in SN2003gd. For this Type II-P supernova, a red supergiant progenitor with a small mass was confirmed ($\sim 8^{+4}_{-2}$ $M_{\odot}$), and a mid-IR excess, along with asymmetric blue-shifted emission lines and an increase in optical extinction were observed as evidence for dust formation in the ejecta as early as day 250 (Hendry et al., 2005; Sugerman et al., 2006). Conversely a larger mass of ^{56}Ni resulting from a more powerful explosion puts a check on the rapid formation

TABLE 10.2: The summary of final dust masses of each component from all model are listed. The masses correspond to 2000 days post-explosion (Sarangi and Cherchneff, 2014).

Dust	M1	M2	M3	M4	M5	M6
Forsterite	5.6(-3)	2.5(-2)	7.6(-3)	5.3(-2)	1.3(-2)	2.6(-2)
Alumina	7.7(-3)	7.6(-3)	1.7(-2)	1.8(-2)	2.2(-3)	4.1(-2)
Carbon	2.1(-2)	2.1(-2)	7.5(-3)	7.3(-3)	2.8(-2)	1.0(-2)
Pure Mg	5.0(-4)	4.2(-4)	1.8(-5)	2.6(-2)	2.2(-4)	1.6(-3)
Pure Si	4.4(-4)	4.4(-4)	6.2(-5)	1.7(-2)	7.4(-5)	1.5(-3)
Pure Fe	1.4(-4)	1.4(-4)	3.0(-5)	1.7(-2)	2.0(-5)	1.9(-4)
Silicon carbide	3.4(-5)	8.8(-5)	4.1(-6)	1.7(-5)	9.0(-7)	7.5(-5)
Iron sulphide	1.8(-6)	2.8(-6)	9.4(-8)	1.1(-4)	5.6(-8)	1.3(-6)
Total	3.5(-2)	5.5(-2)	3.2(-2)	1.4(-1)	4.4(-2)	8.0(-2)

of dust in the ejecta. Importantly though, a high ^{56}Ni production is generally associated with more massive progenitors. Higher the mass of the progenitor star, more is the number of particles present in the gas. Therefore, the energy deposited by the γ-rays and Compton electrons (produced from radioactive ^{56}Ni) get distributed among a larger population of atoms and molecules. This factor balances the destructive activities due to ^{56}Ni to some extent.

Degree of clumpiness: The dependence on gas density is even stronger and is well illustrated by our clumpy ejecta case. A clumpy ejecta favours the dust formation in all ejecta zones at early times, and result in several population of large grains a few years after explosion. Indeed, dust forms in the dense ejecta zones, and the early-formed grains have then time to grow to fairly large grains in the ejecta. A large fraction of these large grains will survive the non-thermal sputtering induced by the reverse shock, sheltered in the dense ejecta clumps, and the thermal sputtering in the hot, inter-clump medium once the clumps are disrupted during the remnant phase (Biscaro and Cherchneff, 2014). Some graphite and silicate pre-solar grains found in meteorites have a supernova origin (Zinner, 2007; Hoppe, 2010). According to the present results, they may be identified as the largest grains of silicates and carbon that form in the dense ejecta clumps of Type II-P supernovae. The grain size distributions are overall controlled by the concentration of monomers from the gas phase. An early formation of such precursors induces the condensation at high concentrations. This is why, the forsterite grains, which appears earliest in the ejecta, form the largest grains in all the models, in spite of being not the most abundant dust component. Figure 10.2 presents the overall grain size distributions from all the models. However, a quantity like overall grain

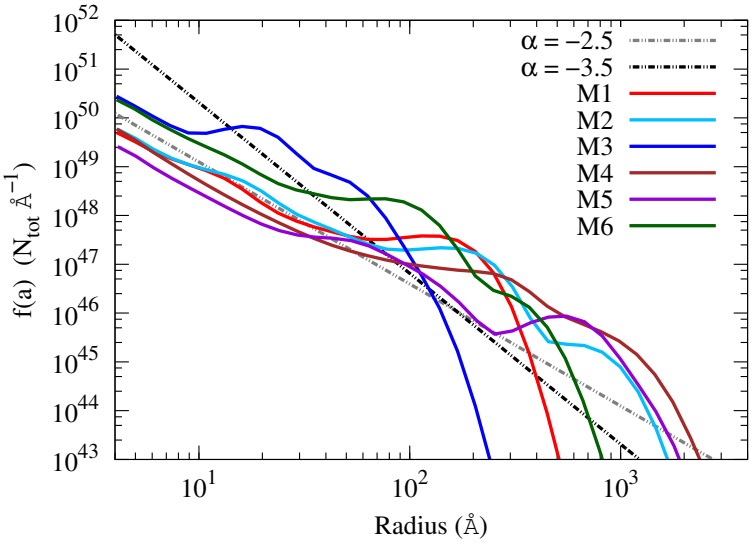

FIGURE 10.2: The overall grain size distribution functions are presented for each model. They are compared to the power law distributions with exponent α= -3.5 (MRN), -2.5.

size distribution should preferably be avoided, as the large grains are discrete particles, and each components have their characteristic sizes. Therefore, it is more physically justified to define the grain size distribution functions of each component separately.

Most important is the fact that grains respond differently to gas density enhancement. Silicate dust production is extremely dependent on gas density because the nucleation phase of this type of grains is characterised by complex chemical pathways, which are density-dependent. The nucleation phase thus controls the final amount of silicate dust mass that forms in the supernova explosion, as shown by Sarangi and Cherchneff, 2013. Other tracers of density increase in the ejecta of Type II-P supernovae are pure metal dust, such as silicon, magnesium, and iron grains, and new molecules that only form with large abundance and mass in the clumpy ejecta, i.e., CO_2. Conversely, the production of alumina and carbon is not too responsive to density increase and is limited by the availability of atomic carbon and aluminium in the ejecta zones where these specific dust grains form. For example, atomic carbon is essentially depleted in CO molecules, which primarily form in the oxygen-rich zone labelled 4, and carbon is dust produced in the outermost, C-rich zone 5. The efficiency at forming carbon dust depends on the C/O ratio of this ejecta zone. For the 15 $M_\odot$ progenitor, the C/O ratio of zone 5 is high ($\sim$ 21), and thus 78 % of the carbon mass yield gets into carbon dust while $\sim$ 20 % stay in the form of carbon chains in the gas phase. For the 19 $M_\odot$ progenitor,

the C/O is small ($\sim$ 4), and only 58 % of the initial carbon mass yield gets into grains for both homogeneous and clumpy ejecta. The final mass of carbon dust formed in Type II-P supernova ejecta is thus limited by the carbon mass yield of the outermost, carbon-rich, ejecta zone, and not by the total carbon yield of the ejected material, as it is often assumed (e.g., Matsuura et al., 2011). Although carbon is one important component of supernova dust $\sim$ 5 years post-outburst, silicates, alumina, and pure metals are also important dust components. Hence, the analysis of the submm flux emitted by cool, thermal dust in remnants must consider these various dust components as a whole to properly assess the mass of dust formed in the ejecta.

Late time evolution: The possibility of new formation of grains or their growth at late times (t > 5 years) in the ejecta should be addressed. The formation of new grains in the expending ejecta after $\sim$ 5 years is hampered by the shortage of the chemical agents responsible of the first nucleation step, i.e., SiO or C_2, which are depleted in the ejecta between 300 and 2000 days depending on the progenitor mass. The growth of existing dust grains via accretion of abundant atoms or molecules like atomic C, Mg, Si, or O_2 on the grain surface will happen on a time scale given by $\tau_{ac} = 1/(n_d \times \sigma_d \times v \times S(T, T_d))$ where n_d, σ_d, and T_d are the number density, the collision cross section, and the temperature of the grains. v and T are the thermal velocity and temperature of the gas and $S(T, T_d)$ is the sticking coefficient. For typical grain size (0.1 μm) and ejecta gas conditions at day 2000 ($n = 10^6$ cm^{-3} and $T = 400$ K), the sticking coefficient is $\sim$ 0.5, and the estimated accretion time τ_{ac} is $\sim 10^4$ years. This time scale exceeds the nebular phase and the remnant adiabatic phase, and by that time, the ejecta will have been reprocessed by the reverse shock in the remnant. Therefore, late grain growth cannot proceed due to the very long accretion time required to add mass to the grains, and the dust observed in supernovae and remnants has formed in the ejecta before $\sim$ 5 years post-outburst.

Overall dust budget: Finally, the synthesis of dust in Type II-P is a multi-parameter-dependent process. To illustrate this point, our total modelled dust masses for various progenitors, the dust masses derived from mid-IR observation of several Type II-P supernovae, and the dust masses assessed from submm data of remnants are plotted in Figure 10.3. The dust masses derived before day 1000 from mid-IR data span a large value range comprised between 10^{-6} M$_\odot$ and 10^{-2} M$_\odot$. This large spread in dust masses reflects the difference in progenitor mass,

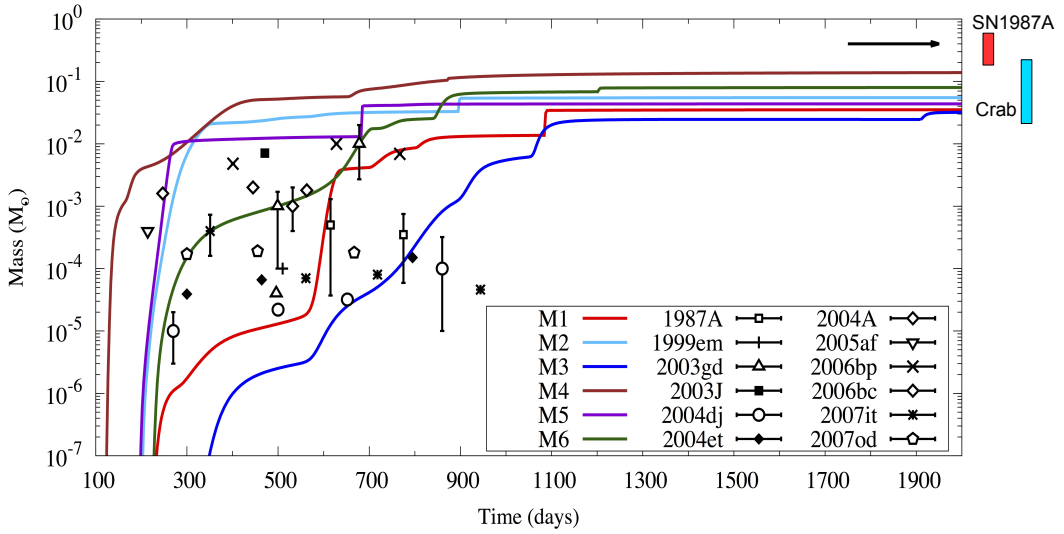

FIGURE 10.3: The evolution of total dust masses in the ejecta for different models are presented as functions of post-explosion time. The masses estimated from the mid-IR observations of local type II-P supernovae are shown in the figure. The dust masses derived from young remnants SN1987A and the Crab Nebula is given in the outside margin of the figure. The masses of dust for the local supernovae shown in this figure are given in Chapter 1 Table 1.2 along with the respective references.

the likely presence of ejecta clumps, the chemical composition of the dust that forms, and the grain size distributions. Our modelled dust mass values for various progenitors, ^{56}Ni mass, and clumpy/non clumpy ejecta models well reproduce this large range of dust masses, and point to the fact that dust synthesis in supernovae depends on several parameters, and cannot be described by assuming a simple dust composition and size distribution. As already pointed out by Sarangi and Cherchneff, 2013, our results indicate a gradual increase of dust production over a timespan of $\sim$ 5 years after explosion, to reach dust mass values in the range $0.03 - 0.14$ M$_\odot$. This value range agrees well with the latest submm dust masses obtained from Herschel and ALMA data for SN1987A and other remnants. As mentioned before, if the dust forms in dense clumps and survive the remnant phase sheltered in these clumps, our clumpy model indicates that Type II-P supernovae may be important contributors to the dust budget of local galaxies.

Fate after reprocessing: The dust grains formed in the ejecta in first few years after explosion, retain their form until they are reprocessed by the reverse shock in the remnant phase. The fate of the dust grains in the reverse shock is analysed by my colleague Chiara Biscaro. The dust undergoes thermal and non-thermal sputtering for a prolonged span of time ($\sim$ 4000 yrs) which leads to erosion of the

TABLE 10.3: The probability of survival (% of the mass) of the dust grains after 4000 years of sputtering are listed as functions of shock-induced temperatures. In case of smooth ejecta, both thermal and non-thermal sputtering is estimated. In the clumpy model only thermal sputtering is assumed, as non-thermal sputtering is negligible in high post-shock gas densities (PhD thesis: Chiara Biscaro) (Biscaro et al., 2014).

T (K)	Forsterite		Alumina	Carbon	SiC
	Smooth	Clumpy	Smooth	Smooth	Smooth
1×10^6	8.9	99.7	47.6	92.1	65.9
1×10^7	0.4	96.4	24.1	85	11.5
3×10^7	0	93	9.4	82.6	3.7
1×10^8	0	89.1	2.1	82.5	2.4

grains. The degree of erosion depends on the velocity of the shock, the shock-induced temperatures, and the mean molecular weight of the ambient gas. Using the pre-shock grain size distributions obtained from this analysis, the chances of survival is estimated. Table 10.3 shows the percentages of different grains that have survived 4000 years of sputtering in a homogeneous as well as clumpy ejecta case (Biscaro et al., 2014) at different shock-induced temperatures. In general larger grains have more changes to survive the eroding phase. Silicates are most vulnerable to shocks. But on the other hand they also are the largest grains in the ejecta. The table shows that the probability of survival of forsterite drastically increase from a homogeneous to a clumpy case. The relatively small grains of forsterite in the smooth ejecta model hardly survive the effect of the sputtering. However, the larger grains of $\sim$ 0.1-1 μm order formed in the clumpy case are resilient to the passage of shock. The C-rich dust grains are more likely to survive at any case. More than 90% of these grains survive the sputtering phases even in a homogeneous model.

Summary of molecules: A large fraction of the material expelled in a supernova event is in molecular form ($\sim$ 20-30 %) with a chemical composition including SiS, CO, O_2, and SO, depending on zoning. These four chemical species will pervade the late stages of supernova evolution, i.e., the supernova remnant not yet hit by the reverse shock. Evidence for molecules in remnants was brought by the detection of the first overtone transition of CO in the young remnant Cas A (Rho et al., 2009). The fundamental band at 4.56 μm was subsequently observed with AKARI (Rho et al., 2012). Our results strongly suggest that a large fraction of cool CO ($\sim$ 0.1 $M_\odot$) formed in the ejecta should pervade the remnant gas not yet shocked by the reverse shock and thus be detectable. Most interesting are the large

masses of SiS ($0.04 - 0.1$ $M_{\odot}$) formed in the innermost zone of supernova ejecta. Emission line analysis in supernova remnants suggest the remnant has retained some memory of the ejecta stratification due to nucleosynthesis and consistent with explosion models (Chevalier and Kirshner, 1978; Fesen et al., 2006; DeLaney et al., 2010; Isensee et al., 2012; Ghavamian et al., 2012). If so, SiS molecules should exist in Cas A and other supernovae remnants in sulphur, silicon, and calcium-rich fast moving knots, and possibly be detectable there at submm wavelengths. The present results on molecules may put constraint on the physical parameters of the ejecta. The formation of SiO dimers is a good example. The SiO dimer formation rate is gas pressure-dependent and usually very low at the low pressure encountered in the ejecta before day 400. When the SiO dimerisation rate derived by Zachariah and Tsang, 1993 is used for the ejecta pressure, SiO and subsequent forsterite dimer formation is postponed to late epochs (t > 700 days) as shown by Cherchneff and Dwek, 2010. In the present models, the SiO dimerisation rate has been increased to account for the density enhancement found in clumps, and the match between SiO observational data and modelled masses was satisfactory. We conclude that the observed SiO line fading and the timing for dust condensation are thus indirect indicators of the clumpy nature of supernova ejecta.

10.2 Comparison with existing studies

The dust formation in a supernova ejecta has been tackled from different point of views over the past couple of decades. In context of our study, we shall now compare the formalisms and the outcomes from various other existing models. Depending on the objectives of these models, we have split the comparative study into three subsections.

10.2.1 Gas phase chemistry and dust masses

Following the observations in SN1987A, attempt to model the synthesis of grains in SN1987A was carried out by Kozasa et al., 1989. More general studies later dealt with the formation of dust in Type II-P supernovae locally (Bianchi and Schneider, 2007) and at high redshift (Todini and Ferrara, 2001; Nozawa et al., 2003). All these studies consider the formation of dust grains from the gas phase using classical nucleation theory (CNT). Some assume a fully-mixed ejecta (Todini

TABLE 10.4: Dust mass estimated by existing dust formation models for metallicity Z = Z_{solar} and Z = 0 (Table adapted from Sarangi and Cherchneff, 2013; Cherchneff, 2013a) is compared with the results from this study. ([a]Chemical kinetic model)

Model	Z	Fully Mixed or Unmixed	Progenitor Mass	Total Dust Mass
Kozasa et al. (1989)	Solar	FM	19 $M_\odot$	–
	Solar	U	19 $M_\odot$	–
Kozasa et al. (2009)	Solar	U	15 $M_\odot$	0.33 $M_\odot$
	Solar	U	20 $M_\odot$	0.68 $M_\odot$
Todini and Ferrara (2001)	Solar	FM	12 $M_\odot$	0.20 $M_\odot$
	Solar	FM	15 $M_\odot$	0.45 $M_\odot$
	Solar	FM	20 $M_\odot$	0.70 $M_\odot$
	Solar	FM	25 $M_\odot$	1.00 $M_\odot$
	0	FM	15 $M_\odot$	0.45 $M_\odot$
	0	FM	20 $M_\odot$	0.08 $M_\odot$
	0	FM	25 $M_\odot$	0.08 $M_\odot$
Nozawa et al. (2003)	0	FM	20 $M_\odot$	0.73 $M_\odot$
	0	U	20 $M_\odot$	0.57 $M_\odot$
Bianchi and Schneider (2007)	Solar	FM	12 $M_\odot$	0.12 $M_\odot$
	Solar	FM	15 $M_\odot$	0.28 $M_\odot$
	Solar	FM	20 $M_\odot$	0.40 $M_\odot$
	Solar	FM	25 $M_\odot$	0.62 $M_\odot$
Cherchneff and Dwek (2010) [a]	0	FM	20 $M_\odot$	0.16 $M_\odot$
	0	U	20 $M_\odot$	0.10 $M_\odot$
This study [a]	Solar	U	M1(15 $M_\odot$)	0.035 $M_\odot$
Sarangi and Cherchneff (2013)	Solar	U	M2(15 $M_\odot$)	0.055 $M_\odot$
Sarangi and Cherchneff (2014)	Solar	U	M3(19 $M_\odot$)	0.032 $M_\odot$
	Solar	U	M4(19 $M_\odot$)	0.138 $M_\odot$
	Solar	U	M5(12 $M_\odot$)	0.044 $M_\odot$
	Solar	U	M6(25 $M_\odot$)	0.080 $M_\odot$

and Ferrara, 2001; Bianchi and Schneider, 2007) on the other hand others consider stratified ejecta (Kozasa et al., 1989; Nozawa et al., 2003; Kozasa et al., 2009). A few of these models consider the impact of the steady-state formation of CO and SiO from the gas phase, including the destruction of CO by Compton electrons, on the final carbon and silicate dust mass (Todini and Ferrara, 2001; Bianchi and Schneider, 2007). This assumption gives rise to the formation of carbon dust in a fully mixed ejecta with a C/O ratio less than 1, a result in contrast with Kozasa et al., 1989. The progenitor masses, metallicity, the physical form of the ejecta considered in these models are listed in Table 10.4 with the corresponding dust mass yields. However, the justification of using CNT based approach to model the ejecta has been questioned by Donn and Nuth, 1985.

CNT-derived dust masses for solar metallicity ejecta have values higher by a factor of 5-10 compared to the upper limits on dust mass derived in this study. This discrepancy follows from several assumptions made. Firstly, the models (Todini and Ferrara, 2001; Bianchi and Schneider, 2007) consider a fully-mixed ejecta which is not confirmed by explosion hydrodynamic models (Hammer et al., 2010), and observations of remnants which point to the memory of nucleosynthesis layers within the remnant, e.g., Cas A (Isensee et al., 2012). Because the dust mass is derived from elemental yields and chemistry is not considered, fully-mixed ejecta always produce more dust. Secondly, in unmixed models, CNT is applied for steady-state conditions which are usually not found in dynamic environments out of equilibrium (Cherchneff and Dwek, 2009). Finally, all CNT-based models ignore the non-equilibrium chemistry related to the formation of molecules and dust clusters, and the specific physics of ejecta where radioactivity greatly impacts the gas-phase chemistry through Compton electron ionisation. The CNT approach includes the quantities like specific surface energy, sticking coefficient, supersaturation ratio, partial vapour pressure, critical clusters, etc., in analysing the dust formation scenario. However, the critical clusters sizes are of molecular dimensions, and application of the bulk properties like surface energy or sticking coefficient on such small particles is not appropriate. In CNT-studies, the condensation sequence is based on assuming condensation temperatures at equilibrium as guidelines. In the present study, the dust condensation sequences ensue from chemical kinetics and thus depend on ejecta parameters like the initial post-explosion elemental yields, the mass of ^{56}Ni produced, and the gas temperature and density. This is well illustrated by the 15, 19, and 25 $M_{\odot}$ for which silicate clusters form before the molecule AlO, when alumina, Al_2O_3, is supposed to be the first skid to condense in O-rich environments at thermodynamic equilibrium (Tielens et al., 1998). Here, alumina production is preceded by that of forsterite because of the early destruction of AlO molecules by Ne^+ ions in the gas.

More generally, previous studies based on CNT over-estimate the total dust mass formed in ejecta. Dust formation sequences assuming thermodynamic equilibrium are very commonly used as benchmarks in the modelling of dust synthesis in O-rich evolved stellar media, but should be avoided when modelling stellar outflows and ejecta, where dynamics and chemistry control the synthesis of condensates.

10.2.2 The grain sizes

As a common practice, the conventional MRN distribution (Mathis et al., 1977) with a power law profile of index $\alpha = -3.5$ is often used in case of supernova ejecta. However the distribution function is characteristic to the interstellar medium and does not represent the scenario of the newly synthesised dust in SNe ejecta. The comparison between the estimated grain size profiles in the current study and the power-law distribution ($\alpha = -3.5, -2.5$) is presented in Figure 10.2. The $\alpha = -2.5$ distribution agrees partially with the obtained results for grains smaller than 20 Å. Nevertheless the two distributions (power law vs model) differ the most around the peak of the obtained grain size profiles which lie between 100 to 500 Å. Derived $f(a)$'s are roughly two orders of magnitude larger compared to the MRN profile around 300 Å. Importantly though, each dust component has its characteristic distribution profile which evolves with time. Neither they can be generalised by any power law distribution, nor do they match with one another at a given time. Therefore, for the sake of future analyses it is recommended to use separate, kinetically derived distributions for each component. The size distribution functions are used as an input tool to model the fluxes in SNe ejecta. Moreover they provide the insight to study the dust survival and destruction scenario during the passage of shock.

Some existing studies have focused on the grain size distributions in supernova ejecta with different approaches. The non-steady state dust formation scenario for carbon and silicates has also been addressed by Nozawa and Kozasa, 2013, without tackling the gas phase chemistry. An initial gas phase concentration of the monomers of carbon and silicates (10^6-10^7 cm^{-3}) are assumed. The growth of grains proceed via accretion using CNT. The monomers molecules such as $MgSiO_3$ and C atoms are considered as precursors to dust formation. However in our case, the synthesis of gas-phase precursors is a continuous process, which proceeds in parallel to the condensation of grains. The precursor seeds are synthesised from complex nucleation network, and they are proved to be resilient against the probable destruction routes in the ejecta. The average grain sizes estimated thorough both the analysis are of the order of 400 Å. However the epochs of dust synthesis and hence the temperatures are very different. Early formation of carbon dust at high temperatures ($\sim$2000 K) is the result of an assumption of initial high monomer concentration. We find low temperature condensation of carbon dust due to late synthesis of gas-phase precursors.

TABLE 10.5: A comparison between the input parameters used by Ercolano et al., 2007 (ERC07) smooth case and this study in order to model the 615 and 775 day SED of SN1987A.

	ERC07	This study	ERC07	This study
	615		775	
Mass ($M_{\odot}$)	2(-4)	1.6(-3)	3(-4)	8.0(-3)
Composition	AC	Sil	AC	Sil(59)/Al(41)
R_{in} (AU)	334	802	381	1029
R_{out}(AU)	2338	1211	2667	1564

10.2.3 Estimation of fluxes

Fitting the SED's derived from observations is an integral part of any study related to cosmic dust. Generally two approaches are popularly used a) modified black body fit (Gomez et al., 2012b; Szalai and Vinkó, 2013; Temim and Dwek, 2013) b) radiative transfer modelling (Gallagher et al., 2012; Ercolano et al., 2007; Andrews et al., 2010). In the first case dust composition, a maximum and minimum grain size and dust temperatures are assumed. For radiative transfer modelling, dust composition, grain size distributions, grain densities in the ejecta cells and the dimensions of the ejecta are necessary inputs. Some of the models consider a homogeneous ejecta (Szalai and Vinkó, 2013; Andrews et al., 2010) while others also use clumpy distribution of dust (Ercolano et al., 2007; Gallagher et al., 2012). However, all these existing models are fitting models where initial input conditions are assumed to achieve a best fit. Amorphous carbon or graphite is the most widely considered dust component, and the grains are assumed to follow MRN distributions. The silicate feature is identified in SN2004et (Kotak et al., 2009) using a black body type emission profile from newly synthesised dust.

In our study we primarily focus on the precise estimation of input conditions prior to comparing the fluxes with the obtained SED's. The dust components are estimated from the chemical model, grain size distribution function from the condensation scheme, the dimensions of the dusty ejecta shell is calculated from the known physical conditions of the ejecta as explained in Chapter 9. In the study, a homogeneous distribution of dust is considered, and the works related to radiative transfer in clumpy model is in progress. The major difference with previous models is that, all the input parameters in this study are calculated according to the ejecta conditions specific to each case. The dust composition is essentially made up of silicates or silicate+alumina. Owing to the delayed synthesis of carbon dust, it hardly can contribute to the mid-IR SED prior to 1000 days.

The analysis indicates that the thickness of the ejecta shell and its distance from the initial position of star (defined as ΔR & R_{in}) can heavily impact the output fluxes, which has not been seriously considered in the previous models. Table 10.5 shows the comparison between the SN1987A models of Ercolano et al., 2007 and this study. The results imply that, with a completely different composition of dust and masses a factor 10-30 higher, the final SED can also be fitted with good agreement. This points towards the large uncertainty of dust masses that is estimated from observed SED's of known supernovae.

10.3 Concluding remarks

Finally now we have arrived at the end of the discussion. Here we list up the overall remarks that can be generalised from the entire study.

(a) About 30-40 % of the ejecta remains in molecular form after day 2000 from explosion. The main molecular constituents are CO, SiS, O_2 and SO.

(b) The total mass of dust is about 1-5 % of the mass of the He-core. The final masses vary between 0.03 to 0.14 $M_\odot$ depending on the input conditions.

(c) Dust formation spans between $\sim$ day 300 to about day 1500 post-explosion. The gradual build up of dust from 10^{-6} to $\sim$ 0.05 $M_\odot$ in a few years suports the observational trends derived from the mid-IR and submm observations.

(d) The molecular clusters resulting from nucleation determines the chemical composition of the dust and the epochs of dust formation.

(e) Dust formation proceeds via concurrent phases of nucleation and condensation. The condensation is an efficient process as about 99% of the nucleation phase end-products end up in dust.

(f) Dust masses are unlikely to increase at late times ($>$ 5 years post-explosion). This is firstly because of the scarcity of gas phase precursors initiating the process, and secondly as the accretion time scales are too long compared to the evolution phase of the ejecta.

(g) The three main dust components dominating the dust budget are silicates, alumina and amorphous carbon. Pure metal clusters become important if clumps and high density are considered.

(h) Molecules such as SiO and AlO get depleted in dust and act as tracers to O-rich dust components. Conversely, the synthesis of CO molecules and amorphous carbon dust are non-correlated.

(i) Supernovae with homogeneous ejecta form moderate size grains of average radius around 100-300 Å. A small population of the grains attains a size $\sim$ 0.1 μm. However, dust condensation in a clumpy ejecta leads to large grains of more than 1 μm order.

(j) Dust masses and grain sizes are inversely related to the amount of radioactive ^{56}Ni produced at the time of explosion. On the other hand, they are directly proportional to the degree of clumpiness.

(k) Relative abundances of C-rich and O-rich dust depend on the mass of the progenitor. The larger the progenitor, the larger is the O-core, and therefore O-rich dust dominates over other components.

(l) The grain size distributions are functions of dust type and epochs of formation. They cannot be generalised as power laws of any exponent.

(m) The dust radiative transfer modelling is highly sensitive to the choice of the dimension of the dusty shell. All the boundary conditions should be derived from the physical conditions of the ejecta.

(n) A clumpy ejecta of a type II-P supernova forms large grains most of which are likely to survive the reverse shock. Therefore, supernovae are efficient yet moderate dust producers in the galaxies.

10.4 Further work

There are several aspects of the study which requires further attention. In this analysis we have addressed the ejecta using a 1D stratified homogeneous model (and by a density enhanced clumpy model). In doing so, we oversimplify certain physical conditions which should now be tackled with more care. Our results cannot explain the elemental mixing between ejecta zones derived from the isotopic ratio analysis of these pre-solar grains, because our models use stratified ejecta with no leakage between zones. Clues on elemental mixing from different ejecta zones may be provided by 3D simulations of supernova explosion from which the chemical composition of clumps are derived a few hours after outburst (Hammer et al., 2010). Considering a clumpy ejecta, the assumption of uniform deposition

of energy by γ-rays and Compton electrons does not hold. Future studies should be targeted towards the estimation of ^{56}Ni mixing in outer layers. The gas temperature evolution function assumed in this study follows a constant exponent. Therefore, the possibility of cooling by molecules such as CO (which is an efficient coolant) are underestimated. Moreover, the estimation of dust temperatures are not addressed in the current scheme. This can hold the key to understand the disparities between the IR and submm observations. In future, the study should focus on the estimation of cooling rates in newly formed dust grains. The works related to the development of a kinetically controlled radiative transfer model in the clumpy ejecta is in process. The final goal is to formulate one consistent model which couples the outputs of the multi-D explosion models to the chemical kinetic code.

The developed formalism is applicable to the study of dust in any circumstellar environment and stellar outflows. In future, I aspire to use my current expertise to address the dust problem in the early universe, and the dust formation scenario in WR and LBV environments.

Appendix A

TABLE A.3: Compton electron-induced reactions, corresponding mean energy per ion pair W_i and Arrhenius coefficient A as a function of ejecta model †

			^{56}Ni = 0.07 $M_\odot$		^{56}Ni = 0.01 $M_\odot$		
Species	Reactions	W_i (eV)	15 $M_\odot$	19 $M_\odot$	12 $M_\odot$	15 $M_\odot$	25 $M_\odot$
CO	$\rightarrow O^+ + C$	768 [a]	7.8(-7)	6.2(-7)	5.0(-7)	1.2(-7)	5.6(-8)
	$\rightarrow C^+ + O$	247 [a]	2.4(-6)	1.9(-6)	1.5(-6)	3.6(-7)	1.7(-7)
	$\rightarrow C + O$	125 [a]	4.8(-6)	3.8(-6)	3.1(-6)	7.2(-7)	3.4(-7)
	$\rightarrow CO^+ + e^-$	34 [a]	1.8(-5)	1.4(-5)	1.1(-5)	2.7(-6)	1.3(-6)
O	$\rightarrow O^+ + e^-$	46.2 [a]	1.3(-5)	1.3(-5)	8.3(-6)	2.0(-6)	9.3(-7)
C	$\rightarrow C^+ + e^-$	36.4 [a]	1.6(-5)	1.3(-5)	1.1(-5)	2.5(-6)	1.2(-6)
SiO	$\rightarrow O^+ + Si$	678 [a]	8.8(-7)	7.0(-7)	5.6(-7)	1.3(-7)	6.4(-8)
	$\rightarrow Si^+ + O$	218 [a]	2.7(-6)	2.2(-6)	1.8(-6)	4.1(-7)	2.0(-7)
	$\rightarrow Si + O$	110 [a]	5.4(-6)	4.3(-6)	3.5(-6)	8.2(-7)	3.9(-7)
	$\rightarrow SiO^+ + e^-$	30 [a]	2.0(-5)	1.6(-5)	1.3(-5)	3.0(-6)	1.4(-6)
N_2	$\rightarrow N^+ + N$	264 [b]	2.3(-6)	1.8(-6)	1.4(-6)	3.4(-7)	1.6(-7)
	$\rightarrow N + N$	133.5 [b]	4.5(-6)	3.5(-6)	2.9(-6)	6.8(-7)	3.2(-7)
	$\rightarrow N_2^+ + e^-$	36.3 [b]	1.6(-5)	1.3(-5)	1.1(-5)	2.5(-6)	1.2(-6)
He	$\rightarrow He^+ + e^-$	46.3 [b]	1.3(-5)	1.0(-5)	8.3(-6)	2.0(-6)	9.3(-7)
Ne	$\rightarrow Ne^+ + e^-$	36.4 [b]	1.6(-5)	1.3(-5)	1.1(-5)	2.5(-6)	1.2(-6)
Ar	$\rightarrow Ar^+ + e^-$	26.2 [b]	2.2(-5)	1.8(-5)	1.5(-5)	3.4(-6)	1.6(-6)

† Arrhenius forms for k_C (see Chapter 3): A $\times \exp(-3386.5/T)$

[a] Reference: Liu & Dalgarno (1995)

[b] Reference: Khare & Kumar (1977)

TABLE A.1: The chemical routes to nucleation of the various clusters considered in the present study. The rates for each reaction is indicated (Sarangi and Cherchneff, 2013)

Reaction	Reactants		Products	A_{ij}	ν	E_a	References
			$(SiO)_n$ clusters				
A1	SiO+SiO	→	Si_2O_2	4.6086×10^{-17}	0	-2821.4	Zachariah and Tsang, 1993
A2	Si_2O_2+SiO	→	Si_3O_3	2.2388×10^{-15}	0	-2878.9	”
A3	Si_2O_2+ Si_2O_2	→	Si_3O_3+SiO	1.5265×10^{-14}	0	-2386.8	”
A4	Si_3O_3+SiO	→	Si_4O_4	1.5265×10^{-14}	0	-2386.8	”
A5	Si_2O_2+ Si_2O_2	→	Si_4O_4	1.5265×10^{-14}	0	-2386.8	”
A6	Si_3O_3+ Si_2O_2	→	Si_4O_4+SiO	1.5265×10^{-14}	0	-2386.8	”
A7	Si_4O_4+SiO	→	Si_5O_5	1.5265×10^{-14}	0	-2386.8	”
A8	Si_3O_3+ Si_2O_2	→	Si_5O_5	1.5265×10^{-14}	0	-2386.8	”
A9	Si_2O_2	→	SiO+SiO	7.7200×10^{-7}	0	0	”
A10	Si_3O_3	→	Si_2O_2+SiO	7.8300×10^{-6}	0	0	”
A11	Si_4O_4	→	Si_3O_3+SiO	9.9000×10^{-4}	0	0	”
A12	Si_4O_4	→	Si_2O_2+Si_2O_2	9.9000×10^{-4}	0	0	”
A13	Si_5O_5	→	Si_3O_3+Si_2O_2	9.9000×10^{-4}	0	0	”
	Forsterite and enstatite dimers ($Mg_4Si_2O_8$ and $Mg_2Si_2O_6$ respectively)						
B1	Si_2O_2+O_2	→	Si_2O_3+O	1.0000×10^{-11}	0	500	Sarangi and Cherchneff, 2013
B2	Si_2O_2+SO	→	Si_2O_3+S	1.0000×10^{-11}	0	500	”
B3	Si_2O_3+Mg	→	$MgSi_2O_3$	1.0000×10^{-12}	0	0	”
B4	$MgSi_2O_3$+O_2	→	$MgSi_2O_4$+O	1.0000×10^{-12}	0	0	”
B5	$MgSi_2O_3$+SO	→	$MgSi_2O_4$+S	1.0000×10^{-12}	0	0	”
B6	$MgSi_2O_4$+Mg	→	$Mg_2Si_2O_4$	1.0000×10^{-12}	0	0	”
B7	$Mg_2Si_2O_4$+O_2	→	$Mg_2Si_2O_5$+O	1.0000×10^{-12}	0	0	”
B8	$Mg_2Si_2O_4$+SO	→	$Mg_2Si_2O_5$+S	1.0000×10^{-12}	0	0	”
B9	$Mg_2Si_2O_5$+O_2	→	$Mg_2Si_2O_6$+O	1.0000×10^{-12}	0	0	”
B10	$Mg_2Si_2O_5$+SO	→	$Mg_2Si_2O_6$+S	1.0000×10^{-12}	0	0	”
B11	$Mg_2Si_2O_6$+Mg	→	$Mg_3Si_2O_6$	1.0000×10^{-12}	0	0	”
B12	$Mg_3Si_2O_6$+O_2	→	$Mg_3Si_2O_7$+O	1.0000×10^{-12}	0	0	”
B13	$Mg_3Si_2O_6$+SO	→	$Mg_3Si_2O_7$+S	1.0000×10^{-12}	0	0	”
B14	$Mg_3Si_2O_7$+Mg	→	$Mg_4Si_2O_7$	1.0000×10^{-12}	0	0	”
B15	$Mg_4Si_2O_7$+O_2	→	$Mg_4Si_2O_8$+O	1.0000×10^{-12}	0	0	”
B16	$Mg_4Si_2O_7$+SO	→	$Mg_4Si_2O_8$+S	1.0000×10^{-12}	0	0	”
			Si_nO_{n+1} clusters				
C1	Si_2O_2+O_2	→	Si_2O_3+O	1.0000×10^{-11}	0	500	Sarangi and Cherchneff, 2013
C2	Si_2O_2+SO	→	Si_2O_3+S	1.0000×10^{-11}	0	500	”
C3	Si_2O_3+O	→	Si_2O_2+O_2	1.0000×10^{-12}	0	0	”
C4	Si_2O_3+S	→	Si_2O_2+SO	1.0000×10^{-12}	0	0	”
C5	Si_3O_3+O_2	→	Si_3O_4+O	1.0000×10^{-13}	0	500	”
C6	Si_3O_3+SO	→	Si_3O_4+S	1.0000×10^{-13}	0	500	”
C7	Si_4O_4+O_2	→	Si_4O_5+O	1.0000×10^{-13}	0	500	”
C8	Si_4O_4+SO	→	Si_4O_5+S	1.0000×10^{-13}	0	500	”
C9	Si_2O_3+SiO	→	Si_3O_4	7.4627×10^{-16}	0	-2878.9	Zachariah and Tsang, 1993
C10	Si_3O_4+SiO	→	Si_4O_5	5.0884×10^{-15}	0	-2386.8	”
C11	Si_2O_2+SiO	→	Si_2O_3+Si	7.4627×10^{-16}	0	-2878.9	”
C12	Si_3O_3+SiO	→	Si_3O_4+Si	5.0884×10^{-15}	0	-2386.8	”
C13	Si_4O_4+SiO	→	Si_4O_5+Si	5.0884×10^{-15}	0	-2386.8	”
C14	Si_2O_3+Si	→	Si_2O_2+SiO	1.0000×10^{-15}	0	4000	”
C15	Si_3O_4+Si	→	Si_3O_3+SiO	1.0000×10^{-15}	0	8000	”
C16	Si_4O_5+Si	→	Si_4O_4+SiO	1.0000×10^{-15}	0	8000	”

TABLE A.2: The chemical routes to nucleation of the various clusters considered in the present study. The rates for each reaction is indicated (Sarangi and Cherchneff, 2013)

Reaction	Reactants		Products	A_{ij}	ν	E_a	References
			Thermal Fragmentation				
TF1	Si_2O_3+M	→	Si_2O_2+O+M	5.0000×10^{-10}	0	55000.0	Cherchneff and Dwek, 2010
TF2	Si_3O_4+M	→	Si_3O_3+O+M	5.0000×10^{-10}	0	55000.0	”
TF3	Si_4O_5+M	→	Si_4O_4+O+M	5.0000×10^{-10}	0	55000.0	”
TF4	$MgSi_2O_3$+M	→	Si_2O_3+Mg+M	1.0000×10^{-10}	0	98600.0	”
TF5	$MgSi_2O_4$+M	→	$MgSi_2O_3$+O+M	1.0000×10^{-10}	0	98600.0	”
TF6	$Mg_2Si_2O_4$+M	→	$MgSi_2O_4$+Mg+M	1.0000×10^{-10}	0	98600.0	”
TF7	$Mg_2Si_2O_5$+M	→	$Mg_2Si_2O_4$+O+M	1.0000×10^{-10}	0	98600.0	”
TF8	$Mg_2Si_2O_6$+M	→	$Mg_2Si_2O_5$+O+M	1.0000×10^{-10}	0	98600.0	”
TF9	$Mg_3Si_2O_6$+M	→	$Mg_2Si_2O_6$+Mg+M	1.0000×10^{-10}	0	98600.0	”
TF10	$Mg_3Si_2O_7$+M	→	$Mg_3Si_2O_6$+O+M	1.0000×10^{-10}	0	98600.0	”
TF11	$Mg_4Si_2O_7$+M	→	$Mg_3Si_2O_7$+Mg+M	1.0000×10^{-10}	0	98600.0	”
TF12	$Mg_4Si_2O_8$+M	→	$Mg_4Si_2O_7$+O+M	1.0000×10^{-10}	0	98600.0	”
TF13	Si_2O_2+M	→	SiO+SiO+M	4.4000×10^{-10}	0	98600.0	”
TF14	Si_3O_3+M	→	Si_2O_2+SiO+M	4.4000×10^{-10}	0	98600.0	”
TF15	Si_4O_4+M	→	Si_3O_3+SiO+M	4.4000×10^{-10}	0	98600.0	”
TF16	Si_4O_4+M	→	Si_2O_2+Si_2O_2+M	4.4000×10^{-10}	0	98600.0	”
TF17	Si_5O_5+M	→	Si_4O_4+SiO+M	4.4000×10^{-10}	0	98600.0	”
TF18	Si_5O_5+M	→	Si_2O_2+Si_3O_3+M	4.4000×10^{-10}	0	98600.0	”

Appendix B

TABLE B.1: Normalised grain size distribution fucntion f(a) for pure-Mg, pure-Fe, iron sulphide and silicon carbide in the 15 $M_{\odot}$ standard model

Size (Å)	f(a)	Size (Å)	f(a)	Size (Å)	f(a)	Size (Å)	f(a)
Pure-Mg		Pure-Fe		FeS		SiC	
2.28	6.05(-01)	2.81	6.11(-01)	3.03	5.45(-01)	2.70	9.45(-03)
2.78	1.42(-01)	3.42	1.42(-01)	3.68	1.73(-01)	3.29	1.51(-02)
3.38	9.31(-02)	4.16	9.21(-02)	4.48	1.23(-01)	4.00	3.73(-02)
4.11	5.49(-02)	5.06	5.33(-02)	5.45	7.00(-02)	4.87	7.27(-02)
5.00	3.46(-02)	6.15	3.28(-02)	6.63	3.35(-02)	5.92	1.22(-01)
6.08	2.21(-02)	7.49	2.08(-02)	8.06	1.27(-02)	7.20	1.75(-01)
7.40	1.42(-02)	9.11	1.34(-02)	9.81	5.12(-03)	8.76	2.08(-01)
9.00	9.44(-03)	11.08	8.63(-03)	11.93	4.18(-03)	10.66	1.90(-01)
10.95	6.42(-03)	13.48	5.52(-03)	14.52	5.42(-03)	12.96	1.18(-01)
13.31	4.38(-03)	16.39	3.50(-03)	17.66	7.02(-03)	15.77	4.39(-02)
16.20	3.00(-03)	19.94	2.49(-03)	21.48	7.91(-03)	19.18	8.56(-03)
19.70	2.26(-03)	24.26	2.41(-03)	26.13	7.04(-03)	23.33	8.11(-04)
23.97	2.10(-03)	29.51	2.85(-03)	31.79	4.43(-03)	28.38	3.76(-05)
29.15	2.22(-03)	35.89	3.22(-03)	38.67	1.75(-03)	34.53	9.31(-07)
35.46	2.16(-03)	43.66	2.98(-03)	47.03	3.88(-04)	42.00	1.38(-08)
43.14	1.66(-03)	53.11	2.01(-03)	57.21	4.62(-05)	51.09	1.30(-10)
52.47	8.78(-04)	64.61	8.71(-04)	69.60	3.01(-06)	62.15	8.22(-13)
63.83	2.90(-04)	78.59	2.18(-04)	84.66	1.16(-07)	75.60	3.55(-15)
77.65	5.54(-05)	95.60	2.95(-05)	102.99	2.85(-09)	91.96	1.07(-17)
94.45	5.93(-06)	116.30	2.17(-06)	125.28	4.74(-11)	111.87	2.31(-20)
114.89	3.67(-07)	141.47	9.24(-08)	152.39	5.50(-13)	136.08	3.57(-23)
139.76	1.40(-08)	172.09	2.47(-09)	185.37	4.56(-15)	165.53	4.01(-26)
170.01	3.48(-10)	209.33	4.38(-11)	225.50	2.76(-17)	201.36	3.30(-29)
206.81	5.92(-12)	254.64	5.34(-13)	274.30	1.26(-19)	244.95	2.01(-32)
251.57	7.04(-14)	309.75	4.60(-15)	333.67	4.46(-22)	297.96	9.09(-36)
306.02	5.97(-16)	376.80	2.85(-17)	405.89	1.24(-24)	362.45	2.78(-39)
372.26	3.68(-18)	458.35	1.31(-19)	493.75	2.77(-27)	440.90	0.00(00)

TABLE B.2: Normalised grain size distribution fucntion f(a) at day 2000 for forsterite, alumina, carbon and pure silicon in the standard 15 $M_{\odot}$ case

Size (Å)	f(a)	Size (Å)	f(a)	Size (Å)	f(a)	Size (Å)	f(a)
Forsterite		Alumina		Carbon		Pure-Si	
3.33	5.76(-01)	3.45	6.20(-01)	3.93	2.43(-02)	2.46	6.23(-01)
4.05	1.29(-01)	4.19	1.38(-01)	4.78	3.35(-05)	2.99	1.42(-01)
4.93	8.55(-02)	5.10	8.84(-02)	5.81	1.01(-05)	3.63	9.13(-02)
6.00	5.44(-02)	6.20	5.10(-02)	7.07	5.48(-07)	4.42	5.21(-02)
7.30	4.14(-02)	7.55	3.26(-02)	8.60	5.55(-08)	5.38	3.17(-02)
8.88	3.51(-02)	9.18	2.25(-02)	10.46	3.41(-09)	6.54	1.98(-02)
10.80	2.95(-02)	11.17	1.63(-02)	12.72	8.30(-10)	7.96	1.27(-02)
13.14	2.14(-02)	13.59	1.13(-02)	15.48	6.63(-08)	9.68	8.24(-03)
15.98	1.22(-02)	16.53	6.91(-03)	18.83	2.33(-06)	11.77	5.41(-03)
19.44	6.00(-03)	20.10	3.81(-03)	22.90	3.78(-05)	14.32	3.56(-03)
23.64	3.05(-03)	24.46	2.13(-03)	27.86	3.33(-04)	17.42	2.33(-03)
28.76	1.64(-03)	29.75	1.21(-03)	33.89	1.82(-03)	21.19	1.50(-03)
34.99	9.89(-04)	36.19	6.49(-04)	41.23	6.83(-03)	25.78	9.49(-04)
42.56	8.15(-04)	44.02	4.16(-04)	50.15	1.92(-02)	31.36	6.45(-04)
51.77	7.75(-04)	53.55	4.80(-04)	61.00	4.30(-02)	38.14	5.82(-04)
62.97	6.36(-04)	65.14	6.95(-04)	74.21	8.09(-02)	46.40	6.97(-04)
76.60	4.07(-04)	79.24	9.08(-04)	90.27	1.31(-01)	56.44	8.65(-04)
93.18	2.49(-04)	96.39	9.78(-04)	109.81	1.81(-01)	68.66	9.38(-04)
113.35	2.12(-04)	117.25	8.16(-04)	133.57	2.04(-01)	83.52	7.99(-04)
137.88	2.15(-04)	142.62	4.98(-04)	162.48	1.73(-01)	101.59	4.76(-04)
167.73	1.94(-04)	173.49	2.16(-04)	197.65	9.75(-02)	123.58	1.77(-04)
204.03	1.36(-04)	211.04	6.33(-05)	240.43	3.17(-02)	150.33	3.73(-05)
248.19	6.58(-05)	256.72	1.15(-05)	292.47	5.29(-03)	182.87	4.27(-06)
301.91	1.92(-05)	312.29	1.21(-06)	355.77	4.27(-04)	222.45	2.75(-07)
367.26	3.13(-06)	379.88	7.28(-08)	432.77	1.71(-05)	270.60	1.10(-08)
446.74	2.77(-07)	462.10	2.68(-09)	526.44	3.76(-07)	329.16	3.06(-10)
543.44	1.41(-08)	562.11	6.30(-11)	640.39	5.03(-09)	400.41	6.04(-12)
661.06	4.41(-10)	683.78	9.99(-13)	778.99	4.36(-11)	487.07	8.34(-14)
804.14	9.02(-12)	831.78	1.09(-14)	947.60	2.54(-13)	592.49	8.21(-16)
978.19	1.25(-13)	1011.80	8.47(-17)	1152.70	1.02(-15)	720.73	5.85(-18)
1189.90	1.21(-15)	1230.80	4.69(-19)	1402.20	2.87(-18)	876.73	3.05(-20)
1447.50	8.32(-18)	1497.20	1.89(-21)	1705.70	5.76(-21)	1066.50	1.17(-22)
1760.70	4.10(-20)	1821.30	5.56(-24)	2074.90	8.36(-24)	1297.30	3.36(-25)
2141.80	1.48(-22)	2215.40	1.21(-26)	2523.90	8.85(-27)	1578.10	7.20(-28)

TABLE B.3: Normalised grain size distribution fucntion f(a) for forsterite, alumina, carbon and pure silicon in the 19 $M_{\odot}$ clumpy model

Size (Å)	f(a)	Size (Å)	f(a)	Size (Å)	f(a)	Size (Å)	f(a)
Forsterite		Alumina		Carbon		Pure-Si	
3.33	6.55(-01)	3.45	6.55(-01)	3.93	8.85(-02)	2.46	7.16(-01)
4.05	1.41(-01)	4.19	1.41(-01)	4.78	6.04(-06)	2.99	1.40(-01)
4.93	8.77(-02)	5.10	8.82(-02)	5.81	7.10(-07)	3.63	7.86(-02)
6.00	4.73(-02)	6.20	4.80(-02)	7.07	7.41(-11)	4.42	3.60(-02)
7.30	2.69(-02)	7.55	2.74(-02)	8.60	2.14(-13)	5.38	1.66(-02)
8.88	1.55(-02)	9.18	1.58(-02)	10.46	6.12(-14)	6.54	7.36(-03)
10.80	9.00(-03)	11.17	9.33(-03)	12.72	4.28(-14)	7.96	3.15(-03)
13.14	5.32(-03)	13.59	5.62(-03)	15.48	2.96(-14)	9.68	1.33(-03)
15.98	3.22(-03)	16.53	3.46(-03)	18.83	1.30(-14)	11.77	5.67(-04)
19.44	2.03(-03)	20.10	2.14(-03)	22.90	3.02(-15)	14.32	2.42(-04)
23.64	1.35(-03)	24.46	1.27(-03)	27.86	1.54(-14)	17.42	9.81(-05)
28.76	9.56(-04)	29.75	6.61(-04)	33.89	1.25(-11)	21.19	3.70(-05)
34.99	7.31(-04)	36.19	2.83(-04)	41.23	2.72(-09)	25.78	1.35(-05)
42.56	6.02(-04)	44.02	1.20(-04)	50.15	1.89(-07)	31.36	5.01(-06)
51.77	5.26(-04)	53.55	8.15(-05)	61.00	5.26(-06)	38.14	1.84(-06)
62.97	4.78(-04)	65.14	7.93(-05)	74.21	7.08(-05)	46.40	6.63(-07)
76.60	4.41(-04)	79.24	7.83(-05)	90.27	5.37(-04)	56.44	2.38(-07)
93.18	4.03(-04)	96.39	8.57(-05)	109.81	2.61(-03)	68.66	9.02(-08)
113.35	3.44(-04)	117.25	1.22(-04)	133.57	8.91(-03)	83.52	3.85(-08)
137.88	2.46(-04)	142.62	1.89(-04)	162.48	2.33(-02)	101.59	2.11(-08)
167.73	1.33(-04)	173.49	2.69(-04)	197.65	4.93(-02)	123.58	1.81(-08)
204.03	5.18(-05)	211.04	3.23(-04)	240.43	8.84(-02)	150.33	2.64(-08)
248.19	1.83(-05)	256.72	3.04(-04)	292.47	1.37(-01)	182.87	5.71(-08)
301.91	1.13(-05)	312.29	2.03(-04)	355.77	1.79(-01)	222.45	1.42(-07)
367.26	1.18(-05)	379.88	8.49(-05)	432.77	1.88(-01)	270.60	3.38(-07)
446.74	1.39(-05)	462.10	2.02(-05)	526.44	1.43(-01)	329.16	7.81(-07)
543.44	1.62(-05)	562.11	2.83(-06)	640.39	6.97(-02)	400.41	1.74(-06)
661.06	1.72(-05)	683.78	5.14(-07)	778.99	1.88(-02)	487.07	3.52(-06)
804.14	1.51(-05)	831.78	2.58(-07)	947.60	2.55(-03)	592.49	6.18(-06)
978.19	9.95(-06)	1011.80	1.18(-07)	1152.70	1.66(-04)	720.73	9.49(-06)
1189.90	4.43(-06)	1230.80	3.21(-08)	1402.20	5.53(-06)	876.73	1.26(-05)
1447.50	1.26(-06)	1497.20	4.80(-09)	1705.70	1.05(-07)	1066.50	1.40(-05)
1760.70	2.44(-07)	1821.30	3.93(-10)	2074.90	1.23(-09)	1297.30	1.20(-05)
2141.80	4.04(-08)	2215.40	1.86(-11)	2523.90	9.56(-12)	1578.10	7.12(-06)
2605.40	9.76(-09)	2695.00	5.54(-13)	3070.20	5.03(-14)	1919.70	2.59(-06)
3169.30	6.31(-09)	3278.30	1.10(-14)	3734.70	1.84(-16)	2335.20	5.23(-07)
3855.30	5.74(-09)	3987.80	1.50(-16)	4543.10	4.75(-19)	2840.60	5.60(-08)
4689.70	4.14(-09)	4850.90	1.45(-18)	5526.40	8.78(-22)	3455.40	3.28(-09)
5704.80	1.99(-09)	5900.90	1.00(-20)	6722.50	1.18(-24)	4203.30	1.15(-10)
6939.50	5.79(-10)	7178.00	5.08(-23)	8177.60	1.15(-27)	5113.10	2.61(-12)
8441.50	9.74(-11)	8731.70	1.90(-25)	9947.50	8.33(-31)	6219.80	4.07(-14)
10269.00	9.56(-12)	10622.00	5.31(-28)	12101.00	4.47(-34)	7566.00	4.50(-16)
12491.00	5.71(-13)	12920.00	1.12(-30)	14720.00	1.78(-37)	9203.60	3.61(-18)
15195.00	2.19(-14)	15717.00	1.80(-33)	17906.00	0.00(00)	11196.00	2.13(-20)
18484.00	5.61(-16)	19119.00	2.25(-36)	21781.00	0.00(00)	13619.00	9.39(-23)
22484.00	9.95(-18)	23257.00	2.20(-39)	26495.00	0.00(00)	16566.00	3.12(-25)
27351.00	1.25(-19)	28291.00	1.71(-42)	32230.00	0.00(00)	20152.00	7.87(-28)

TABLE B.4: Normalised grain size distribution fucntion f(a) for pure-Mg, pure-Fe, iron sulphide and silicon carbide in the 19 $M_{\odot}$ clumpy model

Size (Å)	f(a)	Size (Å)	f(a)	Size (Å)	f(a)	Size (Å)	f(a)
Pure-Mg		Pure-Fe		FeS		SiC	
2.28	6.37(-01)	2.81	6.99(-01)	3.03	6.56(-01)	2.70	2.00(-03)
2.78	1.41(-01)	3.42	1.38(-01)	3.68	1.40(-01)	3.29	6.88(-07)
3.38	8.95(-02)	4.16	7.97(-02)	4.48	8.63(-02)	4.00	2.31(-06)
4.11	5.00(-02)	5.06	3.88(-02)	5.45	4.61(-02)	4.87	3.60(-05)
5.00	2.99(-02)	6.15	2.01(-02)	6.63	2.61(-02)	5.92	3.23(-04)
6.08	1.84(-02)	7.49	1.09(-02)	8.06	1.50(-02)	7.20	1.79(-03)
7.40	1.15(-02)	9.11	6.16(-03)	9.81	8.67(-03)	8.76	6.78(-03)
9.00	7.35(-03)	11.08	3.43(-03)	11.93	5.06(-03)	10.66	1.92(-02)
10.95	4.75(-03)	13.48	1.81(-03)	14.52	3.00(-03)	12.96	4.33(-02)
13.31	3.12(-03)	16.39	9.07(-04)	17.66	1.85(-03)	15.77	8.17(-02)
16.20	2.08(-03)	19.94	4.49(-04)	21.48	1.25(-03)	19.18	1.32(-01)
19.70	1.39(-03)	24.26	2.22(-04)	26.13	1.04(-03)	23.33	1.84(-01)
23.97	9.42(-04)	29.51	1.07(-04)	31.79	1.19(-03)	28.38	2.09(-01)
29.15	6.46(-04)	35.89	4.92(-05)	38.67	1.60(-03)	34.53	1.79(-01)
35.46	4.48(-04)	43.66	2.12(-05)	47.03	2.01(-03)	42.00	1.02(-01)
43.14	3.12(-04)	53.11	8.75(-06)	57.21	2.09(-03)	51.09	3.35(-02)
52.47	2.15(-04)	64.61	3.56(-06)	69.60	1.63(-03)	62.15	5.68(-03)
63.83	1.43(-04)	78.59	1.46(-06)	84.66	8.50(-04)	75.60	4.65(-04)
77.65	9.02(-05)	95.60	6.24(-07)	102.99	2.65(-04)	91.96	1.89(-05)
94.45	5.78(-05)	116.30	3.06(-07)	125.28	4.84(-05)	111.87	4.20(-07)
114.89	4.81(-05)	141.47	2.10(-07)	152.39	1.14(-05)	136.08	5.66(-09)
139.76	5.74(-05)	172.09	2.34(-07)	185.37	1.36(-05)	165.53	4.95(-11)
170.01	7.58(-05)	209.33	3.43(-07)	225.50	2.15(-05)	201.36	2.90(-13)
206.81	9.11(-05)	254.64	6.16(-07)	274.30	3.02(-05)	244.95	1.17(-15)
251.57	9.20(-05)	309.75	1.37(-06)	333.67	3.57(-05)	297.96	3.32(-18)
306.02	7.19(-05)	376.80	3.07(-06)	405.89	3.36(-05)	362.45	6.73(-21)
372.26	3.99(-05)	458.35	6.05(-06)	493.75	2.26(-05)	440.90	9.82(-24)
452.83	1.53(-05)	557.56	1.03(-05)	600.61	9.68(-06)	536.33	1.05(-26)
550.84	5.11(-06)	678.24	1.52(-05)	730.61	2.40(-06)	652.42	8.18(-30)
670.06	2.07(-06)	825.04	1.91(-05)	888.74	3.28(-07)	793.62	4.74(-33)
815.09	7.70(-07)	1003.60	1.97(-05)	1081.10	2.50(-08)	965.40	2.05(-36)
991.51	1.79(-07)	1220.80	1.51(-05)	1315.10	1.13(-09)	1174.30	0.00(00)
1206.10	2.26(-08)	1485.10	7.66(-06)	1599.70	3.22(-11)	1428.50	0.00(00)
1467.20	1.54(-09)	1806.50	2.30(-06)	1946.00	6.12(-13)	1737.70	0.00(00)
1784.70	6.00(-11)	2197.50	3.76(-07)	2367.20	8.10(-15)	2113.80	0.00(00)
2171.00	1.46(-12)	2673.10	3.27(-08)	2879.50	7.73(-17)	2571.30	0.00(00)
2640.90	2.39(-14)	3251.70	1.60(-09)	3502.80	5.51(-19)	3127.90	0.00(00)
3212.50	2.71(-16)	3955.50	4.78(-11)	4260.90	3.01(-21)	3804.90	0.00(00)
3907.80	2.18(-18)	4811.60	9.45(-13)	5183.10	1.30(-23)	4628.40	0.00(00)
4753.60	1.28(-20)	5853.00	1.29(-14)	6305.00	4.45(-26)	5630.20	0.00(00)
5782.50	5.48(-23)	7119.90	1.25(-16)	7669.60	1.21(-28)	6848.80	0.00(00)
7034.10	1.75(-25)	8660.90	8.81(-19)	9329.70	2.59(-31)	8331.10	0.00(00)
8556.50	4.20(-28)	10535.00	4.56(-21)	11349.00	4.30(-34)	10134.00	0.00(00)

Bibliography

D. C. Abbott and L. B. Lucy. Multiline transfer and the dynamics of stellar winds. Astrophysical Journal, 288:679–693, January 1985. doi: 10.1086/162834.

D. K. Aitken, C. H. Smith, S. D. James, P. F. Roche, A. R. Hyland, and P. J. McGregor. 10 micron spectral observations of SN1987A - The first year. Monthly Notices of the Royal Astronomical Society, 235:19P–31P, December 1988.

M K. Alam. The Effect of van der Waals and Viscous Forces on Aerosol Coagulation. Aerosol Science and Technology, 6:41, June 1987. doi: 10.1080/02786828708959118.

J. E. Andrews, J. S. Gallagher, G. C. Clayton, B. E. K. Sugerman, J. P. Chatelain, J. Clem, D. L. Welch, M. J. Barlow, B. Ercolano, J. Fabbri, R. Wesson, and M. Meixner. SN 2007od: A Type IIP Supernova with Circumstellar Interaction. The Astrophysical Journal, 715:541–549, May 2010. doi: 10.1088/0004-637X/715/1/541.

J. E. Andrews, B. E. K. Sugerman, G. C. Clayton, J. S. Gallagher, M. J. Barlow, J. Clem, B. Ercolano, J. Fabbri, M. Meixner, M. Otsuka, D. L. Welch, and R. Wesson. Photometric and Spectroscopic Evolution of the IIP SN 2007it to Day 944. The Astrophysical Journal, 731:47, April 2011. doi: 10.1088/0004-637X/731/1/47.

R. Barbon, F. Ciatti, and L. Rosino. Photometric properties of type II supernovae. Astronomy and Astrophysics, 72:287–292, February 1979.

R. Barbon, V. Buondí, E. Cappellaro, and M. Turatto. The Asiago Supernova Catalogue - 10 years after. Astronomy and Astrophysics Supplement, 139:531–536, November 1999. doi: 10.1051/aas:1999404.

M. J. Barlow, O. Krause, B. M. Swinyard, B. Sibthorpe, M.-A. Besel, R. Wesson, R. J. Ivison, L. Dunne, W. K. Gear, H. L. Gomez, P. C. Hargrave, T. Henning, S. J.

Leeks, T. L. Lim, G. Olofsson, and E. T. Polehampton. A Herschel PACS and SPIRE study of the dust content of the Cassiopeia A supernova remnant. Astronomy and Astrophysics, 518:L138, July 2010. doi: 10.1051/0004-6361/201014585.

E. E. Barnard. On the dark markings of the sky, with a catalogue of 182 such objects. Astrophysical Journal, 49:1–24, January 1919. doi: 10.1086/142439.

E. E. Becklin and J. A. Westphal. Infrared Observations of Comet 1965f. Astrophysical Journal, 145:445, August 1966. doi: 10.1086/148785.

B. Begemann, J. Dorschner, T. Henning, H. Mutschke, J. Gürtler, C. Kömpe, and R. Nass. Aluminum Oxide and the Opacity of Oxygen-rich Circumstellar Dust in the 12-17 Micron Range. The Astrophysical Journal, 476:199–208, February 1997.

Lennart Bergström. Hamaker constants of inorganic materials. Advances in Colloid and Interface Science, 70:125 – 169, 1997. doi: http://dx.doi.org/10.1016/S0001-8686(97)00003-1. URL `http://www.sciencedirect.com/science/article/pii/S0001868697000031`.

T. Bernatowicz, G. Fraundorf, T. Ming, E. Anders, B. Wopenka, E. Zinner, and P. Fraundorf. Evidence for interstellar SiC in the Murray carbonaceous meteorite. Nature, 330:728–730, December 1987. doi: 10.1038/330728a0.

F. Bertoldi, C. L. Carilli, P. Cox, X. Fan, M. A. Strauss, A. Beelen, A. Omont, and R. Zylka. Dust emission from the most distant quasars. Astronomy and Astrophysics, 406:L55–L58, July 2003. doi: 10.1051/0004-6361:20030710.

S. Bianchi and R. Schneider. Dust formation and survival in supernova ejecta. Monthly Notices of the Royal Astronomical Society, 378:973–982, July 2007. doi: 10.1111/j.1365-2966.2007.11829.x.

B. Biscaro, I. Cherchneff, and A. Sarangi. Dust reprocessing by the reverse shock in the supernova remnants. Astronomy & Astrophysics (manuscript in preparation), 2014.

C. Biscaro and I. Cherchneff. Molecules and dust in Cassiopeia A. I. Synthesis in the supernova phase and processing by the reverse shock in the clumpy remnant. Astronomy & Astrophysics, 564:A25, April 2014. doi: 10.1051/0004-6361/201322932.

P. Bouchet and I. J. Danziger. Infrared Photometry and Spectrophotometry of Supernova 1987A - Part Two - 1987NOV to 1991MAR Observations. Astronomy and Astrophysics, 273:451, June 1993.

D. Branch, M. Livio, L. R. Yungelson, F. R. Boffi, and E. Baron. In Search of the Progenitors of Type IA Supernovae. Publications of the Astronomical Society of the Pacific, 107:1019, November 1995. doi: 10.1086/133657.

George D Byrne and Alan C Hindmarsh. Stiff {ODE} solvers: A review of current and coming attractions. Journal of Computational Physics, 70(1):1 – 62, 1987. ISSN 0021-9991. doi: http://dx.doi.org/10.1016/0021-9991(87)90001-5. URL `http://www.sciencedirect.com/science/article/pii/0021999187900015`.

R. M. Catchpole, P. A. Whitelock, M. W. Feast, J. M. Menzies, I. S. Glass, F. Marang, J. D. Laing, J. H. Spencer Jones, G. Roberts, L. A. Balona, B. S. Carter, C. D. Laney, L. T. Evans, K. Sekiguchi, G. G. Hutchinson, R. Maddison, J. Albinson, A. Evans, F. A. Allen, H. Winkler, A. Fairall, C. Corbally, J. K. Davies, and Q. A. Parker. Spectroscopic and photometric observations of SN 1987A. III - Days 135 to 260. Monthly Notices of the Royal Astronomical Society, 231:75P, April 1988.

I. Cherchneff. Dust Formation in Massive Stars and Their Explosive Ends. In C. Leitherer, P. D. Bennett, P. W. Morris, and J. T. Van Loon, editors, Hot and Cool: Bridging Gaps in Massive Star Evolution, volume 425 of Astronomical Society of the Pacific Conference Series, page 237, June 2010.

I. Cherchneff. The inner wind of IRC+10216 revisited: new exotic chemistry and diagnostic for dust condensation in carbon stars. Astronomy & Astrophysics, 545:A12, September 2012. doi: 10.1051/0004-6361/201118542.

I. Cherchneff. Dust production in Supernovae. In Proceedings of The Life Cycle of Dust in the Universe: Observations, Theory, and Laboratory Experiments (LCDU2013). 18-22 November, 2013. Taipei, Taiwan. Editors: Anja Andersen (University of Copenhagen, Denmark), Maarten Baes (Universiteit Gent, Belgium), Haley Gomez (Cardiff University, UK), Ciska Kemper (Academia Sinica, Taiwan), Darach Watson (University of Copenhagen, Denmark), 2013a.

I. Cherchneff. The chemistry of dust formation in red supergiants. In P. Kervella, T. Le Bertre, and G. Perrin, editors, EAS Publications Series, volume 60 of EAS Publications Series, pages 175–184, May 2013b. doi: 10.1051/eas/1360020.

I. Cherchneff and E. Dwek. The Chemistry of Population III Supernova Ejecta. I. Formation of Molecules in the Early Universe. The Astrophysical Journal, 703:642–661, September 2009. doi: 10.1088/0004-637X/703/1/642.

I. Cherchneff and E. Dwek. The Chemistry of Population III Supernova Ejecta. II. The Nucleation of Molecular Clusters as a Diagnostic for Dust in the Early Universe. The Astrophysical Journal, 713:1–24, April 2010. doi: 10.1088/0004-637X/713/1/1.

I. Cherchneff and A. Sarangi. Molecules in Supernova Ejecta. In J. Cernicharo and R. Bachiller, editors, IAU Symposium, volume 280 of IAU Symposium, pages 228–236, December 2011. doi: 10.1017/S1743921311025002.

R. A. Chevalier. Are young supernova remnants interacting with circumstellar gas. Astrophysical Journal Letters, 259:L85–L89, August 1982. doi: 10.1086/183853.

R. A. Chevalier and R. P. Kirshner. Spectra of Cassiopeia A. II - Interpretation. The Astrophysical Journal, 219:931–941, February 1978. doi: 10.1086/155855.

H. Chihara, C. Koike, A. Tsuchiyama, S. Tachibana, and D. Sakamoto. Compositional dependence of infrared absorption spectra of crystalline silicates. I. Mg-Fe pyroxenes. Astronomy and Astrophysics, 391:267–273, August 2002. doi: 10.1051/0004-6361:20020791.

D. D. Clayton. Sudden grain nucleation and growth in supernova and nova ejecta. AP & SS, 65:179–189, September 1979. doi: 10.1007/BF00643499.

D. D. Clayton and L. R. Nittler. Astrophysics with Presolar Stardust. Annual Review of Astronomy & Astrophysics, 42:39–78, September 2004. doi: 10.1146/annurev.astro.42.053102.134022.

D. D. Clayton, W. Liu, and A. Dalgarno. Condensation of Carbon in Radioactive Supernova Gas. Science, 283:1290, February 1999. doi: 10.1126/science.283.5406.1290.

D. D. Clayton, E. A.-N. Deneault, and B. S. Meyer. Condensation of Carbon in Radioactive Supernova Gas. The Astrophysical Journal, 562:480–493, November 2001. doi: 10.1086/323467.

A. Clocchiatti, S. Benetti, J. C. Wheeler, W. Wren, J. Boisseau, E. Cappellaro, M. Turatto, F. Patat, D. A. Swartz, R. P. Harkness, M. S. Brotherton, B. Wills, P. Hemenway, M. Cornell, M. Frueh, and M. B. Kaiser. A Study of SN 1992H in NGC 5377. Astronomical Journal, 111:1286, March 1996. doi: 10.1086/117874.

L. Colangeli, V. Mennella, P. Palumbo, A. Rotundi, and E. Bussoletti. Mass extinction coefficients of various submicron amorphous carbon grains: Tabulated values from 40 NM to 2 mm. Astronomy and Astrophysics Supplement, 113:561, November 1995.

I. J. Danziger, P. Bouchet, R. A. E. Fosbury, C. Gouiffes, and L. B. Lucy. SN 1987A - Observational results obtained at ESO. In M. Kafatos and A. G. Michalitsianos, editors, Supernova 1987A in the Large Magellanic Cloud, pages 37–50, 1988.

I. J. Danziger, L. B. Lucy, P. Bouchet, and C. Gouiffes. Molecules Dust and Ionic Abundances in Supernova 1987A. In S. E. Woosley, editor, Supernovae, page 69, 1991.

K. Davidson and R. A. Fesen. Recent developments concerning the Crab Nebula. Annual review of astronomy and astrophysics, 23:119–146, 1985. doi: 10.1146/annurev.aa.23.090185.001003.

T. DeLaney, L. Rudnick, M. D. Stage, J. D. Smith, K. Isensee, J. Rho, G. E. Allen, H. Gomez, T. Kozasa, W. T. Reach, J. E. Davis, and J. C. Houck. The Three-dimensional Structure of Cassiopeia A. The Astrophysical Journal, 725:2038–2058, December 2010. doi: 10.1088/0004-637X/725/2/2038.

B. Donn and J. A. Nuth. Does nucleation theory apply to the formation of refractory circumstellar grains? Astrophysical Journal, 288:187–190, January 1985. doi: 10.1086/162779.

J. Dorschner, B. Begemann, T. Henning, C. Jaeger, and H. Mutschke. Steps toward interstellar silicate mineralogy. II. Study of Mg-Fe-silicate glasses of variable composition. Astronomy and Astrophysics, 300:503, August 1995.

B. T. Draine. The infrared signature of graphite grains. Astrophysical Journal Letters, 277:L71–L74, February 1984. doi: 10.1086/184206.

P.W. Dunk, N.K. Kaiser, Marc. Mullet-Gas, and et al. TThe Smallest Stable Fullerene, M@C_{28} (M = Ti, Zr, U): Stabilization and Growth from Carbon Vapor. Journal of American Chemical Soceity, 134:9380, April 2012. doi: 10.1021/ja302398h.

E. Dwek and I. Cherchneff. The Origin of Dust in the Early Universe: Probing the Star Formation History of Galaxies by Their Dust Content. The Astrophysical Journal, 727:63, February 2011. doi: 10.1088/0004-637X/727/2/63.

E. Dwek, S. H. Moseley, W. Glaccum, J. R. Graham, R. F. Loewenstein, R. F. Silverberg, and R. K. Smith. Dust and gas contributions to the energy output of SN 1987A on day 1153. Astrophysical Journal, 389:L21–L24, April 1992. doi: 10.1086/186339.

E. Dwek, F. Galliano, and A. P. Jones. The Evolution of Dust in the Early Universe with Applications to the Galaxy SDSS J1148+5251. The Astrophysical Journal, 662:927–939, June 2007. doi: 10.1086/518430.

A. Elmhamdi, N. N. Chugai, and I. J. Danziger. Light curves and Hα luminosities as indicators of ^{56}Ni mass in type IIP supernovae. Astronomy and Astrophysics, 404:1077–1086, June 2003a. doi: 10.1051/0004-6361:20030522.

A. Elmhamdi, I. J. Danziger, N. Chugai, A. Pastorello, M. Turatto, E. Cappellaro, G. Altavilla, S. Benetti, F. Patat, and M. Salvo. Photometry and spectroscopy of the Type IIP SN 1999em from outburst to dust formation. Monthly Notice of the Royal Astronomical Society, 338:939–956, February 2003b. doi: 10.1046/j.1365-8711.2003.06150.x.

B. Ercolano, M. J. Barlow, and P. J. Storey. The dusty MOCASSIN: fully self-consistent 3D photoionization and dust radiative transfer models. Monthly Notices of the Royal Astronomical Society, 362:1038–1046, September 2005. doi: 10.1111/j.1365-2966.2005.09381.x.

B. Ercolano, M. J. Barlow, and B. E. K. Sugerman. Dust yields in clumpy supernova shells: SN 1987A revisited. Monthly Notice of the Royal Astronomical Society, 375:753–763, March 2007. doi: 10.1111/j.1365-2966.2006.11336.x.

D. Fabian, C. Jäger, T. Henning, J. Dorschner, and H. Mutschke. Steps toward interstellar silicate mineralogy. V. Thermal Evolution of Amorphous Magnesium Silicates and Silica. Astronomy and Astrophysics, 364:282–292, December 2000.

D. Fabian, T. Posch, H. Mutschke, F. Kerschbaum, and J. Dorschner. Infrared optical properties of spinels. A study of the carrier of the 13, 17 and 32 mu m emission features observed in ISO-SWS spectra of oxygen-rich AGB stars. Astronomy and Astrophysics, 373:1125–1138, July 2001. doi: 10.1051/0004-6361:20010657.

A. Fassia, W. P. S. Meikle, N. Chugai, T. R. Geballe, P. Lundqvist, N. A. Walton, D. Pollacco, S. Veilleux, G. S. Wright, M. Pettini, T. Kerr, E. Puchnarewicz, P. Puxley, M. Irwin, C. Packham, S. J. Smartt, and D. Harmer. Optical and infrared spectroscopy of the type IIn SN 1998S: days 3-127. Monthly Notices of the Royal Astronomical Society, 325:907–930, August 2001. doi: 10.1046/j.1365-8711.2001.04282.x.

G. J. Ferland, N. Abel, K. Davidson, and N. Smith. Physical Conditions in the Homunculus. In R. Humphreys and K. Stanek, editors, The Fate of the Most Massive Stars, volume 332 of Astronomical Society of the Pacific Conference Series, page 294, September 2005.

R. A. Fesen, M. C. Hammell, J. Morse, R. A. Chevalier, K. J. Borkowski, M. A. Dopita, C. L. Gerardy, S. S. Lawrence, J. C. Raymond, and S. van den Bergh. Discovery of Outlying High-Velocity Oxygen-Rich Ejecta in Cassiopeia A. The Astrophysical Journal, 636:859–872, January 2006. doi: 10.1086/498092.

A. V. Filippenko. Optical Spectra of Supernovae. Annual Review of Astronomy and Astrophysics, 35:309–355, 1997. doi: 10.1146/annurev.astro.35.1.309.

C. Fransson and R. A. Chevalier. Late emission from supernovae - A window on stellar nucleosynthesis. Astrophysical Journal, 343:323–342, August 1989. doi: 10.1086/167707.

R.H. French, R.M. Cannon, L.K. DeNoyer, and Y.-M. Chiang. Full spectral calculation of non-retarded hamaker constants for ceramic systems from interband transition strengths. Solid State Ionics, 75(0):13 – 33, 1995. ISSN 0167-2738. doi: http://dx.doi.org/10.1016/0167-2738(94)00217-G. URL http://www.sciencedirect.com/science/article/pii/016727389400217G. Interfaces in Ionic Materials.

C. Gall, J. Hjorth, and A. C. Andersen. Production of dust by massive stars at high redshift. The Astronomy and Astrophysics Review, 19:43, September 2011. doi: 10.1007/s00159-011-0043-7.

J. S. Gallagher, B. E. K. Sugerman, G. C. Clayton, J. E. Andrews, J. Clem, M. J. Barlow, B. Ercolano, J. Fabbri, M. Otsuka, R. Wesson, and M. Meixner. Optical and Infrared Analysis of Type II SN 2006bc. The Astrophysical Journal, 753:109, July 2012. doi: 10.1088/0004-637X/753/2/109.

P. Gandhi, M. Yamanaka, M. Tanaka, T. Nozawa, K. S. Kawabata, I. Saviane, K. Maeda, T. J. Moriya, T. Hattori, M. Sasada, and R. Itoh. SN 2009js at the Crossroads between Normal and Subluminous Type IIP Supernovae: Optical and Mid-infrared Evolution. The Astrophysical Journal, 767:166, April 2013. doi: 10.1088/0004-637X/767/2/166.

C. W. Gear. Numerical Initial Value Problems in Ordinary Differential Equations. Prentice-Hall, Englewood-Cliffs, NJ, 1971.

R. D. Gehrz and N. J. Woolf. R V Tauri Stars: a New Class of Infrared Object. Astrophysical Journal, 161:L213, September 1970. doi: 10.1086/180605.

C. L. Gerardy, R. A. Fesen, P. Höflich, and J. C. Wheeler. Detection of CO and Dust Emission in Near-Infrared Spectra of SN 1998S. The Astronomical Journal, 119:2968–2981, June 2000. doi: 10.1086/301390.

P. Ghavamian, K. S. Long, W. P. Blair, S. Park, R. Fesen, B. M. Gaensler, J. P. Hughes, J. Rho, and P. F. Winkler. Spitzer Imaging and Spectral Mapping of the Oxygen-rich Supernova Remnant G292.0+1.8. The Astrophysical Journal, 750:39, May 2012. doi: 10.1088/0004-637X/750/1/39.

D. Gobrecht and I. Cherchneff. Forming silicate and alumina dust in the wind of the O-rich AGB IK Tau. In Proceedings of The Life Cycle of Dust in the Universe: Observations, Theory, and Laboratory Experiments (LCDU2013). 18-22 November, 2013. Taipei, Taiwan. Editors: Anja Andersen (University of Copenhagen, Denmark),

Maarten Baes (Universiteit Gent, Belgium), Haley Gomez (Cardiff University, UK), Ciska Kemper (Academia Sinica, Taiwan), Darach Watson (University of Copenhagen, Denmark), 2013.

H. Gomez. Dust in supernova remnants. In Proceedings of The Life Cycle of Dust in the Universe: Observations, Theory, and Laboratory Experiments (LCDU2013). 18-22 November, 2013. Taipei, Taiwan. Editors: Anja Andersen (University of Copenhagen, Denmark), Maarten Baes (Universiteit Gent, Belgium), Haley Gomez (Cardiff University, UK), Ciska Kemper (Academia Sinica, Taiwan), Darach Watson (University of Copenhagen, Denmark)., 2013.

H. L. Gomez, C. J. R. Clark, T. Nozawa, O. Krause, E. L. Gomez, M. Matsuura, M. J. Barlow, M.-A. Besel, L. Dunne, W. K. Gear, P. Hargrave, T. Henning, R. J. Ivison, B. Sibthorpe, B. M. Swinyard, and R. Wesson. Dust in historical Galactic Type Ia supernova remnants with Herschel. Monthly Notices of the Royal Astronomical Society, 420:3557–3573, March 2012a. doi: 10.1111/j.1365-2966.2011.20272.x.

H. L. Gomez, O. Krause, M. J. Barlow, B. M. Swinyard, P. J. Owen, C. J. R. Clark, M. Matsuura, E. L. Gomez, J. Rho, M.-A. Besel, J. Bouwman, W. K. Gear, T. Henning, R. J. Ivison, E. T. Polehampton, and B. Sibthorpe. A Cool Dust Factory in the Crab Nebula: A Herschel Study of the Filaments. The Astrophysical Journal, 760:96, November 2012b. doi: 10.1088/0004-637X/760/1/96.

T. P. M. Goumans and S. T. Bromley. Efficient nucleation of stardust silicates via heteromolecular homogeneous condensation. Monthly Notices of the Royal Astronomical Society, 420:3344–3349, March 2012. doi: 10.1111/j.1365-2966.2011.20255.x.

E. Grün, B. A. S. Gustafson, S. Dermott, and H. Fechtig. Interplanetary Dust. Interplanetary Dust, Edited by E. Grün, B.A.S. Gustafson, S. Dermott, and H. Fechtig. Astronomy and Astrophysics Library. 2001, 804 p., ISBN: 3-540-42067-3. Berlin: Springer, 2001., 2001.

N. J. Hammer, H.-T. Janka, and E. Müller. Three-dimensional Simulations of Mixing Instabilities in Supernova Explosions. The Astrophysical Journal, 714:1371–1385, May 2010. doi: 10.1088/0004-637X/714/2/1371.

M. Hamuy. Observed and Physical Properties of Core-Collapse Supernovae. The Astrophysical Journal, 582:905–914, January 2003. doi: 10.1086/344689.

T. J. Harries, J. D. Monnier, N. H. Symington, and R. Kurosawa. Three-dimensional dust radiative-transfer models: the Pinwheel Nebula of WR 104. Monthly Notices of the Royal Astronomical Society, 350:565–574, May 2004. doi: 10.1111/j.1365-2966.2004.07668.x.

M. A. Hendry, S. J. Smartt, J. R. Maund, A. Pastorello, L. Zampieri, S. Benetti, M. Turatto, E. Cappellaro, W. P. S. Meikle, R. Kotak, M. J. Irwin, P. G. Jonker, L. Vermaas, R. F. Peletier, H. van Woerden, K. M. Exter, D. L. Pollacco, S. Leon, S. Verley, C. R. Benn, and G. Pignata. A study of the Type II-P supernova 2003gd in M74. Monthly Notices of the Royal Astronomical Society, 359:906–926, May 2005. doi: 10.1111/j.1365-2966.2005.08928.x.

T. Henning, B. Begemann, H. Mutschke, and J. Dorschner. Optical properties of oxide dust grains. Astronomy and Astrophysics Supplement, 112:143, July 1995.

W. Herschel. On the Construction of the Heavens. Royal Society of London Philosophical Transactions Series I, 75:213–266, 1785.

D. J. Hillier, K. Davidson, K. Ishibashi, and T. Gull. On the Nature of the Central Source in η Carinae. The Astrophysical Journal, 553:837–860, June 2001. doi: 10.1086/320948.

A.C. Hindmarsh. ODEPACK, a systematized collection of ODE solvers. Lawrence Livermore National Laboratory, 1982. URL `http://books.google.ch/books?id=9XWPmwEACAAJ`.

A. M. Hofmeister, E. Keppel, and A. K. Speck. Absorption and reflection infrared spectra of MgO and other diatomic compounds. Monthly Notices of the Royal Astronomical Society, 345:16–38, October 2003. doi: 10.1046/j.1365-8711.2003.06899.x.

P. Hoppe. Measurements of presolar grains. In Nuclei in the Cosmos, 2010.

P. Hoppe, W. Fujiya, and E. Zinner. Sulfur Molecule Chemistry in Supernova Ejecta Recorded by Silicon Carbide Stardust. The Astrophysical Journal Letters, 745:L26, February 2012. doi: 10.1088/2041-8205/745/2/L26.

Masuo Hosokawa, Kiyoshi Nogi, Makio Naito, and Toyokazu Yokoyama. Nanoparticle Technology Handbook. Elsevier, Amsterdam, second edition edition, 2012. ISBN 978-0-444-56336-1. doi: http://dx.doi.org/10.1016/B978-0-444-56336-1.50010-2. URL `http://www.sciencedirect.com/science/article/pii/B9780444563361500102`.

F. Hoyle. Frontiers of astronomy. New York, Harper [1955], 1955.

R. Indebetouw, M. Matsuura, E. Dwek, G. Zanardo, M. J. Barlow, M. Baes, P. Bouchet, D. N. Burrows, R. Chevalier, G. C. Clayton, C. Fransson, B. Gaensler, R. Kirshner, M. Lakićević, K. S. Long, P. Lundqvist, I. Martí-Vidal, J. Marcaide, R. McCray, M. Meixner, C.-Y. Ng, S. Park, G. Sonneborn, L. Staveley-Smith, C. Vlahakis, and J. van Loon. Dust Production and Particle Acceleration in Supernova 1987A Revealed

with ALMA. The Astrophysical Journal Letters, 782:L2, February 2014. doi: 10.1088/2041-8205/782/1/L2.

C. Inserra, M. Turatto, A. Pastorello, S. Benetti, E. Cappellaro, M. L. Pumo, L. Zampieri, I. Agnoletto, F. Bufano, M. T. Botticella, M. Della Valle, N. Elias Rosa, T. Iijima, S. Spiro, and S. Valenti. The Type IIP SN 2007od in UGC 12846: from a bright maximum to dust formation in the nebular phase. Monthly Notices of the Royal Astronomical Society, 417:261–279, October 2011. doi: 10.1111/j.1365-2966.2011.19128.x.

C. Inserra, M. Turatto, A. Pastorello, M. L. Pumo, E. Baron, S. Benetti, E. Cappellaro, S. Taubenberger, F. Bufano, N. Elias-Rosa, L. Zampieri, A. Harutyunyan, A. S. Moskvitin, M. Nissinen, V. Stanishev, D. Y. Tsvetkov, V. P. Hentunen, V. N. Komarova, N. N. Pavlyuk, V. V. Sokolov, and T. N. Sokolova. The bright Type IIP SN 2009bw, showing signs of interaction. Monthly Notices of the Royal Astronomical Society, 422:1122–1139, May 2012. doi: 10.1111/j.1365-2966.2012.20685.x.

K. Isensee, G. Olmschenk, L. Rudnick, T. DeLaney, J. Rho, J. D. Smith, W. T. Reach, T. Kozasa, and H. Gomez. Nucleosynthetic Layers in the Shocked Ejecta of Cassiopeia A. The Astrophysical Journal, 757:126, October 2012. doi: 10.1088/0004-637X/757/2/126.

Jacob N. Israelachvili. Intermolecular and Surface Forces. Academic Press, San Diego, third edition edition, 2011. ISBN 978-0-12-375182-9. doi: http://dx.doi.org/10.1016/B978-0-12-375182-9.10011-9. URL `http://www.sciencedirect.com/science/article/pii/B9780123751829100119`.

M Z. Jacobson. Fundamentals of Atmospheric modeling. Cambridge University Press, second edition, 2005.

M. Z. Jacobson and R. P. Turco. A sparse-matrix, vectorized Gear code for atmospheric models. Asmospheric Environment, 28:273–284, 1994.

C. Jäger, F. Huisken, H. Mutschke, I. L. Jansa, and T. Henning. Formation of Polycyclic Aromatic Hydrocarbons and Carbonaceous Solids in Gas-Phase Condensation Experiments. The Astrophysical Journal, 696:706–712, May 2009. doi: 10.1088/0004-637X/696/1/706.

A. Jerkstrand, C. Fransson, and C. Kozma. The ^{44}Ti-powered spectrum of SN 1987A. Astronomy & Astrophysics, 530:A45, June 2011. doi: 10.1051/0004-6361/201015937.

C. C. Joggerst, A. Almgren, and S. E. Woosley. Three-dimensional Simulations of Rayleigh-Taylor Mixing in Core-collapse Supernovae with Castro. The Astrophysical Journal, 723:353–363, November 2010. doi: 10.1088/0004-637X/723/1/353.

J. Kamenetzky, R. McCray, R. Indebetouw, M. J. Barlow, M. Matsuura, M. Baes, J. A. D. L. Blommaert, A. Bolatto, L. Decin, L. Dunne, C. Fransson, J. Glenn, H. L. Gomez, M. A. T. Groenewegen, R. Hopwood, R. P. Kirshner, M. Lakicevic, J. Marcaide, I. Marti-Vidal, M. Meixner, P. Royer, A. Soderberg, G. Sonneborn, L. Staveley-Smith, B. M. Swinyard, G. Van de Steene, P. A. M. van Hoof, J. T. van Loon, J. Yates, and G. Zanardo. Carbon Monoxide in the Cold Debris of Supernova 1987A. The Astrophysical Journal Letters, 773:L34, August 2013. doi: 10.1088/2041-8205/773/2/L34.

F. Kemper, W. J. Vriend, and A. G. G. M. Tielens. Erratum: "The Absence of Crystalline Silicates in the Diffuse Interstellar Medium" (¡A href="/abs/2004ApJ...609..826K"¿ApJ, 609, 826 [2004]¡/A¿). The Astrophysical Journal, 633:534–534, November 2005. doi: 10.1086/447764.

M. Kiewe, A. Gal-Yam, I. Arcavi, D. C. Leonard, J. Emilio Enriquez, S. B. Cenko, D. B. Fox, D.-S. Moon, D. J. Sand, A. M. Soderberg, and T. CCCP. Caltech Core-Collapse Project (CCCP) Observations of Type IIn Supernovae: Typical Properties and Implications for Their Progenitor Stars. The Astrophysical Journal, 744:10, January 2012. doi: 10.1088/0004-637X/744/1/10.

K. Kifonidis, T. Plewa, H.-T. Janka, and E. Müller. Non-spherical core collapse supernovae. I. Neutrino-driven convection, Rayleigh-Taylor instabilities, and the formation and propagation of metal clumps. Astronomy & Astrophysics, 408:621–649, September 2003. doi: 10.1051/0004-6361:20030863.

K. Kifonidis, T. Plewa, L. Scheck, H.-T. Janka, and E. Müller. Non-spherical core collapse supernovae. II. The late-time evolution of globally anisotropic neutrino-driven explosions and their implications for SN 1987 A. Astronomy and Astrophysics, 453:661–678, July 2006. doi: 10.1051/0004-6361:20054512.

T. M. Koehler, H.-P. Gail, and E. Sedlmayr. MgO dust nucleation in M-Stars: calculation of cluster properties and nucleation rates. Astronomy and Astrophysics, 320:553–567, April 1997.

C. Koike, H. Hasegawa, N. Asada, and T. Hattori. The extinction coefficients in mid- and far-infrared of silicate and iron-oxide minerals of interest for astronomical observations. Astrophysics and Space Science, 79:77–85, September 1981. doi: 10.1007/BF00655906.

C. Koike, C. Kaito, T. Yamamoto, H. Shibai, S. Kimura, and H. Suto. Extinction spectra of corundum in the wavelengths from UV to FIR. Icarus, 114:203–214, March 1995. doi: 10.1006/icar.1995.1055.

C. Koike, H. Chihara, A. Tsuchiyama, H. Suto, H. Sogawa, and H. Okuda. Compositional dependence of infrared absorption spectra of crystalline silicate. II. Natural and synthetic olivines. Astronomy and Astrophysics, 399:1101–1107, March 2003. doi: 10.1051/0004-6361:20021831.

R. Kotak. Core-Collapse Supernovae as Dust Producers. In F. Bresolin, P. A. Crowther, and J. Puls, editors, IAU Symposium, volume 250 of IAU Symposium, pages 437–442, June 2008. doi: 10.1017/S1743921308020802.

R. Kotak, P. Meikle, S. D. van Dyk, P. A. Höflich, and S. Mattila. Early-Time Spitzer Observations of the Type II Plateau Supernova SN 2004dj. The Astrophysical Journal Letters, 628:L123–L126, August 2005. doi: 10.1086/432719.

R. Kotak, P. Meikle, M. Pozzo, S. D. van Dyk, D. Farrah, R. Fesen, A. V. Filippenko, R. J. Foley, C. Fransson, C. L. Gerardy, P. A. Höflich, P. Lundqvist, S. Mattila, J. Sollerman, and J. C. Wheeler. Spitzer Measurements of Atomic and Molecular Abundances in the Type IIP SN 2005af. The Astrophysical Journal Letters, 651: L117–L120, November 2006. doi: 10.1086/509655.

R. Kotak, W. P. S. Meikle, D. Farrah, C. L. Gerardy, R. J. Foley, S. D. Van Dyk, C. Fransson, P. Lundqvist, J. Sollerman, R. Fesen, A. V. Filippenko, S. Mattila, J. M. Silverman, A. C. Andersen, P. A. Höflich, M. Pozzo, and J. C. Wheeler. Dust and The Type II-Plateau Supernova 2004et. The Astrophysical Journal, 704:306–323, October 2009. doi: 10.1088/0004-637X/704/1/306.

T. Kozasa, H. Hasegawa, and K. Nomoto. Formation of dust grains in the ejecta of SN 1987A. The Astrophysical Journal, 344:325–331, September 1989. doi: 10.1086/167801.

T. Kozasa, T. Nozawa, N. Tominaga, H. Umeda, K. Maeda, and K. Nomoto. Dust in Supernovae: Formation and Evolution. In T. Henning, E. Grün, and J. Steinacker, editors, Cosmic Dust - Near and Far, volume 414 of Astronomical Society of the Pacific Conference Series, page 43, December 2009.

O. Krause, S. M. Birkmann, T. Usuda, T. Hattori, M. Goto, G. H. Rieke, and K. A. Misselt. The Cassiopeia A Supernova Was of Type IIb. Science, 320:1195–, May 2008. doi: 10.1126/science.1155788.

S. Lepp, A. Dalgarno, and R. McCray. Molecules in the ejecta of SN 1987A. The Astrophysical Journal, 358:262–265, July 1990. doi: 10.1086/168981.

M. Limongi, O. Straniero, and A. Chieffi. Massive Stars in the Range 13-25 M_{solar}: Evolution and Nucleosynthesis. II. The Solar Metallicity Models. The Astrophysical Journal Supplement Series, 129:625–664, August 2000. doi: 10.1086/313424.

W. Liu and A. Dalgarno. Silicon monoxide in SN 1987A. The Astrophysical Journal, 428:769–776, June 1994. doi: 10.1086/174285.

W. Liu and A. Dalgarno. The Oxygen Temperature of SN 1987A. The Astrophysical Journal, 454:472, November 1995. doi: 10.1086/176498.

W. Liu, A. Dalgarno, and S. Lepp. Carbon monoxide in SN 1987A. The Astrophysical Journal, 396:679–685, September 1992. doi: 10.1086/171749.

W.C. Lu, C.Z. Wang, and et al. Carbon Rings. Journal of Physical Chemistry, 97:3460, April 1993. doi: 10.1021/j100116a003.

W.C. Lu, C.Z. Wang, and et al. Structures and Fragmentations of Small Silicon Oxide Clusters by ab Initio Calculations. Journal of Physical Chemistry A, 107:6936, 2003. doi: 10.1021/jp027860h.

L. B. Lucy, I. J. Danziger, C. Gouiffes, and P. Bouchet. Dust Condensation in the Ejecta of SN 1987 A. In G. Tenorio-Tagle, M. Moles, and J. Melnick, editors, IAU Colloq. 120: Structure and Dynamics of the Interstellar Medium, volume 350 of Lecture Notes in Physics, Berlin Springer Verlag, page 164, 1989. doi: 10.1007/BFb0114861.

G. M. MacAlpine and T. J. Satterfield. The Crab Nebula's Composition and Precursor Star Mass. The Astronomical Journal, 136:2152–2157, November 2008. doi: 10.1088/0004-6256/136/5/2152.

Y. N. Makurin, A. A. Sofronov, A. I. Gusev, and A. L. Ivanovsky. Electronic structure and chemical stabilization of C $_{28}$ fullerene. Chemical Physics, 270:293–308, August 2001. doi: 10.1016/S0301-0104(01)00342-1.

P. G. Martin. Cosmic dust. Its impact on astronomy. Oxford Studies in Physics, Oxford: Clarendon Press, 1978, 1978.

T. Matheson, A. V. Filippenko, R. Chornock, D. C. Leonard, and W. Li. Helium Emission Lines in the Type IC Supernova 1999CQ. The Astronomical Journal, 119: 2303–2310, May 2000a. doi: 10.1086/301352.

T. Matheson, A. V. Filippenko, L. C. Ho, A. J. Barth, and D. C. Leonard. Detailed Analysis of Early to Late-Time Spectra of Supernova 1993J. The Astronomical Journal, 120:1499–1515, September 2000b. doi: 10.1086/301519.

J. S. Mathis, W. Rumpl, and K. H. Nordsieck. The size distribution of interstellar grains. The Astrophysical Journal, 217:425–433, October 1977. doi: 10.1086/155591.

M. Matsuura, E. Dwek, M. Meixner, M. Otsuka, B. Babler, M. J. Barlow, J. Roman-Duval, C. Engelbracht, K. Sandstrom, M. Lakićević, J. T. van Loon, G. Sonneborn, G. C. Clayton, K. S. Long, P. Lundqvist, T. Nozawa, K. D. Gordon, S. Hony, P. Panuzzo, K. Okumura, K. A. Misselt, E. Montiel, and M. Sauvage. Herschel Detects a Massive Dust Reservoir in Supernova 1987A. Science, 333:1258–, September 2011. doi: 10.1126/science.1205983.

J. C. Mauerhan, N. Smith, J. M. Silverman, A. V. Filippenko, A. N. Morgan, S. B. Cenko, M. Ganeshalingam, K. I. Clubb, J. S. Bloom, T. Matheson, and P. Milne. SN 2011ht: confirming a class of interacting supernovae with plateau light curves (Type IIn-P). Monthly Notices of the Royal Astronomical Society, 431:2599–2611, May 2013. doi: 10.1093/mnras/stt360.

R. McCray. Supernova 1987A revisited. Annual Review of Astronomy and Astrophysics, 31:175–216, 1993. doi: 10.1146/annurev.aa.31.090193.001135.

B. K. McMillin, P. Biswas, and M. R. Zachariah. In situ characterization of vapor phase growth of iron oxide-silica nanocomposites: Part I. 2-D planar laser-induced fluorescence and Mie imaging. Journal of Material Research, 11:1552, June 1996.

W. P. S. Meikle, J. Spyromilio, D. A. Allen, G.-F. Varani, and R. J. Cumming. Spectroscopy of supernova 1987A at 1-4 microns. II - Days 377 to 1114. Monthly Notices of the Royal Astronomical Society, 261:535–572, April 1993.

W. P. S. Meikle, R. Kotak, D. Farrah, S. Mattila, S. D. Van Dyk, A. C. Andersen, R. Fesen, A. V. Filippenko, R. J. Foley, C. Fransson, C. L. Gerardy, P. A. Höflich, P. Lundqvist, M. Pozzo, J. Sollerman, and J. C. Wheeler. Dust and the Type II-plateau Supernova 2004dj. The Astrophysical Journal, 732:109, May 2011. doi: 10.1088/0004-637X/732/2/109.

R. Minkowski. Spectra of Supernovae. Publications of the Astronomical Society of the Pacific, 53:224, August 1941. doi: 10.1086/125315.

F. J. Molster. Astromineralogy: Crystalline silicates (invited review). In S. Kwok, M. Dopita, and R. Sutherland, editors, Planetary Nebulae: Their Evolution and Role in the Universe, volume 209 of IAU Symposium, page 291, 2003.

F. J. Molster, L. B. F. M. Waters, and F. Kemper. The Mineralogy of Interstellar and Circumstellar Dust in Galaxies. In T. Henning, editor, Lecture Notes in Physics, Berlin Springer Verlag, volume 815 of Lecture Notes in Physics, Berlin Springer Verlag, pages 143–201, 2010. doi: 10.1007/978-3-642-13259-9_3.

S. H. Moseley, E. Dwek, W. Glaccum, J. R. Graham, and R. F. Loewenstein. Far-infrared observations of thermal dust emission from supernova 1987A. Nature, 340: 697–699, August 1989. doi: 10.1038/340697a0.

H. Mutschke, A. C. Andersen, D. Clément, T. Henning, and G. Peiter. Infrared properties of SiC particles. Astronomy and Astrophysics, 345:187–202, May 1999.

E. P. Ney and R. J. Gould. Infrared Radiation from B Stars. Astrophysical Journal, 140:388, July 1964. doi: 10.1086/147933.

L. R. Nittler. Presolar Stardust In The Solar System: Recent Advances for Nuclear Astrophysics. In Nuclei in the Cosmos (NIC X), 2008.

K. I. Nomoto, K. Iwamoto, and T. Suzuki. The evolution and explosion of massive binary stars and Type Ib-Ic-IIb-IIL supernovae. Physics Reports, 256:173–191, May 1995. doi: 10.1016/0370-1573(94)00107-E.

T. Nozawa and T. Kozasa. Formulation of Non-steady-state Dust Formation Process in Astrophysical Environments. The Astrophysical Journal, 776:24, October 2013. doi: 10.1088/0004-637X/776/1/24.

T. Nozawa, T. Kozasa, H. Umeda, K. Maeda, and K. Nomoto. Dust in the Early Universe: Dust Formation in the Ejecta of Population III Supernovae. The Astrophysical Journal, 598:785–803, December 2003. doi: 10.1086/379011.

T. Nozawa, T. Kozasa, N. Tominaga, K. Maeda, H. Umeda, K. Nomoto, and O. Krause. Formation and Evolution of Dust in Type IIb Supernovae with Application to the Cassiopeia A Supernova Remnant. The Astrophysical Journal, 713:356–373, April 2010. doi: 10.1088/0004-637X/713/1/356.

V. Ossenkopf, T. Henning, and J. S. Mathis. Constraints on cosmic silicates. Astronomy & Astrophysics, 261:567–578, August 1992.

A. Pastorello, S. Valenti, L. Zampieri, H. Navasardyan, S. Taubenberger, S. J. Smartt, A. A. Arkharov, O. Bärnbantner, H. Barwig, S. Benetti, P. Birtwhistle, M. T. Botticella, E. Cappellaro, M. Del Principe, F. di Mille, G. di Rico, M. Dolci, N. Elias-Rosa, N. V. Efimova, M. Fiedler, A. Harutyunyan, P. A. Höflich, W. Kloehr, V. M. Larionov, V. Lorenzi, J. R. Maund, N. Napoleone, M. Ragni, M. Richmond, C. Ries, S. Spiro,

S. Temporin, M. Turatto, and J. C. Wheeler. SN 2005cs in M51 - II. Complete evolution in the optical and the near-infrared. Monthly Notices of the Royal Astronomical Society, 394:2266–2282, April 2009. doi: 10.1111/j.1365-2966.2009.14505.x.

Y. C. Pei, S. M. Fall, and J. Bechtold. Confirmation of dust in damped Lyman-alpha systems. The Astrophysical Journal, 378:6–16, September 1991. doi: 10.1086/170401.

M. Pettini, L. J. Smith, R. W. Hunstead, and D. L. King. Metal enrichment, dust, and star formation in galaxies at high redshifts. 3: Zn and CR abundances for 17 damped Lyman-alpha systems. The Astrophysical Journal, 426:79–96, May 1994. doi: 10.1086/174041.

M. Pozzo, W. P. S. Meikle, J. T. Rayner, R. D. Joseph, A. V. Filippenko, R. J. Foley, W. Li, S. Mattila, and J. Sollerman. Optical and infrared observations of the TypeIIP SN2002hh from days 3 to 397. Monthly Notices of the Royal Astronomical Society, 368:1169–1195, May 2006. doi: 10.1111/j.1365-2966.2006.10204.x.

Sotiris E. Pratsinis. Flame aerosol synthesis of ceramic powders . Progress in Energy and Combustion Science, 24(3):197, 1998. doi: http://dx.doi.org/10.1016/S0360-1285(97)00028-2.

T. Rauscher, A. Heger, R. D. Hoffman, and S. E. Woosley. Nucleosynthesis in Massive Stars with Improved Nuclear and Stellar Physics. The Astrophysical Journal, 576:323–348, September 2002. doi: 10.1086/341728.

A C. Reber, S. Paranthaman, P. A. Clayborne, and et al. From SiO Molecules to Silicates in Circumstellar Space: Atomic Structures, Growth Patterns, and Optical Signatures of Si_nO_m Clusters. ACS Nano, 2:1729, August 2008. doi: 10.1021/nn7003958.

J. Rho, T. Kozasa, W. T. Reach, J. D. Smith, L. Rudnick, T. DeLaney, J. A. Ennis, H. Gomez, and A. Tappe. Freshly Formed Dust in the Cassiopeia A Supernova Remnant as Revealed by the Spitzer Space Telescope. The Astrophysical Journal, 673:271–282, January 2008. doi: 10.1086/523835.

J. Rho, T. H. Jarrett, W. T. Reach, H. Gomez, and M. Andersen. Carbon Monoxide in the Cassiopeia a Supernova Remnant. The Astrophysical Journal Letters, 693:L39–L43, March 2009. doi: 10.1088/0004-637X/693/1/L39.

J. Rho, T. Onaka, J. Cami, and W. T. Reach. Spectroscopic Detection of Carbon Monoxide in the Young Supernova Remnant Cassiopeia A. The Astrophysical Journal Letters, 747:L6, March 2012. doi: 10.1088/2041-8205/747/1/L6.

P. F. Roche, D. K. Aitken, and C. H. Smith. Silicon monoxide in supernova 1987A. Monthly Notices of the Royal Astronomical Society, 252:39P–42P, September 1991.

Jarl B. Rosenholm, Kai-Erik Peiponen, and Evgeny Gornov. Materials cohesion and interaction forces. Advances in Colloid and Interface Science, 141:48 – 65, 2008. doi: http://dx.doi.org/10.1016/j.cis.2008.03.001. URL http://www.sciencedirect.com/science/article/pii/S0001868608000407.

M. Salaris and S. Cassisi. Evolution of Stars and Stellar Populations. John Wiley & Sons, Ltd, 2006.

A. Sarangi and I. Cherchneff. The Chemically Controlled Synthesis of Dust in Type II-P Supernovae. The Astrophysical Journal, 776:107, October 2013. doi: 10.1088/0004-637X/776/2/107.

A. Sarangi and I. Cherchneff. Condensation of Dust in the Ejecta of Type II-P Supernovae. Astronomy & Astrophysics (submitted), 2014.

Russell W. Saunders and John M.C. Plane. Fractal growth modelling of nanoparticles. Journal of Aerosol Science, 37:1737 – 1749, 2006. doi: http://dx.doi.org/10.1016/j.jaerosci.2006.08.007. URL http://www.sciencedirect.com/science/article/pii/S0021850206001534.

Mark G Sceats. Brownian coagulation in aerosolsthe role of long range forces. Journal of Colloid and Interface Science, 129:105 – 112, 1989. doi: http://dx.doi.org/10.1016/0021-9797(89)90419-0. URL http://www.sciencedirect.com/science/article/pii/0021979789904190.

E. M. Schlegel. A new subclass of Type II supernovae? Monthly Notices of the Royal Astronomical Society, 244:269–271, May 1990.

T. Shigeyama and K. Nomoto. Theoretical light curve of SN 1987A and mixing of hydrogen and nickel in the ejecta. Astrophysical Journal, 360:242–256, September 1990. doi: 10.1086/169114.

S. J. Smartt, J. R. Maund, M. A. Hendry, C. A. Tout, G. F. Gilmore, S. Mattila, and C. R. Benn. Detection of a Red Supergiant Progenitor Star of a Type II-Plateau Supernova. Science, 303:499–503, January 2004. doi: 10.1126/science.1092967.

S. J. Smartt, J. J. Eldridge, R. M. Crockett, and J. R. Maund. The death of massive stars - I. Observational constraints on the progenitors of Type II-P supernovae. Monthly Notices of the Royal Astronomical Society, 395:1409–1437, May 2009. doi: 10.1111/j.1365-2966.2009.14506.x.

N. Smith, J. M. Silverman, A. V. Filippenko, M. C. Cooper, T. Matheson, F. Bian, B. J. Weiner, and J. M. Comerford. Systematic Blueshift of Line Profiles in the Type

IIn Supernova 2010jl: Evidence for Post-shock Dust Formation? The Astronomical Journal, 143:17, January 2012. doi: 10.1088/0004-6256/143/1/17.

J. Spyromilio and B. Leibundgut. Carbon monoxide in supernova 1995ad. Monthly Notices of the Royal Astronomical Society, 283:L89–L93, December 1996.

J. Spyromilio, W. P. S. Meikle, R. C. M. Learner, and D. A. Allen. Carbon monoxide in supernova 1987A. Nature, 334:327–329, July 1988. doi: 10.1038/334327a0.

J. Spyromilio, B. Leibundgut, and R. Gilmozzi. Carbon Monoxide in type II supernovae. Astronomy and Astrophysics, 376:188–193, September 2001. doi: 10.1051/0004-6361:20010948.

J. Steinacker, M. Baes, and K. D. Gordon. Three-Dimensional Dust Radiative Transfer*. Annual Review of Astronomy and Astrophysics, 51:63–104, August 2013. doi: 10.1146/annurev-astro-082812-141042.

B. E. K. Sugerman, B. Ercolano, M. J. Barlow, A. G. G. M. Tielens, G. C. Clayton, A. A. Zijlstra, M. Meixner, A. Speck, T. M. Gledhill, N. Panagia, M. Cohen, K. D. Gordon, M. Meyer, J. Fabbri, J. E. Bowey, D. L. Welch, M. W. Regan, and R. C. Kennicutt. Massive-Star Supernovae as Major Dust Factories. Science, 313:196–200, July 2006. doi: 10.1126/science.1128131.

H. Suto, C. Koike, H. Sogawa, A. Tsuchiyama, H. Chihara, and K. Mizutani. Infrared spectra of fayalite crystal. Astronomy and Astrophysics, 389:568–571, July 2002. doi: 10.1051/0004-6361:20020501.

T. Szalai and J. Vinkó. Twelve type II-P supernovae seen with the eyes of Spitzer. Astronomy & Astrophysics, 549:A79, January 2013. doi: 10.1051/0004-6361/201220015.

T. Szalai, J. Vinkó, Z. Balog, A. Gáspár, M. Block, and L. L. Kiss. Dust formation in the ejecta of the type II-P supernova 2004dj. Astronomy & Astrophysics, 527:A61, March 2011. doi: 10.1051/0004-6361/201015624.

T. Temim and E. Dwek. The Importance of Physical Models for Deriving Dust Masses and Grain Size Distributions in Supernova Ejecta. I. Radiatively Heated Dust in the Crab Nebula. The Astrophysical Journal, 774:8, September 2013. doi: 10.1088/0004-637X/774/1/8.

F.-K. Thielemann, K. Nomoto, and M.-A. Hashimoto. Core-Collapse Supernovae and Their Ejecta. Astrophysical Journal, 460:408, March 1996. doi: 10.1086/176980.

F.-K. Thielemann, R. Hirschi, M. Liebendörfer, and R. Diehl. Massive Stars and Their Supernovae. In R. Diehl, D. H. Hartmann, and N. Prantzos, editors, Lecture Notes in Physics, Berlin Springer Verlag, volume 812 of Lecture Notes in Physics, Berlin Springer Verlag, pages 153–232, 2011.

A. G. G. M. Tielens, L. B. F. M. Waters, F. J. Molster, and K. Justtanont. Circumstellar Silicate Mineralogy. Astrophysics and Space Science, 255:415–426, 1998. doi: 10.1023/A:1001585120472.

P. Todini and A. Ferrara. Dust formation in primordial Type II supernovae. Monthly Notices of the Royal Astronomical Society, 325:726–736, August 2001. doi: 10.1046/j.1365-8711.2001.04486.x.

R. J. Trumpler. Absorption of Light in the Galactic System. Publications of the Astronomical Society of the Pacific, 42:214, August 1930. doi: 10.1086/124039.

M. Turatto. Classification of Supernovae. In K. Weiler, editor, Supernovae and Gamma-Ray Bursters, volume 598 of Lecture Notes in Physics, Berlin Springer Verlag, pages 21–36, 2003.

H. Umeda and K. Nomoto. Nucleosynthesis of Zinc and Iron Peak Elements in Population III Type II Supernovae: Comparison with Abundances of Very Metal Poor Halo Stars. The Astrophysical Journal, 565:385–404, January 2002. doi: 10.1086/323946.

H. Umeda and K. Nomoto. How Much ^{56}Ni Can Be Produced in Core-Collapse Supernovae? Evolution and Explosions of 30-100 M_{solar} Stars. The Astrophysical Journal, 673:1014–1022, February 2008. doi: 10.1086/524767.

J. Vinkó, K. Sárneczky, Z. Balog, S. Immler, B. E. K. Sugerman, P. J. Brown, K. Misselt, G. M. Szabó, S. Csizmadia, M. Kun, P. Klagyivik, R. J. Foley, A. V. Filippenko, B. Csák, and L. L. Kiss. The Young, Massive, Star Cluster Sandage-96 After the Explosion of Supernova 2004dj in NGC 2403. The Astrophysical Journal, 695:619–635, April 2009. doi: 10.1088/0004-637X/695/1/619.

H. J. Walker. A brief history of infrared astronomy. Astronomy and Geophysics, 41(5): 10, October 2000. doi: 10.1046/j.1468-4004.2000.41510.x.

X. Wang, Y. Yang, T. Zhang, J. Ma, X. Zhou, W. Li, Y.-Q. Lou, and Z. Li. The Progenitor of SN 2004dj in a Star Cluster. The Astrophysical Journal Letters, 626: L89–L92, June 2005. doi: 10.1086/431903.

T. A. Weaver and S. E. Woosley. Nucleosynthesis in massive stars and the ^{12}C(α, γ)^{16}O reaction rate. Physics Reports, 227:65–96, May 1993. doi: 10.1016/0370-1573(93)90058-L.

J. C. Wheeler and S. Benetti. Supernovae, page 451. Cox, A. N., 2000.

D. H. Wooden, D. M. Rank, J. D. Bregman, F. C. Witteborn, A. G. G. M. Tielens, M. Cohen, P. A. Pinto, and T. S. Axelrod. Airborne spectrophotometry of SN 1987A from 1.7 to 12.6 microns - Time history of the dust continuum and line emission. Astrophysical Journal Supplement Series, 88:477–507, October 1993. doi: 10.1086/191830.

S. E. Woosley. SN 1987A - After the peak. The Astrophysical Journal, 330:218–253, July 1988. doi: 10.1086/166468.

S. E. Woosley and A. Heger. Nucleosynthesis and remnants in massive stars of solar metallicity. Physics Reports, 442:269–283, April 2007. doi: 10.1016/j.physrep.2007.02.009.

S. E. Woosley and T. A. Weaver. The Evolution and Explosion of Massive Stars. II. Explosive Hydrodynamics and Nucleosynthesis. Astrophysical Journal Supplement, 101:181, November 1995. doi: 10.1086/192237.

S. E. Woosley, D. Hartmann, and P. A. Pinto. Hard emission at late times from SN 1987A. The Astrophysical Journal, 346:395–404, November 1989. doi: 10.1086/168019.

S. E. Woosley, A. Heger, and T. A. Weaver. The evolution and explosion of massive stars. Reviews of Modern Physics, 74:1015–1071, November 2002. doi: 10.1103/RevModPhys.74.1015.

M. R. Zachariah and W. Tsang. Application of Ab-Initio Molecular Orbital and Reaction Rate Theories to Nucleation Kinetics. Aerosol Science & Technology, 19:499, 1993.

E. Zinner. 1.02 - presolar grains. In Treatise on Geochemistry, pages 1 – 33. Pergamon, Oxford, 2007. doi: http://dx.doi.org/10.1016/B0-08-043751-6/01144-0. URL `http://www.sciencedirect.com/science/article/pii/B0080437516011440`.

E. Zinner, M. Jadhav, F. Gyngard, and L. R. Nittler. Bonanza: Isotopic Anatomy of a Large Presolar SiC Grain of Type X. Meteoritics and Planetary Science Supplement, 73:5137, September 2010.

V. G. Zubko, V. Mennella, L. Colangeli, and E. Bussoletti. Optical constants of cosmic carbon analogue grains - I. Simulation of clustering by a modified continuous distribution of ellipsoids. Monthly Notices of the Royal Astronomical Society, 282:1321–1329, October 1996.